Computational Design of Catalysts for Electrochemical Hydrogen Evolution and Nitrogen Reduction

By Xin Liu

School of Chemical Engineering and Advanced Materials

Faculty of Engineering, Computer and Mathematical Science

A thesis submitted for the degree of Doctor of Philosophy

The University of Adelaide

Feb 2021

Table of Contents

Abstract

The development of efficient and carbon-neutral energy conversion technologies is a key issue for modern society's sustainability. The electrochemical hydrogen evolution reaction (HER) is regarded as a practical means for the production of high-purity hydrogen from abundant water. Such systems utilize renewable energy sources (wind or solar et al.) to power the electrocatalysis process with components of air (CO_2, N_2) and water as feedstocks to produce fuels or commodity chemicals, for example, electrochemical nitrogen reduction reaction (eNRR). Consequently, understanding the reaction mechanisms and the connection between catalytic performance and the intrinsic property of materials is of great importance. Density functional theory (DFT) based simulation methods proved powerful in exploring the in-depth insights of reaction mechanisms. This Thesis aims to apply DFT based computational methods to the study of electrocatalytic reactions like HER and eNRR and provide guidance for the design of catalysts for such processes.

The first two chapters provide a systematic review of theoretical progress in exploring key electrocatalytic reactions' reaction mechanisms. The in-depth insights are presented based on the elucidation of reaction mechanisms, and the origins of different types of catalysts are discussed. The experimental aspects that could be combined with theoretical predictions are also addressed in this part. A significant emphasis is placed on comparing the different design principles for various types of materials.

The first part of this thesis focuses on understanding alkaline HER mechanism using Pt/Ru dimer catalysts as the model catalysts. So far, the mechanistic understandings of alkaline HER are limited, especially for the debate on whether there is a singular descriptor for connecting the performance with the thermodynamic quantities. The dissociative chemisorption energy of water (ΔE_{diss}) as a singular activity descriptor following the analysis of several potential activity descriptors. ΔE_{diss} is proposed both because it has the capacity to identify the smallest theoretical thermodynamic overpotential and because it scales linearly with the kinetic barrier. These findings will

be of immediate benefit to the guide rational development of electrocatalysts via electronic structural engineering to regulate ΔE_{diss} for the alkaline HER.

The second part of the Thesis focuses on revealing the reaction mechanisms for eNRR on newly emerged materials. Firstly, a full picture (activity trends, electronic origins, and design strategies) of single-atom catalysts (SACs) supported on nitrogen-doped carbons as eNRR electrocatalysts are established. To construct such a picture, this work presents systematic studies of 60 types of transition metal SACs supported on nitrogen-containing carbon materials. The results show that the intrinsic activity trends could be established on the basis of the nitrogen adatom adsorption energy (ΔE_{N*}). Furthermore, the influence of metal and support (ligands) on ΔE_{N*} proved to be related to the bonding/antibonding orbital population and regulating the scaling relations for adsorption of intermediates, respectively. Accordingly, a two-step strategy is then proposed for improving the eNNR activity of TM-SACs. Also, the stability of N doped carbon supports and their selectivity in comparison to the competing hydrogen evolution need to be taken into consideration for screening the durable and efficient candidates. Finally, an effective strategy for designing active, stable, and elective SACs based on the mechanistic insights is elaborated to guide future eNRR studies. Secondly, the electrochemical nitrogen reduction reaction (eNRR) activity on binary metal boride is investigated as a model system of metal borides. To elaborate the mechanisms, molybdenum borides (Mo_2B, α-MoB, and MoB_2) were first modeled; the results indicate that the crystal structures greatly impact the N_2 adsorption and therefore, the electrocatalytic activity. Our electronic structure investigation suggests that boron p orbital hybrids with dinitrogen π* orbital, and the population on p-π* orbital determine the N_2 adsorption strength. Therefore, the isolated boron site of Mo_2B with less filled p_z orbital benefits the activation of N_2 and weaken the triple bond of dinitrogen. This isolated boron site concept was successfully extended to other metal borides in the form of M_2B (M stands for Ti, Cr, Mn, Fe, Co, Ni, Ta, W). Mo_2B, Fe_2B, and Co_2B were discovered as the most promising candidates with low limiting potentials due to the appropriate adsorption strength of reaction intermediates led by moderate p_z filling.

This part provides insights for designing metal borides as promising eNRR catalysts.

The third part of this Thesis explores the reaction mechanisms for C-N bond formation during urea production of $CO_{(2)}$ electrolysis with nitrogen containing feedstocks which is an emerging opportunity for the electrosynthesis of commodity chemicals. The feedstocks for such reactions are CO or CO_2 as carbon source, nitrate, nitrite, or NO_x as the nitrogen source. The bottleneck for such systems still remains the lack of understanding of detailed reaction mechanisms and key reaction intermediates, which impedes the ration-al design of efficient catalyst materials for these reactions. To fill this knowledge gap, we applied ab initio molecular dynamics (AIMD) with explicit water molecules under different electrode potentials to explore the C-N bond formation mechanisms toward urea ($CO(NH_2)_2$) production on Cu (100) surface in neutral electrolyte. Based on the kinetic barrier values, we established reaction pathways towards urea and ammonia; the former involves C-N bond formation while the latter does not. We found a potential-dependent mechanism that accounts for the selective production of urea. For more positive electrode potentials, i.e., near -0.75 V vs standard hydrogen electrode (SHE), the coupling between NH* and CO* is kinetically viable which leads to the formation of urea. At more negative potentials, e.g., around -1.5 V vs. SHE, CO_2 reduction was accelerated and suppress urea and ammonia formations. These findings propose the potential-dependent mechanisms for C-N bond formation, which would benefit the design of new catalyst materials for electrosynthesis of more value-added products.

At last, the challenges and perspectives of computational simulations based on DFT methods for electrocatalysis were discussed. These methods proved powerful in revealing the reaction mechanism as well as guiding the rational design of catalysts for electrocatalytic processes such as HER and NRR. Moreover, advanced simulation methods based on AIMD methods would be capable of capturing more realistic reaction environment and provide new comprehensive insights for the electrochemical process.

Declaration

I certify that this work contains no material which has been accepted for the award of any other degree or diploma in my name, in any university or other tertiary institution and, to the best of my knowledge and belief, contains no material previously published or written by another person, except where due reference has been made in the text. In addition, I certify that no part of this work will, in the future, be used in a submission in my name, for any other degree or diploma in any university or other tertiary institution without the prior approval of the University of Adelaide and where applicable, any partner institution responsible for the joint-award of this degree.

I acknowledge that copyright of published works contained within this thesis resides with the copyright holder(s) of those works.

I also give permission for the digital version of my thesis to be made available on the web, via the University's digital research repository, the Library Search and also through web search engines, unless permission has been granted by the University to restrict access for a period of time.

Name of Candidate: Xin Liu

Signature:

Date: 07/Feb/2021

Acknowledgments

This thesis would not be accomplished without the support and help from my supervisors, friends, and families. Here, I would like to express my gratitude to them all.

First and foremost, I would like to thank my principal supervisor, Professor Shi-Zhang Qiao for his inspiring guidance, supportive encouragement, and professional supervision throughout my PhD candidature. He also gives me the room to take challenge and adventure when conducting research in some emerging fields, which I appreciate the most during my study. I could not get any achievements without his guidance and support in my Ph.D study. And I will benefit from his training as a researcher in my future career. I sincerely appreciate my co-supervisor Dr. Yan Jiao, for her insightful suggestions and continuous encouragement.

I am also grateful to all the members in the Qiao's group who give me many supports and suggestions during my PhD study. My special thanks go to Dr. Yao Zheng, Dr Huanyu Jin, Dr Chaochen Xu, Dr. Ke Zhang for their support, cooperation, company and kindness.

It is a great pleasure to express my appreciation to Michelle Fitton, Sue Earle from School of Chemical Engineering and Advanced Materials for their administrative helps, Dr. Kenneth Davey also from our school and Prof. Mietek Jaroniec from Kent State University for fruitful discussions and suggestions for paper writing.

I would also like to acknowledge the Australian Government, The University of Adelaide, and Australia Research Council for their financial support.

Finally, I would express my deepest gratitude to my parents Shiyu Liu and Wanfang Yang who raised me up with love, and didn't give up when I was badly ill to depth as a small baby. They provide me the chance to live a life that matters and all they have to support me to pursue my career. I appreciate my elder sister Xiujuan Liu and brother-in-law, Peng Yu, for their consideration and care for our parents, especially when mom

Chapter 1: Introduction

1.1 Significance of the Project

Electrochemical methods provide an attractive alternative to current energy and commodity chemical productions. The advantages of electrochemical systems are that they are can be integrated with renewable energy, and thus hopefully will help in the problem of reliance on fossil resources.[1-3] As the core of electrocatalysis systems, the electrocatalysts determine the energy conversion efficiency and thus designing high performance is of great importance for the development of these systems. Hydrogen evolution reaction, being the most fundamental and most generally involved reaction in the energy conversion process, serves as the cornerstone in both mechanistic study and application development. Another key process is nitrogen fixation, which is the basis for the electrochemical production of ammonia as the fertilizer or energy carrier.[3,4]

Thanks to the recent progress of computational methods based on density functional theory (DFT), the area of catalysts design made tremendous progress in the last two decades.[5,6] Computational predictions of the activity trends agreed with experimental observations from electrochemical measurements. For example, Norskov et. al. found that the theoretical overpotential from DFT calculations could estimate the exchange current density of oxygen reduction reaction and hydrogen evolution reaction in acid. However, even though much efforts made, there's still no systematic explanation on the slow alkaline HER reaction kinetics.[7] For electrochemical nitrogen reduction reaction (eNRR), a more general picture is still absent for the design principles of new catalysts such as single atom catalysts and metal borides. Moreover, a new electrocatalysis system would bring more opportunities for producing commodity chemicals with added-values.[8,9] For electrocatalysts design, computational modeling could help elucidate the reaction mechanisms and speed up the screening and optimization of catalysts candidates.

1.2 Research Objectives

The major goals of this Thesis are to reveal the reaction mechanisms by computational

methods for electrocatalysis processes such as the HER and NRR. In particular, the objectives of this thesis are:

- *To understand* the reaction mechanism of hydrogen evolution reaction in alkaline and explore whether there is the singular activity descriptor.

- *To build up* a full picture covering electronic origins, activity trends and design principles of single atom catalysts for eNRR.

- *To explore* the potential of metal nitrides as eNRR catalysts and the activity origins of isolated boron sites.

- *To investigate* the C-N bond formation mechanisms via ab initio molecular dynamics.

- *To address the significance* of simulation methods as a powerful tool to explore the reaction mechanisms.

- *To explore* the new research paradigm by combining theoretical simulations and experiments.

1.3 Thesis Outline

This thesis is presented in the form of journal publications. It contains research results on the mechanistic study by density functional theory (DFT) computations as well as the design principles of new eNRR catalysts. Recent progress and challenges were reviewed, followed by discussions of the applications of simulation methods based on DFT methods in electrocatalysis. Specifically, the chapters in the Thesis are presented in the following sequence:

➢ *Chapter 1* introduces the significance of this project and outlines the research objectives and key contributions to the understanding of reaction mechanisms and rational design of catalysts.

➢ *Chapter 2* reviews the recent progresses and challenges of single site catalysts (SSCs) for electrochemical nitrogen reduction.

➢ *Chapter 3* presents the mechanism insights for metal dimer catalysts for alkaline hydrogen evolution reaction.

➢ *Chapter 4* investigates single transition metal catalysts for the electrochemical nitrogen reduction reaction.

- *Chapter 5* studies binary metal borides as potential catalysts for electrochemical nitrogen reduction reaction and elucidates the activity origins of isolated boron sites.

- *Chapter 6* explores the mechanisms of C-N formations during electrochemical $CO_{(2)}$ reduction with nitrogenous feedstocks.

- *Chapter 7* presents the conclusion and perspectives for further work on computational study on revealing the electrocatalytic reaction mechanisms as well as the rational design of catalysts.

1.4 References

1. Otto, A.; Grube, T.; Schiebahn, S.; Stolten, D. Closing the loop: captured CO_2 as a feedstock in the chemical industry. *Energy & Environmental Science* **2015**, *8*, 3283-3297.

2. Montoya, J. H.; Seitz, L. C.; Chakthranont, P.; Vojvodic, A.; Jaramillo, T. F.; Nørskov, J. K. Materials for solar fuels and chemicals. *Nature Materials* **2017**, *16*, 70-81.

3. Comer, B. M.; Fuentes, P.; Dimkpa, C. O.; Liu, Y.-H.; Fernandez, C. A.; Arora, P.; Realff, M.; Singh, U.; Hatzell, M. C.; Medford, A. J. Prospects and Challenges for Solar Fertilizers. *Joule* **2019**, *3*, 1578-1605.

4. Suryanto, B. H. R.; Du, H.-L.; Wang, D.; Chen, J.; Simonov, A. N.; MacFarlane, D. R. Challenges and prospects in the catalysis of electroreduction of nitrogen to ammonia. *Nature Catalysis* **2019**, *2*, 290-296.

5. Nørskov, J. K.; Rossmeisl, J.; Logadottir, A.; Lindqvist, L.; Kitchin, J. R.; Bligaard, T.; Jónsson, H. Origin of the Overpotential for Oxygen Reduction at a Fuel-Cell Cathode. *The Journal of Physical Chemistry B* **2004**, *108*, 17886-17892.

6. Nitopi, S.; Bertheussen, E.; Scott, S. B.; Liu, X.; Engstfeld, A. K.; Horch, S.; Seger, B.; Stephens, I. E.; Chan, K.; Hahn, C. J. C. r. Progress and perspectives of electrochemical CO_2 reduction on copper in aqueous electrolyte. **2019**, *119*, 7610-7672.

7. Liu, X.; Jiao, Y.; Zheng, Y.; Davey, K.; Qiao, S.-Z. A computational study on Pt and Ru dimers supported on graphene for the hydrogen evolution reaction: new insight into the alkaline mechanism. *Journal of Materials Chemistry A* **2019**, *7*, 3648-3654.

8. Jouny, M.; Lv, J. J.; Cheng, T.; Ko, B. H.; Zhu, J. J.; Goddard, W. A., 3rd; Jiao, F. Formation of carbon-nitrogen bonds in carbon monoxide electrolysis. *Nature Chemistry* **2019**, *11*, 846-851.

9. Chen, C.; Zhu, X.; Wen, X.; Zhou, Y.; Zhou, L.; Li, H.; Tao, L.; Li, Q.; Du, S.; Liu, T.; Yan, D.; Xie, C.; Zou, Y.; Wang, Y.; Chen, R.; Huo, J.; Li, Y.; Cheng, J.; Su, H.; Zhao, X.; Cheng, W.; Liu, Q.; Lin, H.; Luo, J.; Chen, J.; Dong, M.; Cheng, K.; Li, C.; Wang, S. Coupling N_2 and CO_2 in H_2O to synthesize urea under ambient conditions. *Nature Chemistry* **2020**, *12*, 717-724.

Chapter 2: Literature Review

2.1 Introduction and Significance

This Chapter reviews the recent advances in single site catalysts (SSCs) for electrochemical nitrogen reduction reaction (eNRR). The growing concerns of the greenhouse effect and demands for developing carbon-neutral technologies are one of the biggest challenges for the modern chemical industry. As one of the most important chemicals, ammonia is of great importance for agriculture as well as could serve as a high-quality hydrogen carrier. Developing an alternative to the traditional Haber-Bosch process via an electrochemical method display great potential due to the capability of integrating with renewable energy sources and using common available $N_{2(g)}$ and H_2O as feedstocks. Recently, single site catalysts received great attention for the application as electrocatalysts due to their unique physical, chemical, and electronic properties. The flexibility of regulating the composition and coordination environments of single site catalysts (SSCs) provides new opportunities for designing new generation eNRR catalysts. At the same time, there are already some progress from both experimental and theoretical aspects in the research of eNRR.

This Chapter presents a comprehensive summary of recent advances in the fundamental insights from the computational simulations as well as experimental observations. A special emphasis is placed on elucidations of the reaction mechanisms, according to which the rational design of eNRR catalysts is achieved. This chapter shed light on the difference of origins of various types of single site catalysts (SSCs), namely, single metal, non-metal, vacancy site catalyst, and outlined the core considerations when designing the eNRR catalysts. Furthermore, the aforementioned mechanisms are discussed compared with experimental measurements and advanced in-situ spectroscopy observations. Finally, the outlook of future development of single site eNRR catalysts for the application of eNRR are presented from both theoretical and experimental aspects; some emerging computational technologies are also addressed to accelerating the design of new catalysts.

2.2 Theoretical and Experimental Insights into Single Site Catalysts for Electrochemical Nitrogen Reduction

This Chapter is included as it appears as a manuscript by **Xin Liu**, Huanyu Jin, Yan Jiao*, Yao Zheng, Shi-Zhang Qiao*, Theoretical and Experimental Insights into Single Site Catalysts for Electrochemical Nitrogen Reduction. ***To be submitted.***

Statement of Authorship

Title of Paper	Theoretical and Experimental Insights into Single Site Catalysts for Electrochemical Nitrogen Reduction
Publication Status	☐ Published ☐ Accepted for Publication ☐ Submitted for Publication ☑ Unpublished and Unsubmitted work written in manuscript style
Publication Details	Theoretical and Experimental Insights into Single Site Catalysts for Electrochemical Nitrogen Reduction. *To be submitted.*

Principal Author

Name of Principal Author (Candidate)	Xin Liu		
Contribution to the Paper	Proposed ideas, conduct computations wrote the manuscript.		
Overall percentage (%)	80		
Certification:	This paper reports on original research I conducted during the period of my Higher Degree by Research candidature and is not subject to any obligations or contractual agreements with a third party that would constrain its inclusion in this thesis. I am the primary author of this paper.		
Signature		Date	3/Feb/2021

Co-Author Contributions

By signing the Statement of Authorship, each author certifies that:

   i. the candidate's stated contribution to the publication is accurate (as detailed above);

   ii. permission is granted for the candidate in include the publication in the thesis; and

   iii. the sum of all co-author contributions is equal to 100% less the candidate's stated contribution.

Name of Co-Author	Huanyu Jin		
Contribution to the Paper	Contributes to the experimental parts in the manuscript.		
Signature		Date	3/Feb/2021

Name of Co-Author	Yan Jiao		
Contribution to the Paper	Discussed the concepts, supervised the research project, and revised the manuscript.		
Signature		Date	3/Feb/2021

Name of Co-Author	Yao Zheng		
Contribution to the Paper	Discussed the concepts, and revised the manuscript.		
Signature		Date	3/Feb/2021

Name of Co-Author	Shi-Zhang Qiao		
Contribution to the Paper	Discussed concepts, supervised the research project, and revised the manuscript.		
Signature		Date	3/Feb/2021

Theoretical and Experimental Insights into Single Site Catalysts for Electrochemical Nitrogen Reduction

Xin Liu[†, ‡], Huanyu Jin[†, ‡], Yan Jiao[†, ‡], Yao Zheng[†, ‡], Shi-Zhang Qiao[†, ‡*]*

†School of Chemical Engineering and Advanced Materials, The University of Adelaide, Adelaide, South Australia 5005, Australia. ‡Centre for Materials in Energy and Catalysis, The University of Adelaide, Adelaide, South Australia 5005, Australia.

ABSTRACT. As one of the most import chemicals in human society, ammonia is crucial to modern agriculture and could be served as an efficient energy carrier. Electrochemical nitrogen reduction powered by renewable energy source, as a promising alternative to energy-extensive Haber-Bosch process, received more and more attentions in recent years. Although some exciting progress has been made, there are still considerable scientific and technical challenges in improving performance of NH_3 production via electrochemical methods. Single site catalysts (SSCs emerge as promising candidates for electrochemical nitrogen reduction reaction (eNRR) because of the unique coordinating environment and flexibility of adjusting the active centers. In this review we summarized the in-depth understanding regarding to the reaction mechanism from computational simulations to experimental exploration for various SSCs. We highlight the design principles for due to the inherent property of different SSCs (namely, single metal, non-metal, vacancy site catalysts). Experimental electrochemical measurements along with the advanced characterizations (in-situ spectroscopy, isotope labelling) are introduced for examining the activity as well as elucidating the reaction mechanisms for SSCs. This review provides insightful guidance for designing SSCs for electrochemical nitrogen reduction methods via the combination of both theoretical and experimental methods.

INTRODUCTION

The well-known Haber-Bosch process enables the large-scale production of ammonia and thus made significant contributions to the continued expansion of human population since early 1900s.[1] It is also estimated that half of the population are feed by the nitrogenous fertilizers.[2] Ammonia is also considered as an ideal renewable energy carrier by virtue of the large hydrogen content (17.6 wt %) and high energy density (4.32 kW h L^{-1}, liquid).[3, 4] In addition, compared to other fuels,

ammonia has many advantages including liquefiable, storable, and transportable.[5] However, this energy extensive process also consumes about 2% of global energy (over 2 exajoule/year) and release over 300Mt of CO_2.[6] The reliance of fossil fuels (mainly natural gas) as H_2 source makes this process be faced with environmental crisis and cannot meet the need for sustainable development of human society. Developing an alternative technology to the Haber-Bosch process is of great significance and whether electrochemical system could be utilized as the platform to accomplish ammonia production from widely available water and $N_{2(g)}$ attracts growing interests. The advantage of such systems is not only a higher energy efficiency under ambient conditions but also that it could be coupled with renewable energy (like wind or solar plant). It also features as a carbon-neutral routine because of avoiding natural gas as the hydrogen source and other fossil resources as the energy input.[7] However, to date, the efficiency reported is far from satisfactory because of the absence of highly active, selective and durable electrocatalysts.[7]

As an emerging area of heterogeneous catalysis, single site catalysts (SSCs) provide a new platform for exploring the potential of their applications in both traditional thermo-catalytic and electrocatalytic process.[8] For nitrogen reduction reaction, a Mo-based molecular catalyst was first reported by Yandulov et al to reduce dinitrogen molecule at the room temperature.[9] Due to the similarity between these molecular catalysts and SSCs, it is of primary interests to explore whether single site catalysts could serve as the electrocatalysts for converting gaseous $N_{2(g)}$ into ammonia.[10, 11] What's more, the unique structure of SSCs, center coordinated by suitable ligands, could provide a large pool of candidates to be selected as potential NRR catalysts, from single noble metal site, single non-metal site, to single vacancy site.[12-23] For the mechanism aspects, the last two decades have witnessed the rapid development of simulation tools based computational chemistry (especially methods bashed on density functional theory) and their wide applications in revealing

the reaction mechanisms as well as directing the rational design of heterogenous catalysts.[11, 24] For SSCs, the atomic structure is somehow more well defined compared with nanoparticles, which is easy to be capture by atomic modelling based on density functional theory (DFT). However, although abundant reports on the catalytic performance of specific single site catalyst, or computational screening of a large set of potential candidate catalysts for NRR, there are few reviews that systematically summarize the reaction mechanisms of SSCs at the atomic level and, shed light on the design principles of single site catalyst for NRR by combining the experimental observations and theoretical insights.[25, 26]

In this review, we first provide a detailed discussion on the reaction pathways of electrochemical reaction and the difference between different pathways. Then, we focus on the theoretical insights in the design of single metal, non-metal, and vacancy site catalysts as NRR catalysts, which covers all the classifications. The experimental measurements of catalytic performance, spectroscopy observations and mechanism analysis merging both experiments and simulations are summarized by the type of single site catalysts. Finally, major challenges and perspectives for future research on SSCs are presented.

MECHANISTIC INSIGHTS FROM ATOMIC SIMULATIONS.

In this section, mechanistic insights from density functional theory (DFT) calculations are summarized. We first briefly outlined all the reaction pathways of dinitrogen reduction to ammonia. Then based on all these reaction pathways, we introduced the theoretical progress on the designing of different types of single site catalyst, the in-depth mechanisms governing the intrinsic activity of catalysts. Single metal site catalysts come to the first since they are most studied systems, and single non-metal site catalysts, as the new emerging concept, are discussed in the second place.

Finally, as an example, design principle of single vacancy site of metal nitrides is introduced in details.

Reaction Pathways. We summarized all the proposed reaction pathways from $N_{2(g)}$ to ammonia in Figure 1. Figure 1a depicts the dissociative reaction mechanism, where the $N\equiv N$ bond was break before the hydrogenation (usually from hydrogen molecules) or pronation (from aqueous $H^+_{(aq)}$). This mechanism accounts for the Haber-Bosch process under high temperature because of the high kinetic barrier of dissociation step. After the dissociation step, each nitrogen atom could form one $NH_{3(g)}$ molecule. Under ambient conditions, the associative pathways are more possible and depending on the relative position of protonation takes place, it can be divided into associative distal and associative alternating pathway as shown in Figure 1b and 1c. For associative distal pathway, the $N\equiv N$ doesn't dissociate until the release of the first ammonia molecule and all the protonations are on the distal nitrogen atom. However, for the alternating pathway, the protonations are both on nitrogen atoms of adsorbed N_2 molecule. If associative alternating mechanism account for the ammonia production, N_xH_y intermediates would be present on the catalyst surface and some of them could be detected by the advanced spectroscopy technologies and we will cover this subject in the following section.[27] For metal nitrides, the Mars-van Krevelen (MvK) mechanism may attributed for the production of ammonia as proposed by Abghoui and Skúlason.[28] Figure 1d depicts this pathway, a surface vacancy is formed first via the protonation of surface nitrogen atom to ammonia. The surface vacancy would be filled by gaseous $N_{2(g)}$ molecule, and the adsorbed N_2 would be reduced to ammonia by consecutive protonations. As the release of two ammonia molecules, the vacancy would be regenerated and ready to adsorb another $N_{2(g)}$ molecule. At last, Figure 1e displayed the enzymatic pathway, although it is valid for bio-

catalysis process, till now there is still no convincing evidence proving the existence of this mechanism for heterogenous electrocatalysis.

Single Metal Site Catalyst. The first report of a single Mo-based molecular catalyst to reduce dinitrogen at ambient conditions sparked exploration of heterogeneous single metal site catalysts for electrochemical nitrogen reduction reaction.[9] Computational study based on density functional theory (DFT) calculations is helpful for elucidating the mechanisms and help the rational design of high-performance electrocatalysts. For NRR, early computational work mainly focused on the case studies, which would include less than three candidates and compared the theoretical activity in terms of limiting potential.[29, 30] For example, Luo et al reported that compared with FeN_3 motif, FeN_4 motif showed better ability of activating nitrogen molecule due to a higher spin density (as shown in Fig. 2a).[29] Based on Bader charge analysis, they also found that along the nitrogen reduction pathway, the adsorption configurations could be divided into three parts. The nitrogen doped graphene provide electrons which could be transferred to adsorbed dinitrogen through the iron metal center. A more recent work by Ling et al also claimed that Mo_1-N_1C_2 catalyst displayed a low limiting potential of -0.40 V vs reversible hydrogen electrode (RHE).[30] However, these works have limitations in directing experimental synthesis of ideal catalysts because of the high gap exists between simulations and reality.

To accelerate the design of highly active and efficient catalysts, high through-put technologies based on DFT methods are usually used to screen candidates.[31-36] Since these methods could cover a large number of candidates, and predicted activity of these candidates based on the same criterion, more meaningful results could be obtained. For single atom catalyst in electrochemical reduction, Chen and co-workers proposed a two-step procedure to select promising candidates of transition metal supported on defective boron nitride for further exploration as displayed in Figure 2b.[31] First,

the adsorption energies of nitrogen molecule were calculated and then only metal centers with a negative adsorption Gibbs free energy (Sc to Zn, Ru, Rh, Pd, and Ag) were retained while those with positive adsorption energies are ruled out (Mo, Sc to Zn, Ru, Rh, Pd, and Ag). Second, as it is known that for transition metal low index surface, the first and last reaction step of electrochemical nitrogen reduction is crucial in determining the limiting potential, a further screening of adsorption energy of *NNH and *NH$_2$ was applied and only the Mo center showed a balanced *NNH and *NH$_2$ adsorption ability. Last, three possible pathways on Mo-BN were examined and they found a low limiting potential of -0.19 V vs RHE through the enzymatic mechanism. Similar methodologies were also adopted by Ling et al to screen 30 types of transition metal SSCs supported by 9 types of nitrogen doped graphene, and 10 promising candidate were extracted out.[33]

To achieve a rational design of single atom catalysts for electrochemical nitrogen reduction, an in-depth understanding of underline mechanisms is needed. Our previous work carried out DFT simulation for transition metal single atom catalyst supported on three types of nitrogen doped carbons.[12] A general profile on the activity trends, electronic origins, and design strategies was build up. As shown in Figure 2c, the role of metal centers was found to be controlling the adsorption strength of atomic nitrogen atom and the variations of ΔE_{N^*} lied in the populations of bonding/antibonding. Because of the scaling relationship, the theoretical limiting potential showed a volcano shape relationship with the adsorption energy of specific intermediates (Fig. 2d).[35] The effect of carbon supports or in other terms, various ligands are revealed by comparing 20 transition metal SSCs on g-C$_3$N$_4$ and nitrogen doped carbons with three or four anchoring sites for metal center. Results in Figure 2e indicated that the carbon supports could alter the scaling relations and thus affect the activity of NRR. Consequently, the effect of both transition metal center as well as

the carbon catalyst support was elucidated. In addition, stability[12] and selectivity[36] should be taken into accounts for catalyst design, we would cover these aspects in the following sections.

Single non-metal site catalyst. It is generally accepted and well documented that some transition metal centers could effectively activate N_2 due to their advantageous combination of unoccupied and occupied d orbitals, which are of appropriate energy and symmetry to synergically accept electron density from and back donate to N_2 (upper panel in Fig. 3a).[37, 38] However, for main-group compounds, the absence of both empty and filled orbitals makes it hard to provide π back-bonding. A recent breakthrough by Marc-André Légaré and co-workers showed that a di-coordinate borylene is capable of activating N_2, this work inspired the design of heterogeneous catalysts for electrochemical nitrogen reduction.

With the discovery of graphene, two-dimensional (2D) nanomaterials have emerged as some of the most promising candidates for heterogeneous electrocatalysts as well as most common support for anchoring single atom catalysts due to unique physical, chemical, and electronic properties.[8, 25, 39] Du, Wang and co-workers first revealed that B-decorated g-C_3N_4 can achieve a record low onset potential for nitrogen reduction.[40] A more recent work by Sun et al explored eight types of 2D materials as the support for single boron site (displayed in Fig. 3b.), and 21 concept-catalysts were screened. And the results indicated that graphene and h-MoS_2 are the optimal supports offering excellent energy efficiency in terms of low limiting potential and selectivity against competing hydrogen evolution reaction (Fig.3c). Another instance is utilizing MXenes, two-dimensional transition metal carbides, as the substrate for single boron catalysts.[41] Zheng et al showed that the introduced boron atom preferred to locate at the oxygen vacancy, and it enables the B-N bond forming as Figure 3d displays. The as-designed MXenes B-doped Mo_2CO_2 and

W_2CO_2 exhibited the most promising catalytic activity, with ΔG_{PDS} as low as 0.20 and 0.24 eV, respectively. More explorations of potential candidate employing boron sites as the active center could be found, however, experimental validations of related catalysts are still limited.[42-50]

More detailed explanations regarding to the bonding mechanisms between N_2 and boron atom displayed in Fig.3f from Gan, Wand and co-workers.[48] For sp^3 state of boron, electrons are depleted from the σ orbital of N_2 and filled in the π^* of N_2 and boron sp^3 states, while for sp^2 state of boron, the filled p_z interacts with π^* of N_2 and sp^2 interacts with the σ orbital of N_2. For the latter case, the authors found that there are less electrons transferred based on Bader Charge analysis. A more recent work from our group explored several binary metal borides as potential catalysts for electrocatalysts.[51] We found that isolated boron sites in M_2B (M stands for metals) have less filling of p_z orbital, and favored a vertical adsorption mode of N_2 molecule. The degree of N_2 activation increased when the p_z orbital filling is less based on integrated crystal orbital Hamilton population (ICOHP) analysis. Hence, the filling of p_z orbital could be used as an indicator for screening potential catalysts. Summarizing, the activity of boron sites towards electrochemical reduction could be significantly affected by the local chemical environment, and a better understanding of the origins of activity would benefit the design of single boron site catalysts.[48, 51]

Single Vacancy Site Catalyst. Besides single metal or non-metal site discussed in previous sections, the single vacancy site also attracted considerate attentions as a novel and effective active center to activate molecular nitrogen and boost its conversion towards ammonia.[52] Oxygen, nitrogen, and sulfur vacancies were all reported to have the potential as catalysts for electrochemical reduction. Among these different types of vacancies, mechanistic studies on the nitrogen vacancy are the most complicated. We would use simulation study on nitrogen vacancy

as an example and introduce the considerations from theoretical aspects to screen promising materials with singe vacancy site as the active center.

First, the stability of the vacancy needs to be taken into consideration, and the nitrogen vacancy implies that these materials do contain nitrogen, for example, metal nitrides. As introduced in previous section, in the Mars-van Krevelen (MvK) mechanism, the first ammonia is formed from the protonation of a surface nitrogen atom with a vacancy induced. The resulting nitrogen vacancy would be replenished by a gaseous N_2 molecule, the reaction continuously proceeds in this way. The stability of nitrogen vacancy is thus of great importance, i.e., for if the vacancy is not stable at the surface in contact with the aqueous solution, it would migrate to the bulk of nitrides and thus more nitrogen atoms on the surface of nitrides would fill the vacancy and reacted with protons, and at the same time, the gaseous N_2 would not be involved in the reaction. This process has been reported by in a more recent work, and there are experimental methods could examine this process which will be covered in the following section. And we would focus on theoretical methods for the present section. To evaluate this process, Abghoui and Skúlason proposed that two parameters to address this problem. The thermodynamic stability of the nitrogen vacancy at the catalyst surface could be calculated via $\Delta E_{vac} = E_{vac,2} - E_{vac,1}$, where ΔE_{vac} is the energy difference of a nitride slab with a nitrogen vacancy at the surface and in the first subsurface layer. The kinetic aspect was measured by calculating the migrating barrier of nitrogen vacancy. As shown in Figure 3a, from the aspects of thermodynamics, for the most of the nitrides, ΔE_{vac} is close to zero or negative, which indicates the migration is thermodynamically favorable. Thus, the barrier of migrating determines whether the vacancy is stable, and according to the results, some candidates (ZrN, NbN, CrN, VN) exhibit high migration barrier larger than 1eV and thus show stability at room temperature.

For nitrides, Mars-van Krevelen (MvK) mechanisms are believed to account for the conversion of molecular N_2 towards ammonia. During this process, the replenishment of nitrogen vacancy and endurance of the catalytic cycle is of great significance. The solvated N_2 adsorbed on the vacancy and one nitrogen atom of N_2 would fill in the vacancy and the other one would form the second ammonia molecule via protonation. For nitrides, Skúlason et al found that both exposed surface and crystal structures would have influence on the replenishment. Figure 3b and 3c depicts the thermodynamics of replenishment of nitrogen vacancy of nitrides in rocksalt (RS) and zincblende (ZB) structures. It was found that an associative mechanism is possible for RS (100) surfaces (except for CrN), and ZB (110) surfaces (except for ZrN and VN). However, a dissociative mechanism could also attribute to the replenishment of nitrogen vacancy. Figure 3d and 3e displayed the atomic configurations of these two mechanisms.

After examining the stability and replenishment of nitrogen vacancy, the catalytic activity is the next factor that need to be taken into consideration. Figure 3f and 3g the free energy profiles of nitrogen reduction via MvK mechanism on the (100) surface of RS ZrN and the (100) surface of RS MnN, respectively. The potential determining step for ZrN is the first protonation step with a ΔG of 0.99 eV, which indicated that when a potential of -0.99V vs RHE is applied, the free energy diagrams of electrochemical steps would be downhill. However, for some cases, the free energy change of $N_{2(g)}$ dissociation is positive, and due to the nature of chemical step that cannot be overcome by an applied electrode potential. In this scenario, the dissociation mechanism is instead to take place for these nitride as shown in Figure 3g, where the PDS would be the electrochemical step and could be overcome by adjusting the applied potential.

Another critical issue is the decomposition of metal nitrides when an external potential is applied. The decomposition potential of suitable candidates should be more negative than the onset

potential of ammonia production to ensure the stability of catalysts under the reaction conditions. According the results in Figure 3h, ZrN is the only candidate that meets this standard. However, for VN and NbN, there is still chance since the present results are only from the thermodynamic aspects and high kinetic barrier may also protect the metal nitrides from decomposition. Here, another issue also needs to be taken consideration that the nitrogen dopants are widely used for carbon materials, which have the possibility of being protonated and releasing ammonia. If the ammonia is released, it will introduce interference for the detection of catalytic product of NH_3. Qiao and coworkers, proposed a thermodynamic evaluation method to calculate the potential of nitrogen atom protonation.[12] As shown in Figure 3i, the onset potentials of nitrogen atom protonation in various chemical environment are displayed. The theoretical predicted limiting potential should be compared with the nitrogen atom protonation potential to make sure the nitrogen doped carbon support of single site catalysts.

EXPERIMENT EXPLORATION OF SINGLE SITE CATALYST

In this section, recent experimental progress of single site catalysts has been summarized. We discuss various single site catalysts including single metal/non-metal atom catalysts as well as single vacancy site catalysts from fundamental conception to functional application. We place a significant emphasis on in-situ characterizations for the design and investigation of single site catalysts followed by the design principles and experimental protocol. In addition, many advanced in-situ characterizations have been developed to investigate the active site and reaction intermediates, which can facilitate the in-depth understanding of the electrocatalytic mechanisms.[27, 53]

Single Metal Site Catalysts. As reported by Zhang and co-workers in 2011, single atom catalysts with atomically isolated metal sites have emerged in various research fields.[8, 10, 54] Theoretically, all the metal atoms in SSCs are exposed on the surface and thus can achieve maximum utilization of active sites. Such unique structure can significantly minimize use of metal and reduce the cost of catalysts. Initially, single atom catalysts are mainly focus on noble metal such as Pt, Au and Ru etc.[20, 54, 55] Recently, earth abundant transition metal-based single atom catalysts have been developed with superior performance.[56-58] For electrochemical NRR, various metal-based single atom catalysts revel high activity and stability under ambient conditions.[17, 59, 60]

Single Nobel Metal Site Catalysts. Ruthenium has exhibited the best performance for ammonia synthesis in the Haber-Bosch process.[61, 62] Therefore, many efforts have been made to achieve electrochemical NRR with Ru-based catalysts.[4, 17, 59] By tuning the adsorption energy of nitrogen molecule and proton on Ru single atoms, desirable activity and selectivity for NRR could be realized. For example, Geng and co-workers synthesized a Ru single atom catalyst on nitrogen-doped carbon (NC) via a metal organic framework (MOF)-assisted method.[11] This catalyst can achieve a high NH_3 yield of 120.9 ug $mg_{cat.}^{-1}$ h^{-1} with a Faradaic efficiency (FE) of 29.6% with partial current density of -0.13 mA cm^{-2}. The author also conducted N_2 temperature-programmed desorption for the catalysts to confirm the chemical adsorption of N_2 on Ru site. Compared with Ru nanoparticles, the Ru single atom catalyst shows higher binding strength and facilitating following N_2 activation. In another work, Tao et al. synthesized Ru@/NC and Ru@ZrO_2/NC catalysts by annealing Ru doped UiO-66 MOF. Ru single atom exhibit an enhanced FE compared with metallic Ru nanoparticles by suppressing HER.[17] Furthermore, after adding ZrO_2, the completive HER has been suppressed and a high FE of 21% has been realized. It should be noted that Ru nanoparticles on NC still shows the highest NH_3 yield of 3.665 mg mg_{Ru}^{-1} h^{-1} at -0.21 V

versus reversible hydrogen electrode (vs. RHE) but with low FE. Consequently, the balance of NH$_3$ yield and FE is important in designing NRR catalysts.

Another type of noble-metal based SSCs is Au based catalyst.[10] According to DFT calculations, bulk metallic Au shows very poor NRR performance.[63] However, atomic-engineered Au SSCs reveals high activity for NRR under ambient conditions.[64] Wang et al. prepared a Au SSC on C$_3$N$_4$ platform.[64] By virtue of the optimal Au atom utilization, the Au$_1$/C$_3$N$_4$ can achieve a NH$_3$ yield rate of 1305 μg h^{-1} mg$_{Au}^{-1}$ with a FE of 11.1% at -0.1 V vs. RHE, which is higher than that of Au NPs/C$_3$N$_4$ and C$_3$N$_4$, respectively. Qin and co-workers anchored Au single atom on NC using a temple-assisted method. The AuSAs-NDPC can achieve a NH$_3$ yield rate of 2.32 μg h^{-1} cm^{-2} with the maximum FE of 12.3% at the potential of -0.2 V vs. RHE. The open porous structure and the unique single atomic site of Au endows the AuSAs-NDPC with excellent NRR performance.

Single Non-noble Metal Site Catalysts. Inspired by nitrogenase, molybdenum and iron based electrocatalysts for NRR has been investigated systematically.[65] According to DFT prediction, Mo and Fe based SSCs shown promising potential for NRR under ambient conditions by virtue of their appropriate N$_2$ adsorption energy and poor HER activity.[12] Hui et al. reported a zerovalent single molybdenum atoms on graphdiyne (Mo^0/GDY) catalyst for NRR. The DFT calculations elucidate that both Mo and C1 site can facilitate the N$_2$ and H adsorption.[19] Experimentally, the Mo^0/GDY exhibits a NH$_3$ yield of 145.4 μg·mg$_{cat.}^{-1}$ h^{-1} and FE > 21% in 0.1 M Na$_2$SO$_4$. Xin and co-workers reported a single Mo atom anchored to NC as a catalysts for NRR. This catalysts can achieve a high NH$_3$ yield of 34 μg mg$_{cat.}^{-1}$ h^{-1} with a FE of 14.6 in 0.1 M KOH. By controlling the loading of Mo, the atomic Mo-N site was confirmed as the active site for NRR.

Compared with other elements, Fe has been recognised as NRR catalytic site in both industrial Haber−Bosch process and biological nitrogen fixation.[66] Consequently, Fe single atom catalysts attracts many attentions. Li et al. reported a Fe single-atom anchored on MoS_2 for electrochemical NRR.[10] As shown in Figure 5a, Fe single atoms were immobilized on MoS_2 nanosheets as an electrocatalysts for NRR. The aberration-corrected high-angle annular dark-field scanning transmission electron microscopy (HAADF-STEM) images confirm that the Fe single atoms are straddled atop Mo, and their SSC concentrations can be controlled by the dosage of Fe precursors (Figure 5b). The SSCs-MoS_2-Fe-2.0 with maximum Fe SSC density exhibited best performances with a NH_3 production rate of 36.1 mmol g^{-1} h^{-1} (97.5 µg h^{-1} cm^{-2}) and FE of 31.6% at the current density of 1.38 mA cm^{-2} (Figure 5c). Both DFT calculations and experimental data elucidate that the enhanced performance originates from the engagement of protrusions. Wang et al. anchoring Fe single atom on NC via annealing polypyrrole−iron coordination complex as NRR electrocatalysts.[67] Different from other works, the FeSA-N-C catalysts shows a positive onset potential of 0.193 V for NRR. In addition, this catalysts shows an ultra-high FE of 56.55% and desirable NH_3 yield rate of 7.48 µg mg^{-1} h^{-1} at 0 V vs. RHE in 0.1 M KOH. Molecular dynamics [3] simulations suggest the FeSA-N-C catalysts shows a small energy barrier of 2.38 kJ mol^{-1} for nitrogen adsorption and facilitate the NRR during the electrolysis. Recently, several of Fe based SSCs with different coordination environments has been reported.[15, 68] The researcher found that less coordination will lead to an enhanced NRR performance by inducing an optimized N_2 adsorption energy. Recently, other metal-based SSCs such as Co-N_4 and Cu-N_2 has been developed towards NRR.[18, 69] With the optimization of metal and host interaction, the metal-based SSCs has the great potential for electrochemical NRR under ambient conditions.

Non-metal Single-Atom Catalysts. Other than metal-based SSCs, non-metal-based SSCs has several advantages such as low-cost, high activity and simple synthesis.[13, 70] In addition, non-metal site usually shows unique adsorption energy towards NRR.[71] Yang et al. reported O, S, Se and Te doped carbon for NRR (Figure 5d).[71] As the high contrast of Se, Te and C, the Se and Te single atoms can be seen in the atomic-level HAADF-STEM image (Figure 5e). Guided by DFT calculations, the Te and Se-doped C achieve enhanced NRR performance with a NH_3 production rates of 1.91 µg h^{-1} cm^{-2} at -0.50 V vs. RHE and 1.14 µg h^{-1} cm^{-2} at 0.45 V vs. RHE, respectively. The FE of Te and Se-doped C catalysts reaches 4.67 % at -0.50 V vs. RHE and 3.92 % at -0.45 V vs. RHE (Figure 5f). In addition, the TOFs of Te and Se-doped C are determined to be 9.67×10^{-5} and 3.90×10^{-5} s^{-1}, respectively.

According to DFT calculations, boron shows the best N_2 activation performance in non-metal SSCs.[40] Consequently, boron single site has been experimentally studied towards NRR. Yu and co-worker reported a boron doped graphene for electrocatalytic N_2 reduction.[21] The catalysts with unique BC_3 structure (doping level 6.2 %) shows a NH_3 production rate of 9.8 µg h^{-1} cm^{-2} with a FE of 10.8 % at -0.5 V vs RHE. The unique BC_3 site revels the lowest energy barrier for N_2 activation, resulting in the best performance. Similarly, Qiu and co-workers prepared a metal-free boron carbide (B_4C) nanosheets via liquid exfoliation for electrochemical NRR in acidic media.[72] This catalyst reveals a high NH_3 yield of 26.57 µg h^{-1} mg$^{-1}_{cat.}$ with a FE of 15.95% at -0.75 V vs. RHE. According to DFT calculations, the B site is the active site for N_2 adsorption and activation.

Single Vacancy Site Catalysts. Defect (vacancy) engineering can regulate the atomic coordination environment of catalysts' surface and generate highly active sites for NRR.[73] Recently, defect engineering revealed its great potential to optimize the electronic structure and coordination property of catalysts, resulting in appropriate N_2 adsorption and activation energy

towards NRR.[14] Recently, defect engineered catalysts has been reported widely for NRR which show enhanced performance compared to pristine catalysts. The correlation between defect site and activity has been investigate by merging theoretical calculations and experiments. Currently, various vacancy-sites such as oxygen vacancy, sulfur vacancy and nitrogen vacancy have been reported for electrochemical NRR under ambient conditions.[22, 23, 74] Lai and co-worker reported an oxygen vacancy-rich $NiCo_2O_4$ on hollow N-carbon polyhedral catalyst which shows enhanced NRR performance.[16] As expected, V_o-rich $NiCo_2O_4$@HNCP catalyst showed enhanced NH_3 production yield of 4.1 μg h^{-1} cm^{-2}/17.8 μg h^{-1} mg^{-1} and a FE of 5.3%. The oxygen vacancies can enhance the reactivity of the active sites, leading to reduced stabilization energy of NNH groups. Due to the similar chemical properties, sulfur vacancies have great potential in improving the activity of electrochemical NRR. Zhang and co-workers found that the S defect on MoS_2 can facilitate NRR by lowering the energy barrier of N_2 activation.[75] The defect-engineered MoS_2 shows a high NH_3 yield 8.08×10^{-11} mol s^{-1} cm^{-1} with a FE of 1.17% -0.5 V vs. RHE in 0.1 m Na_2SO_4.

The active site for electrochemical NRR needs twofold properties: for one thing, it can accept the lone-pair electrons for effective N_2 adsorption and for the other thing it can donate electrons to antibonding orbitals of dinitrogen molecules for the nitrogen triple-bond activation.[40, 74] Theoretically, one of the most ideal vacancy for NRR is nitrogen vacancies on transition metal nitride (TMN) because of its unique vacancy properties for dinitrogen molecule adsorption and poor HER activity. Jin et al. reported a 2D layered W_2N_3 with nitrogen vacancy for NRR, which shows a NH_3 production rate as high as 11.66 ± 0.98 μg h^{-1} mg_{cata}^{-1} with a desirable FE of $11.67 \pm 0.93\%$ at -0.2 V vs. RHE under ambient conditions (Figure 5a-5c).[74] The electron deficient environment induced by nitrogen vacancies on W_2N_3 can effectively facilitate the acceptance of

the lone-pair electrons of N_2 and promote the subsequent reduction steps. Considering the possible contamination for the N in the nitride, they also conducted long-term stability test for 24 h. The total amount of nitrogen in the ammonia produced within 24 h is higher than the nitrogen content in the catalysts, indicating that the ammonia originates from NRR. Yang et al. verified the Mars-van Krevelen mechanism using vanadium nitride (VN) nanoparticles as a platform.[73] By in-situ spectroscopy and control experiments, the composition of the active materials was confirmed as $VN_{0.7}O_{0.45}$ and the in-situ formed nitrogen vacancies on $VN_{0.7}O_{0.45}$ was allocated as the active site for NRR. The nitride shows an NH_3 production rate and FE of 3.3×10^{-10} mol s^{-1} cm^{-2} and 6.0% at -0.1 V within 1 h, respectively. The catalyst is also stable for NH_3 production with a rate of 1.1×10^{-10} mol s^{-1} cm^{-2} and a FE of 1.6% for 116 h.

Advanced Approaches for Detecting Reaction Intermediates. Currently, the NH_3 production rate in electrochemical NRR is very low. Many factors may introduce contaminations in the product and cause false positive data.[76, 77] Consequently, a series of rigorous testing protocols need to be followed carefully.[78] As these testing protocols has been reported in other references, we don't discuss this issue in this review. We mainly focus on the advanced approaches including in-situ measurement and isotope labelling method that can monitoring reaction intermediate and eliminating the potential false positive result during NRR. One the most important protocols that can eliminate the influence of contamination is ^{15}N isotope labelling experiment.[76] After removing the $^{15}NO_x$ using rigorous testing protocols, the nitrogen isotope can directly confirm the process of NRR. Normally, the discriminate between nitrogen isotopes can be identified easily n nuclear magnetic resonance (NMR) measurement (Figure 6a).[79] The doublet coupling (~72 Hz) assignable to $^{15}NH_4^+$ and the triplet coupling (~ 52 Hz) represents the signal of $^{14}NH_4^+$. The NMR method can be further optimized by changing the pulse sequences, non-deuterated solvent compatibility,

supporting electrolyte compatibility, required proton concentration, and locking solvent compatibility. In addition, the ^{15}N isotope labelling experiment can confirm the reaction mechanism by probing the active site of the catalysts. By carefully designing the $^{15}N_2$ isotope labelling experiments, Yang et al. quantified the active site and elucidate the NRR pathway on VN following the MvK mechanism successfully.[80] Using $^{15}N_2$ as the gas feed, the ^{15}N species can be detected on both ammonia product and the VN catalyst, confirming that the surface N and N vacancies are the active sites in facilitating the catalytic turnovers in the ENRR

Recently, advanced in-situ spectroscopic characterizations have been developed to probe the reaction intermediate during NRR.[27, 53] These characterizations not only can unveil the reaction mechanism of NRR, but also can confirm the nitrogen source of the ammonia product. Lv et al. conducted electrochemical attenuated total reflectance Fourier transform infrared (ATR-FTIR) spectroscopy measurements in NRR.[81] As shown in Figure 6b, they first conducted DFT calculations to predict the NRR reaction pathway on V_O and hydroxyl on the surface of $Bi_4O_5Iti5i_2$ (V_O-$Bi_4O_5I_2$-OH). Then, the ATR-FTIR spectra shows that the H-N-H bending vibration at ~1442 cm^1 started to appear at ~ 0.1 V, which originates from the NH_x species (Figure 6c). These results justify an associative mechanism on V_O-$Bi_4O_5I_2$-OH, which can be well correlated with the theoretical calculations. In addition, in-situ FTIR can determine reaction intermediate in N_2 and Ar saturated electrolytes. Yao et al conducted in-situ FTIR on a Ru thin film in an acidic electrolyte.[82] Figure 6d shows the potential dependence of the band centers of N=N stretching and the corresponding cyclic voltammetry curves. The band intensities significantly enhanced from 0 to -0.15 V, indicating the increased coverage of absorbed $*N_2H_x$ intermediate. However, in Ar-saturated electrolyte, only Ru–H stretching can be observed (Figure 6e), which is due to the adsorption of *H at working potentials. The advanced in-situ FTIR results confirm that the $*N_2H_x$

is a reaction intermediates which are unstable and easy to desorb from the Ru surface and decompose into ammonia. Consequently, most of Ru based catalysts shows low overpotential during NRR. In addition, no N-related infrared absorption bands were observed on Ru surfaces in a N_2 saturated 0.1 M KOH solution, indicating that the adsorption of nitrogen molecules on Ru surfaces was weak.

The interaction between N_2 and catalyst will facilitate the exploration of reaction intermediates and reaction pathway. Li et al. measured the differential of surface potential to probe the interfacial polarization in Ar to N_2 gas feed (Figures 6f).[10] During the measurement, the nitrogen molecule will be polarized on the active site, inducing a polarization field and generate potential difference. Such polarization-induced potential will provide pathway for electron transfer from catalysts to N_2 and improve the NRR performance. Other than interaction, Yao et al. conducted online differential electrochemical mass spectrometry (DEMS) for mass-resolved determination of reaction intermediates and products, which can confirm the NRR activity and identified the reaction pathway on zero-valent bismuth catalysts.[83] As shown in Figure 6g, the intensity of the m/z signal for NH_3 is depended on working potential. At -0.7 V vs. RHE, the intensity reaches the peck position, which matches well with the electrochemical data. This online measurement confirms the generation of ammonia under different working potentials.

Recently, researchers combined the operando synchrotron-radiation Fourier transform infrared spectroscopy (SR-FTIR) with isotope labelling method to achieve comprehensive detection of reaction intermediates during nitrogen fixation to urea.[84] Firstly, the SR-FTIR was conducted which shows potential-dependent signals with stretching vibrations of NH_2 and NH at ~3171, ~3291 and ~3441 cm^{-1} shown in Figure 6h. In order to avoid the contamination from the environment, the isotope-labelling operando SR-FTIR experiments were conducted. As shown in

Figure 6i, the vibrations bands of $^{15}NH_2$, ^{15}NH are blue shifted by 20-30 cm^{-1}, which is attributed to the isotope effect. This method can confirm the electroreduction of N_2 during the reaction.

CONCLUSIONS

In summary, the progress of single site catalysts as the eNRR catalysts are summarized for both the fundamental insights from computational modelling and measurements as well as exploration of reaction mechanisms from extensive experimental methods. We concluded that combining theoretical modelling and practical experiments are useful means to elucidate the mechanisms of NRR and could direct the rational design of the single site catalysts (SSCs). In addition, through detailed discussions, we showed that due to the inherent difference of various SSCs, the considerations during the design of catalyst are distinct. Our review could help in designing new SSCs for electrochemical nitrogen reduction and benefit other catalytic reactions like $CO_{2(g)}$ reduction.

ASSOCIATED CONTENT

AUTHOR INFORMATION

Corresponding Author

*Shi-Zhang Qiao. s.qiao@adelaide.edu.au;

*Yan Jiao. yan.jiao@adelaide.edu.au.

Author Contributions

Xin Liu and Huanyu Jin contributed equally. The manuscript was written through contributions of all authors. All authors have given approval to the final version of the manuscript.

Notes

The authors declare no competing financial interest

REFERENCES

1. Smil, V., Detonator of the population explosion. *Nature* **1999,** *400* (6743), 415-415.

2. Zhang, X.; Davidson, E. A.; Mauzerall, D. L.; Searchinger, T. D.; Dumas, P.; Shen, Y., Managing nitrogen for sustainable development. *Nature* **2015,** *528* (7580), 51-59.

3. Chu, S.; Majumdar, A., Opportunities and challenges for a sustainable energy future. *Nature* **2012,** *488* (7411), 294-303.

4. Tang, C.; Qiao, S.-Z., How to explore ambient electrocatalytic nitrogen reduction reliably and insightfully. *Chemical Society Reviews* **2019,** *48* (12), 3166-3180.

5. Renewable Energy to Fuels Through Utilization of Energy-Dense Liquids (REFUEL) Program Overview, **2016**.

6. Schiffer, Z. J.; Manthiram, K., Electrification and Decarbonization of the Chemical Industry. *Joule* **2017,** *1* (1), 10-14.

7. Foster, S. L.; Bakovic, S. I. P.; Duda, R. D.; Maheshwari, S.; Milton, R. D.; Minteer, S. D.; Janik, M. J.; Renner, J. N.; Greenlee, L. F., Catalysts for nitrogen reduction to ammonia. *Nature Catalysis* **2018,** *1* (7), 490-500.

8. Li, L.; Chang, X.; Lin, X.; Zhao, Z.-J.; Gong, J., Theoretical insights into single-atom catalysts. *Chemical Society Reviews* **2020,** *49* (22), 8156-8178.

9. Yandulov, D. V., Catalytic Reduction of Dinitrogen to Ammonia at a Single Molybdenum Center. *Science* **2003,** *301* (5629), 76-78.

10. Wang, Y.; Su, H.; He, Y.; Li, L.; Zhu, S.; Shen, H.; Xie, P.; Fu, X.; Zhou, G.; Feng, C.; Zhao, D.; Xiao, F.; Zhu, X.; Zeng, Y.; Shao, M.; Chen, S.; Wu, G.; Zeng, J.; Wang, C., Advanced Electrocatalysts with Single-Metal-Atom Active Sites. *Chemical Reviews* **2020,** *120* (21), 12217-12314.

11. Geng, Z.; Liu, Y.; Kong, X.; Li, P.; Li, K.; Liu, Z.; Du, J.; Shu, M.; Si, R.; Zeng, J., Achieving a Record-High Yield Rate of 120.9 μg NH$_3$ mgcat.$^{-1}$ h^{-1} for N$_2$ Electrochemical Reduction over Ru Single-Atom Catalysts. *Advanced Materials* **2018,** *30* (40), 1803498.

12. Liu, X.; Jiao, Y.; Zheng, Y.; Jaroniec, M.; Qiao, S.-Z., Building Up a Picture of the Electrocatalytic Nitrogen Reduction Activity of Transition Metal Single-Atom Catalysts. *Journal of the American Chemical Society* **2019,** *141* (24), 9664-9672.

13. Zhao, Y.; Ling, T.; Chen, S.; Jin, B.; Vasileff, A.; Jiao, Y.; Song, L.; Luo, J.; Qiao, S.-Z., Non-metal Single-Iodine-Atom Electrocatalysts for the Hydrogen Evolution Reaction. *Angewandte Chemie International Edition* **2019,** *58* (35), 12252-12257.

14. Zhao, Y.; Zhao, Y.; Shi, R.; Wang, B.; Waterhouse, G. I. N.; Wu, L.-Z.; Tung, C.-H.; Zhang, T., Tuning Oxygen Vacancies in Ultrathin TiO_2 Nanosheets to Boost Photocatalytic Nitrogen Fixation up to 700 nm. *Advanced Materials* **2019,** *31*, 1806482.

15. Guo, X.; Gu, J.; Hu, X.; Zhang, S.; Chen, Z.; Huang, S., Coordination tailoring towards efficient single-atom catalysts for N_2 fixation: A case study of iron-nitrogen-carbon (Fe@N-C) systems. *Catalysis Today* **2020,** *350*, 91-99.

16. Lai, F.; Feng, J.; Ye, X.; Zong, W.; He, G.; Yang, C.; Wang, W.; Miao, Y.-E.; Pan, B.; Yan, W.; Liu, T.; Parkin, I. P., Oxygen vacancy engineering in spinel-structured nanosheet wrapped hollow polyhedra for electrochemical nitrogen fixation under ambient conditions. *Journal of Materials Chemistry A* **2020,** *8* (4), 1652-1659.

17. Tao, H.; Choi, C.; Ding, L.-X.; Jiang, Z.; Han, Z.; Jia, M.; Fan, Q.; Gao, Y.; Wang, H.; Robertson, A. W.; Hong, S.; Jung, Y.; Liu, S.; Sun, Z., Nitrogen Fixation by Ru Single-Atom Electrocatalytic Reduction. *Chem* **2019,** *5* (1), 204-214.

18. Liu, Y.; Xu, Q.; Fan, X.; Quan, X.; Su, Y.; Chen, S.; Yu, H.; Cai, Z., Electrochemical reduction of N_2 to ammonia on Co single atom embedded N-doped porous carbon under ambient conditions. *Journal of Materials Chemistry A* **2019,** *7* (46), 26358-26363.

19. Hui, L.; Xue, Y.; Yu, H.; Liu, Y.; Fang, Y.; Xing, C.; Huang, B.; Li, Y., Highly Efficient and Selective Generation of Ammonia and Hydrogen on a Graphdiyne-Based Catalyst. *Journal of the American Chemical Society* **2019,** *141* (27), 10677-10683.

20. Zhang, J.; Liu, J.; Xi, L.; Yu, Y.; Chen, N.; Sun, S.; Wang, W.; Lange, K. M.; Zhang, B., Single-Atom Au/NiFe Layered Double Hydroxide Electrocatalyst: Probing the Origin of Activity for Oxygen Evolution Reaction. *Journal of the American Chemical Society* **2018,** *140* (11), 3876-3879.

21. Yu, X.; Han, P.; Wei, Z.; Huang, L.; Gu, Z.; Peng, S.; Ma, J.; Zheng, G., Boron-Doped Graphene for Electrocatalytic N_2 Reduction. *Joule* **2018,** *2* (8), 1610-1622.

22. Yao, J.-X.; Bao, D.; Zhang, Q.; Shi, M.-M.; Wang, Y.; Gao, R.; Yan, J.-M.; Jiang, Q., Tailoring Oxygen Vacancies of $BiVO_4$ toward Highly Efficient Noble-Metal-Free Electrocatalyst for Artificial N_2 Fixation under Ambient Conditions. *Small Methods* **2018,** *3*, 1800333.

23. Li, X.; Li, T.; Ma, Y.; Wei, Q.; Qiu, W.; Guo, H.; Shi, X.; Zhang, P.; Asiri, A. M.; Chen, L.; Tang, B.; Sun, X., Boosted Electrocatalytic N_2 Reduction to NH_3 by Defect-Rich MoS_2 Nanoflower. *Advanced Energy Materials* **2018,** *8* (30), 1801357.

24. Nørskov, J. K.; Rossmeisl, J.; Logadottir, A.; Lindqvist, L.; Kitchin, J. R.; Bligaard, T.; Jónsson, H., Origin of the Overpotential for Oxygen Reduction at a Fuel-Cell Cathode. *The Journal of Physical Chemistry B* **2004,** *108* (46), 17886-17892.

25. Zhai, Y.; Zhu, Z.; Zhu, C.; Chen, K.; Zhang, X.; Tang, J.; Chen, J., Single-atom catalysts boost nitrogen electroreduction reaction. *Materials Today* **2020,** *38*, 99-113.

26. Wan, Y.; Xu, J.; Lv, R., Heterogeneous electrocatalysts design for nitrogen reduction reaction under ambient conditions. *Materials Today* **2019,** *27*, 69-90.

27. Yao, Y.; Zhu, S.; Wang, H.; Li, H.; Shao, M., A Spectroscopic Study on the Nitrogen Electrochemical Reduction Reaction on Gold and Platinum Surfaces. *Journal of the American Chemical Society* **2018,** *140* (4), 1496-1501.

28. Abghoui, Y.; Garden, A. L.; Hlynsson, V. F.; Bjorgvinsdottir, S.; Olafsdottir, H.; Skulason, E., Enabling electrochemical reduction of nitrogen to ammonia at ambient conditions through rational catalyst design. *Phys Chem Chem Phys* **2015,** *17* (7), 4909-18.

29. Li, X.-F.; Li, Q.-K.; Cheng, J.; Liu, L.; Yan, Q.; Wu, Y.; Zhang, X.-H.; Wang, Z.-Y.; Qiu, Q.; Luo, Y., Conversion of Dinitrogen to Ammonia by FeN_3-Embedded Graphene. *Journal of the American Chemical Society* **2016,** *138* (28), 8706-8709.

30. Ling, C.; Bai, X.; Ouyang, Y.; Du, A.; Wang, J., Single Molybdenum Atom Anchored on N-Doped Carbon as a Promising Electrocatalyst for Nitrogen Reduction into Ammonia at Ambient Conditions. *The Journal of Physical Chemistry C* **2018,** *122* (29), 16842-16847.

31. Zhao, J.; Chen, Z., Single Mo Atom Supported on Defective Boron Nitride Monolayer as an Efficient Electrocatalyst for Nitrogen Fixation: A Computational Study. *Journal of the American Chemical Society* **2017,** *139* (36), 12480-12487.

32. Chen, Z.; Zhao, J.; Cabrera, C. R.; Chen, Z., Computational Screening of Efficient Single-Atom Catalysts Based on Graphitic Carbon Nitride (g-C_3N_4) for Nitrogen Electroreduction. *Small Methods* **2018,** *3* (6), 1800368.

33. Ling, C.; Ouyang, Y.; Li, Q.; Bai, X.; Mao, X.; Du, A.; Wang, J., A General Two-Step Strategy Based High-Throughput Screening of Single Atom Catalysts for Nitrogen Fixation. *Small Methods* **2019,** *3* (9), 1800376.

34. Chen, X.; Ong, W.-J.; Zhao, X.; Zhang, P.; Li, N., Insights into electrochemical nitrogen reduction reaction mechanisms: Combined effect of single transition-metal and boron atom. *Journal of Energy Chemistry* **2021,** *58*, 577-585.

35. Tang, S.; Dang, Q.; Liu, T.; Zhang, S.; Zhou, Z.; Li, X.; Wang, X.; Sharman, E.; Luo, Y.; Jiang, J., Realizing a Not-Strong-Not-Weak Polarization Electric Field in Single-Atom Catalysts Sandwiched by Boron Nitride and Graphene Sheets for Efficient Nitrogen Fixation. *Journal of the American Chemical Society* **2020,** *142* (45), 19308-19315.

36. Choi, C.; Back, S.; Kim, N.-Y.; Lim, J.; Kim, Y.-H.; Jung, Y., Suppression of Hydrogen Evolution Reaction in Electrochemical N_2 Reduction Using Single-Atom Catalysts: A Computational Guideline. *ACS Catalysis* **2018,** *8* (8), 7517-7525.

37. Van Der Ham, C. J. M.; Koper, M. T. M.; Hetterscheid, D. G. H., Challenges in reduction of dinitrogen by proton and electron transfer. *Chemical Society Review.* **2014,** *43* (15), 5183-5191.

38. Légaré, M.-A.; Bélanger-Chabot, G.; Dewhurst, R. D.; Welz, E.; Krummenacher, I.; Engels, B.; Braunschweig, H., Nitrogen fixation and reduction at boron. *Science* **2018,** *359* (6378), 896-900.

39. Jin, H.; Guo, C.; Liu, X.; Liu, J.; Vasileff, A.; Jiao, Y.; Zheng, Y.; Qiao, S.-Z., Emerging Two-Dimensional Nanomaterials for Electrocatalysis. *Chemical Reviews* **2018,** *118* (13), 6337-6408.

40. Ling, C.; Niu, X.; Li, Q.; Du, A.; Wang, J., Metal-Free Single Atom Catalyst for N_2 Fixation Driven by Visible Light. *Journal of the American Chemical Society* **2018,** *140* (43), 14161-14168.

41. Zheng, S.; Li, S.; Mei, Z.; Hu, Z.; Chu, M.; Liu, J.; Chen, X.; Pan, F., Electrochemical Nitrogen Reduction Reaction Performance of Single-Boron Catalysts Tuned by MXene Substrates. *The Journal of Physical Chemistry Letters* **2019,** *10* (22), 6984-6989.

42. Liu, C.; Li, Q.; Zhang, J.; Jin, Y.; Macfarlane, D. R.; Sun, C., Theoretical Evaluation of Possible 2D Boron Monolayer in N_2 Electrochemical Conversion into Ammonia. *The Journal of Physical Chemistry C* **2018,** *122* (44), 25268-25273.

43. Qiu, W.; Xie, X. Y.; Qiu, J.; Fang, W. H.; Liang, R.; Ren, X.; Ji, X.; Cui, G.; Asiri, A. M.; Cui, G.; Tang, B.; Sun, X., High-performance artificial nitrogen fixation at ambient conditions using a metal-free electrocatalyst. *Nat Commun* **2018,** *9* (1), 3485.

44. Chu, Z.-Q.; Stampfl, C.; Duan, X.-M., Boron-Doped g-C6N6 Layer as a Metal-Free Photoelectrocatalyst for N_2 Reduction Reaction. *The Journal of Physical Chemistry C* **2019,** *123* (47), 28739-28743.

45. Ma, B.; Peng, Y.; Ma, D.; Deng, Z.; Lu, Z., Boron-doped InSe monolayer as a promising electrocatalyst for nitrogen reduction into ammonia at ambient conditions. *Applied Surface Science* **2019,** *495*, 143463.

46. Zhang, X.; Wu, T.; Wang, H.; Zhao, R.; Chen, H.; Wang, T.; Wei, P.; Luo, Y.; Zhang, Y.; Sun, X., Boron Nanosheet: An Elemental Two-Dimensional (2D) Material for Ambient Electrocatalytic N_2-to-NH_3 Fixation in Neutral Media. *ACS Catalysis* **2019,** *9* (5), 4609-4615.

47. Liu, B.; Zheng, Y.; Peng, H.-Q.; Ji, B.; Yang, Y.; Tang, Y.; Lee, C.-S.; Zhang, W., Nanostructured and Boron-Doped Diamond as an Electrocatalyst for Nitrogen Fixation. *ACS Energy Letters* **2020,** *5* (8), 2590-2596.

48. Yin, H.; Gan, L.-Y.; Wang, P., The identification of optimal active boron sites for N_2 reduction. *Journal of Materials Chemistry A* **2020,** *8* (7), 3910-3917.

49. Zheng, M.; Li, Y.; Ding, K.; Zhang, Y.; Chen, W.; Lin, W., A boron-decorated melon-based carbon nitride as a metal-free photocatalyst for N_2 fixation: a DFT study. *Physical Chemistry Chemical Physics* **2020,** *22* (38), 21872-21880.

50. Zhou, S.; Yang, X.; Xu, X.; Dou, S. X.; Du, Y.; Zhao, J., Boron Nitride Nanotubes for Ammonia Synthesis: Activation by Filling Transition Metals. *Journal of the American Chemical Society* **2020,** *142* (1), 308-317.

51. Liu, X.; Jiao, Y.; Zheng, Y.; Qiao, S.-Z., Isolated Boron Sites for Electroreduction of Dinitrogen to Ammonia. *ACS Catalysis* **2020,** *10* (3), 1847-1854.

52. Yan, D.; Li, H.; Chen, C.; Zou, Y.; Wang, S., Defect Engineering Strategies for Nitrogen Reduction Reactions under Ambient Conditions. *Small Methods* **2019,** *3* (6), 1800331.

53. Yao, Y.; Zhu, S.; Wang, H.; Li, H.; Shao, M., A Spectroscopic Study of Electrochemical Nitrogen and Nitrate Reduction on Rhodium Surfaces. *Angewandte Chemie International Edition* **2020,** *59* (26), 10479-10483.

54. Qiao, B.; Wang, A.; Yang, X.; Allard, L. F.; Jiang, Z.; Cui, Y.; Liu, J.; Li, J.; Zhang, T., Single-atom catalysis of CO oxidation using Pt_1/FeOx. *Nature Chemistry* **2011,** *3* (8), 634-641.

55. Yao, Y.; Hu, S.; Chen, W.; Huang, Z.-Q.; Wei, W.; Yao, T.; Liu, R.; Zang, K.; Wang, X.; Wu, G.; Yuan, W.; Yuan, T.; Zhu, B.; Liu, W.; Li, Z.; He, D.; Xue, Z.; Wang, Y.; Zheng, X.; Dong, J.; Chang, C.-R.; Chen, Y.; Hong, X.; Luo, J.; Wei, S.; Li, W.-X.; Strasser, P.; Wu, Y.; Li, Y., Engineering the electronic structure of single atom Ru sites via compressive strain boosts acidic water oxidation electrocatalysis. *Nature Catalysis* **2019,** *2* (4), 304-313.

56. Xue, Y.; Huang, B.; Yi, Y.; Guo, Y.; Zuo, Z.; Li, Y.; Jia, Z.; Liu, H.; Li, Y., Anchoring zero valence single atoms of nickel and iron on graphdiyne for hydrogen evolution. *Nature Communications* **2018,** *9* (1), 1460.

57. Han, Y.; Wang, Y. G.; Chen, W.; Xu, R.; Zheng, L.; Zhang, J.; Luo, J.; Shen, R. A.; Zhu, Y.; Cheong, W. C.; Chen, C.; Peng, Q.; Wang, D.; Li, Y., Hollow N-Doped Carbon Spheres with Isolated Cobalt Single Atomic Sites: Superior Electrocatalysts for Oxygen Reduction. *J Am Chem Soc* **2017,** *139* (48), 17269-17272.

58. Yao, Y.; Huang, Z.; Xie, P.; Wu, L.; Ma, L.; Li, T.; Pang, Z.; Jiao, M.; Liang, Z.; Gao, J.; He, Y.; Kline, D. J.; Zachariah, M. R.; Wang, C.; Lu, J.; Wu, T.; Li, T.; Wang, C.; Shahbazian-Yassar, R.; Hu, L., High temperature shockwave stabilized single atoms. *Nature Nanotechnology* **2019,** *14* (9), 851-857.

59. Peng, W.; Luo, M.; Xu, X.; Jiang, K.; Peng, M.; Chen, D.; Chan, T.-S.; Tan, Y., Spontaneous Atomic Ruthenium Doping in Mo_2CTX MXene Defects Enhances Electrocatalytic Activity for the Nitrogen Reduction Reaction. *Advanced Energy Materials* **2020,** *10* (25), 2001364.

60. Qin, Q.; Heil, T.; Antonietti, M.; Oschatz, M., Single-Site Gold Catalysts on Hierarchical N-Doped Porous Noble Carbon for Enhanced Electrochemical Reduction of Nitrogen. *Small Methods* **2018,** *2* (12), 1800202.

61. Kitano, M.; Kanbara, S.; Inoue, Y.; Kuganathan, N.; Sushko, P. V.; Yokoyama, T.; Hara, M.; Hosono, H., Electride support boosts nitrogen dissociation over ruthenium catalyst and shifts the bottleneck in ammonia synthesis. *Nature Communications* **2015,** *6* (1), 6731.

62. Ozaki, A., Development of alkali-promoted ruthenium as a novel catalyst for ammonia synthesis. *Accounts of Chemical Research* **1981,** *14* (1), 16-21.

63. Skúlason, E.; Bligaard, T.; Gudmundsdóttir, S.; Studt, F.; Rossmeisl, J.; Abild-Pedersen, F.; Vegge, T.; Jónsson, H.; Nørskov, J. K., A theoretical evaluation of possible transition metal electro-catalysts for N_2 reduction. *Physical Chemistry Chemical Physics* **2012,** *14* (3), 1235-1245.

64. Wang, X.; Wang, W.; Qiao, M.; Wu, G.; Chen, W.; Yuan, T.; Xu, Q.; Chen, M.; Zhang, Y.; Wang, X.; Wang, J.; Ge, J.; Hong, X.; Li, Y.; Wu, Y.; Li, Y., Atomically dispersed Au1 catalyst towards efficient electrochemical synthesis of ammonia. *Science Bulletin* **2018,** *63* (19), 1246-1253.

65. McKenna, C. E.; Jones, J. B.; Eran, H.; Huang, C. W., Reduction of cyclopropene as criterion of active-site homology between nitrogenase and its Fe-Mo cofactor. *Nature* **1979,** *280* (5723), 611-612.

66. Vicente, E. J.; Dean, D. R., Keeping the nitrogen-fixation dream alive. *Proceedings of the National Academy of Sciences* **2017,** *114* (12), 3009.

67. Wang, M.; Liu, S.; Qian, T.; Liu, J.; Zhou, J.; Ji, H.; Xiong, J.; Zhong, J.; Yan, C., Over 56.55% Faradaic efficiency of ambient ammonia synthesis enabled by positively shifting the reaction potential. *Nature Communications* **2019,** *10* (1), 341.

68. Wang, Y.; Cui, X.; Zhao, J.; Jia, G.; Gu, L.; Zhang, Q.; Meng, L.; Shi, Z.; Zheng, L.; Wang, C.; Zhang, Z.; Zheng, W., Rational Design of Fe-N/C Hybrid for Enhanced Nitrogen Reduction Electrocatalysis under Ambient Conditions in Aqueous Solution. *ACS Catalysis* **2019,** *9* (1), 336-344.

69. Zang, W.; Yang, T.; Zou, H.; Xi, S.; Zhang, H.; Liu, X.; Kou, Z.; Du, Y.; Feng, Y. P.; Shen, L.; Duan, L.; Wang, J.; Pennycook, S. J., Copper Single Atoms Anchored in Porous Nitrogen-Doped Carbon as Efficient pH-Universal Catalysts for the Nitrogen Reduction Reaction. *ACS Catalysis* **2019,** *9* (11), 10166-10173.

70. Jin, H.; Liu, X.; Chen, S.; Vasileff, A.; Li, L.; Jiao, Y.; Song, L.; Zheng, Y.; Qiao, S.-Z., Heteroatom-Doped Transition Metal Electrocatalysts for Hydrogen Evolution Reaction. *ACS Energy Letters* **2019,** *4* (4), 805-810.

71. Yang, Y.; Zhang, L.; Hu, Z.; Zheng, Y.; Tang, C.; Chen, P.; Wang, R.; Qiu, K.; Mao, J.; Ling, T.; Qiao, S.-Z., The Crucial Role of Charge Accumulation and Spin Polarization in Activating Carbon-Based Catalysts for Electrocatalytic Nitrogen Reduction. *Angewandte Chemie International Edition* **2020,** *59* (11), 4525-4531.

72. Qiu, W.; Xie, X.-Y.; Qiu, J.; Fang, W.-H.; Liang, R.; Ren, X.; Ji, X.; Cui, G.; Asiri, A. M.; Cui, G.; Tang, B.; Sun, X., High-performance artificial nitrogen fixation at ambient conditions using a metal-free electrocatalyst. *Nat. Commun.* **2018,** *9* (1), 3485.

73. Yang, X.; Nash, J.; Anibal, J.; Dunwell, M.; Kattel, S.; Stavitski, E.; Attenkofer, K.; Chen, J. G.; Yan, Y.; Xu, B., Mechanistic Insights into Electrochemical Nitrogen Reduction Reaction on Vanadium Nitride Nanoparticles. *Journal of the American Chemical Society* **2018,** *140* (41), 13387-13391.

74. Jin, H.; Li, L.; Liu, X.; Tang, C.; Xu, W.; Chen, S.; Song, L.; Zheng, Y.; Qiao, S.-Z., Nitrogen vacancies on 2D layered W_2N_3: a stable and efficient active site for nitrogen reduction reaction. *Advanced Materials* **2019,** *31* (32), 1902709.

75. Zhang, L.; Ji, X.; Ren, X.; Ma, Y.; Shi, X.; Tian, Z.; Asiri, A. M.; Chen, L.; Tang, B.; Sun, X., Electrochemical Ammonia Synthesis via Nitrogen Reduction Reaction on a MoS2 Catalyst: Theoretical and Experimental Studies. *Advanced Materials* **2018,** *30* (28), 1800191.

76. Andersen, S. Z.; Colic, V.; Yang, S.; Schwalbe, J. A.; Nielander, A. C.; McEnaney, J. M.; Enemark-Rasmussen, K.; Baker, J. G.; Singh, A. R.; Rohr, B. A.; Statt, M. J.; Blair, S. J.; Mezzavilla, S.; Kibsgaard, J.; Vesborg, P. C. K.; Cargnello, M.; Bent, S. F.; Jaramillo, T. F.; Stephens, I. E. L.; Norskov, J. K.; Chorkendorff, I., A rigorous electrochemical ammonia synthesis protocol with quantitative isotope measurements. *Nature* **2019,** *570* (7762), 504-508.

77. Suryanto, B. H. R.; Du, H.-L.; Wang, D.; Chen, J.; Simonov, A. N.; MacFarlane, D. R., Challenges and prospects in the catalysis of electroreduction of nitrogen to ammonia. *Nature Catalysis* **2019,** *2,* 290–296.

78. Choi, J.; Suryanto, B. H. R.; Wang, D.; Du, H.-L.; Hodgetts, R. Y.; Ferrero Vallana, F. M.; MacFarlane, D. R.; Simonov, A. N., Identification and elimination of false positives in electrochemical nitrogen reduction studies. *Nature Communications* **2020,** *11* (1), 5546.

79. Nielander, A. C.; McEnaney, J. M.; Schwalbe, J. A.; Baker, J. G.; Blair, S. J.; Wang, L.; Pelton, J. G.; Andersen, S. Z.; Enemark-Rasmussen, K.; Čolić, V.; Yang, S.; Bent, S. F.; Cargnello, M.; Kibsgaard, J.; Vesborg, P. C. K.; Chorkendorff, I.; Jaramillo, T. F., A Versatile Method for Ammonia Detection in a Range of Relevant Electrolytes via Direct Nuclear Magnetic Resonance Techniques. *ACS Catalysis* **2019,** *9* (7), 5797-5802.

80. Yang, X.; Kattel, S.; Nash, J.; Chang, X.; Lee, J. H.; Yan, Y.; Chen, J. G.; Xu, B., Quantification of Active Sites and Elucidation of the Reaction Mechanism of the Electrochemical Nitrogen Reduction Reaction on Vanadium Nitride. *Angewandte Chemie International Edition* **2019,** *58* (39), 13768-13772.

81. Lv, C.; Zhong, L.; Yao, Y.; Liu, D.; Kong, Y.; Jin, X.; Fang, Z.; Xu, W.; Yan, C.; Dinh, K. N.; Shao, M.; Song, L.; Chen, G.; Li, S.; Yan, Q.; Yu, G., Boosting Electrocatalytic Ammonia Production through Mimicking "π Back-Donation". *Chem* **2020,** *6* (10), 2690-2702.

82. Yao, Y.; Wang, H.; Yuan, X.-z.; Li, H.; Shao, M., Electrochemical Nitrogen Reduction Reaction on Ruthenium. *ACS Energy Letters* **2019,** *4* (6), 1336-1341.

83. Yao, D.; Tang, C.; Li, L.; Xia, B.; Vasileff, A.; Jin, H.; Zhang, Y.; Qiao, S.-Z., In Situ Fragmented Bismuth Nanoparticles for Electrocatalytic Nitrogen Reduction. *Advanced Energy Materials* **2020,** *10* (33), 2001289.

84. Chen, C.; Zhu, X.; Wen, X.; Zhou, Y.; Zhou, L.; Li, H.; Tao, L.; Li, Q.; Du, S.; Liu, T.; Yan, D.; Xie, C.; Zou, Y.; Wang, Y.; Chen, R.; Huo, J.; Li, Y.; Cheng, J.; Su, H.; Zhao, X.; Cheng, W.; Liu, Q.; Lin, H.; Luo, J.; Chen, J.; Dong, M.; Cheng, K.; Li, C.; Wang, S., Coupling N_2 and CO_2 in H_2O to synthesize urea under ambient conditions. *Nature Chemistry* **2020,** *12* (8), 717-724.

85. Liu, D.; Chen, M.; Du, X.; Ai, H.; Lo, K. H.; Wang, S.; Chen, S.; Xing, G.; Wang, X.; Pan, H., Development of Electrocatalysts for Efficient Nitrogen Reduction Reaction under Ambient Condition. *Advanced Functional Materials* **2020**, 2008983.

86. Liu, C.; Li, Q.; Wu, C.; Zhang, J.; Jin, Y.; Macfarlane, D. R.; Sun, C., Single-Boron Catalysts for Nitrogen Reduction Reaction. *Journal of the American Chemical Society* **2019,** *141* (7), 2884-2888.

87. Abghoui, Y.; Garden, A. L.; Howalt, J. G.; Vegge, T.; Skúlason, E., Electroreduction of N_2 to Ammonia at Ambient Conditions on Mononitrides of Zr, Nb, Cr, and V: A DFT Guide for Experiments. *ACS Catalysis* **2015,** *6* (2), 635-646.

88. Yang, Y.; Zhang, L.; Hu, Z.; Zheng, Y.; Tang, C.; Chen, P.; Wang, R.; Qiu, K.; Mao, J.; Ling, T.; Qiao, S.-Z., The Crucial Role of Charge Accumulation and Spin Polarization in Activating Carbon-Based Catalysts for Electrocatalytic Nitrogen Reduction. **2020,** *59* (11), 4525-4531.

89. Nitopi, S.; Bertheussen, E.; Scott, S. B.; Liu, X.; Engstfeld, A. K.; Horch, S.; Seger, B.; Stephens, I. E. L.; Chan, K.; Hahn, C.; Norskov, J. K.; Jaramillo, T. F.; Chorkendorff, I., Progress and Perspectives of Electrochemical CO2 Reduction on Copper in Aqueous Electrolyte. *Chemical Review* **2019,** *119* (12), 7610-7672.
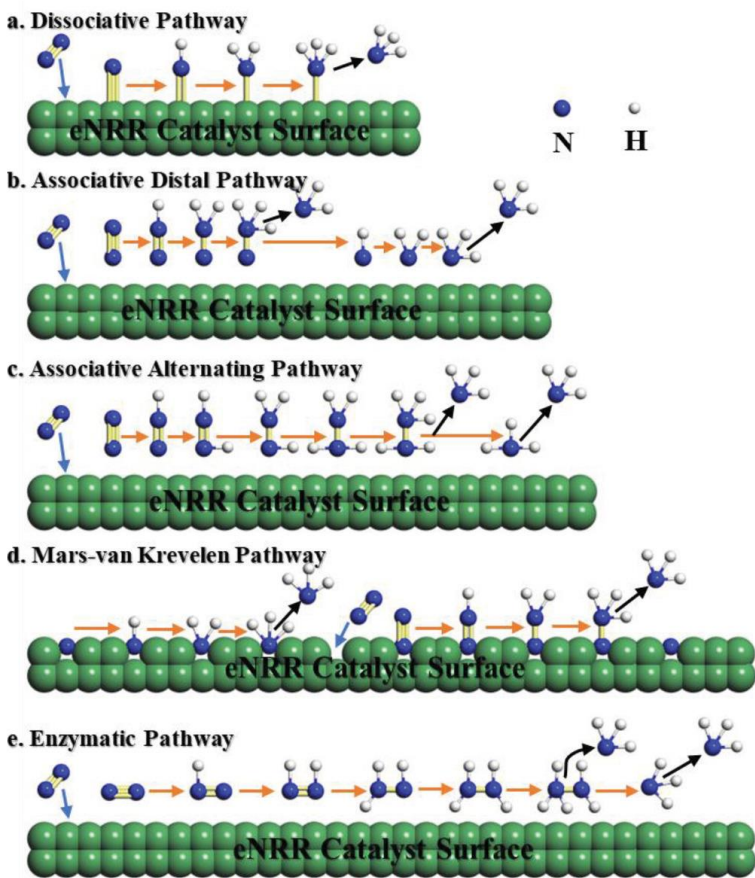
Figure1. Schematic diagrams of reaction pathways for the electrochemical nitrogen reduction reaction. Reproduced with permission.[85] Copyright 2020, Wiley-VCH.
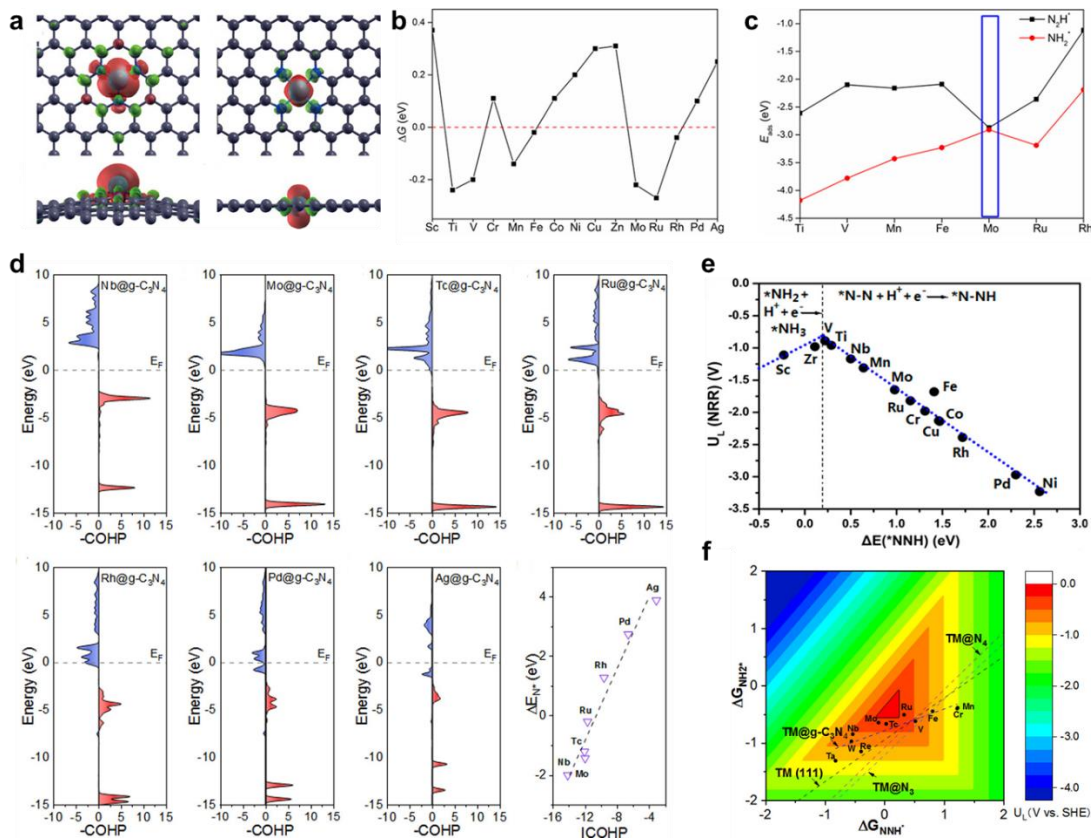
Figure 2. Mechanism insights for single metal site catalyst for NRR. (a) Optimized structure of FeN$_3$- and FeN$_4$-graphene with isosurface of spin-resolved density pictures. Reproduced with permission.[29] Copyright 2016, American Chemical Society; (b) Gibbs free energies of N$_2$ molecule. (c) Adsorption energies of N$_2$H and NH$_2$ species on SSCs by defective BN nanosheets. Reproduced with permission.[31] Copyright 2017, American Chemical Society; (d) Projected crystal orbital Hamilton population (pCOHP) between the metal center and the nitrogen adatom and illustration of the correlation between integrated COHP and the adsorption energy of nitrogen adatom (ΔE_{N*}). Reproduced with permission.[12] Copyright 2019, American Chemical Society; (e) Relationship between NRR limiting potential (U$_L$) and the binding energy of *N-NH ($\Delta E_{(*NNH)}$). Reproduced with permission.[35] Copyright 2020, American Chemical Society; (f) Contour plots of the limiting potential as a function of ΔG_{NNH*} and ΔG_{NH2*}. Reproduced with permission.[12] Copyright 2019, American Chemical Society.

a

Metal N₂ complex

σ donation from N₂

$M \leftarrow N\equiv N$
empty *d* orbital   occupied σ orbital

π backdonation to N₂

$M \rightarrow N\equiv N$
occupied *d* orbital   empty π* orbital

Borylene N₂ complex *(this work)*

$B \leftarrow N\equiv N$
empty *sp²* orbital   occupied σ orbital

$B \rightarrow N\equiv N$
occupied *p* orbital   empty π* orbital

Key: ↿⇂ = single electrons of opposite spin   ◖◗ = orbital lobes of opposite phase

b

Graphene   BN   BS   BP
S-triazine   Tri-s-triazine   h-MoS₂   t-MoS₂

c

NRR Favourable

HER Favourable

ΔG_{max}^{HER} (eV) vs ΔG_{max}^{NRR} (eV)

G-A, h-S1, BP-A, T-A, BP-S1, h-A, BS-A, T-S3, S-S3, T-S2, BN-A, t-A, S-S2

d

Top view
Side view
e/Å³

e

ΔG_{PDS} (eV)

Group IV   Group V   Group VI
*NH₂-*NH₃   *N₂-*N₂H

Ti, Zr, Hf, V, Nb, Ta, Cr, Mo, W

f

1.13 Å

B *sp*   N₂*B   N₂ *p*

π*
$sp_{y,z}^{B}$-π*   σ
$sp_{y,z}^{B}$-σ   π

pDOS (1/eV)

bonding
antibonding
N-B
Energy (eV)
−pCOHP

sp^3 ↻ π*
π* backdonation to N₂

sp^3 ↻ σ
σ donation from N₂

1.12 Å

B *sp*   N₂*B   N₂ *p*

π*
p_z^{B}-π*   σ
$sp_{x,y}^{B}$-σ   π

pDOS (1/eV)

bonding
antibonding
N-B
Energy (eV)
−pCOHP

p_z^{B} ↻ π*
π* backdonation to N₂

sp^2 ↻ σ
σ donation from N₂

54

Figure 3. Mechanism insights for single non-metal catalyst for electrochemical nitrogen reduction. (a) Nitrogen binding motifs to transition metals and borylenes. Reproduced with permission.[38] Copyright 2019, American Association for the Advancement of Science. (b) Proposed 2D materials and potential B-sites. (c) Selectivity of nitrogen reduction compared with hydrogen evolution. Reproduced with permission.[86] Copyright 2019, American Chemical Society. (d) Top: the atomic structure of B-doped MXene. Charge density difference of N_2 adsorption on B-doped Mo_2CO_2 via side-on (left) and end-on (right) patterns. (e) Free energy change at PDS for all single-boron MXene catalysts. Reproduced with permission.[41] Copyright 2019, American Chemical Society. (f) Optimized structure and differential charge density (lower panel) of N_2 adsorption on B/C_2N-a (upper panel) and B/C_2N-s (lower panel), and the bonding mechanism. Reproduced with permission.[48] Copyright 2020, Royal Chemical Society.
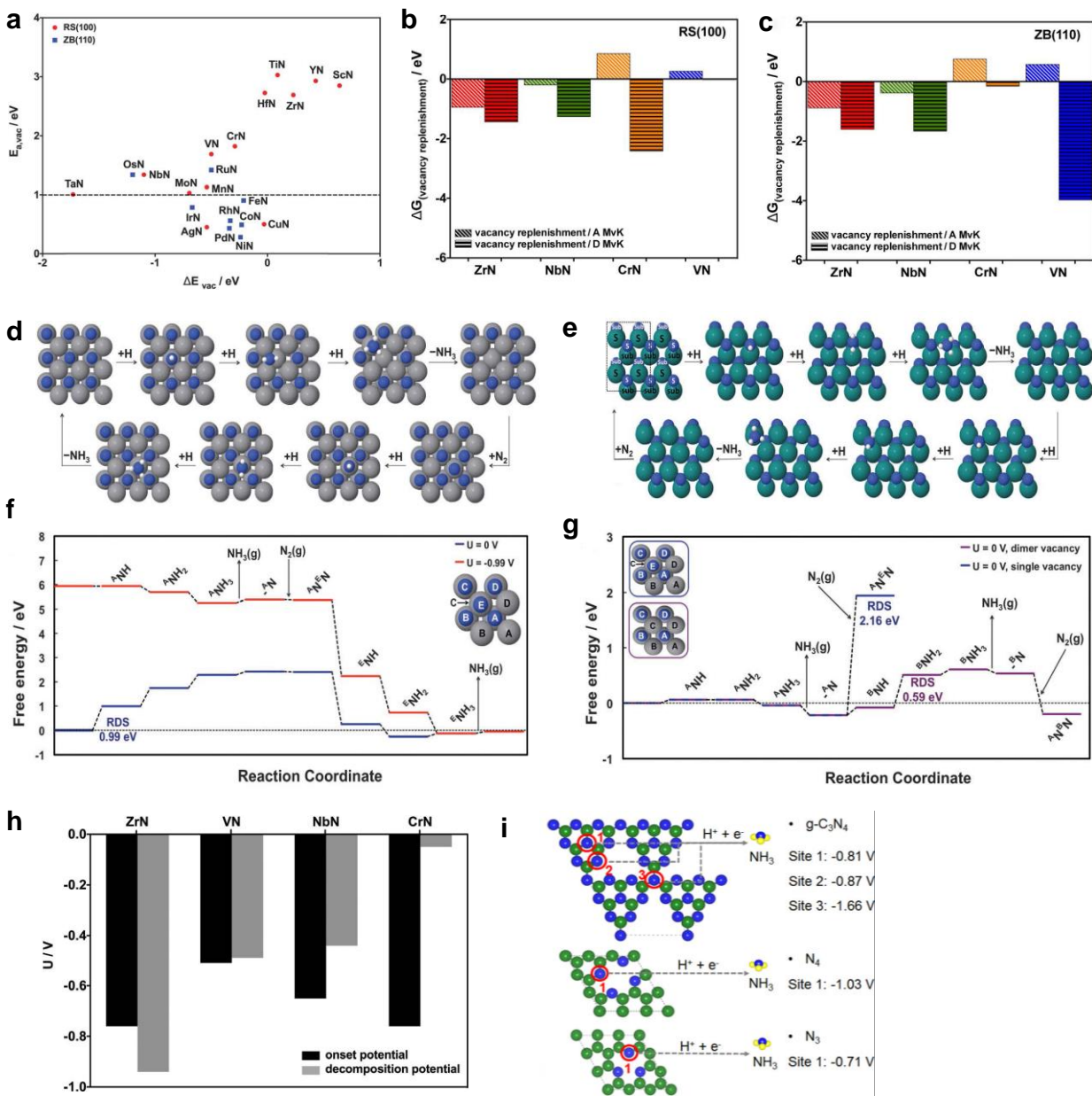
Figure 4. Theoretical considerations for single vacancy site as active centers for NRR. (a) Energy difference (ΔE_{vac}) of a vacancy in the surface layer and in the first subsurface layer of a nitride and the associated activation barrier of vacancy migration ($E_{a,vac}$). The dashed line at $E_{a,vac} = 1$ eV represents the cutoff above which metal nitrides are considered sufficiently stable for further study. Reproduced with permission.[28] Copyright 2015, Royal Chemical Society. Free energy changes for replenishing the vacancy associatively and dissociatively on (b) RS(100), and (c) ZB(110).

Reproduced with permission.[87] Copyright 2019, American Chemical Society. MvK mechanism for ammonia formation on the (100) facet of the RS structure (f) and the (110) facet of the ZB structure (g) of metal nitrides. (h) Decomposition potential for stable and active metal nitrides and the calculated onset potentials for electrocatalytic NH_3 formation at 300K. Reproduced with permission.[28] Copyright 2015, Royal Chemical Society.(i) Decomposition potentials of N-doped substrate. Reproduced with permission.[12] Copyright 2019, American Chemical Society.
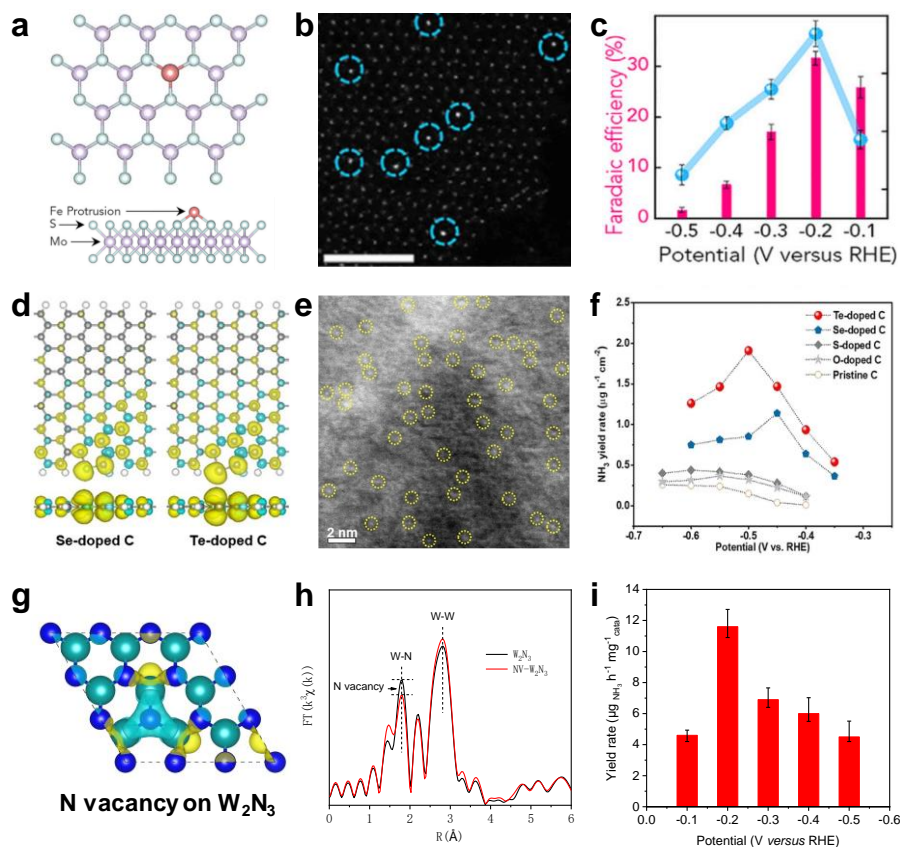
Figure 5. Experimental classification of SSCs. (a) Crystalline structures of protrusion-like shape of Fe single atom immobilized onto monolayer MoS_2. (b) HAADF-STEM images SACs-MoS_2-Fe catalysts. (c) FE and NH_3 production rates of SACs-MoS_2-Fe-2.0 applied at different working potentials in a flow cell. Reproduced with permission.[10] Copyright 2020, Elsevier. (d) Iso-surface of the spin-resolved density pictures of Se and Te-doped carbon. (e) HAADF-STEM image of Te-doped carbon catalyst. (f) NH_3 yield rate of carbon with different elemental doping at different working potentials. Reproduced with permission.[88] Copyright 2020, Wiley-VCH. (g) Charge density difference induced by nitrogen vacancy on NV-W_2N_3. (h) Fourier transform extended X-ray adsorption fine structure results of synchrotron-based W L_3 edge X-ray adsorption spectra of W_2N_3 and NV-W_2N_3. (i) NH_3 yield rate of NV-W_2N_3 at different working potentials. Reproduced with permission.[74] Copyright 2020, Wiley-VCH.
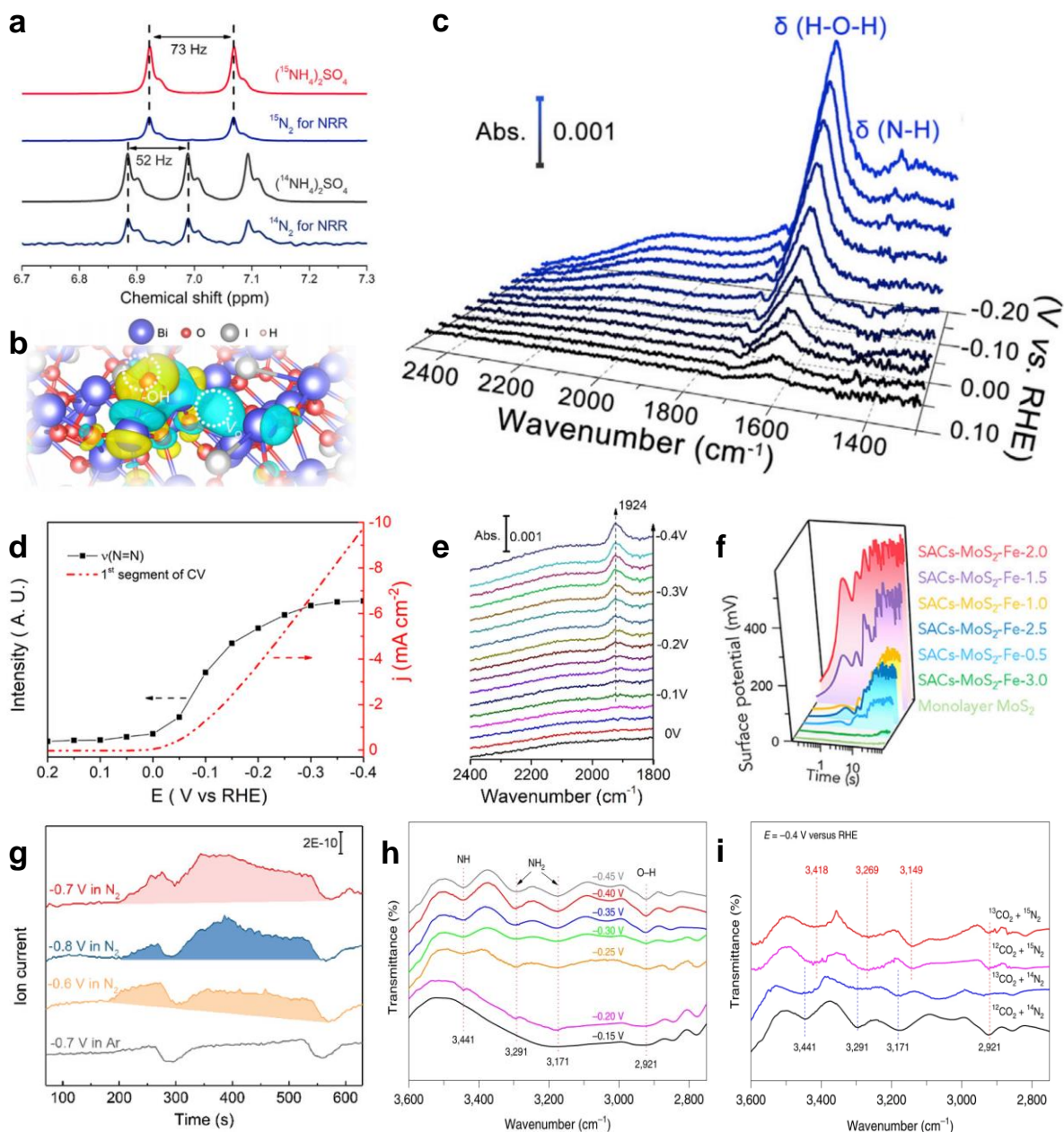
Figure 6. Advanced approaches for active site determination and intermediates detection. (a) ^{1}H NMR spectra of the electrolytes after eNRR using ^{15}N$_2$ [89] and ^{14}N$_2$ (down) as the gas feed. (b) DFT calculation and (c) in-situ ATR-FTIR measurement for reaction pathway determination and reaction intermediates detection. Reproduced with permission.[81] Copyright 2020, Elsevier. (d) The potential dependence of IR absorption of the N=N stretching (left) and the first segment of the CV curves (right) of ruthenium film in N$_2$-saturated 0.1 M HClO$_4$ electrolytes. (c) FTIR spectra on the

ruthenium film obtained at potentials from 0 to −0.4 V in an Ar-saturated 0.1 M HClO$_4$ electrolyte. Reproduced with permission.[82] Copyright 2019, American Chemical Society. (f) The surface potential differences with different of N$_2$-bubbling time. Reproduced with permission.[10] Copyright 2020, Elsevier. (g) Online DEMS measurement result of the catalysts at different reaction potentials and conditions. Reproduced with permission.[83] Copyright 2020, Wiley-VCH. (h) and (j) Isotope-labelling operando SR-FTIR spectra of the catalysts at different working potentials. Reproduced with permission.[84] Copyright 2020, Springer Nature.

Chapter 3: A Computational Study on Pt And Ru Dimers Supported on Graphene for The Hydrogen Evolution Reaction: New Insight into The Alkaline Mechanism

3.1 Introduction and Significance

A practical means for production of high-purity hydrogen as a clean fuel is via the electrochemical hydrogen evolution reaction (HER) from abundant water. In acid (pH<1) HER, a widely acknowledged descriptor, ΔG_{H*}, has successfully explained activity origins - and has been applied to direct rational design of electrocatalysts.

For alkaline (pH>13) HER however, also a critical reaction in producing high-purity hydrogen, it is not clear whether there is a singular activity descriptor. This therefore impedes provision of general guidelines for development of electrocatalysts.

In this we compare the acid HER activity of judiciously selected Pt, Ru dimer structures, and systematically investigate the underlying origin of catalytic activity for alkaline HER. Both thermodynamic and kinetic aspects are accounted for:

• We find that PtRu@NG displays an optimal theoretical activity with greater atomic utilization when compared with Pt-based catalysts;

• We show that current alkaline HER descriptors ΔG_{H*} and ΔG_{OH*} are unsuitable for evaluation of theoretical overpotential;

• We propose the dissociative chemisorption energy of water, ΔE_{diss}, as a singular activity descriptor for alkaline HER. This is because it has capacity to identify the smallest theoretical thermodynamic overpotential and because it scales linearly with the kinetic barrier;

• We present new insight into the mechanism route from electronic structure (d-band center) via ΔE_{diss} to alkaline HER activity.

This chapter will be of immediate benefit to guide rational development of new electrocatalysts for alkaline HER via electronic structural engineering to regulate ΔE_{diss}.

3.2 A Computational Study on Pt And Ru Dimers Supported on Graphene for The Hydrogen Evolution Reaction: New Insight into The Alkaline Mechanism

This Chapter is included as it appears as a journal paper published by **Xin Liu**, Yan Jiao*, Yao Zheng, Kenneth Davey, and Shi-Zhang Qiao*. A Computational Study on Pt And Ru Dimers Supported on Graphene for The Hydrogen Evolution Reaction: New Insight into The Alkaline Mechanism. ***Journal of Materials Chemistry A***. 2019, 7, 3648-3654.

Statement of Authorship

Title of Paper	Computational study on Pt, Ru dimer supported on graphene for hydrogen evolution reaction: new insight into the alkaline mechanism
Publication Status	☑ Published ☐ Accepted for Publication ☐ Submitted for Publication ☐ Unpublished and Unsubmitted work written in manuscript style
Publication Details	Liu, X., Jiao, Y., Zheng, Y., Davey, K., & Qiao, S.. Journal of Materials Chemistry A, 2019, 7, 3648.

Principal Author

Name of Principal Author (Candidate)	Xin Liu		
Contribution to the Paper	Proposed ideas, conduct computations wrote the manuscript.		
Overall percentage (%)	80		
Certification:	This paper reports on original research I conducted during the period of my Higher Degree by Research candidature and is not subject to any obligations or contractual agreements with a third party that would constrain its inclusion in this thesis. I am the primary author of this paper.		
Signature		Date	3/Feb/2021

Co-Author Contributions

By signing the Statement of Authorship, each author certifies that:

    i.   the candidate's stated contribution to the publication is accurate (as detailed above);

    ii.   permission is granted for the candidate in include the publication in the thesis; and

    iii.   the sum of all co-author contributions is equal to 100% less the candidate's stated contribution.

Name of Co-Author	Yan Jiao		
Contribution to the Paper	Discussed the concepts, supervised the research project, and revised the manuscript.		
Signature		Date	3/Feb/2021

Name of Co-Author	Yao Zheng		
Contribution to the Paper	Discussed the concepts, and revised the manuscript.		
Signature		Date	3/Feb/2021

Name of Co-Author	Kenneth Davey		
Contribution to the Paper	Discussed the concepts, and revised the manuscript.		
Signature		Date	3/Feb/2021

Name of Co-Author	Shi-Zhang Qiao		
Contribution to the Paper	Discussed concepts, supervised the research project and revised the manuscript.		
Signature		Date	3/Feb/2021

PAPER

Check for updates

A computational study on Pt and Ru dimers supported on graphene for the hydrogen evolution reaction: new insight into the alkaline mechanism†

Xin Liu, Yan Jiao, [ID]* Yao Zheng, [ID] Kenneth Davey and Shi-Zhang Qiao [ID]*

The electrochemical hydrogen evolution reaction (HER) is regarded as a practical means for the production of high-purity hydrogen from abundant water. Understanding the HER mechanism is therefore crucial to the design of high performance HER catalysts. Although approaches based on activity descriptors for the acidic HER have proven to be successful in revealing the origin of activity, and in directing the synthesis of electrocatalysts, the alkaline HER mechanisms and the activity descriptors remain largely unexplained. This impedes the overall design of electrocatalysts. Here, we systematically investigate the HER mechanism and the underlying origin of catalytic activity for the HER using Pt and Ru dimer structures as model catalysts. For the acidic HER, we found that PtRu dimer on nitrogen-doped graphene displayed a hydrogen adsorption free energy of −0.07 eV with higher atomic utilization. For the alkaline HER, we propose the dissociative chemisorption energy of water (ΔE_{diss}) as a singular activity descriptor following the analysis of several potential activity descriptors. ΔE_{diss} is proposed both because it has the capacity to identify the smallest theoretical thermodynamic overpotential and because it scales linearly with the kinetic barrier. We present new insight into the mechanism route from the electronic structure (d-band center) *via* ΔE_{diss} to alkaline HER activity. We conclude that this work will be of immediate benefit to guide rational development of electrocatalysts *via* electronic structural engineering to regulate ΔE_{diss} for the alkaline HER.

Introduction

A promising means for the production of high-purity hydrogen as a clean fuel is *via* the electrochemical hydrogen evolution reaction (HER) from abundant water.[1] In the acidic HER, the hydrogen adsorption free energy (ΔG_{H^*}) is well-documented as a singular activity descriptor. This is because it can be used to establish activity trends and to explain activity origin for a variety of materials.[2,3] Moreover, the electronic states around the Fermi level have been shown to highly correlate with ΔG_{H^*}, and thereby provide guidelines for the development of HER electrocatalysts *via* targeted engineering of the electronic structure.[3,4] Therefore, finding cheap and earth-abundant alternatives is crucial for the acidic HER development because of the limited resource of currently used noble metals. When compared with the acidic HER, the mechanism for the alkaline HER is less studied.[1,5] It is not clear whether there is a singular activity descriptor. This lack of understanding impedes the development of new electrocatalysts.[6] Both thermodynamics and kinetics aspects should be considered to develop such understanding.

From a thermodynamic view, it was thought reasonable to speculate that the adsorption energy of H* and/or OH* could affect the intrinsic activity of the alkaline HER. Yan *et al.* therefore proposed the hydrogen binding energy (HBE) as a descriptor.[7,8] However, a pH-dependent HBE trend was not observed for well-defined single crystal surfaces, and therefore it is difficult to explain the different activities of the same metal surface in different pH value solutions.[9] Markovic *et al.* proposed that the proton source in the alkaline HER was from water, and that the adsorption energetics of OH* (ΔG_{OH^*}) effect the overall activity.[10–12] Durst *et al.* reported, however, that at high pH (0.1 M NaOH), the oxophilicity of a catalyst (denoting OH* adsorption strength) does not affect alkaline HER activity.[13] It can be concluded therefore that neither H* nor OH* can serve as a singular activity descriptor.

As for the kinetics, it was conjectured that the kinetic barriers of water dissociation (E_{a}) might significantly affect overall reaction rates.[1,14] The high performance of a number of alkaline HER electrocatalysts has been reported to originate from their small E_{a}. Although these three key factors, ΔG_{H^*}, ΔG_{OH^*} and E_{a} have been proposed to affect the overall alkaline HER performance, and DFT calculations can be used to evaluate each factor individually, a quantitative analysis of the contribution of each to the overall catalytic activity has not been demonstrated. As a consequence, difficulties remain in predicting intrinsic activity trends

School of Chemical Engineering, The University of Adelaide, Adelaide, South Australia, 5005, Australia. E-mail: s.qiao@adelaide.edu.au; yan.jiao@adelaide.edu.au

† Electronic supplementary information (ESI) available. See DOI: 10.1039/c8ta11626a

65

for various families of materials.[1,6,15,16] In order to predict general activity trends and to provide guidelines for materials design, it is therefore important, and timely, to reveal an alkaline HER mechanism and to try to identify a singular activity descriptor.

Because judicious selection of a model system was considered crucial, it was determined that neither a single crystal system (because of difficulties in extending results to practical electrocatalysts) nor shape-controlled nanoparticles (difficult to model) would be suitable.[6,10] Dimer structures with two anchored-metal atoms, however, are advantageous compared with recently reported single atom catalysts (SACs). Advantages include that they (a) share the 'simplicity' of single crystals and SACs, which means they are readily easy to model with explicit active centres, (b) are capable of including low-coordinated metal atoms, which are believed to be the active centers for nanoparticle materials, and (c) permit introduction of an extra metal site which might be more approximate to the situation of multi-sites taking effects in nanoparticles.[17] In view of recent reports of successful syntheses of dimer structures, it was concluded that this model system could be used to investigate the reaction mechanism of the alkaline HER and, from it, determine a singular activity descriptor.[18–22]

Here, we systematically study Pt (optimal ΔG_{H*}) and Ru (small E_a) dimer structures supported on defective and nitrogen-doped graphene (DG and NG) for the HER by DFT calculations. We examine the stability of dimer structures and compare acidic HER (pH = 0) activity by calculating ΔG_{H*}. For the alkaline HER (pH = 14), following findings from calculations of the free energy diagram and transition states, we propose the dissociative chemisorption energy of water (ΔE_{diss}) as a singular activity descriptor. The results suggest that this descriptor quantifies both thermodynamic (theoretical overpotential) and kinetic (barrier, *i.e.* E_a) factors. Further analyses show that ΔE_{diss} scales linearly with the d-band center, and thereby provides new potential for the development of materials design *via* engineering of the electronic structure to regulate ΔE_{diss} to increase alkaline HER activity.

Results and discussion

Dimer formation

To ensure the stability of six dimer structures, namely, Pt$_2$@DG, Ru$_2$@DG, PtRu@DG, Pt$_2$@NG, Ru$_2$@NG and PtRu@NG (Fig. 1a), we calculated the formation energy ($\Delta E_{formation}$). The
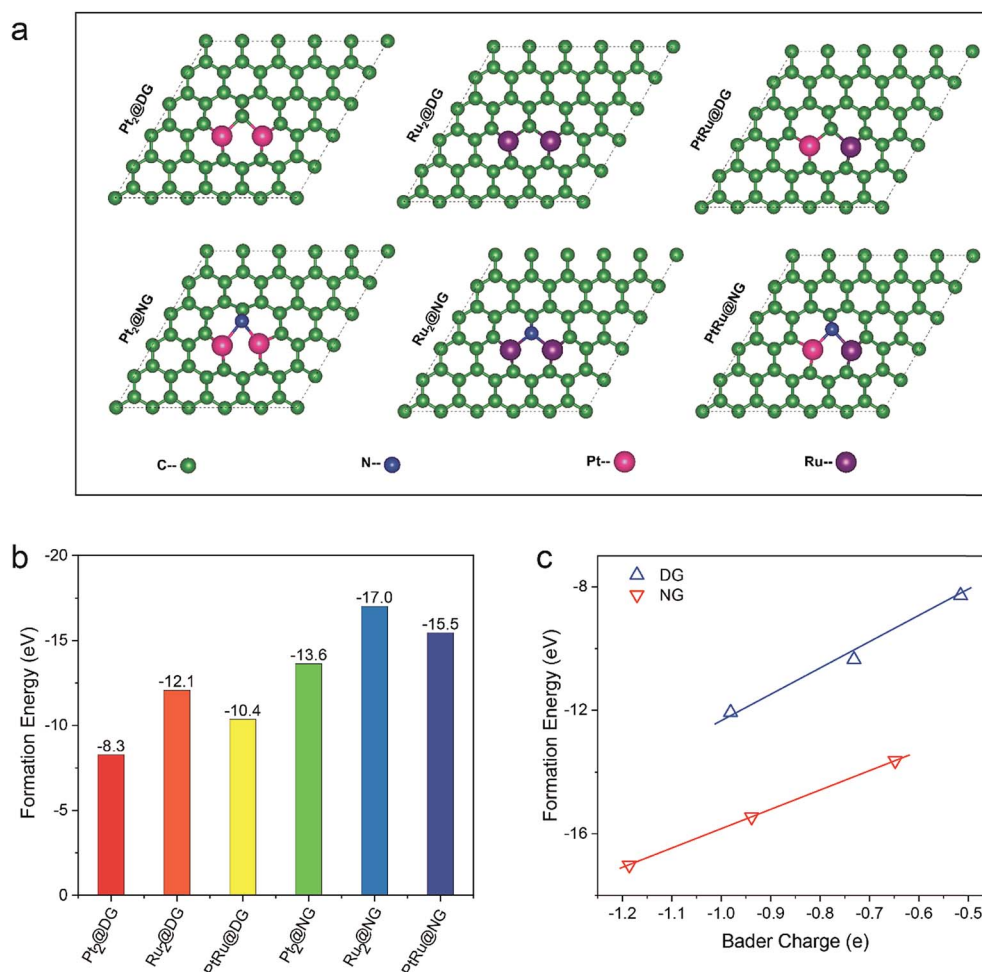
Fig. 1   (a) Atomic models of dimer structures supported on defective or nitrogen doped graphene; (b) formation energy of all six dimers; (c) the correlation between Bader charge difference and formation energy.

results are summarized in Fig. 1b, in which, a greater absolute value indicates a more stable state. As seen, all formation energies are negative, indicating that defective, nitrogen-doped graphene stabilizes these metal dimers. As seen in Fig. S1,† there is a strong resonance between the 2p orbital of C/N and the d orbital of Pt/Ru, which demonstrates the chemical bonding of C/N and Pt/Ru. This aids also in explaining the stabilization effect. Additionally, the results demonstrate that nitrogen doping facilitates thermodynamically the formation of dimer structures. Further, Bader charge analysis was used to quantitatively investigate the charge transfer during dimer formation. Fig. 1c summarizes the general relationship between $\Delta E_{formation}$ and the charge transferred. For each group of dimer structures, there is a linear relationship between structural stability and the transferred charge: the more charge transferred, the more negative the formation energy.

Hydrogen adsorption

Established hydrogen adsorption free energies (ΔG_{H*}) were used to compare the acidic HER activity of these dimer structures.[23] Thirty four possible initial configurations of hydrogen adsorption (Fig. S2†) were examined. The results of the more thermodynamically stable configurations are summarized in Fig. 2a, b and S3.† It is noted that for all six dimer configurations, the most favourable hydrogen adsorption site is the bridge between two metal atoms. The results suggest that the change of the metal atom, and switch of the graphene support, significantly alters hydrogen adsorption as well as HER activity.

Amongst these structures, Pt_2@DG exhibited the most negative ΔG_{H*} of −0.78 eV. This is similar to that recently reported for a Pt single atom catalyst.[24] Interestingly, PtRu@NG (Fig. 2b) shows a significantly greater HER activity with a ΔG_{H*} of −0.07 eV. This value is similar to that on a Pt single crystal surface ($\Delta G_{H*} = -0.09$ eV); however, PtRu@NG achieves similar activity with higher atomic utilization.[23]

To determine the underlying reason, we carried out electronic structure analysis. It was found that ΔG_{H*} scales linearly with the depth of the d-band center position relative to the Fermi level (Fig. 2c). This can be explained by analysing the hybridization between dimer structures and the hydrogen of PtRu@NG (Fig. 2d). The Fermi level crosses the bonding states of the metal d-band, therefore the filling of the bonding orbital determines the binding strength. A deeper d-band center indicates more filling of the bonding states, and thereby stronger H* adsorption and a more negative ΔG_{H*}. Therefore Pt_2@DG with a deeper d-band center exhibits a more negative ΔG_{H*}, whilst PtRu@NG exhibits a weaker H* adsorption.

Free energy diagram for the alkaline HER

Free energy diagrams for the alkaline HER were plotted to determine the potential-determining step, and the role of the adsorption energetics of H* and OH*. The full reaction pathway
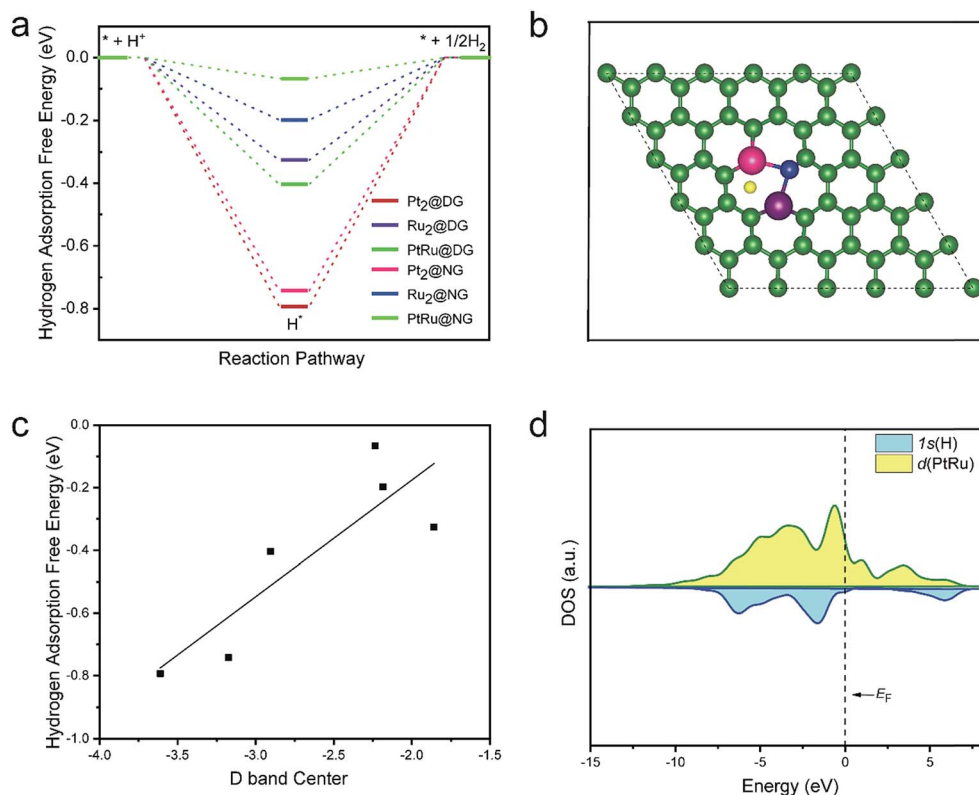
Fig. 2 (a) Hydrogen adsorption free energy diagram; (b) H adsorption configuration on PtRu@NG; (c) linear correlation between the d-band center and ΔG_{H*}; (d) projected density of states (PDOS) of the hydrogen adsorption configuration on PtRu@NG. Colour code: yellow, hydrogen; for other atoms please refer to Fig. 1.

3650 | *J. Mater. Chem. A*, 2019, **7**, 3648–3654

This journal is © The Royal Society of Chemistry 2019

67

includes dissociation of water molecules to form adsorbed hydrogen and hydroxide (H* + OH*), desorption of OH* to form OH$^-$, and desorption of H* to form H$_2$. All possible sites of these intermediates shown in Fig. S2† were tested to identify the most stable configurations. The results show that for Pt$_2$@DG (Fig. 3a), the hydrogen adsorption is so strong that desorption of hydrogen to form H$_2$ becomes difficult. This is therefore regarded as the potential-determining step. In this case, ΔG_{H*} can be used as an activity descriptor for evaluating the HER, a situation similar to the HBE for nanostructured Pt-group metals.[8] From Fig. 3b it can be seen that for Ru$_2$@NG with a relatively smaller $|\Delta G_{H*}|$, desorption of hydroxides (ΔG_{OH*}) is significantly more uphill and is identified as the potential-determining step (PDS). This is in agreement with the observations of Markovic et al.[10]

As shown in Fig. 3c and S4† for all six dimer structures, both hydrogen desorption and hydroxide desorption are thermodynamically uphill. Therefore, the theoretical overpotential should be equal to the larger value between the absolute value of ΔG_{H*} and ΔG_{OH*}.[25] It is clear that a balance between ΔG_{H*} and ΔG_{OH*} (as shown in Fig. 3d) is critical to achieve the smallest theoretical overpotential applied so as to make this elementary step exergonic – and to have an appreciable overall reaction rate.

Therefore, thermodynamically speaking, both hydrogen and hydroxide adsorption energetics should be taken into account to reveal an alkaline HER mechanism. However, neither ΔG_{H*} nor ΔG_{OH*} can reasonably serve as a singular activity descriptor.

Water dissociation kinetics

In addition to thermodynamic considerations, it is generally thought that the kinetic barrier of water dissociation (E_a) could affect the overall reaction rates. To investigate this we conducted climbing image nudged elastic band (CI-NEB) calculations so as to take kinetic factors into account. The results are summarized in Fig. 4 and Table S1.† We identified the transition states (TS) linking adsorbed water molecules and co-adsorbed H* and OH* and concluded that O–H bonding was stretched during the dissociation, and that after the breaking of the O–H bond, hydrogen and hydroxide anchored on different sites. As shown in Fig. 4a and Table S1,† Pt$_2$@DG ($E_a = 0.74$ eV) and Pt$_2$@NG ($E_a = 0.85$ eV) exhibit a greater kinetic barrier value for water dissociation compared with the other dimers. Importantly, this finding is consistent with previous reports that Pt is a poor water-dissociation catalyst.[1] From a kinetic viewpoint therefore, Pt$_2$@DG and Pt$_2$@NG dimer structures display the lowest water dissociation rate.

Amongst the dimer structures, Ru$_2$@NG (Fig. 4b) had the smallest water dissociation barrier of 0.35 eV. This means that it will facilitate the H–OH cleaving of water molecules. We analysed the length of the stretched O–H bond in TS and found that there was a linear correlation between the bond length and the kinetic barrier (E_a). As seen in Fig. S5,† the longer the bond length of O–H in TS, the greater the kinetic barrier. For example, results in Table S1† indicate that the bond lengths of stretched O–H in TS for Pt$_2$@DG and Pt$_2$@NG are 1.42 and 1.45 Å, respectively, whilst for Ru$_2$@NG, the O–H bond length is 1.36 Å and the kinetic
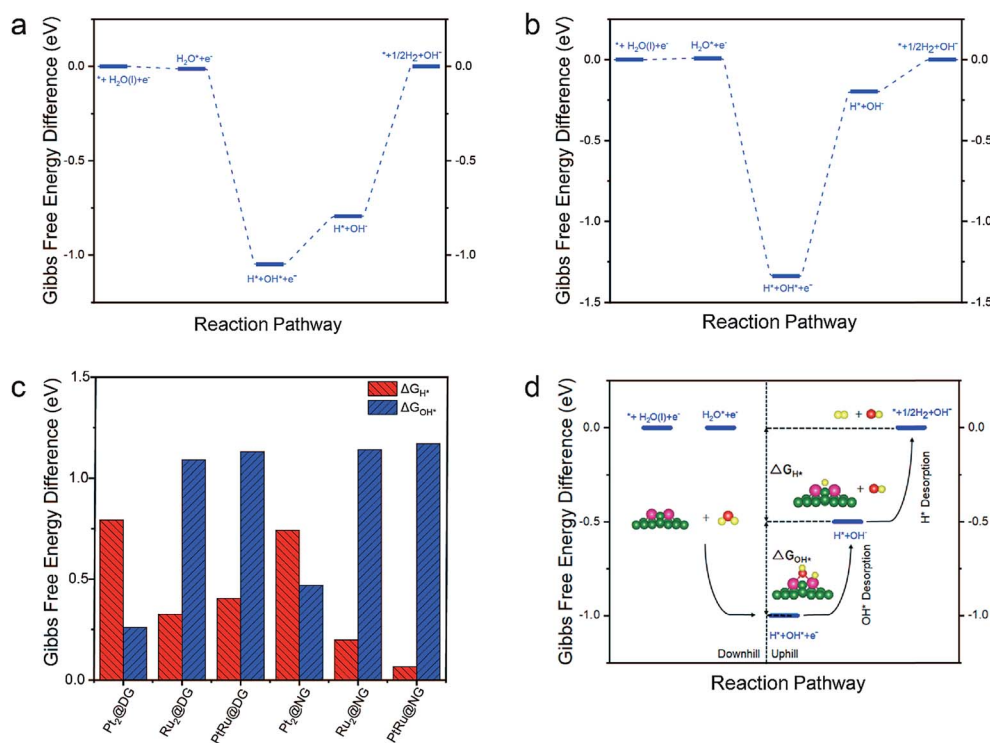
Fig. 3 Free energy diagrams of the alkaline hydrogen evolution reaction (HER) on: (a) Pt$_2$@DG and (b) Ru$_2$@NG; (c) free energy changes of the hydrogen and hydroxide desorption step for all six dimer structures; (d) schematic of the alkaline HER elementary steps and relevant free energy change. For colour code please refer to Fig. 1 and 2.

This journal is © The Royal Society of Chemistry 2019

J. Mater. Chem. A, 2019, 7, 3648–3654 | 3651

68
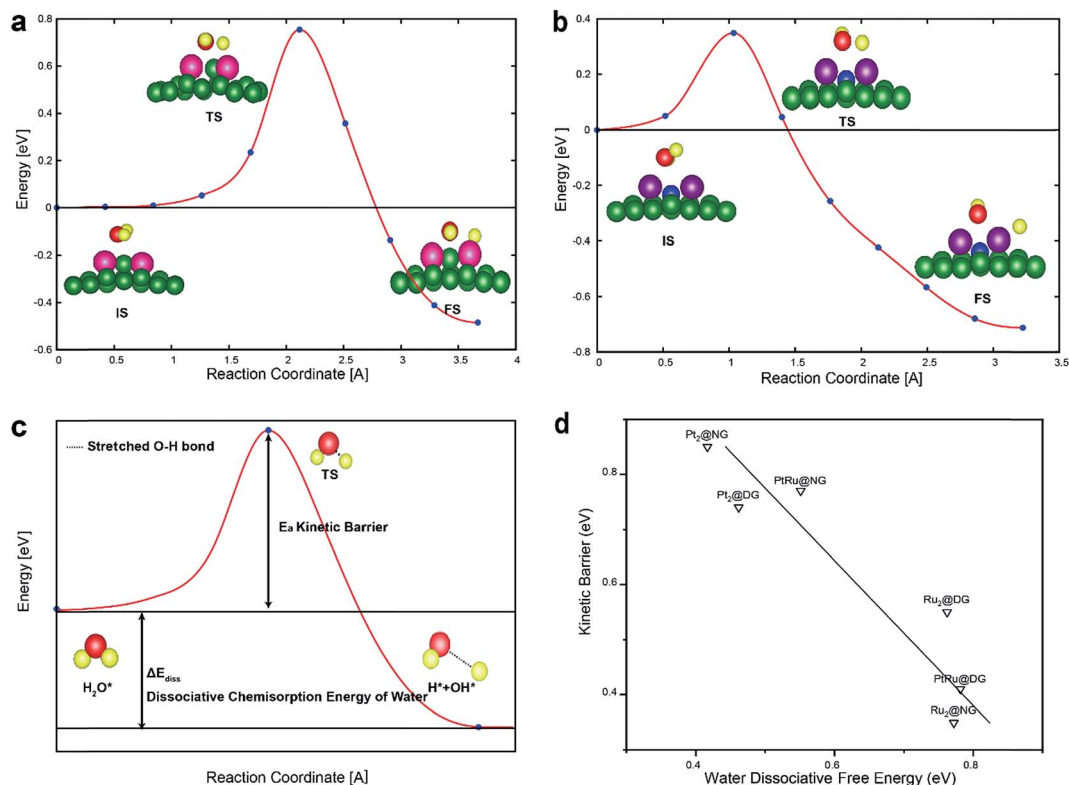
Fig. 4 Kinetic barrier of water dissociation for: (a) Pt₂@DG and (b) Ru₂@NG; (c) schematic diagram of the water dissociation step and relevant energetics; (d) correlation between the dissociative chemisorption energy of water and kinetic barrier. IS, TS and FS indicate initial, transition and final states, respectively. For colour code please refer to Fig. 2.

barrier is the lowest ($E_a = 0.35$ eV). It is reasonable to suggest that stretching O–H from the balanced distance makes the energy of water molecules increase, and the extent of configuration distortion indicates instability of TS. It is concluded therefore that the bond length of stretched O–H is an indicator of E_a.

Because it is significantly more difficult to calculate transition states than the stability of adsorbed intermediates, we constructed a mathematical model based only on energetics of intermediates to explore the correlation between kinetic barriers and the energetics for each elementary step. We investigated whether there is, in fact, a correlation between ΔG_{H*}, ΔG_{OH*}, the d-band center and the dissociative chemisorption energy of water (ΔE_{diss} in Fig. 4c) with E_a. The results (Fig. S6†) indicated that there is a poor linear relationship between each of ΔG_{H*}, ΔG_{OH*}, and the d-band center with E_a. As seen in Fig. 4d, ΔE_{diss}, however, displayed a meaningful linear correlation with E_a. This underscores that the kinetic barrier scales linearly with the dissociative chemisorption energy of water in Bronsted–Evans–Polanyi (BEP) type relationships.[26] The interpretation of this is that the more stable the adsorbed hydrogen and hydroxide (H* + OH*), the lower the barrier for water dissociation.

Further catalyst design principles

Although the theoretical overpotential and kinetic barriers can be evaluated, it is difficult to establish general alkaline HER activity trends for a range of materials and to provide guidelines

for the design of electrocatalysts. This problem arises because it is not clear whether contributions of the three factors, ΔG_{H*}, ΔG_{OH*}, and E_a, are independent. Taking Ru₂@NG as an example, although the splitting of water molecules is kinetically favourable ($E_a = 0.35$ eV), the OH* generated by dissociation can barely desorb from the active sites. This hinders consequent reaction steps. In contrast, Pt₂@DG ($E_a = 0.74$ eV), despite its sluggish water dissociation, may have better performance for the alkaline HER because of a low theoretical overpotential. It was concluded that there is a need therefore to find a singular activity descriptor that can correlate well with both kinetic barriers and theoretical overpotential.

Because of this established linear correlation between ΔE_{diss} and E_a, we explored the possibility of a correlation of ΔE_{diss} with ΔG_{H*} and ΔG_{OH*} from which we might establish a relationship between ΔE_{diss} and theoretical overpotential. In order to make sure analyses were based on a similar physical base, we included only Pt₂@DG, Pt₂@NG, Ru₂@DG and Ru₂@NG. The underlying reason for selecting homogeneous metal dimers was that, after cautious examination of the co-adsorption patterns of H* and OH* for all six dimer structures, we found the adsorption configuration could be readily classified in two groups. The first is the four homogeneous dimer structures involving hydrogen on the top site of the metal atom and hydroxide on the bridge site of the two metal atoms. The second is those with heterogeneous metal dimers, PtRu@DG and PtRu@NG, which display different H* and OH* adsorption configurations,
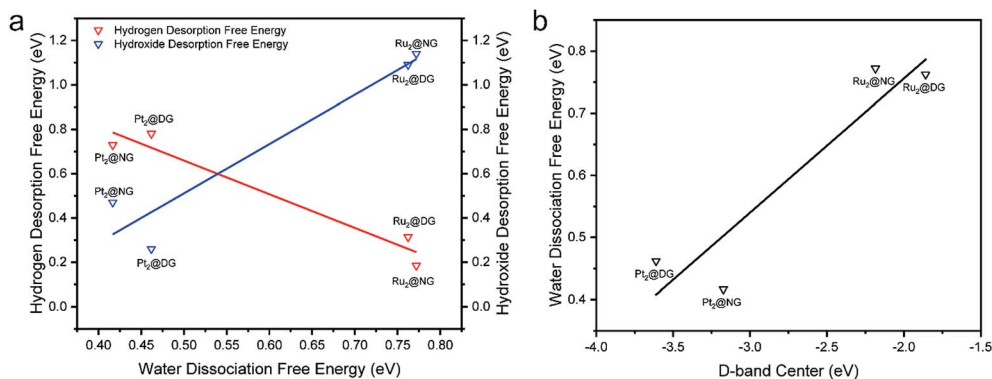
Fig. 5 (a) The relationship of the dissociative chemisorption energy of water (ΔE_{diss}) with hydrogen adsorption ($\Delta G_{\text{H*}}$) and the hydroxide desorption ($\Delta G_{\text{OH*}}$); (b) linear relationship between ΔE_{diss} and the d-band center.

namely, hydrogen on the top of Pt and hydroxide on the top of Ru. For the selected homogeneous metal dimer models, Fig. 5a shows that $\Delta G_{\text{OH*}}$ scales linearly with ΔE_{diss}, whilst $\Delta G_{\text{H*}}$ scales negatively linearly with ΔE_{diss}. Because we adopted the computational hydrogen electrode as a reference, 0 V *vs.* RHE is the equilibrium potential. The lines on this figure therefore show the limiting potential for hydrogen desorption (red line) and hydroxide desorption (blue line). Following from these results it is clear that when ΔE_{diss} is low, the formation of H$_2$ following hydrogen desorption is more endergonic than hydroxide desorption, and the H* → 1/2H$_2$ step becomes the potential-determining step. Clearly, when the dissociative chemisorption of water shows high values, the blue line is above the red line, meaning the OH* desorption step H* + OH* → H* + OH$^-$ becomes the potential-determining step. The red and blue lines of Fig. 5a intersect at about −0.55 eV of ΔE_{diss} and form an inverse volcano-shaped relationship. The top of this inverted volcano indicates the lowest theoretical overpotential for the alkaline HER on homogeneous metal dimer structures. It is concluded therefore that ΔE_{diss} and not $\Delta G_{\text{H*}}$ or $\Delta G_{\text{OH*}}$ is the most appropriate singular activity descriptor to evaluate thermodynamics in terms of theoretical overpotential.

According to the aforementioned observation and discussion, we propose that a suitable value of ΔE_{diss} will lead to a balanced $\Delta G_{\text{H*}}$ and $\Delta G_{\text{OH*}}$ values, and an optimal theoretical overpotential can therefore be achieved. Alongside an appropriate kinetic barrier which can be determined using ΔE_{diss} from Fig. 4d, this combination of thermodynamics and kinetics will be ideal for alkaline HER activity. Additionally, a linear correlation was found between the position of the d-band center relative to the Fermi level and ΔE_{diss} as shown in Fig. 5b. This suggests that water dissociation energetics are determined fundamentally by the electronic structure of the surface.

A new mechanism route that starts from the electronic structure (d-band center) to the singular activity descriptor (ΔE_{diss}) and intrinsic alkaline HER activity has therefore been highlighted. This new insight should serve as a guide for the design of electrocatalysts *via* electronic structural engineering to regulate ΔE_{diss}.

Conclusions

DFT calculations were used to construct the free energy diagram along the reaction pathway for the acidic (pH = 0) and alkaline (pH = 14) HER on newly proposed Pt and Ru metal dimer structures supported on graphene. For the acidic HER, PtRu@NG exhibited an optimal $\Delta G_{\text{H*}}$(−0.07 eV). For the alkaline HER we propose the dissociative chemisorption energy of water (ΔE_{diss}) as a singular activity descriptor on metal dimer structural models. ΔE_{diss} quantifies kinetic factors in addition to reaction thermodynamics because the kinetic barrier (E_{a}) scales linearly in BEP-like relationships. Because ΔE_{diss} correlates linearly with the d-band center of the metals on the substrate, a mechanism route for the alkaline HER has been highlighted. This new insight can serve as a guide for the development of electrocatalysts *via* electronic structural engineering to regulate ΔE_{diss}.

Conflicts of interest

The authors declare no competing financial interest.

Acknowledgements

References

1 Y. Zheng, Y. Jiao, Y. H. Zhu, L. H. Li, Y. Han, Y. Chen, M. Jaroniec and S. Z. Qiao, *J. Am. Chem. Soc.*, 2016, **138**, 16174–16181.
2 Z. W. Seh, J. Kibsgaard, C. F. Dickens, I. B. Chorkendorff, J. K. Norskov and T. F. Jaramillo, *Science*, 2017, **355**, 146–153.
3 Y. Jiao, Y. Zheng, K. Davey and S.-Z. Qiao, *Nat. Energy*, 2016, **1**, 16130.

This journal is © The Royal Society of Chemistry 2019

J. Mater. Chem. A, 2019, **7**, 3648–3654 | **3653**

70

4 H. Li, C. Tsai, A. L. Koh, L. L. Cai, A. W. Contryman, A. H. Fragapane, J. H. Zhao, H. S. Han, H. C. Manoharan, F. Abild-Pedersen, J. K. Norskov and X. L. Zheng, *Nat. Mater.*, 2016, **15**, 48–53.

5 P. J. Rheinländer, J. Herranz, J. Durst and H. A. Gasteiger, *J. Electrochem. Soc.*, 2014, **161**, F1448–F1457.

6 Y. Zheng, Y. Jiao, A. Vasileff and S. Z. Qiao, *Angew. Chem., Int. Ed.*, 2018, **57**, 7568–7579.

7 W. Sheng, M. Myint, J. G. Chen and Y. Yan, *Energy Environ. Sci.*, 2013, **6**, 1509–1512.

8 W. C. Sheng, Z. B. Zhuang, M. R. Gao, J. Zheng, J. G. G. Chen and Y. S. Yan, *Nat. Commun.*, 2015, **6**, 5848.

9 I. Ledezma-Yanez, W. D. Z. Wallace, P. Sebastián-Pascual, V. Climent, J. M. Feliu and M. T. Koper, *Nat. Energy*, 2017, **2**, 17031.

10 D. Strmcnik, P. P. Lopes, B. Genorio, V. R. Stamenkovic and N. M. Markovic, *Nano Energy*, 2016, **29**, 29–36.

11 D. Strmcnik, M. Uchimura, C. Wang, R. Subbaraman, N. Danilovic, D. van der Vliet, A. P. Paulikas, V. R. Stamenkovic and N. M. Markovic, *Nat. Chem.*, 2013, **5**, 300–306.

12 R. Subbaraman, D. Tripkovic, D. Strmcnik, K. C. Chang, M. Uchimura, A. P. Paulikas, V. Stamenkovic and N. M. Markovic, *Science*, 2011, **334**, 1256–1260.

13 J. Durst, A. Siebel, C. Simon, F. Hasche, J. Herranz and H. A. Gasteiger, *Energy Environ. Sci.*, 2014, **7**, 2255–2260.

14 B. You, X. Liu, G. Hu, S. Gul, J. Yano, D.-e. Jiang and Y. Sun, *J. Am. Chem. Soc.*, 2017, **139**, 12283–12290.

15 Y. Wu, X. Liu, D. Han, X. Song, L. Shi, Y. Song, S. Niu, Y. Xie, J. Cai, S. Wu, J. Kang, J. Zhou, Z. Chen, X. Zheng, X. Xiao and G. Wang, *Nat. Commun.*, 2018, **9**, 1425.

16 J. Zhang, T. Wang, P. Liu, Z. Liao, S. Liu, X. Zhuang, M. Chen, E. Zschech and X. Feng, *Nat. Commun.*, 2017, **8**, 15437.

17 X.-F. Yang, A. Wang, B. Qiao, J. Li, J. Liu and T. Zhang, *Acc. Chem. Res.*, 2013, **46**, 1740–1748.

18 M. Xiao, H. Zhang, Y. Chen, J. Zhu, L. Gao, Z. Jin, J. Ge, Z. Jiang, S. Chen, C. Liu and W. Xing, *Nano Energy*, 2018, **46**, 396–403.

19 L. Zhang, J. M. T. A. Fischer, Y. Jia, X. Yan, W. Xu, X. Wang, J. Chen, D. Yang, H. Liu, L. Zhuang, M. Hankel, D. J. Searles, K. Huang, S. Feng, C. L. Brown and X. Yao, *J. Am. Chem. Soc.*, 2018, **140**, 10757–10763.

20 J. Wang, Z. Huang, W. Liu, C. Chang, H. Tang, Z. Li, W. Chen, C. Jia, T. Yao and S. Wei, *J. Am. Chem. Soc.*, 2017, **139**, 17281–17284.

21 Y. Jiao, Y. Zheng, P. Chen, M. Jaroniec and S.-Z. Qiao, *J. Am. Chem. Soc.*, 2017, **139**, 18093–18100.

22 Y. Li, H. Su, S. H. Chan and Q. Sun, *ACS Catal.*, 2015, **5**, 6658–6664.

23 J. K. Norskov, T. Bligaard, A. Logadottir, J. R. Kitchin, J. G. Chen, S. Pandelov and J. K. Norskov, *J. Electrochem. Soc.*, 2005, **152**, J23–J26.

24 N. Cheng, S. Stambula, D. Wang, M. N. Banis, J. Liu, A. Riese, B. Xiao, R. Li, T.-K. Sham and L.-M. Liu, *Nat. Commun.*, 2016, **7**, 13638.

25 A. A. Peterson and J. K. Norskov, *J. Phys. Chem. Lett.*, 2012, **3**, 251–258.

26 J. K. Norskov, T. Bligaard, J. Rossmeisl and C. H. Christensen, *Nat. Chem.*, 2009, **1**, 37–46.

Supporting Information

Computational Study on Pt, Ru Dimer Supported on Graphene for Hydrogen Evolution Reaction: New Insight into the Alkaline Mechanism

Xin Liu, Yan Jiao*, Yao Zheng, Kenneth Davey and Shi-Zhang Qiao*

School of Chemical Engineering, The University of Adelaide, Adelaide, SA 5005, Australia

Corresponding Author

*E-mail: s.qiao@adelaide.edu.au.

*E-mail: yan.jiao@adelaide.edu.au.

This PDF file includes:

Models and Computational Details

Figures S1 to S6

Table S1

Reference 1-12

Models and computational details

Three noble metal dimers (Pt$_2$, Ru$_2$, and PtRu) supported on defective graphene (DG) and nitrogen-doped graphene (NG) (Fig.1a) were constructed. The configuration of metal atoms anchored to two adjacent single vacancies are based on previous experimental and computational studies.[1, 2] We firstly examine the stability of all of the six dimers on graphene by computing the formation energy for each structure. Energy reference of a single metal atom was set to be within a close-packed unit cell, and that of the substrate is the corresponding support without metal dopants. The formation energy can be calculated as follows:

$$\Delta E_{formation} = E_{dimer} - (E_{metal-dopant} + E_{support})$$

where E_{dimer}, $E_{metal-dopant}$, $E_{support}$ is the energy of catalyst with dimer structure, doping metal, and defective or nitrogen doped graphene, respectively.

Afterwards, we explored the key species i.e. hydrogen and hydroxide adsorption behaviour, on these six dimer structures. Five possible hydrogen or hydroxide adsorption sites for homogeneous Pt$_2$, Ru$_2$ dimer structures were considered as outlined in Fig. S1a. For heterogeneous PtRu dimer structures, seven possible adsorption configuration were proposed and tested to find the most thermodynamically stable adsorption site, as is shown in Fig. S1b. Beyond single reaction intermediates adsorption, the co-adsorption of hydrogen and hydroxide on dimers was also investigated for four (for homogenous dimer structures) or six (for heterogeneous dimer structures) possible configuration guesses. The transition state was also calculated to evaluate kinetic barrier of water dissociation.

All the calculations were performed by means of spin-polarized density functional theory (DFT) methods as implemented in the Vienna ab initio Simulation Package;[3-6] the projector-augmented-wave pseudopotential was utilized to treat the core electrons, while the Perdew−Burke−Ernzerhof exchange-correlation functional of the generalized gradient approximation was used for describing the electron interactions.[7] A plane-wave cutoff energy of 400 eV was adopted for all the calculations. The vacuum space in the z-direction was set as 20 Å to prevent the interaction between periodic images. The van der Waals interactions were described using the empirical correction in Grimme's scheme.[8] The reciprocal space was sampled using a 5 × 5 × 1 k-points for fully relaxed geometry

optimization until the maximal residual force was < 0.02 eV/Å. For electronic structure calculations, a 10 × 10 × 1 k-points grid was used, and the Bader charge analysis was performed to reveal the charge transfer process.[9] The minimum energy path (MEP) of water dissociation on defective or nitrogen doped graphene supported metal dimers was obtained by the climbing image nudged elastic band (CI-NEB) method.[10]

The calculation of the free energy diagrams was performed by using the concept of computational hydrogen electrode (CHE).[11] In this framework, the chemical potential of the electron-proton pair (H^+ + e^-) can be referenced by the chemical potential of gaseous H_2 at equilibrium (0 V vs reversible hydrogen electrode). The change of free energy can be calculated as follows:

$\Delta G = \Delta E + \Delta E_{ZPE} - T\Delta S + \Delta G_{pH} + \Delta G_{sol}$

where ΔE is the electronic energy difference directly obtained by DFT calculation. ΔE_{ZPE} is the change in zero-point energies (ZPE), T is the room temperature (T = 298.15K), and ΔS is the entropy change. ZPE and vibrational entropy of adsorbed species were obtained after frequency calculations, and entropy of gas molecules (H_2 and H_2O) were taken from standard values.[12] At different pH values, $\Delta G_{pH} = 0.059 \times pH$. ΔG_{sol} represents the correction terms for solvent effect (0 eV for H* and 0.5 eV for OH*). [1, 11]
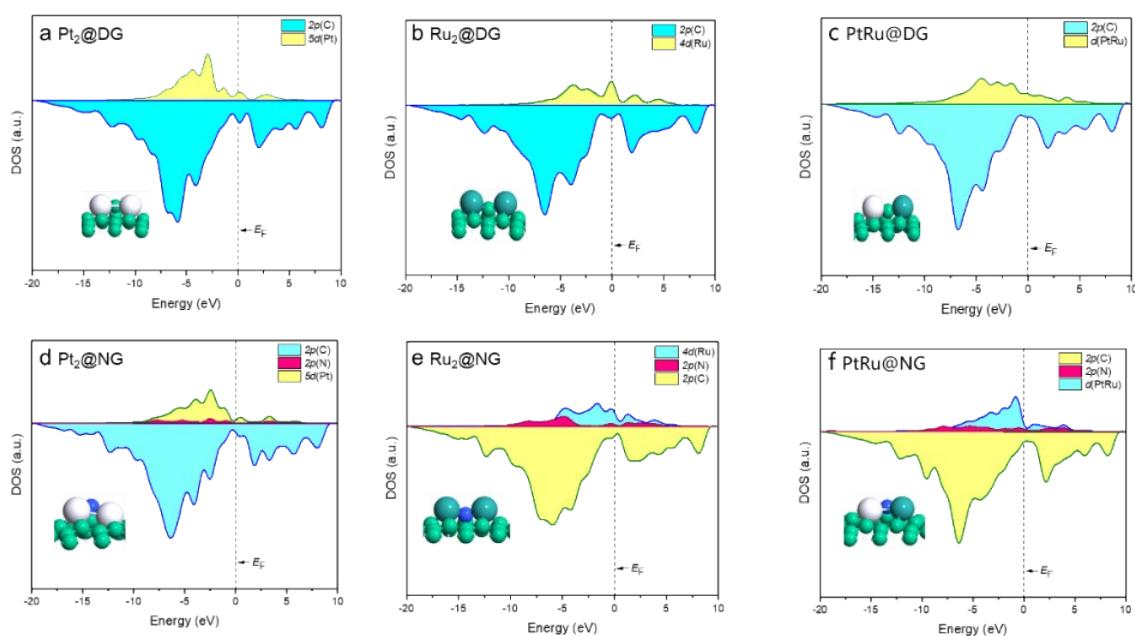
Figure S1. Projected density of states illustrating the 2p orbital of carbon or nitrogen, the d orbital of Pt and Ru, for (a) $Pt_2@DG$; (b) $Ru_2@DG$; (c) $PtRu@DG$; (d) $Pt_2@NG$; (e) $Ru_2@NG$; (f) $Pt_2@NG$.
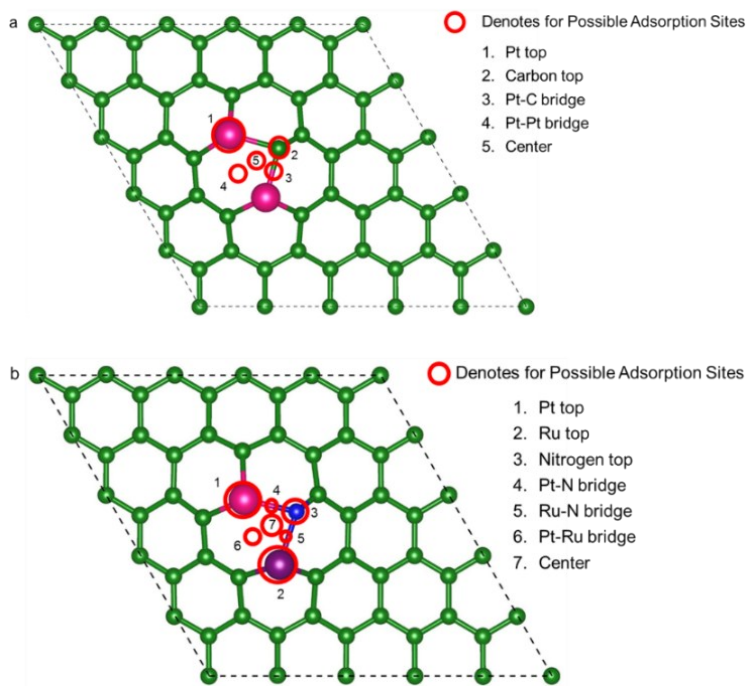
Figure S2. Illustration of possible adsorption sites on dimer including top, bridge and centre sites: (a) five possible sites on $Pt_2@DG$, (b) seven possible sites on $PtRu@NG$.
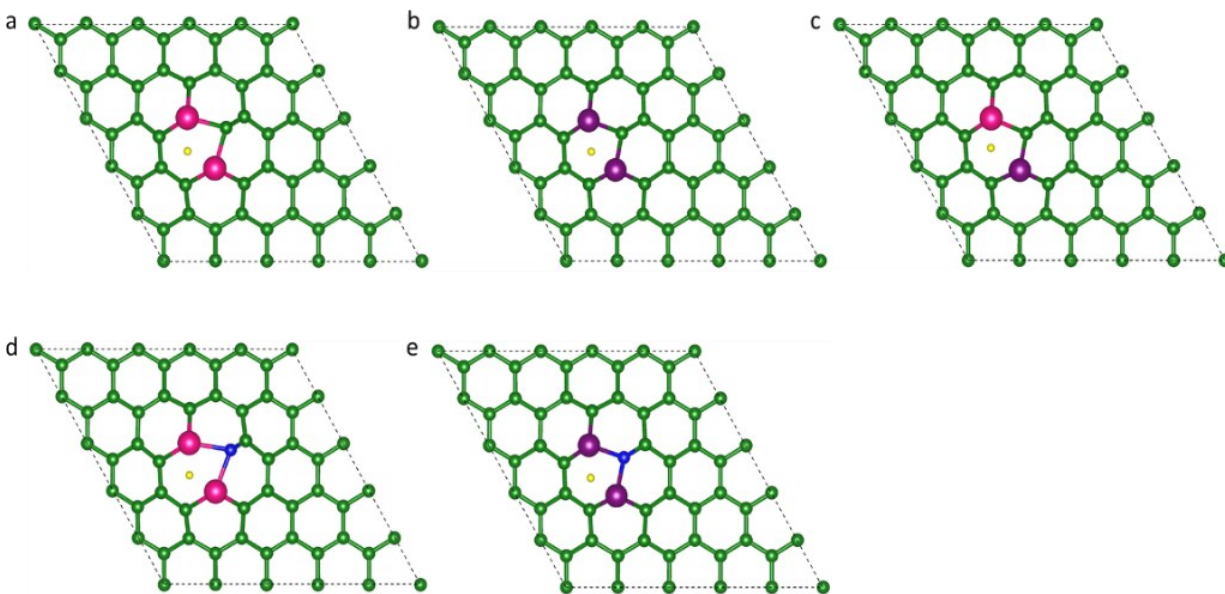
Figure S3. Illustration of hydrogen adsorption pattern on (a) Pt$_2$@DG, (b) Ru$_2$@DG, (c) PtRu@DG, (d) Pt$_2$@NG, (e) Ru$_2$@NG.
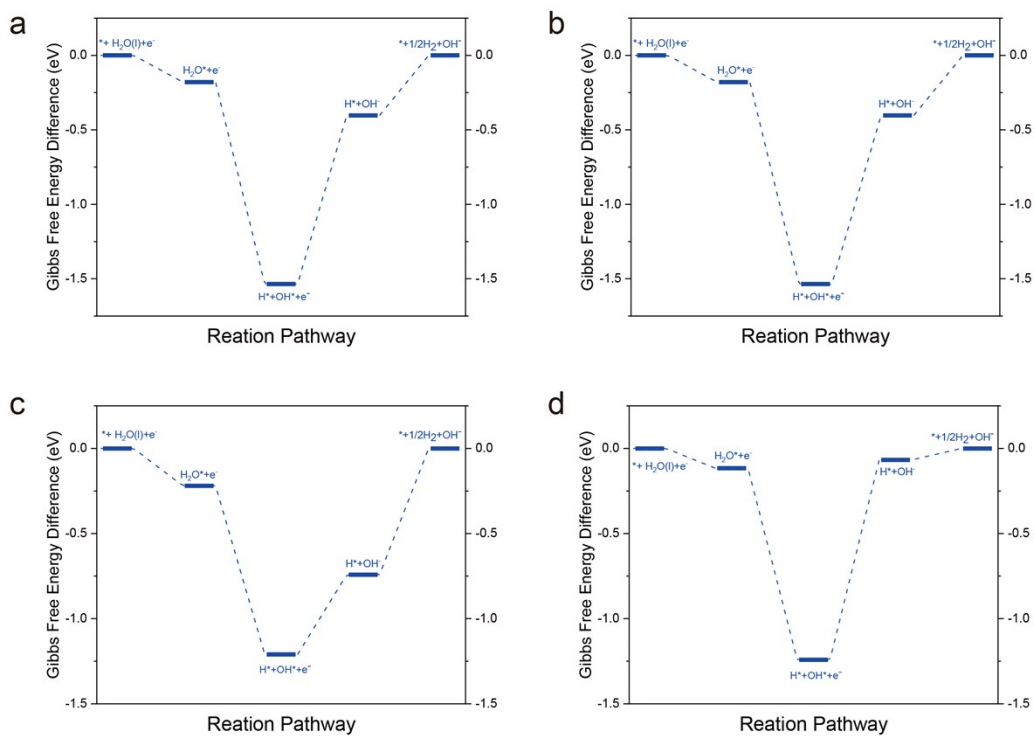
Figure S4. Gibbs free energy diagram of alkaline hydrogen evolution reaction on (a) Ru$_2$@DG; (b) PtRu@DG; (c) Pt$_2$@NG; (d) PtRu@NG.
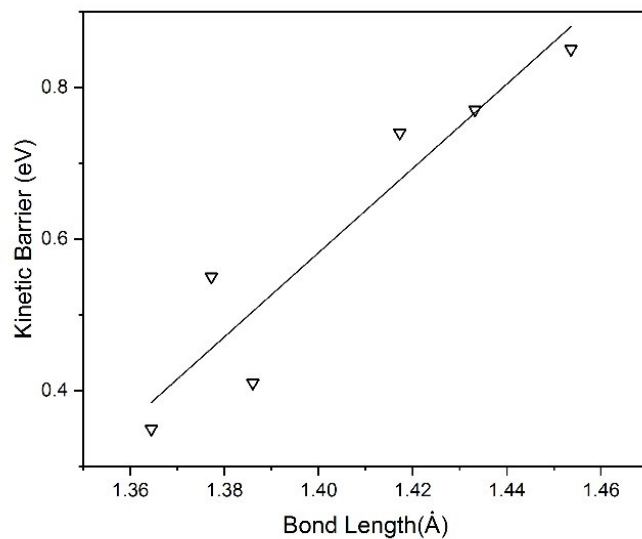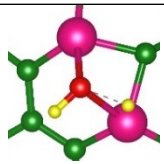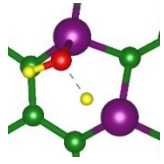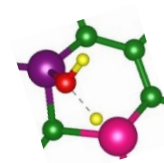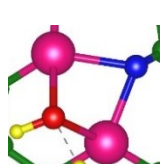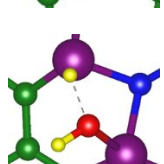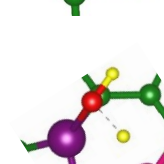
Figure S5. The linear correlation between the bond length of stretched O-H and kinetic barrier (E_a).
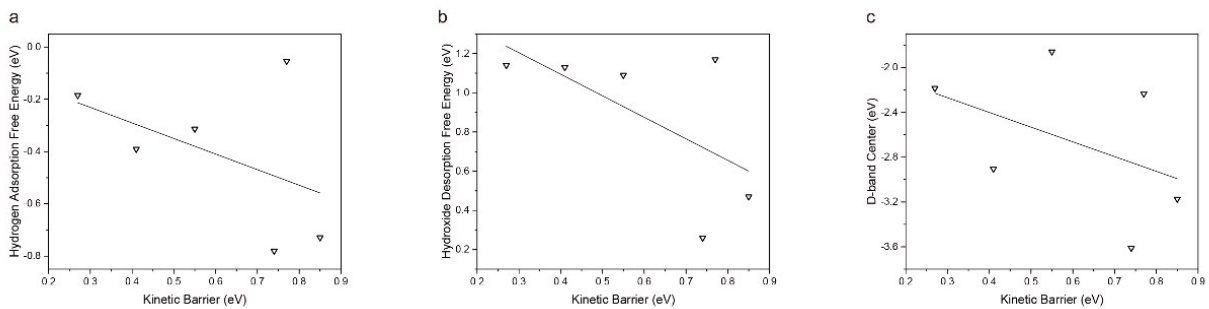
Figure S6. Correlation between kinetic barriers (E_a) with (a) hydrogen adsorption free energy; (b) hydroxide desorption free energy; (c) d-band centre.

Table S1. Summary of kinetic barrier of water dissociation on dimer structure, relevant transition states (TS) models and the bond length of stretched O-H of TS.

Dimer Name	Dimer Structure	Kinetic Barrier (eV)	O-H Bond length (Å)
Pt$_2$@DG		0.74	1.42
Ru$_2$@DG		0.55	1.38
PtRu@DG		0.41	1.39
Pt$_2$@NG		0.85	1.45
Ru$_2$@NG		0.35	1.36
PtRu@NG		0.77	1.43

Reference

1. Y. W. Li, H. B. Su, S. H. Chan and Q. Sun, *Acs Catal*, 2015, **5**, 6658-6664.

2. Z. He, K. He, A. W. Robertson, A. I. Kirkland, D. Kim, J. Ihm, E. Yoon, G.-D. Lee and J. H. Warner, *Nano letters*, 2014, **14**, 3766-3772.

3. G. Kresse and J. Furthmüller, *Computational materials science*, 1996, **6**, 15-50.

4. G. Kresse and J. Furthmüller, *Physical review B*, 1996, **54**, 11169.

5. G. Kresse and J. Hafner, *Physical Review B*, 1993, **47**, 558.

6. G. Kresse and J. Hafner, *Physical Review B*, 1994, **49**, 14251.

7. J. P. Perdew, K. Burke and M. Ernzerhof, *Phys Rev Lett*, 1996, **77**, 3865.

8. S. Grimme, *Journal of computational chemistry*, 2006, **27**, 1787-1799.

9. W. Tang, E. Sanville and G. Henkelman, *Journal of Physics: Condensed Matter*, 2009, **21**, 084204.

10. G. Henkelman, B. P. Uberuaga and H. Jónsson, *The Journal of chemical physics*, 2000, **113**, 9901-9904.

11. J. K. Norskov, T. Bligaard, A. Logadottir, J. R. Kitchin, J. G. Chen, S. Pandelov and J. K. Norskov, *J Electrochem Soc*, 2005, **152**, J23-J26.

12. W. M. Haynes, *CRC handbook of chemistry and physics*, CRC press, 2014.

Chapter 4: Building up a Picture of the Electrocatalytic Nitrogen Reduction Activity of Transition Metal Single-Atom Catalysts.

4.1 Introduction and Significance

The lack of efficient electrocatalysts impedes the development of electrochemical nitrogen reduction reaction (eNRR) as an alternative to Haber-Bosch process. The development of heterogeneous electrocatalyst is dependent on the understanding of fundamental chemistry in electrocatalytic nitrogen reduction process. Inspired by the homogeneous molecular catalysts, single atom catalysts (SACs), sharing the similarity that metal centers are coordinated with well-designed ligands, emerges as a frontier in the field of eNRR. Although some single atom catalysts (SACs) have been theoretically predicted or experimentally verified to be active for eNRR, previous works were focused either on the experimental evaluation or computational screening of their performance but gave very limited guidelines for the design of targeted electrocatalysts.

In order to facilitate the design of SACs as eNRR electrocatalysts in an educated direction, instead of trial-and-error attempts, we explore a large dataset including twenty metal centers coordinated by three supports (three types of ligands) to reveal the fundamental chemistry in this system. We build up a full picture (activity trends, electronic origins and design strategies) of the potential of transition metal SACs for eNRR based on the detailed mechanistic studies. The roles of both supports (ligands) and metal centers on the eNRR activity are revealed in depth. Finally, the acquired knowledge of chemistry in this system was used to direct the rational design, which resulted in the proposal of two-step strategy for the design of eNRR electrocatalysts.

The highlights of this chapter include:

• We demonstrate that different potential determining steps (PDS) exist for transition metal SACs, which results in the variation of the limiting potential and explains the complexity of designing eNRR electrocatalysts.

• We propose a sole activity descriptor, nitrogen adatom adsorption energy (ΔE_{N*}), for eNRR reaction.

• We reveal that the origin of the ΔE_{N*} variation is attributed to the influence of the population of metal centres on the bonding/anti-bonding orbital, and the catalyst supports (ligands) indirectly affect the eNRR performance by regulating the scaling relationship of intermediates adsorption.

We propose the following two-step strategy for the design of SACs for eNRR: (1) selection of the most promising family of SACs (suitable ligands to anchor metal centers) whose scaling relation is close to the activity peak; (2) further improvement of the performance via breaking the scaling relation by tuning the adsorption strength.

4.2 Building up a Picture of the Electrocatalytic Nitrogen Reduction Activity of Transition Metal Single-Atom Catalysts.

This Chapter is included as it appears as a journal paper published by **Xin Liu**, Yan Jiao*, Yao Zheng, Mietek Jaroniec, Shi-Zhang Qiao*. Building up a Picture of the Electrocatalytic Nitrogen Reduction Activity of Transition Metal Single-Atom Catalysts. ***Journal of the American Chemical Society***. 2019, 141, 9664-9672.

Statement of Authorship

Title of Paper	Building Up a Picture of the Electrocatalytic Nitrogen Reduction Activity of Transition Metal Single-Atom Catalysts
Publication Status	☑ Published ☐ Accepted for Publication ☐ Submitted for Publication ☐ Unpublished and Unsubmitted work written in manuscript style
Publication Details	Liu, X., Jiao, Y., Zheng, Y., Jaroniec, M., & Qiao, S. J. Am. Chem. Soc. 2019, 141, 9664−9672

Principal Author

Name of Principal Author (Candidate)	Xin Liu		
Contribution to the Paper	Proposed ideas, conduct computations and wrote the manuscript.		
Overall percentage (%)	80		
Certification:	This paper reports on original research I conducted during the period of my Higher Degree by Research candidature and is not subject to any obligations or contractual agreements with a third party that would constrain its inclusion in this thesis. I am the primary author of this paper.		
Signature		Date	3/Feb/2021

Co-Author Contributions

By signing the Statement of Authorship, each author certifies that:

i.   the candidate's stated contribution to the publication is accurate (as detailed above);

ii.   permission is granted for the candidate in include the publication in the thesis; and

iii.   the sum of all co-author contributions is equal to 100% less the candidate's stated contribution.

Name of Co-Author	Yan Jiao		
Contribution to the Paper	Discussed the concepts, supervised the research project, and revised the manuscript.		
Signature		Date	3/Feb/2021

Name of Co-Author	Yao Zheng		
Contribution to the Paper	Discussed the concepts, and revised the manuscript.		
Signature		Date	3/Feb/2021

Name of Co-Author	Mietek Jaroniec			
Contribution to the Paper	Discussed the concepts, and revised the manuscript.			
Signature			Date	3/Feb/2021

Name of Co-Author	Shi-Zhang Qiao			
Contribution to the Paper	Discussed concepts, supervised the research project, and revised the manuscript.			
Signature			Date	3/Feb/2021

Building Up a Picture of the Electrocatalytic Nitrogen Reduction Activity of Transition Metal Single-Atom Catalysts

Xin Liu,[†] Yan Jiao,*,[†] Yao Zheng,[†] Mietek Jaroniec,[‡] and Shi-Zhang Qiao*,[†]

[†]School of Chemical Engineering, The University of Adelaide, Adelaide, South Australia 5005, Australia
[‡]Department of Chemistry and Biochemistry, Kent State University, Kent, Ohio 44242, United States

S *Supporting Information*

ABSTRACT: The lack of chemical understanding and efficient catalysts impedes the development of electrocatalytic nitrogen reduction reaction (eNRR) for ammonia production. In this work, we employed density functional theory calculations to build up a picture (activity trends, electronic origins, and design strategies) of single-atom catalysts (SACs) supported on nitrogen-doped carbons as eNRR electrocatalysts. To construct such a picture, this work presents systematic studies of the eNRR activity of SACs covering 20 different transition metal (TM) centers coordinated by nitrogen atoms contained in three types of nitrogen-doped carbon substrates, which gives 60 SACs. Our study shows that the intrinsic activity trends could be established on the basis of the nitrogen adatom adsorption energy (ΔE_{N*}). Furthermore, the influence of metal and support (ligands) on ΔE_{N*} proved to be related to the bonding/antibonding orbital population and regulating the scaling relations for adsorption of intermediates, respectively. Accordingly, a two-step strategy is proposed for improving the eNNR activity of TM-SACs, which involves the following: (i) selection of the most promising family of SACs (g-C$_3$N$_4$ supported SACs as predicted in this work) and (ii) further improvement of the activity of the best candidate in the aforementioned family via tuning the adsorption strength of the key intermediates. Also, the stability of N-doped carbon supports and their selectivity in comparison to the competing hydrogen evolution need to be taken into consideration for screening the durable and efficient candidates. Finally, an effective strategy for designing active, stable, and selective SACs based on the mechanistic insights is elaborated to guide future eNRR studies.
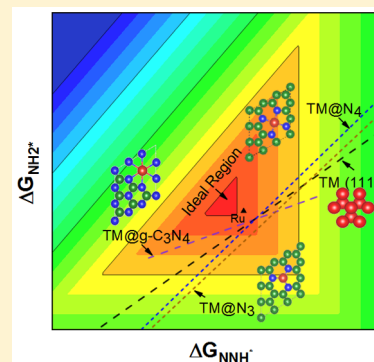
■ INTRODUCTION

Industrial nitrogen chemistry plays a crucial role in modern life to produce fertilizers and chemicals.[1] One of the core industrial processes, ammonia synthesis via Haber−Bosch process at high temperature and pressures, suffers from the reliance on fossil fuels and high CO$_2$ emissions.[2,3] Today, ammonia production via electrochemical nitrogen reduction reaction (eNRR) at ambient conditions has spurred a growing interest, because this method is environmentally friendly and flexible.[2−7] To date, most of the reported catalysts for eNRR are transition metal (TM)-based; however, they show poor activity with low Faradaic efficiency and high overpotential.[8−12] Improvement of the performance of eNRR catalysts remains one of the greatest challenges in this area.[13]

Ever since the first report of a single Mo-based molecular catalyst coordinated by trisamidoamine ligands to reduce dinitrogen at ambient conditions via a distal pathway, many metal centers (Fe, Co, Ru, Os, Rh, etc.) coordinated by a variety of ligands (PNP-, PCP-, and NNN-type, etc.) proved to be active to reduce dinitrogen.[6,14,15] These results provide guidelines for electrocatalyst design and indicate that a suitable match of ligands and metal center can facilitate catalytic nitrogen reduction. Recently, as an emerging area of heterogeneous catalysis, single-atom catalysts (SACs) provide a platform for exploring new eNRR electrocatalysts as well as

revealing the fundamental mechanisms.[7,16] There are two reasons: first, SACs share structural similarity with molecular catalysts (metal centers coordinated by ligands), which proves to be effective for dinitrogen reduction; second, by coupling different metals centers with a variety of supports, SACs could contribute to a large pool for the search of electrocatalyst candidates and hence provide enough samples to reveal the mechanisms as well as the roles of metal centers and supports.[17−23] These inspired us to check if the "ligand−metal" concept from homogeneous molecular catalysis could be used to guide the design of SACs for eNRR in heterogeneous electrocatalysis.[7]

Although major efforts have been undertaken toward the evaluation of different materials, including metal alloys,[24] carbides,[25,26] nitrides,[3] oxides,[27] and also single-atom catalysts (SACs),[19,21−23] the rational design of active, durable, and efficient electrocatalysts for eNRR is still far from satisfactory. Therefore, revealing the mechanistic aspects of eNRR with the help of the density functional theory (DFT) calculations is vital for the rational design of high-performance eNRR electrocatalysts.[3,9,11,12] As predicted by previous DFT studies, the poor activity in terms of high eNRR overpotentials

originates from the scaling relations between adsorption energies of nitrogen-containing intermediates (NH_x and N_2H_x) on the surface of pure transition metal (TM)-based catalysts and prevents TM-based electrocatalysts to approach the region of optimal eNRR activity.[11,12,28] In addition, for bulk TM surfaces, the Faradaic efficiency is relatively low because of the competing hydrogen evolution reaction (HER) as indicated by both theoretical predictions and experimental examinations.[8,11] Another critical issue for nitrogen-containing materials, which needs urgent attention, is the possible decomposition of catalysts that could affect the evaluation of the catalytic performance.[29,30] All these concerns need to be taken into account when designing SACs as eNRR electrocatalysts.

Particularly for SACs, the available reports often represent the case studies, such as experimental evaluation or theoretical prediction of one particular SAC, like Ru[19,23] or Fe centers on nitrogen-doped carbons[17] or single boron atoms incorporated into g-C_3N_4.[31] Other computational works focus on the computational screening of eNRR electrocatalysts with the lowest overpotentials, normally done by exploring different metal centers on one specific support, for example, single Mo atoms embedded in defective boron nitride.[18,32] However, a full picture of the potential of TM-SACs as eNRR electrocatalysts has not been presented yet, which can only be constructed on in-depth study of the mechanism and has a great potential for the development of general design strategies. In such a full picture, the following questions need to be answered: (1) Is it possible to find the intrinsic activity trends for SACs in terms of some descriptor(s)? (2) What is the effect of electronic structure of SACs on the activity trends? (3) How can one utilize the knowledge of the reaction mechanisms for the rational design of active, stable, and efficient eNRR catalysts?

In this work, we employed DFT calculations to build up a full picture of the potential of TM-SACs as eNRR electrocatalysts by considering three key aspects: activity trends, electronic origins, and design strategies. Because ligands in molecular NRR catalysts are usually electron-rich P- or N-based, we selected three types of nitrogen-doped carbon (NC) materials (g-C_3N_4 and nitrogen-doped carbons with three or four coordinating nitrogen atoms) as the SACs supports to provide different coordination environments for 20 metal centers.[6,15,33] Hence, the roles of metal centers and supports (ligands) could be revealed. We first investigated the reaction pathway on the g-C_3N_4 supported TM-SACs followed by identifying the potential determining step (PDS) and evaluating the limiting potentials. With the help of the established scaling relations for adsorption energies of intermediates, the intrinsic activity trends in terms of the limiting potential proved to be related to the nitrogen adatom adsorption strength (ΔE_{N*}). Furthermore, our work demonstrates that the variation of ΔE_{N*} on different metal centers originates from the bonding/antibonding orbital population. The coordination environments provided by different NC supports regulate the linear scaling relations and thus indirectly affect the activity. On the basis of these findings, we propose a promising strategy for the rational design of eNRR electrocatalysts by suitable matching of the support and metal center followed by regulating the adsorption strength of the key intermediates to reduce the limiting potential. In addition, the stability and selectivity of the selected electrocatalysts are verified in comparison to HER, which is a competing reaction to eNRR.

■ COMPUTATIONAL DETAILS

Spin-polarized density functional theory (DFT) method was employed for all calculations using the Vienna ab initio Simulation Package (VASP). The projector-augmented-wave pseudopotential was utilized to treat the core electrons, while the Perdew−Burke−Ernzerhof (PBE) exchange-correlation functional of the generalized gradient approximation (GGA) was used for describing the electron interactions.[34−37] A plane-wave cutoff energy was set to 400 eV for all calculations. The vacuum space in the z-direction was set as 20 Å to prevent the interaction between periodic images. The van der Waals interactions were described using the empirical correction in Grimme's scheme.[38] The reciprocal space was sampled using $5 \times 5 \times 1$ k-points for fully relaxed geometry optimization until the maximal residual force was <0.02 eV/Å. For electronic structure calculations, an $11 \times 11 \times 1$ k-points grid was used. The projected crystal orbital Hamilton population (pCOHP) was employed to reveal the nature of bonding between SACs and intermediates.[39−42]

The calculation of the free energy diagrams was performed by using the concept of computational hydrogen electrode (CHE).[43] In this framework, the free energy of the electron−proton pair ($H^+ + e^-$) can be referenced to the chemical potential of gaseous H_2 at equilibrium (0 V vs standard hydrogen electrode). The change of free energy can be calculated as follows,

$$\Delta G = \Delta E + \Delta E_{ZPE} - T\Delta S$$

where ΔE is the electronic energy difference directly obtained by DFT calculations. ΔE_{ZPE} is the change in the zero-point energy (ZPE), T is the room temperature ($T = 298.15$ K), and ΔS is the entropy change. ZPE and vibrational entropy of adsorbed species were obtained after frequency calculations (Table S1), and entropies of gas molecules (H_2, N_2, and NH_3) were taken from standard values.[44]

First, we focus on TM-SACs supported on g-C_3N_4 (TM@g-C_3N_4, Figure 1a), which proves to be a suitable molecular scaffold to
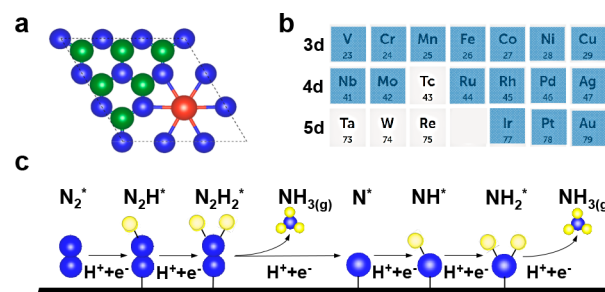
Figure 1. Atomic models and the distal reaction pathway of nitrogen reduction. (a) Single transition metal atom catalyst anchored to g-C_3N_4 matrix. (b) Metals considered for screening. Blue shades indicate the corresponding elements for which the eNRR activities were obtained experimentally. (c) Scheme of proton-coupled electron transfer for nitrogen reduction via a distal pathway. Color code: metal in red, carbon in green, nitrogen in blue, and hydrogen in yellow.

stabilize single metal atoms under electrochemical conditions.[33,45] Figure 1b shows all the metal elements included in this work, whereas blue-colored transition metals exhibit the eNRR activity experimentally studied so far, in the form of either oxides, nitrides, or pure metal nanoparticles. We screened 20 metal centers including all metals in 3d, 4d, and 5d blocks to comprehensively explore the effect of metal centers on the eNRR intrinsic activity (as shown in Figure 1b). Thereafter, we extended our study to other nitrogen-doped carbons with three (TM@N_3) or four pyridinic nitrogen atoms (TM@N_4) as coordinating sites for metals (Figure S1). This is designed for revealing the effect of supports through the ligand effect on the eNRR performance, which is less investigated as compared to the studies of

85
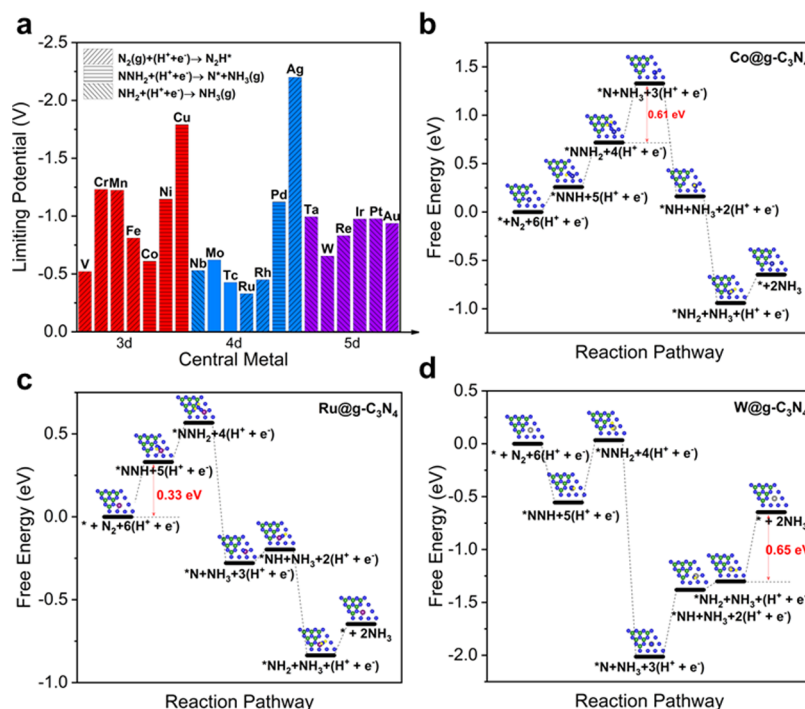
Figure 2. (a) Summary of limiting potentials for eNRR via a distal pathway for transition metal single-atom catalysts on g-C_3N_4. Free energy diagrams of (b) Co@g-C_3N_4, (c) Ru@g-C_3N_4, and (d) W@g-C_3N_4, respectively. The reference potential is set to 0 V vs SHE.

different metals but probably plays a significant role in controlling the activity as it is observed in the case of molecular catalysts.[6,45,46] Due to the high kinetic barrier for N_2 dissociation, especially under ambient environment, the distal pathway is the preferred mechanism; therefore, we exclude the dissociative pathway and focus on the distal route.[47,48] All intermediates are listed in Tables S2–S7. The computational details for NC stability and Faradaic efficiency are given in the Supporting Information, Supplementary Notes 1 and 2.

■ RESULTS AND DISCUSSION

Evaluation of Limiting Potential. The limiting potential, defined as the lowest negative potential at which the pathway becomes exergonic, was used to evaluate the intrinsic activity of electrocatalysts.[33] In this work, the evaluation of the potential performance is the foundation for obtaining a full picture of the eNRR activity for SACs. Figure 2a summarizes the limiting potential for all SACs supported on g-C_3N_4. According to this figure, there is a repeated trend of the limiting potentials for the elements in the same row of periodic table: the lowest values are located in the middle of a group of metals; i.e., Co for 3d metal (−0.61 V), Ru for 4d metal (−0.33 V), and W for 5d metal (−0.65 V). For the elements at both ends of a given row, the limiting potential is generally higher, such as in the case of Cu, Ag, and Au; the poor activity was reported for Au SAC.[21] In addition, as compared to Ru (0001) with a limiting potential of −1.05 V, these three candidates (Co@g-C_3N_4, Ru@g-C_3N_4, and W@g-C_3N_4) show significantly lower limiting potential, require less applied potential to drive the reaction toward forming ammonia at an appropriate rate, and therefore have better intrinsic activity.

To further reveal the reaction mechanism, we plotted the free energy diagrams for eNRR on Co@g-C_3N_4, Ru@g-C_3N_4, and W@g-C_3N_4 and benchmarked them to the well-investigated Ru (0001) surface. Inparts b−d of Figure 2, the proton/electron pairs transferred to the electrode surface led to the consecutive protonation of nitrogen species (with resulting

reaction intermediates *NNH, *NNH$_2$, *N, *NH, and *NH$_2$) and release of ammonia at the third and last step. It is worth noting that, for previously studied late transition metal electrocatalysts (both flat and step surface), the first protonation step is normally the most thermodynamically uphill step.[11] For example, for the Ru (0001) flat surface, the limiting potential could be attributed to N_2 + $(H^+ + e^-)$ → *NNH step with a positive free energy change of ~1 eV.[11] In our case, although the first protonation step is still endergonic (as shown in Figure 2b and c), the free energy change is significantly reduced due to the stabilization of NNH* by Ru@g-C_3N_4, Co@g-C_3N_4, and W@g-C_3N_4. Take Ru@g-C_3N_4 as an example: all free energy changes after the first step are lower than that for the first proton-coupled electron transfer (PCET); therefore, PDS reflects the protonation of N_2 to *NNH. The same PDS is observed for other previously reported SACs, e.g., FeN$_3$-embedded graphene and single Mo supported on defective boron nitride (BN).[18,49] However, the limiting potentials for these previously reported SACs are much more negative (e.g., Mo@BN shows a limiting potential of −0.75 V); in comparison, Ru@g-C_3N_4 shows more positive limiting potential of −0.33 V, demonstrating its outstanding eNRR activity.[18] This observation also agrees with previous reports of Ru single-atom catalysts with ultralow limiting potentials.[19,23]

As for Co@g-C_3N_4 (Figure 2b) and W@ g-C_3N_4 (Figure 2d), due to the lower free energy level of *NNH, the first protonation step is not the potential-determining step (PDS). Instead, the third protonation step with the release of the first ammonia molecule (*NNH$_2$ + H^+ + e^- → NH$_{3(g)}$ + *N) and the sixth protonation step with the release of the second ammonia molecule (*NH$_2$ + H^+ + e^- → NH$_{3(g)}$) become PDS for Co@g-C_3N_4 and W@g-C_3N_4, correspondingly. As shown in Figure 2a, along with the change of the limiting potential for different elements, the PDS also varies. For similar electro-
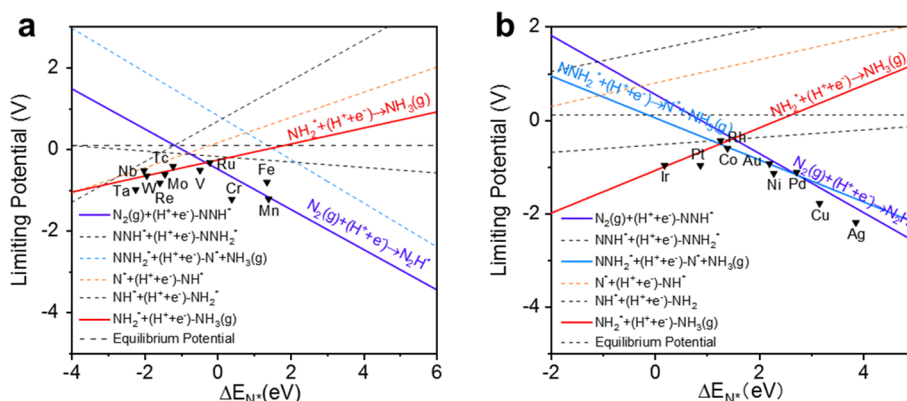
Figure 3. Limiting potential defined as the negative of the free energy change of each proton-coupled electron transfer (PCET) step, which behaves as a function of the adsorption energy of *N (ΔE_{N*}) at 0 V vs SHE. Each colored line represents one PCET step derived from the scaling relations established in the previous section. The gray dashed line indicates theoretical equilibrium potential. The lowest line dictates the potential-determining step as well as the limiting potential. The scatters are directly calculated from the results of the free energy diagrams as validations. (a) For the early transition metal and (b) for late transition metal.

catalytic reduction reactions, there have been considerations that, if PDS does not vary for a group of materials, the performance of an electrocatalyst can be optimized by (de)stabilizing one specific intermediate.[50] This is, however, not the case for g-C$_3$N$_4$ supported SACs for eNRR due to the existence of multiple PDSs, which bring more complexity for the rational design of eNRR electrocatalysts. This discussion also indicates that the evaluation of the limiting potentials alone is not enough for the rational design of catalysts, and the underlying reasons for multiple PDSs are yet to be uncovered. Therefore, it is highly desirable to build up a full picture, in which both the interpretation (to reveal the origins of multiple PDSs) and applications (to direct the design of electrocatalysts) of the results are needed.

Establishment of the Activity Trends. The first step to build up a full picture of the SAC activity for eNRR is to sort the predicted performances of various SACs into meaningful trends as a function of some parameter(s). As mentioned in Computational Details, to evaluate the limiting potential, the free energy diagrams were constructed based on the energetics of all reaction intermediates. In this scenario where multiple reaction intermediates exist, the determination of the limiting potential requires the consideration of each reaction step—a multiple-parameter problem. Reducing the number of parameters from multiple parameters to only one (or two) parameter(s) could simplify the problem and facilitate the rational design of catalysts. Therefore, it is worth investigating if the adsorption strengths of reaction intermediates are correlated or not. We noticed that, for pure transition metal flat surface, the energies of various intermediates (NH$_x$ and N$_2$H$_x$ admolecules) exhibit a scaling relation.[51] This provides an opportunity for identifying PDS and estimating the limiting potential for SACs if similar relations could be established for them. To establish the scaling relations, the calculations of the adsorption energies were carried out for *NNH, *NNH$_2$, *N, *NH, and *NH$_2$ on all single-atom catalysts studied. As seen in Figure S2, the adsorption energies of *NNH, *NNH$_2$, *NH, and *NH$_2$ scale linearly with the adsorption energy of *N (ΔE_{N*}) on a wide range (from ~−2 to ~4 eV), which is analogous to what has been found for pure transition metal flat and step surfaces.[11] In addition, this scaling relation can be divided into two groups: early (marked in blue) and late (marked in red) transition metal SACs. On the basis of these

scaling relations, we can now establish the relationship between the limiting potential with that of ΔE_{N*} by plotting the free energy change of each reaction step.

Estimation of the free energy change for each elementary step is displayed by six colored solid lines in Figure 3: (a) for early transition metals and (b) for late transition metals based on the observation of different linear relationships for these two groups of metals. The interpretation of these lines is that, at a given value of ΔE_{N*}, the lowest line dictates the limiting potential and the elementary step represented by this line is the potential-determining step. To validate this method for predicting the limiting potential, we presented the scatter plots of the limiting potential values for each SAC calculated directly from the free energy diagram. As can be seen in Figure 3, the scatter plots agree well with the estimation indicated by the lines, and this validates the PDS prediction ability based on the scaling relations. Our analysis shows that the method involving reduction of the number of parameters (i.e., adsorption energies in this case) is applicable for TM@g-C$_3$N$_4$ materials, and the determination of the inherent eNRR activity based on ΔE_{N*} represents a facile way for estimating the limiting potential.

Figure 3 also explains the impact of different metal centers on the limiting potential. As the metal changes, ΔE_{N*} varies and the adsorption strength of all intermediates (because of the scaling relations) changes too. For example, in Figure 3, at relatively negative range of ΔE_{N*}, the red line (corresponding to the last reaction step *NH$_2$ + H$^+$ + e$^-$ → NH$_{3(g)}$) is the lowest one, which indicates that the last step is PDS. In this range, SACs bind the intermediates so strongly that desorption of *NH$_2$ to form ammonia is difficult to achieve. Meanwhile, for the right branch in Figure 3a and b, adsorption of reaction intermediates is weak; therefore, the N$_{2(g)}$ + (H$^+$ + e$^-$) → *NNH step is difficult to proceed due to the weak adsorption in this ΔE_{N*} range (represented by the blue line in Figure 3). Meanwhile, for some SACs such as Co@ g-C$_3$N$_4$, the third step to release the first ammonia (*NNH$_2$ + H$^+$ + e$^-$ → NH$_{3(g)}$ + *N) is PDS, as indicated by the light blue line in Figure 3b. In this case, ΔE_{N*} is positive but with a small value, and the limiting potential of this step is more negative than that of the first protonation step. The above analysis of the activity trends sheds light on the role of different metal centers in determining

87
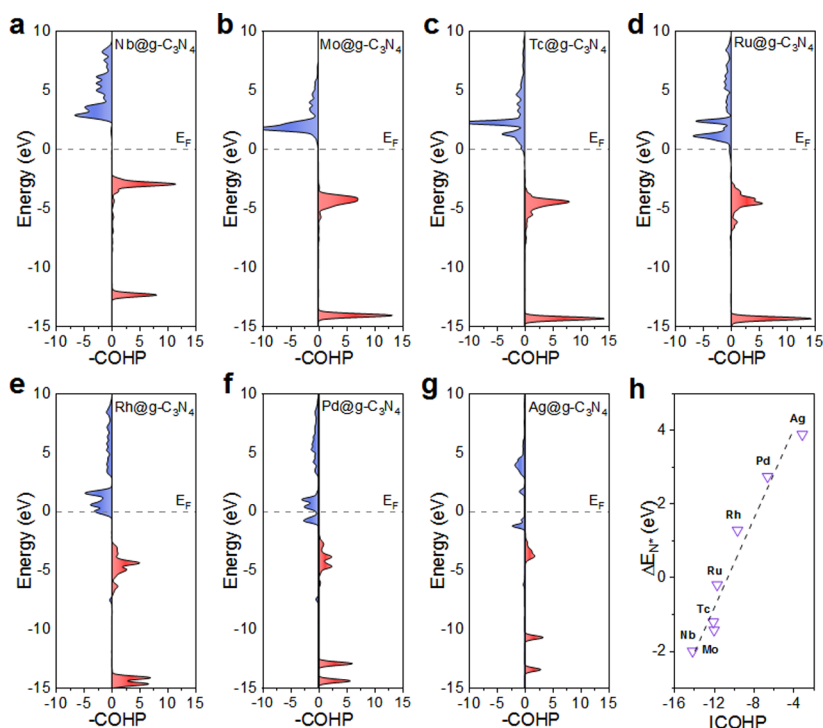
Figure 4. From (a) to (g): projected crystal orbital Hamilton population (pCOHP) between the metal center from Nb to Ag and the nitrogen adatom. (h) Illustration of the correlation between integrated COHP (ICOHP) and the adsorption energy of nitrogen adatom (ΔE_{N*}). Red stands for bonding contributions, while blue stands for antibonding contributions.
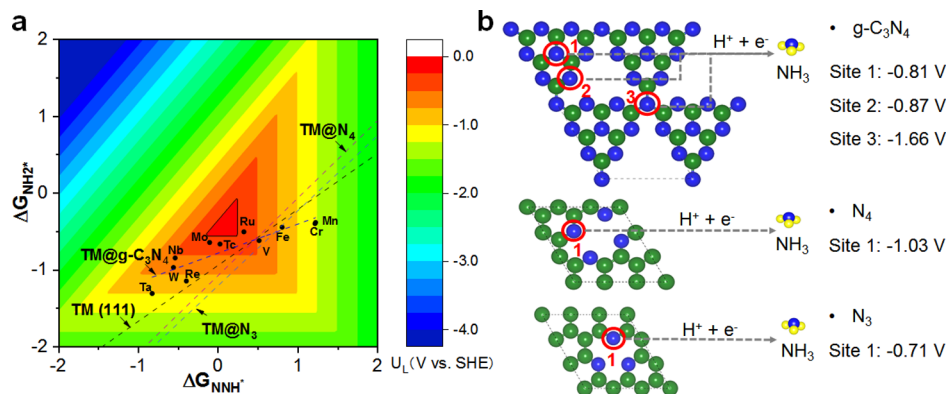
Figure 5. Color-filled contour plots of the limiting potential as a function of the Gibbs free energy of *NNH (ΔG_{NNH*}) and *NH$_2$ (ΔG_{NH2*}). (a) Comprehensive comparisons of the limiting potential of SACs consisting of different metal centers and supports, and the pure metal (111) surface is included as a reference. (b) Decomposition energies of N-doped substrate (g-C$_3$N$_4$ and nitrogen-doped carbon with four or three nitrogen atoms as the coordinating sites). Data for transition metal (111) surface in (a) are reproduced from ref 11. All potential values in (b) are referenced to the standard hydrogen electrode (SHE).

ΔE_{N*}, which has not been explored yet, although the screening of SACs with low limiting potentials has been done.[18,32]

Origins of the ΔE_{N*} Variation. Previous sections demonstrate that ΔE_{N*} determines the limiting potential and the role of metal centers. However, the underlying origin and ΔE_{N*} trends on SACs with different metal centers remain to be explained. To reveal the underlying mechanism and further reveal the role of different metal centers, we conducted analysis of various electronic structures of these SACs. As shown in Figure S3, the d-band center and the highest peak of the projected density of states (PDOS) below the Fermi level of the metal center show poor linear correlation with ΔE_{N*}.[52,53] The PDOS values of *N configurations of the fourth period SACs in Figure S4 show that there are discrete states for metal

both d and sp bands, which are different from the continuous form of those for pure metals.[54] Therefore, the filling of sp states is not a constant number when the metal center varies, and that is why indexes based on the d-band theory could not reproduce the adsorption energy trend.[51,54]

To explain this trend, we introduced projected crystal orbital Hamilton population (pCOHP) to analyze the interaction between the metal center and the nitrogen adatom. We follow the usual way of displaying COHPs, namely, drawing negative (i.e., bonding) contributions to the right and positive (i.e., antibonding) contributions to the left. It is clear that, for Nb and Mo (Figure 4a and b), all valence states (below the Fermi level, E_F) appear as bonding, while antibonding orbital populations are detected only in the conduction bands

88

Table 1. Calculated HER Limiting Potentials for TM@g-C$_3$N$_4$ and g-C$_3$N$_4$ Substrates (V vs SHE) and Faradaic Efficiency (FE) Values for eNRR in Comparison to HER^a

	g-C$_3$N$_4$	V	Cr	Mn	Fe	Co	Ni	Cu	Nb	Mo	Tc
HER	−0.54[57]	−0.19	−0.55	−0.29	−0.33	−0.22	−0.47	−0.29	−0.27	−0.35	−0.31
FE		0	0	0	0	0	0	0	0	0	1%

	Ru	Rh	Pd	Ag	Ta	W	Re	Ir	Pt	Au
HER	−0.42	−0.47	−0.37	−0.78	−0.54	−0.69	−0.76	−0.20	−0.64	−1.06
FE	97%	73%	0	0	1%	0	0	0	0	0

^{a}HER limiting potential for g-C$_3$N$_4$ is taken from ref 57. For Cr, Ag, W, Re, Pt, and Au, the substrate g-C$_3$N$_4$ is more active than the metal center so, in these cases the HER limiting potential of g-C$_3$N$_4$ was used for calculating FE values.

(above E_F). This explains the strong adsorption of *N on Nb@g-C$_3$N$_4$ and Mo@g-C$_3$N$_4$. Meanwhile, for elements from Tc to Ag, as shown in Figure 4c−g, the filling of antibonding orbital population increases, which is in accordance with the decrease of binding strength as indicated by more positive ΔE_{N*}. In addition, we calculated the integrated COHP (ICOHP) by calculating the energy integral up to the highest occupied bands (below E_F), which directly gives more quantitative information. As shown in Figure 4h, there is a linear correlation between ICOHP and ΔE_{N*}. This linear correlation gives a quantitative explanation for the role of different metal centers in determining the bonding/antibonding orbital populations, which is the origin of the observed trends for the adsorption energies of intermediates.

Guidelines for the Design of SACs as eNRR Electrocatalysts. Before presenting the guidelines for the design of SACs for eNRR, we need to discuss the effect of the different supports through the ligand effect, which is the other aspect that probably impacts the catalyst activity. Therefore, we extend our previous discoveries for TM@g-C$_3$N$_4$ to the SACs supported on NC (TM@N$_4$ and TM@N$_3$, as shown in Figure S1), which are widely used for the synthesis of SACs but provide different coordination environments for metal centers. As identified in previous sections, the PDS values are related to at least two key intermediates (*NNH and *NH$_2$), which have a crucial effect on the eNRR activity. In the cases of TM@N$_4$ and TM@N$_3$, as shown in Figure S5, ΔE_{N*} also scales linearly with ΔE_{NNH*} and ΔE_{NH2*}, which indicates similar situations for binding intermediates on TM@g-C$_3$N$_4$, TM@N$_4$, and TM@N$_3$. On the basis of these results, to give a comprehensive understanding of the effects of both metal centers and supports (ligands) on the eNRR activity, we then constructed the color contour plots of the limiting potential as a function of the Gibbs free energy for *NNH (ΔG_{NNH*}) and *NH$_2$ (ΔG_{NH2*}) in Figure 5a. As shown in Figure 5a, there is an activity maximum marked by the red region surrounded by black lines, which could be achieved if one can independently tune ΔG_{NNH*} and ΔG_{NH2*}. Although no SAC candidate is located in this ideal region, it gives some guidelines for improving the activity.

Interpretation of Figure 5a leads to the following three observations. First, the inherent limitation for each family of SACs is demonstrated by the straight line, which is the linear scaling relations between ΔG_{NNH*} and ΔG_{NH2*} for all TM-SACs. This is reasonable because both ΔE_{NNH*} and ΔE_{NH2*} scale linearly with ΔE_{N*} and all other parameters to calculate the free energy are constant. More importantly, it also suggests that the supports (ligands) regulate the scaling relations for adsorption of intermediates and thus indirectly determine the eNRR activity. Hence, we proved that for SACs the coordination environment, as in the case of molecular catalysts,

is vital for the activity. Second, the results shown in Figure 5a also give a direct comparison of different families of SACs and pure metal (111) surface (as a reference). Clearly, not all SACs show better activity than the bulk metal surface (111) because the lines representing the estimated limiting potential in Figure 5a intersect.[11] In the activity peak region (red and orange), g-C$_3$N$_4$ supported SACs are better than those on other NC supports and pure metals because they approach closer to the optimal region. This could also be regarded as deviation from the nonideal scaling relations of pure transition metals and thus provide new opportunities for searching eNRR electrocatalysts. Third, this plot also clearly shows and compares the limiting potentials for all studied SACs. Ru@g-C$_3$N$_4$ is predicted to be the most promising candidate, which is closest to the ideal region. Moreover, this plot also gives some suggestions for a two-step design strategy. The first step, as indicated above, is to find the most promising family of TM-SACs, and the second step is to further improve the activity of the best candidate in this family. For example, we would suggest the TM@g-C$_3$N$_4$ family here, and Ru@g-C$_3$N$_4$ (−0.33 V) is the best in this family. However there is still some room for improvement of the limiting potential. To "move in" the optimal activity region, *NNH could potentially be stabilized with a reduced ΔG_{NNH*} while keeping ΔG_{NH2*} unchanged. By combining these two steps, this work sheds light on the routines for improving the activity of SACs supported on NC based on the in-depth mechanisms of eNRR on these catalysts.

Furthermore, besides the activity (limiting potential) considerations, for the practical implementations of SACs supported on NC as eNRR electrocatalysts, the stability of nitrogen-doped substrates and their selectivity in comparison to HER need to be investigated to reflect the real catalytic performance.[3,6,29,55,56] Thus, we conducted some calculations based on thermodynamics to address these two issues. The data showing the stability of the N-doped substrates studied are presented in Figure 5b (detailed computational methods are given in Supporting Information, Supplementary Note 1). N-doped carbon with four coordinating nitrogen atoms (N$_4$) is the most stable with a decomposition potential of −1.03 V vs SHE, while the decomposition potential for g-C$_3$N$_4$ is −0.81 V vs SHE, and that for N$_3$ is −0.71 V vs SHE. These results are in accordance with previous studies devoted to HER on the SACs supported on the NC substrate that under moderate reduction potential (∼−0.3 V vs RHE) it is stable.[58−60] Accordingly, to ensure the durability of the support and avoid risks of contamination due to the decomposition of N-doped substrate, the desired eNRR electrocatalysts should have more positive eNRR limiting potential than that for the substrate decomposition. For TM@g-C$_3$N$_4$, if the substrate stability is taken into consideration, only eight (V, Co, Nb, Mo, Tc, Ru, Rh, and W) of 20 can be considered as stable because they

89

have less negative eNRR limiting potentials than that for the substrate decomposition.

The eNRR selectivity in comparison to that of for HER (as possible competing reaction) was also calculated for TM@g-C$_3$N$_4$(shown in Table 1). The computational details are given in Supporting Information, Supplementary Note 2. The results indicate that only Ru@g-C$_3$N$_4$ and Rh@g-C$_3$N$_4$ could be efficient eNRR electrocatalysts with acceptable Faradaic efficiencies, which is much better than those for pure transition metal surfaces.[11] Although Co@g-C$_3$N$_4$ and W@g-C$_3$N$_4$ show promising activity for eNRR, the more facile HER surpasses eNRR, and thus, the selectivity of eNRR is expected to be very low. Therefore, by combining the stability and selectivity analysis, it is seen that only Ru@g-C$_3$N$_4$ and Rh@g-C$_3$N$_4$ have the potential for eNRR and could be further examined experimentally. At this point, the theoretical evaluations of the activity, stability, and selectivity of SACs supported on NC provide a reasonable procedure for the design of active and efficient eNRR electrocatalysts for experimental examinations.

CONCLUSIONS

In summary, taking TM-SACs supported on nitrogen-doped carbon materials as model systems, we revealed the mechanistic aspects of chemistry in the eNRR process and obtained a full picture (activity trends, electronic origins, and design strategies) of the potential of TM-SACs as eNRR electrocatalysts. We conducted extensive DFT computations to evaluate the limiting potentials of these TM-SACs and revealed the reaction mechanisms by electronic structure analysis. Our study concludes that the intrinsic activity of these TM-SACs is a function of the nitrogen adatom adsorption energy (ΔE_{N*}). Furthermore, the variation of ΔE_{N*} is attributed to the influence of metal centers on the bonding/antibonding orbital populations. Similarly to the case of molecular catalysts, the supports could also affect the eNRR performance by introducing different ligand effects. These findings led to a two-step strategy for the design of eNRR catalysts by selecting the most promising family of TM-SACs (e.g., TM@g-C$_3$N$_4$ in this work) and further improvement of the best candidate in this family by selective tuning of adsorption energies of the key intermediates. Comparison of the stability of NC support with the eNRR limiting potential and examination of the selectivity need to be adopted to further screen the candidates for eNRR. Our work establishes a bridge from the origins of electronic structures and activity trends to the rational design of active and efficient TM-SACs for eNRR. These three aspects form a full picture of the potential of TM-SACs as eNRR electrocatalysts. This systematic work could aid the discovery of more efficient and effective TM-SACs for eNRR and could also be extended to other multielectron electrocatalytic reactions.

ASSOCIATED CONTENT

Ⓢ Supporting Information

The Supporting Information is available free of charge on the ACS Publications website at DOI: 10.1021/jacs.9b03811.

> Details on the calculations of the free energy diagrams; calculated zero point energies, entropy, and structures of different reaction intermediates; scaling relations for different SACs; projected density of states; correlation of d-band center and adsorption energies; computational details for calculating energies of substrate decomposition and selectivity with HER. (PDF)

AUTHOR INFORMATION

Corresponding Authors
*yan.jiao@adelaide.edu.au
*s.qiao@adelaide.edu.au

ORCID Ⓞ
Yan Jiao: 0000-0003-1329-4290
Yao Zheng: 0000-0002-2411-8041
Mietek Jaroniec: 0000-0002-1178-5611
Shi-Zhang Qiao: 0000-0002-4568-8422

Notes
The authors declare no competing financial interest.

REFERENCES

(1) Erisman, J. W.; Sutton, M. A.; Galloway, J.; Klimont, Z.; Winiwarter, W. How a century of ammonia synthesis changed the world. *Nat. Geosci.* **2008**, *1* (10), 636−639.

(2) Chen, J. G.; Crooks, R. M.; Seefeldt, L. C.; Bren, K. L.; Bullock, R. M.; Darensbourg, M. Y.; Holland, P. L.; Hoffman, B.; Janik, M. J.; Jones, A. K.; Kanatzidis, M. G.; King, P.; Lancaster, K. M.; Lymar, S. V.; Pfromm, P.; Schneider, W. F.; Schrock, R. R. Beyond fossil fuel-driven nitrogen transformations. *Science* **2018**, *360* (6391), eaar6611.

(3) Yang, X.; Nash, J.; Anibal, J.; Dunwell, M.; Kattel, S.; Stavitski, E.; Attenkofer, K.; Chen, J. G.; Yan, Y.; Xu, B. Mechanistic Insights into Electrochemical Nitrogen Reduction Reaction on Vanadium Nitride Nanoparticles. *J. Am. Chem. Soc.* **2018**, *140* (41), 13387−13391.

(4) Hoffman, B. M.; Lukoyanov, D.; Yang, Z. Y.; Dean, D. R.; Seefeldt, L. C. Mechanism of nitrogen fixation by nitrogenase: the next stage. *Chem. Rev.* **2014**, *114* (8), 4041−4062.

(5) Guo, C. X.; Ran, J. R.; Vasileff, A.; Qiao, S. Z. Rational design of electrocatalysts and photo(electro) catalysts for nitrogen reduction to ammonia (NH$_3$) under ambient conditions. *Energy Environ. Sci.* **2018**, *11* (1), 45−56.

(6) Foster, S. L.; Bakovic, S. I. P.; Duda, R. D.; Maheshwari, S.; Milton, R. D.; Minteer, S. D.; Janik, M. J.; Renner, J. N.; Greenlee, L. F. Catalysts for nitrogen reduction to ammonia. *Nat. Catal.* **2018**, *1* (7), 490−500.

(7) Minteer, S. D.; Christopher, P.; Linic, S. Recent Developments in Nitrogen Reduction Catalysts: A Virtual Issue. *ACS Energy Lett.* **2019**, *4* (1), 163−166.

(8) Nash, J.; Yang, X.; Anibal, J.; Wang, J. H.; Yan, Y. S.; Xu, B. J. Electrochemical Nitrogen Reduction Reaction on Noble Metal Catalysts in Proton and Hydroxide Exchange Membrane Electrolyzers. *J. Electrochem. Soc.* **2017**, *164* (14), F1712−F1716.

(9) Yao, Y.; Zhu, S.; Wang, H.; Li, H.; Shao, M. A Spectroscopic Study on the Nitrogen Electrochemical Reduction Reaction on Gold and Platinum Surfaces. *J. Am. Chem. Soc.* **2018**, *140* (4), 1496−1501.

(10) Wang, D.; Azofra, L. M.; Harb, M.; Cavallo, L.; Zhang, X.; Suryanto, B. H. R.; MacFarlane, D. R. Energy-Efficient Nitrogen Reduction to Ammonia at Low Overpotential in Aqueous Electrolyte under Ambient Conditions. *ChemSusChem* **2018**, *11* (19), 3416−3422.

(11) Skulason, E.; Bligaard, T.; Gudmundsdottir, S.; Studt, F.; Rossmeisl, J.; Abild-Pedersen, F.; Vegge, T.; Jonsson, H.; Norskov, J. K. A theoretical evaluation of possible transition metal electro-

catalysts for N_2 reduction. *Phys. Chem. Chem. Phys.* **2012**, *14* (3), 1235−1245.

(12) Montoya, J. H.; Tsai, C.; Vojvodic, A.; Norskov, J. K. The Challenge of Electrochemical Ammonia Synthesis: A New Perspective on the Role of Nitrogen Scaling Relations. *ChemSusChem* **2015**, *8* (13), 2180−2186.

(13) Seh, Z. W.; Kibsgaard, J.; Dickens, C. F.; Chorkendorff, I. B.; Norskov, J. K.; Jaramillo, T. F. Combining theory and experiment in electrocatalysis: Insights into materials design. *Science* **2017**, *355* (6321), 146−153.

(14) Yandulov, D. V.; Schrock, R. R. Catalytic reduction of dinitrogen to ammonia at a single molybdenum center. *Science* **2003**, *301* (5629), 76−78.

(15) Macleod, K. C.; Holland, P. L. Recent developments in the homogeneous reduction of dinitrogen by molybdenum and iron. *Nat. Chem.* **2013**, *5* (7), 559−565.

(16) Wang, A. Q.; Li, J.; Zhang, T. Heterogeneous single-atom catalysis. *Nat. Rev. Chem.* **2018**, *2* (6), 65−81.

(17) Li, X. F.; Li, Q. K.; Cheng, J.; Liu, L.; Yan, Q.; Wu, Y.; Zhang, X. H.; Wang, Z. Y.; Qiu, Q.; Luo, Y. Conversion of Dinitrogen to Ammonia by FeN3-Embedded Graphene. *J. Am. Chem. Soc.* **2016**, *138* (28), 8706−8709.

(18) Zhao, J.; Chen, Z. Single Mo Atom Supported on Defective Boron Nitride Monolayer as an Efficient Electrocatalyst for Nitrogen Fixation: A Computational Study. *J. Am. Chem. Soc.* **2017**, *139* (36), 12480−12487.

(19) Geng, Z.; Liu, Y.; Kong, X.; Li, P.; Li, K.; Liu, Z.; Du, J.; Shu, M.; Si, R.; Zeng, J. Achieving a Record-High Yield Rate of 120.9 ug NH_3 $mg_{cat.-1}$ h^{-1} for N_2 Electrochemical Reduction over Ru Single-Atom Catalysts. *Adv. Mater.* **2018**, 1803498.

(20) Huang, P. C.; Liu, W.; He, Z. H.; Xiao, C.; Yao, T.; Zou, Y. M.; Wang, C. M.; Qi, Z. M.; Tong, W.; Pan, B. C.; Wei, S. Q.; Xie, Y. Single atom accelerates ammonia photosynthesis. *Sci. China: Chem.* **2018**, *61* (9), 1187−1196.

(21) Wang, X.; Wang, W.; Qiao, M.; Wu, G.; Chen, W.; Yuan, T.; Xu, Q.; Chen, M.; Zhang, Y.; Wang, X.; Wang, J.; Ge, J.; Hong, X.; Li, Y.; Wu, Y.; Li, Y. Atomically dispersed Au1 catalyst towards efficient electrochemical synthesis of ammonia. *Sci. Bull.* **2018**, *63* (19), 1246−1253.

(22) Han, L.; Liu, X.; Chen, J.; Lin, R.; Liu, H.; Lü, F.; Bak, S.; Liang, Z.; Zhao, S.; Stavitski, E.; Luo, J.; Adzic, R. R.; Xin, H. L. Atomically Dispersed Molybdenum Catalysts for Efficient Ambient Nitrogen Fixation. *Angew. Chem., Int. Ed.* **2019**, *58* (8), 2321−2325.

(23) Tao, H. C.; Choi, C.; Ding, L. X.; Jiang, Z.; Han, Z. S.; Jia, M. W.; Fan, Q.; Gao, Y. N.; Wang, H. H.; Robertson, A. W.; Hong, S.; Jung, Y. S.; Liu, S. Z.; Sun, Z. Y. Nitrogen Fixation by Ru Single-Atom Electrocatalytic Reduction. *Chem.* **2019**, *5* (1), 204−214.

(24) Wang, Z.; Li, C.; Deng, K.; Xu, Y.; Xue, H.; Li, X.; Wang, L.; Wang, H. Ambient Nitrogen Reduction to Ammonia Electrocatalyzed by Bimetallic PdRu Porous Nanostructures. *ACS Sustainable Chem. Eng.* **2019**, *7* (2), 2400−2405.

(25) Azofra, L. M.; Li, N.; MacFarlane, D. R.; Sun, C. Promising prospects for 2D d2−d4M3C2 transition metal carbides (MXenes) in N_2 capture and conversion into ammonia. *Energy Environ. Sci.* **2016**, *9* (8), 2545−2549.

(26) Cheng, H.; Ding, L. X.; Chen, G. F.; Zhang, L.; Xue, J.; Wang, H. Molybdenum Carbide Nanodots Enable Efficient Electrocatalytic Nitrogen Fixation under Ambient Conditions. *Adv. Mater.* **2018**, *30* (46), 1803694.

(27) Hu, L.; Khaniya, A.; Wang, J.; Chen, G.; Kaden, W. E.; Feng, X. F. Ambient Electrochemical Ammonia Synthesis with High Selectivity on Fe/Fe Oxide Catalyst. *ACS Catal.* **2018**, *8* (10), 9312−9319.

(28) Kulkarni, A.; Siahrostami, S.; Patel, A.; Norskov, J. K. Understanding Catalytic Activity Trends in the Oxygen Reduction Reaction. *Chem. Rev.* **2018**, *118* (5), 2302−2312.

(29) Hu, B.; Hu, M.; Seefeldt, L.; Liu, T. L. Electrochemical Dinitrogen Reduction to Ammonia by Mo2N: Catalysis or Decomposition? *ACS Energy Lett.* **2019**, *4* (5), 1053−1054.

(30) Du, H. L.; Gengenbach, T. R.; Hodgetts, R.; MacFarlane, D. R.; Simonov, A. N. Critical Assessment of the Electrocatalytic Activity of Vanadium and Niobium Nitrides toward Dinitrogen Reduction to Ammonia. *ACS Sustainable Chem. Eng.* **2019**, *7* (7), 6839−6850.

(31) Ling, C.; Niu, X.; Li, Q.; Du, A.; Wang, J. Metal-Free Single Atom Catalyst for N_2 Fixation Driven by Visible Light. *J. Am. Chem. Soc.* **2018**, *140* (43), 14161−14168.

(32) Liu, C. W.; Li, Q. Y.; Zhang, J.; Jin, Y. G.; MacFarlane, D. R.; Sun, C. H. Conversion of dinitrogen to ammonia on Ru atoms supported on boron sheets: a DFT study. *J. Mater. Chem. A* **2019**, *7* (9), 4771−4776.

(33) Zheng, Y.; Jiao, Y.; Zhu, Y.; Cai, Q.; Vasileff, A.; Li, L. H.; Han, Y.; Chen, Y.; Qiao, S. Z. Molecule-Level g-C_3N_4 Coordinated Transition Metals as a New Class of Electrocatalysts for Oxygen Electrode Reactions. *J. Am. Chem. Soc.* **2017**, *139* (9), 3336−3339.

(34) Kresse, G.; Hafner, J. Ab initio molecular-dynamics simulation of the liquid-metal−amorphous-semiconductor transition in germanium. *Phys. Rev. B: Condens. Matter Mater. Phys.* **1994**, *49* (20), 14251−14269.

(35) Kresse, G.; Hafner, J. Ab initio molecular dynamics for liquid metals. *Phys. Rev. B: Condens. Matter Mater. Phys.* **1993**, *47* (1), 558−561.

(36) Kresse, G.; Furthmuller, J. Efficient iterative schemes for ab initio total-energy calculations using a plane-wave basis set. *Phys. Rev. B: Condens. Matter Mater. Phys.* **1996**, *54* (16), 11169−11186.

(37) Kresse, G.; Furthmuller, J. Efficiency of ab-initio total energy calculations for metals and semiconductors using a plane-wave basis set. *Comput. Mater. Sci.* **1996**, *6* (1), 15−50.

(38) Grimme, S. Semiempirical GGA-type density functional constructed with a long-range dispersion correction. *J. Comput. Chem.* **2006**, *27* (15), 1787−1799.

(39) Dronskowski, R.; Blochl, P. E. Crystal Orbital Hamilton Populations (Cohp) - Energy-Resolved Visualization of Chemical Bonding in Solids Based on Density-Functional Calculations. *J. Phys. Chem.* **1993**, *97* (33), 8617−8624.

(40) Deringer, V. L.; Tchougreeff, A. L.; Dronskowski, R. Crystal Orbital Hamilton Population (COHP) Analysis As Projected from Plane-Wave Basis Sets. *J. Phys. Chem. A* **2011**, *115* (21), 5461−5466.

(41) Maintz, S.; Deringer, V. L.; Tchougreeff, A. L.; Dronskowski, R. Analytic projection from plane-wave and PAW wavefunctions and application to chemical-bonding analysis in solids. *J. Comput. Chem.* **2013**, *34* (29), 2557−2567.

(42) Maintz, S.; Deringer, V. L.; Tchougreeff, A. L.; Dronskowski, R. LOBSTER: A tool to extract chemical bonding from plane-wave based DFT. *J. Comput. Chem.* **2016**, *37* (11), 1030−1035.

(43) Norskov, J. K.; Bligaard, T.; Logadottir, A.; Kitchin, J. R.; Chen, J. G.; Pandelov, S.; Stimming, U. Trends in the exchange current for hydrogen evolution. *J. Electrochem. Soc.* **2005**, *152* (3), J23−J26.

(44) Haynes, W. M. *CRC handbook of chemistry and physics*; CRC Press: 2014.

(45) Jiao, Y.; Zheng, Y.; Chen, P.; Jaroniec, M.; Qiao, S. Z. Molecular Scaffolding Strategy with Synergistic Active Centers To Facilitate Electrocatalytic CO_2 Reduction to Hydrocarbon/Alcohol. *J. Am. Chem. Soc.* **2017**, *139* (49), 18093−18100.

(46) Mitchell, S.; Vorobyeva, E.; Perez-Ramirez, J. The Multifaceted Reactivity of Single-Atom Heterogeneous Catalysts. *Angew. Chem., Int. Ed.* **2018**, *57* (47), 15316−15329.

(47) Liu, J. C.; Ma, X. L.; Li, Y.; Wang, Y. G.; Xiao, H.; Li, J. Heterogeneous Fe3 single-cluster catalyst for ammonia synthesis via an associative mechanism. *Nat. Commun.* **2018**, *9* (1), 1610.

(48) van der Ham, C. J.; Koper, M. T.; Hetterscheid, D. G. Challenges in reduction of dinitrogen by proton and electron transfer. *Chem. Soc. Rev.* **2014**, *43* (15), 5183−5191.

(49) Hu, S. Z.; Chen, X.; Li, Q.; Zhao, Y. F.; Mao, W. Effect of sulfur vacancies on the nitrogen photofixation performance of ternary metal sulfide photocatalysts. *Catal. Sci. Technol.* **2016**, *6* (15), 5884−5890.

(50) Jiao, Y.; Zheng, Y.; Jaroniec, M.; Qiao, S. Z. Origin of the electrocatalytic oxygen reduction activity of graphene-based catalysts:

91

a roadmap to achieve the best performance. *J. Am. Chem. Soc.* **2014**, *136* (11), 4394−4403.

(51) Abild-Pedersen, F.; Greeley, J.; Studt, F.; Rossmeisl, J.; Munter, T. R.; Moses, P. G.; Skulason, E.; Bligaard, T.; Norskov, J. K. Scaling properties of adsorption energies for hydrogen-containing molecules on transition-metal surfaces. *Phys. Rev. Lett.* **2007**, *99* (1), 016105.

(52) Xin, H. L.; Vojvodic, A.; Voss, J.; Norskov, J. K.; Abild-Pedersen, F. Effects of d-band shape on the surface reactivity of transition-metal alloys. *Phys. Rev. B: Condens. Matter Mater. Phys.* **2014**, *89* (11), 115114.

(53) Jiao, Y.; Zheng, Y.; Davey, K.; Qiao, S.-Z. Activity origin and catalyst design principles for electrocatalytic hydrogen evolution on heteroatom-doped graphene. *Nat. Energy* **2016**, *1* (10), 16130.

(54) Nørskov, J. K.; Studt, F.; Abild-Pedersen, F.; Bligaard, T. *Fundamental concepts in heterogeneous catalysis*; John Wiley & Sons: 2014.

(55) Suryanto, B. H. R.; Du, H. L.; Wang, D. B.; Chen, J.; Simonov, A. N.; MacFarlane, D. R. Challenges and prospects in the catalysis of electroreduction of nitrogen to ammonia. *Nat. Catal.* **2019**, *2* (4), 290−296.

(56) Greenlee, L. F.; Renner, J. N.; Foster, S. L. The Use of Controls for Consistent and Accurate Measurements of Electrocatalytic Ammonia Synthesis from Dinitrogen. *ACS Catal.* **2018**, *8* (9), 7820−7827.

(57) Zheng, Y.; Jiao, Y.; Zhu, Y.; Li, L. H.; Han, Y.; Chen, Y.; Du, A.; Jaroniec, M.; Qiao, S. Z. Hydrogen evolution by a metal-free electrocatalyst. *Nat. Commun.* **2014**, *5*, 3783.

(58) Fei, H.; Dong, J.; Arellano-Jimenez, M. J.; Ye, G.; Dong Kim, N.; Samuel, E. L.; Peng, Z.; Zhu, Z.; Qin, F.; Bao, J.; Yacaman, M. J.; Ajayan, P. M.; Chen, D.; Tour, J. M. Atomic cobalt on nitrogen-doped graphene for hydrogen generation. *Nat. Commun.* **2015**, *6* (1), 8668.

(59) Chen, W.; Pei, J.; He, C. T.; Wan, J.; Ren, H.; Zhu, Y.; Wang, Y.; Dong, J.; Tian, S.; Cheong, W. C.; Lu, S.; Zheng, L.; Zheng, X.; Yan, W.; Zhuang, Z.; Chen, C.; Peng, Q.; Wang, D.; Li, Y. Rational Design of Single Molybdenum Atoms Anchored on N-Doped Carbon for Effective Hydrogen Evolution Reaction. *Angew. Chem., Int. Ed.* **2017**, *56* (50), 16086−16090.

(60) Chen, W.; Pei, J.; He, C. T.; Wan, J.; Ren, H.; Wang, Y.; Dong, J.; Wu, K.; Cheong, W. C.; Mao, J.; Zheng, X.; Yan, W.; Zhuang, Z.; Chen, C.; Peng, Q.; Wang, D.; Li, Y. Single Tungsten Atoms Supported on MOF-Derived N-Doped Carbon for Robust Electrochemical Hydrogen Evolution. *Adv. Mater.* **2018**, *30* (30), 1800396.

92

Supporting Information

Building up a Picture of the Electrocatalytic Nitrogen Reduction Activity of Transition Metal Single Atom Catalysts

Xin Liu,[†] Yan Jiao,[*,†] Yao Zheng,[†] Mietek Jaroniec,[‡] Shi-Zhang Qiao[*, †]

†School of Chemical Engineering, The University of Adelaide, Adelaide, SA 5005, Australia.

‡Department of Chemistry and Biochemistry, Kent State University, Kent, Ohio 44242, United States

E-mail: * s.qiao@adelaide.edu.au; * yan.jiao@adelaide.edu.au

Supplemental Note 1

Based on DFT calculations, we evaluated the possibility of substrate decomposition. The decomposition of N-doped substrate to release NH_3 can be expressed as:

$$C_xN_y + 3(H^+ + e^-) \rightarrow C_xN_{y-1} + NH_{3(g)}$$
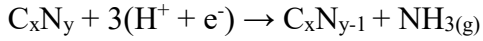
where C_xN_y stands for N-doped substrate (g-C_3N_4, N_3 and N_4), and C_xN_{y-1} stands for the corresponding remaining structure after losing one nitrogen atom.

Therefore the overall free energy change for the decomposition reaction can be expressed as:

$$\Delta E_d = E_{NH3} + E_{CxNy-1} - (3E_{H^+ + e^-} + E_{CxNy})$$

$$\Delta G_d = \Delta E_d + \Delta E_{ZPE} - T\Delta S$$

where E_{NH3}, E_{CxNy-1}, $E_{H^+ + e^-}$, E_{CxNy} is the energy of ammonia molecule, corresponding remaining structure after decomposition, proton/electron pair, and N-doped substrate, respectively. ΔE_{ZPE} is the change in the zero-point energy (ZPE), T is the room temperature (T = 298.15K), and ΔS is the entropy change. We also adopted the concept of computational hydrogen electrode to calculate the energy of proton/electron pair. Therefore, the required potential (U_d vs SHE) to make the decomposition happen and release NH_3 can be expressed as:

$$U_d = -\Delta G_d/3e$$

Supplemental Note 2

HER is regarded as the major competing reaction to eNRR; if we assume: (1) the mass and electron transfer are not the rate determining factors for both HER and eNRR, (2) only HER and eNRR are competing reactions, and (3) the selectivity of eNRR in comparison to HER could be estimated by Boltzmann distribution, the Faradaic efficiency of eNRR can be expressed as:

$$f_{eNRR} = \frac{1}{1 + e^{-\frac{\delta G}{k_B T}}} \times 100\%$$

where δG is Gibbs free energy difference between HER and eNRR potential determining step, k_B is the Boltzmann constant, and T is the room temperature.[1]

a b
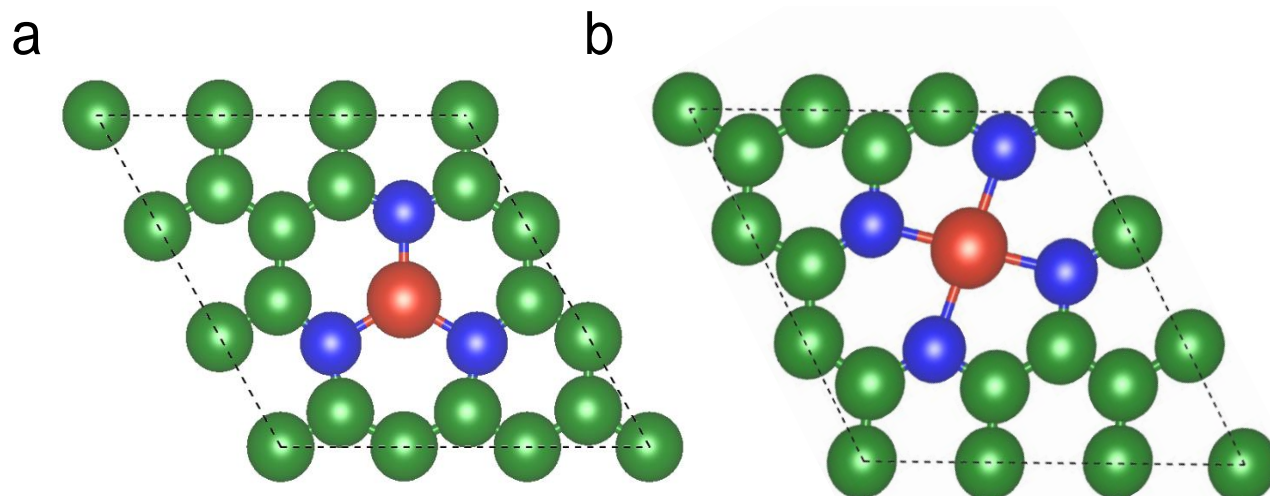
Figure S1. Atomic models of a single transition metal atom catalyst anchored on nitrogen-doped carbons. (a) Three nitrogen atoms as coordinating sites (TM@N$_3$) and (b) four nitrogen atoms as coordinating sites (TM@N$_4$).
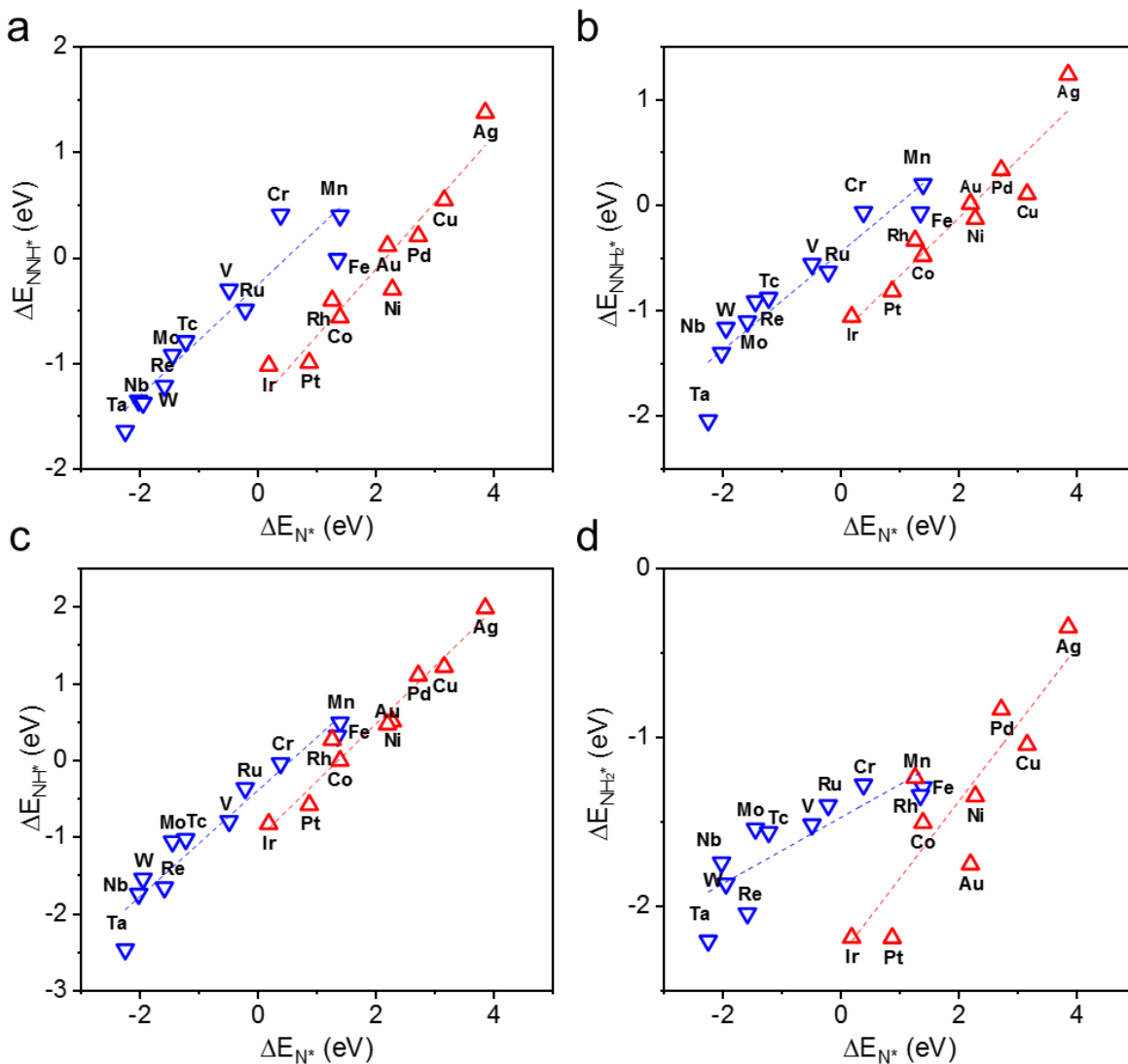
Figure S2. The correlation between the adsorption energy of (a) *NNH, (b) *NNH2, (c) *NH, and (d) *NH2 and the adsorption energy of N on various single transition metal atom catalysts supported on g-C_3N_4.
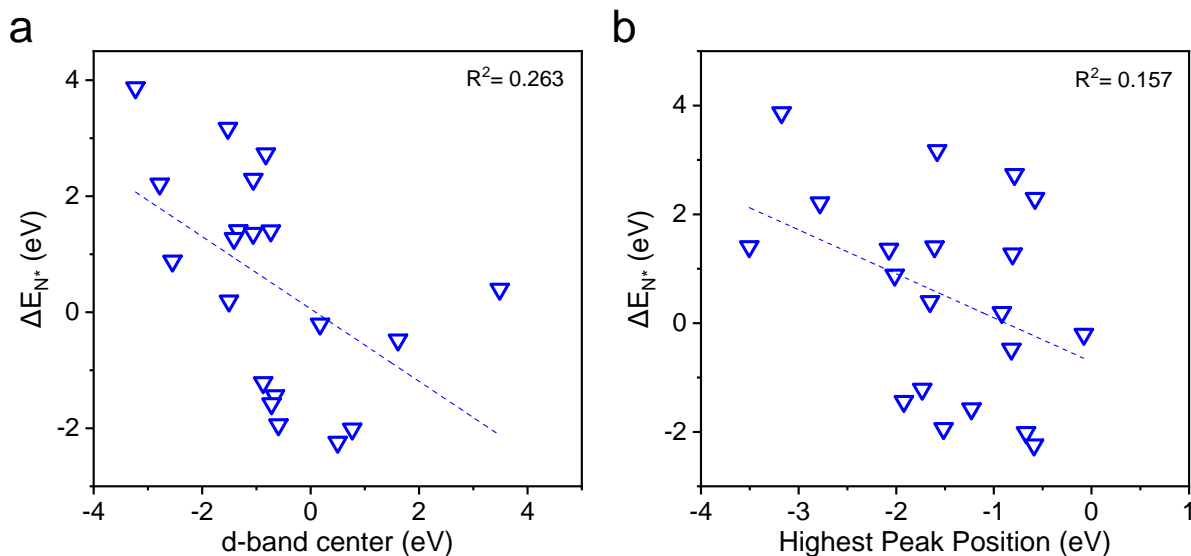
Figure S3. The correlation between the adsorption energy of nitrogen adatom with (a) the d-band center; (b) the position of the highest peak below the Fermi level.
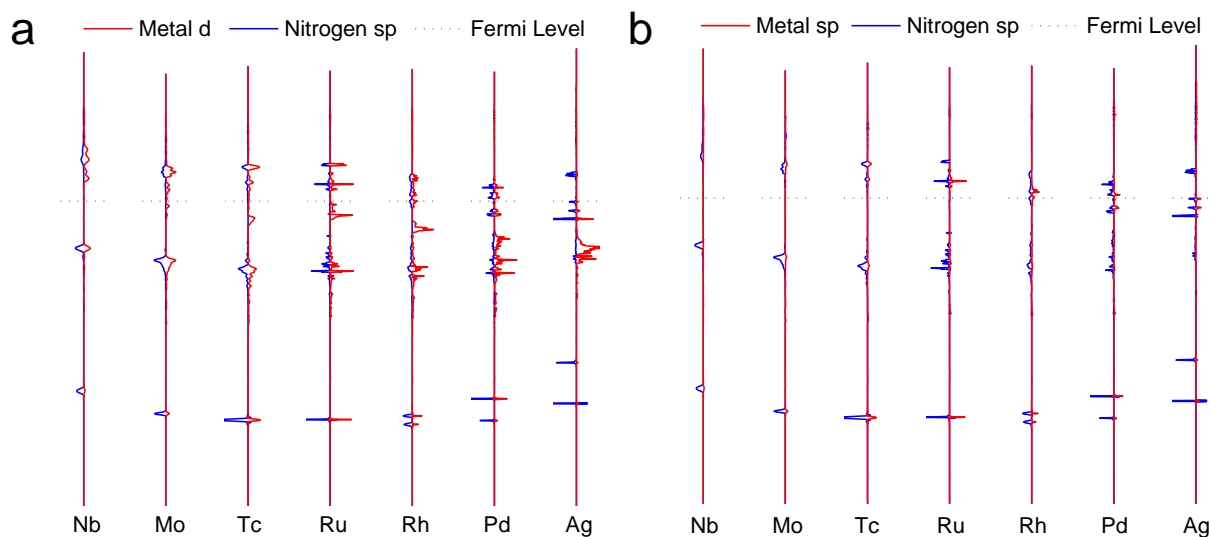
Figure S4. Projected density of states of metal center and nitrogen adatom. Schematic illustrations of (a) 4d orbitals and (b) sp orbitals of transition metal center and sp orbital of nitrogen adatom.
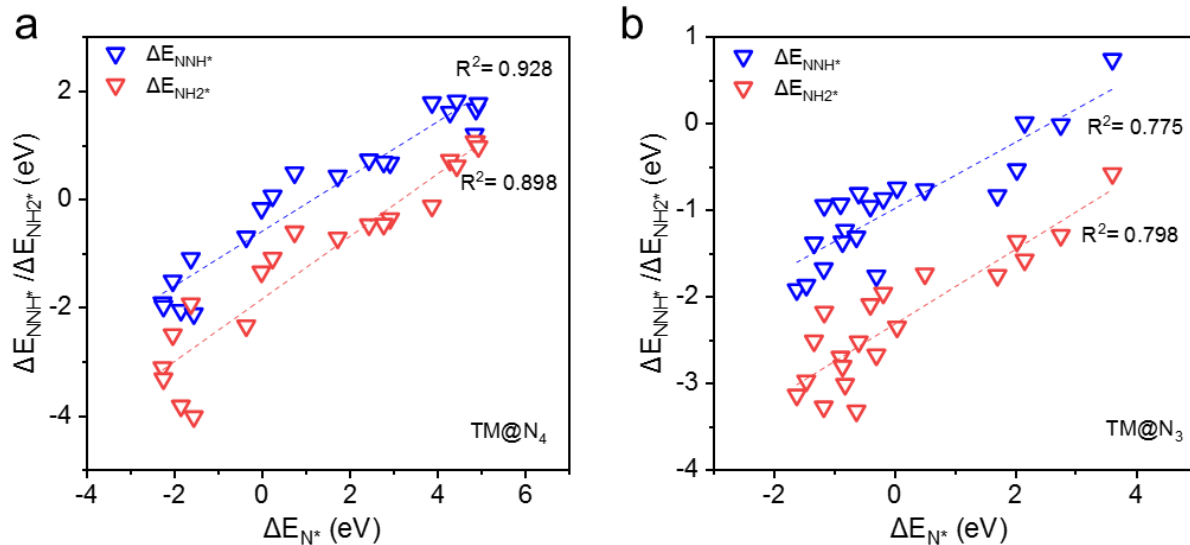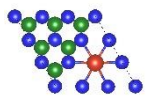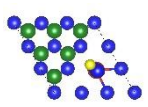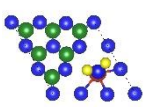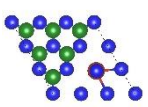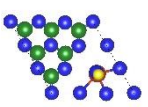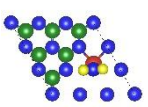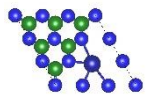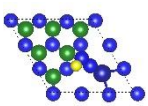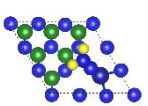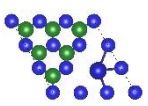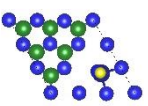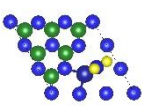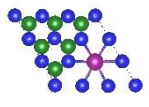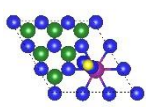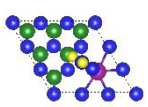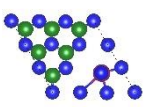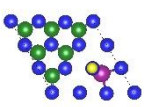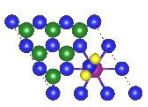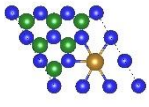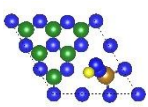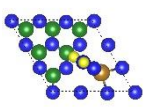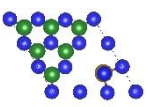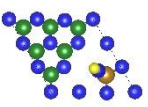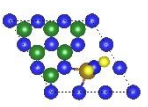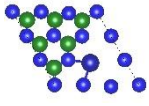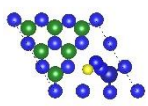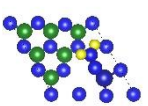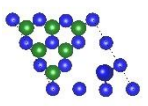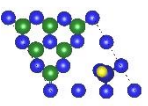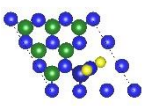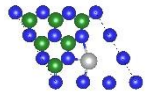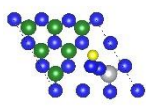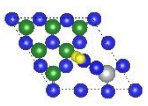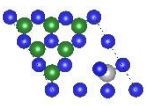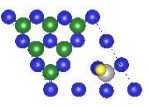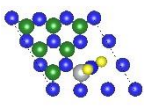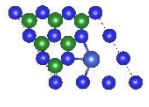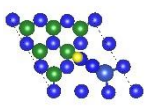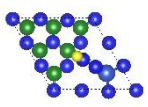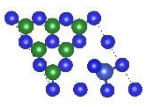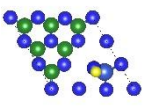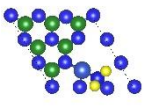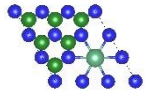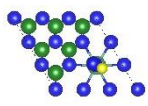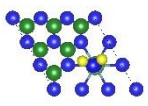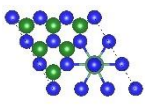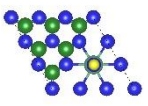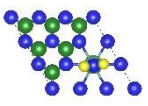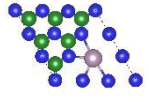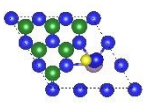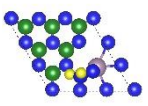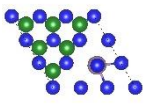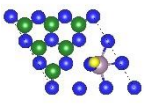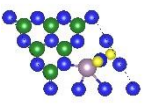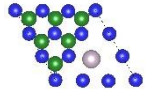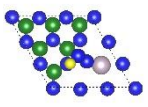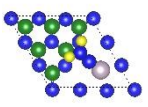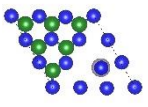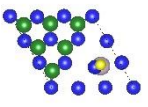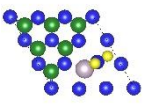
Figure S5. The correlation between the adsorption energy of *NNH and *NH$_2$ with the adsorption energy of N on various single transition metal atom catalysts supported on (a) N$_4$ and (b) N$_3$.

Supplemental Tables
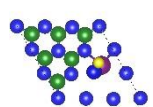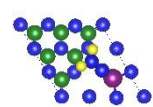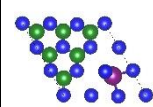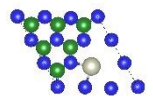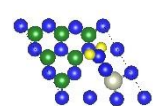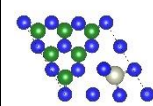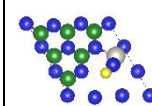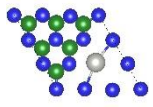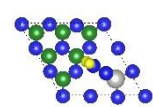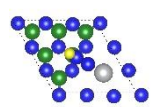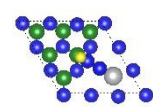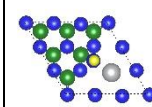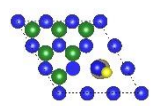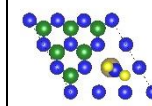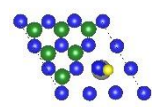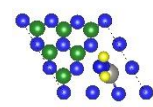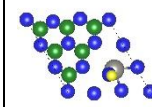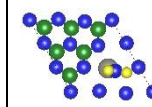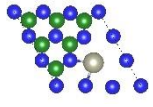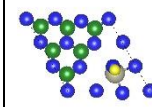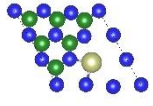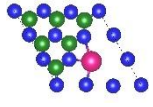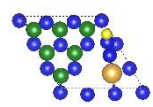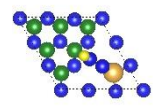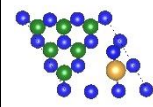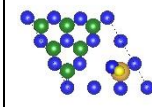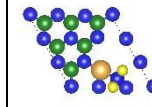
Table S1. Calculated zero point energies (ZPE) and entropy of different adsorption species and gas molecules. T=298.15 K.

Adsorbed species/Gas Molecule	*NNH	*NNH$_2$	*N	*NH	*NH$_2$	H$_2$	N$_2$	NH$_3$
ZPE	1.16	1.34	1.41	1.48	1.71	0.27	0.15	0.91
TS	1.18	0.98	1.27	1.09	0.92	0.41	0.59	0.60

Table S2. Structures of TM@g-C$_3$N$_4$ and the reaction intermediates for N$_2$ reduction via distal pathway on TM@g-C$_3$N$_4$. Part.1 from V to Tc.
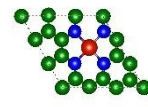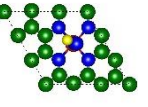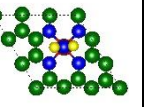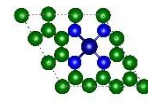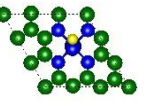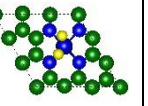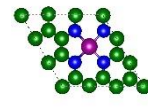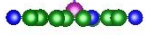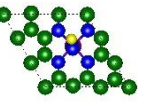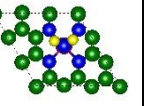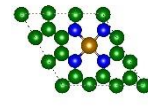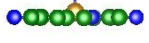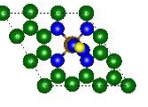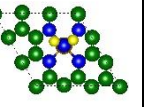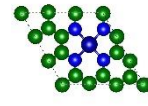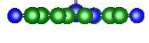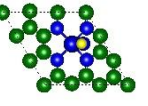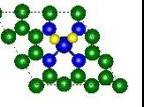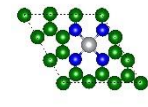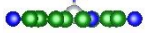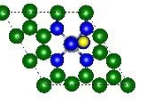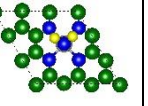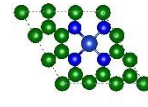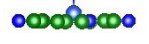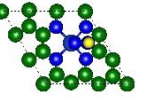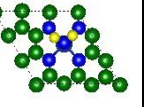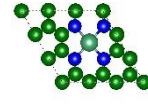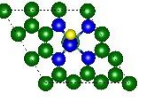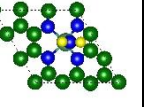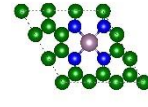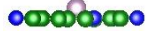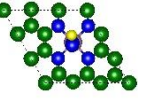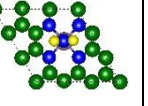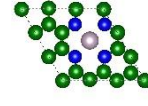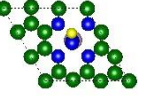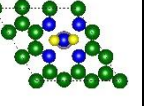
	SACs	*NNH	*NNH$_2$	*N	*NH	*NH$_2$
V@g-C$_3$N$_4$						
Cr@g-C$_3$N$_4$						
Mn@g-C$_3$N$_4$						
Fe@g-C$_3$N$_4$						
Co@g-C$_3$N$_4$						
Ni@g-C$_3$N$_4$						
Cu@g-C$_3$N$_4$						
Nb@g-C$_3$N$_4$						
Mo@g-C$_3$N$_4$						
Tc@g-C$_3$N$_4$						

Table S3. Structures of TM@g-C₃N₄ and the reaction intermediates for N₂ reduction via distal pathway on TM@g-C₃N₄. Part.2 from Ru to Au.
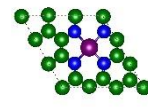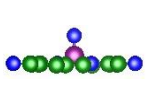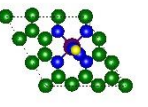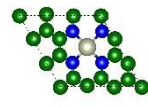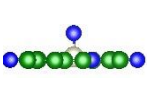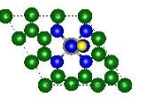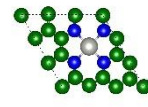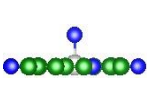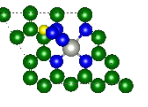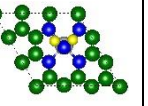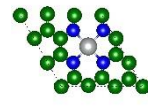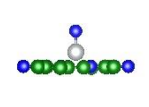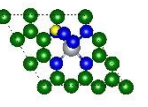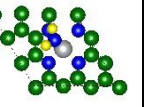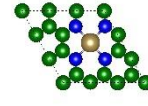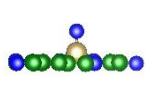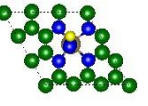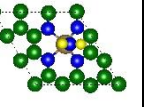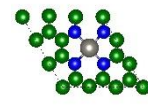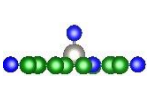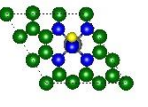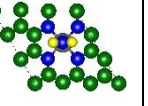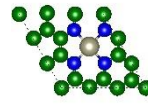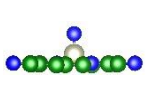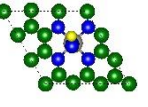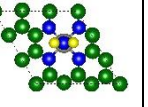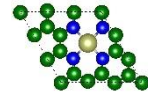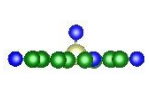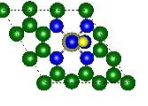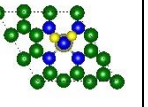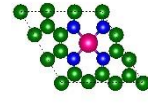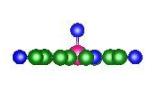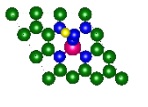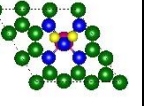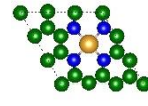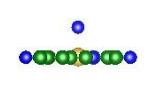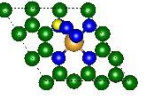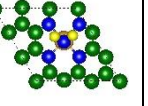
	SACs	*NNH	*NNH₂	*N	*NH	*NH₂
Ru@g-C₃N₄						
Rh@g-C₃N₄						
Pd@g-C₃N₄						
Ag@g-C₃N₄						
Ta@g-C₃N₄						
W@g-C₃N₄						
Re@g-C₃N₄						
Ir@g-C₃N₄						
Pt@g-C₃N₄						
Au@g-C₃N₄						
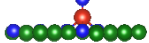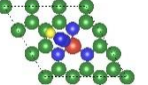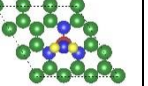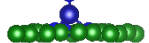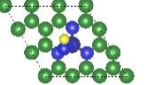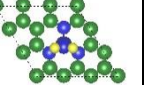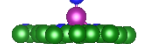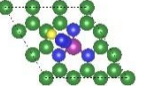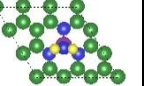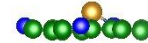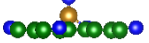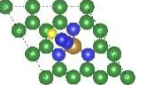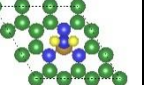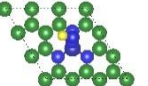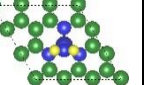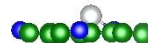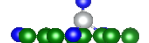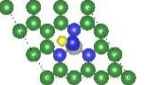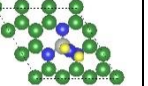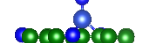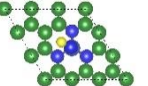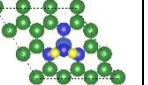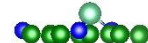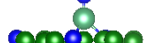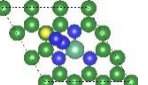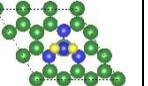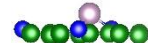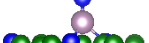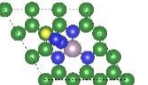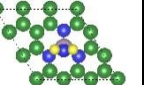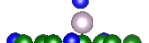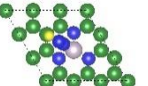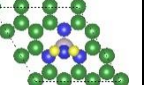
Table S4. Structures of TM@N$_4$ and the reaction intermediates for N$_2$ reduction via distal pathway on TM@N$_4$. Part.1 from V to Tc.

	SACs	*N	*NNH	*NH$_2$
V@N$_4$				
Cr@N$_4$				
Mn@N$_4$				
Fe@N$_4$				
Co@N$_4$				
Ni@N$_4$				
Cu@N$_4$				
Nb@N$_4$				
Mo@N$_4$				
Tc@N$_4$				

Table S5. Structures of TM@N$_4$ and the reaction intermediates for N$_2$ reduction via distal pathway on TM@N$_4$. Part.2 from Ru to Au.

	SACs	*N	*NNH	*NH$_2$
Ru@N$_4$				
Rh@N$_4$				
Pd@N$_4$				
Ag@N$_4$				
Ta@N$_4$				
W@N$_4$				
Re@N$_4$				
Ir@N$_4$				
Pt@N$_4$				
Au@N$_4$				

Table S6. Structures of TM@N$_3$ and the reaction intermediates for N$_2$ reduction via distal pathway on TM@N$_3$. Part.1 from V to Tc.

	SACs	*N	*NNH	*NH$_2$
V@N$_3$				
Cr@N$_3$				
Mn@N$_3$				
Fe@N$_3$				
Co@N$_3$				
Ni@N$_3$				
Cu@N$_3$				
Nb@N$_3$				
Mo@N$_3$				
Tc@N$_3$				

Table S7. Structures of TM@N$_3$ and the reaction intermediates for N$_2$ reduction via distal pathway on TM@N$_3$. Part.2 from Ru to Au.

	SACs	*N	*NNH	*NH$_2$
Ru@N$_3$				
Rh@N$_3$				
Pd@N$_3$				
Ag@N$_3$				
Ta@N$_3$				
W@N$_3$				
Re@N$_3$				
Ir@N$_3$				
Pt@N$_3$				
Au@ N$_3$				
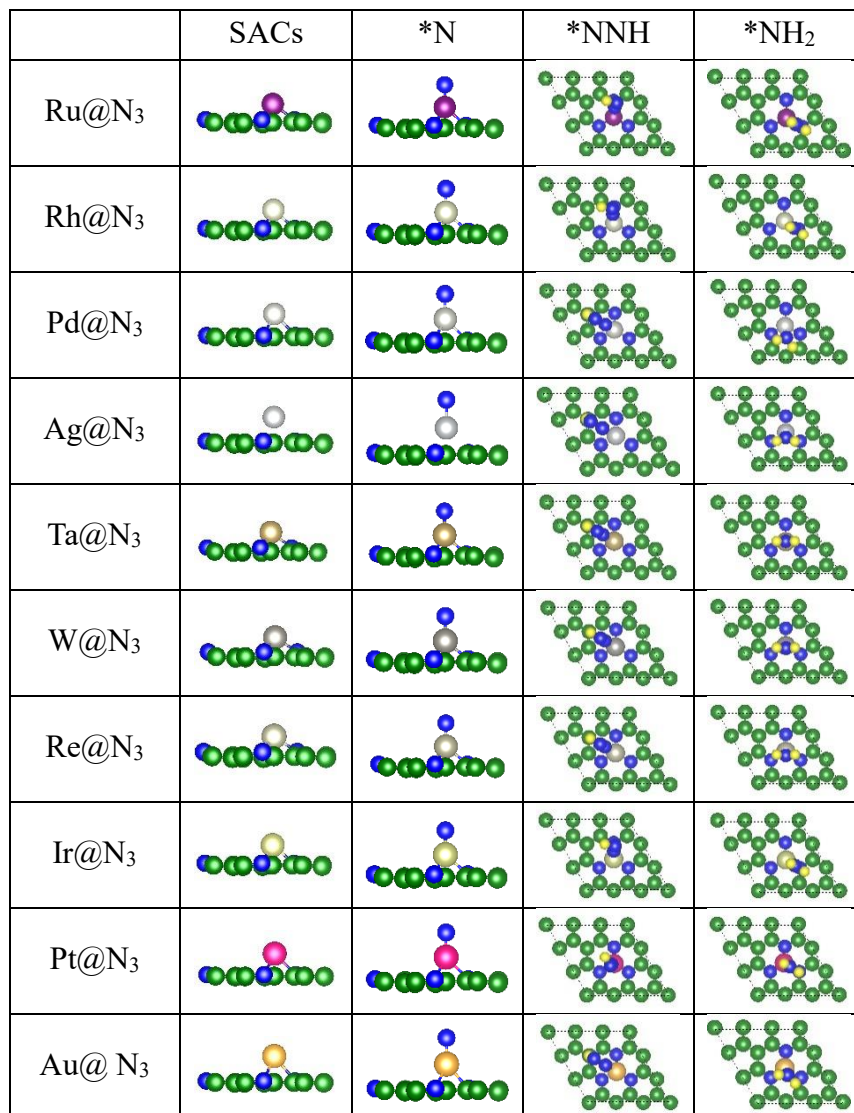
Reference

1. Zhao, W.; Zhang, L.; Luo, Q.; Hu, Z.; Zhang, W.; Smith, S.; Yang, J., *ACS Catal.* **2019**, 3419-3425.

Chapter 5: Isolated Boron Sites for Electroreduction of Dinitrogen to Ammonia

5.1 Introduction and Significance

The lack of efficient electrocatalysts with high activity and selectivity is regarded as the bottleneck for electrochemical nitrogen reduction reaction (eNRR). Several experimental or computational works propose that boron-based materials are promising candidates due to the unique electronic structure of boron as the active sites for reduction of N_2. However, limited work has been done to synthesize and test these materials for eNRR, which impedes the popularization of boron-based electrocatalysts.

In this chapter, aiming to provide useful guidelines for experimental explorations, we systematically explored eNRR performance of over ten (10) model binary borides and revealed the underlying mechanisms by density functional theory (DFT) calculations. The highlights of this chapter include:

• We demonstrate that the crystal structure of borides has a significant influence on the electronic structures of boron sites, as shown by electron localization function (ELF).

• We reveal that the energy levels of the p-orbital of boron site and antibonding π^* orbital of N_2 are well matched; the partial occupation of the formed p-π^* orbitals can lead to the difference in the activation of dinitrogen molecule.

• We show that the isolated boron sties of Mo_2B with less pz orbital filling could effectively activate N_2 and convert it into NH_3 with a limiting potential of -0.82 V vs reversible hydrogen electrode (RHE).

• We extend this concept of isolated boron site to the searching of new borides for eNRR: Fe_2B and Co_2B with moderate p_z filling and adsorption strength of reaction intermediates have promising activities with a limiting potential of -0.75 V and -0.84 V vs RHE.
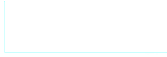
5.2 Isolated Boron Sites for Electroreduction of Dinitrogen to Ammonia

This Chapter is included as it appears as a journal paper published by **Xin Liu**, Yan Jiao*, Yao Zheng, Shi-Zhang Qiao*. Isolated Boron Sites for Electroreduction of Dinitrogen to Ammonia. *ACS Catalysis*. 2020, 10, 1847-1854.

Statement of Authorship

Title of Paper	Isolated Boron Sites for Electroreduction of Dinitrogen to Ammonia
Publication Status	☑ Published ☐ Accepted for Publication ☐ Submitted for Publication ☐ Unpublished and Unsubmitted work written in manuscript style
Publication Details	Liu, X., Jiao, Y., Zheng, Y., & Qiao, S. ACS Catal. 2020, 10, 1847−1854.

Principal Author

Name of Principal Author (Candidate)	Xin Liu
Contribution to the Paper	Proposed ideas, conduct computations wrote the manuscript.
Overall percentage (%)	80
Certification:	This paper reports on original research I conducted during the period of my Higher Degree by Research candidature and is not subject to any obligations or contractual agreements with a third party that would constrain its inclusion in this thesis. I am the primary author of this paper.
Signature		Date	3/Feb/2021

Co-Author Contributions

By signing the Statement of Authorship, each author certifies that:

i.   the candidate's stated contribution to the publication is accurate (as detailed above);

ii.   permission is granted for the candidate in include the publication in the thesis; and

iii.   the sum of all co-author contributions is equal to 100% less the candidate's stated contribution.

Name of Co-Author	Yan Jiao
Contribution to the Paper	Discussed the concepts, supervised the research project, and revised the manuscript.
Signature		Date	3/Feb/2021

Name of Co-Author	Yao Zheng
Contribution to the Paper	Discussed the concepts, and revised the manuscript.
Signature		Date	3/Feb/2021

Name of Co-Author	Shi-Zhang Qiao		
Contribution to the Paper	Discussed concepts, supervised the research project, and revised the manuscript.		
Signature		Date	3/Feb/2021

Isolated Boron Sites for Electroreduction of Dinitrogen to Ammonia

Xin Liu, Yan Jiao,* Yao Zheng, and Shi-Zhang Qiao*

Cite This: *ACS Catal.* 2020, 10, 1847−1854

Read Online

ACCESS | Metrics & More | Article Recommendations | Supporting Information

ABSTRACT: Exploring electrocatalysts with high activity is essential for the production of ammonia via an electrochemical routine. By employing density functional theory calculations, we investigated the electrochemical nitrogen reduction reaction (eNRR) activity on binary metal borides, a model system of metal borides. To elaborate the mechanisms, molybdenum borides (Mo_2B, α-MoB, and MoB_2) were first modeled; the results indicate that the crystal structures greatly impact the N_2 adsorption and therefore the electrocatalytic activity. Our electronic structure investigation suggests that boron p-orbital hybrids with dinitrogen π^*-orbital, and the population on p−π^*-orbital determine the N_2 adsorption strength. Therefore, the isolated boron site of Mo_2B with less filled p_z-orbital benefits the activation of N_2 and weaken the triple bond of dinitrogen. This isolated boron sites concept was successfully extended to other metal borides in the form of M_2B (M stands for Ti, Cr, Mn, Fe, Co, Ni, Ta, W). Mo_2B, Fe_2B, and Co_2B were discovered as the most promising candidates with low limiting potentials due to appropriate adsorption strength of reaction intermediates led by moderate p_z filling. This work provides insights for designing metal borides as promising eNRR electrocatalysts.

KEYWORDS: electrochemical nitrogen reduction, metal borides, density functional theory, electrocatalysis, nitrogen activation
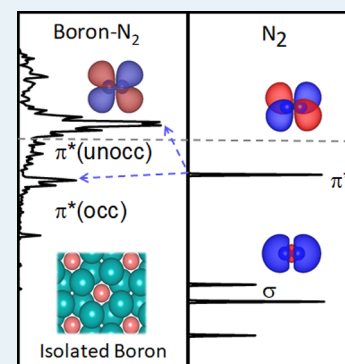
INTRODUCTION

As a fertilizer feedstock and carbon-free energy carrier, ammonia is essential to the global agriculture as well as future energy supply.[1,2] As a main approach to catalytically synthesizing ammonia, the Haber−Bosch process has drawbacks such as high energy consumption, heavy CO_2 emissions, and limiting scale of economies in production. Search for an alternative technology that is environmentally friendly and carbon neutral attracts growing interests. Electrochemical nitrogen reduction reaction (eNRR), analogous to the biological nitrogen fixation, captures protons from the electrolyte and electrons from the electrode to reduce dinitrogen (N_2) to ammonia under ambient conditions.[3,4] Additionally, when eNRR is powered up by sustainable energy resources (e.g., solar or wind energy), CO_2 emission can be avoided, also enabling distributed ammonia production in remote area due to its small footprint. The key for such ammonia production is an electrocatalyst that could activate and reduce N_2 to NH_3 under ambient conditions. However, most reported electrocatalysts for eNRR exhibit poor activity and selectivity because of high overpotential as well as the competing hydrogen evolution reaction (HER).[5] Therefore, exploring highly active electrocatalyst materials for electrochemical nitrogen reduction remains a significant challenge.

Over the past few years, transition metals (TM) are regarded as the active centers for nitrogen reduction reaction in thermal, biological, or molecular catalytic process.[2,6,7] Performance of TM-based catalysts were proposed to be optimizable according to Sabatier principle, which states that optimal catalyst shows a "just right" binding strength of a key reaction intermediate.[8]

However, a theoretical study by Skulason et al. suggested that for pure transition metal flat (111) or step (211) surfaces, even metals near the top of the activity volcano exhibit large theoretical overpotentials and suffer from the competing hydrogen evolution reaction. In this sense, searching for catalyst materials with alternative key elements should be explored. Very recently, a nonmetal boron site (borylenes) in molecular catalyst has been proved to be active for nitrogen reduction.[9,10] The empty sp^2-orbital of borylenes could accommodate the lone pair electrons of N_2, and the occupied p-orbital of borylenes can interact with the empty π^*-orbital of dinitrogen to activate dinitrogen.[11] This opens a new avenue for designing eNRR electrocatalysts utilizing boron as the active center.[12] Some other reports also suggested the potential of boron as an active site for electrocatalytic nitrogen fixation under ambient conditions including boron nanosheets,[13−15] boron carbide nanosheets,[16] boron-doped graphene,[17] or single boron site supported by two-dimensional materials.[18−20] The embedded or protogenos boron atom serves as Lewis acid site to provide enhanced binding capability to N_2 and promote the subsequent reduction steps.[18,20] However, existing reports are limited to metal-free catalysts; only a few of materials have been synthesized and tested for eNRR, which impedes the popularization of boron-based electrocatalysts.[13,16,17] There-

fore, exploring new boron-containing materials as well as revealing the principle of rational design of the boron site as the active site are of paramount importance to develop eNRR electrocatalysts.

Metal borides, because of the composition diversity and crystal structures, constitute a large number of compounds (more than 1000 binary and ternary borides have been prepared and characterized) with interesting properties and applications.[21] Since metal borides are generally very stable in both acidic and alkaline medium, molybdenum borides have been extensively studied for hydrogen evolution reaction (HER).[22−26] The results indicated that both crystal structure and boron content could significantly affect the electrocatalytic performance.[24] These previous works show that metal borides can be synthesized with different compositions, metal-to-boron ratios, and crystal structures and inspire us to investigate the potential of metal borides as eNRR electrocatalysts.[22,27,28]

In this work, we employed density functional theory (DFT) calculations to systematically study the eNRR activity of binary borides as a model system. Since molybdenum borides are the most popular binary borides in electrocatalysis, we first focus on Mo_2B, α-MoB, and MoB_2 to reveal the relationship between the boron states and eNRR performances. The results indicated that the crystal structure of borides has a significant influence on N_2 adsorption; isolated boron site of Mo_2B could effectively activate N_2 and convert it into NH_3 with a limiting potential of −0.82 V vs reversible hydrogen electrode (RHE). Further analysis showed that the energy level of the p-orbital of boron site and antibonding π^*-orbital of N_2 are well matched, and the formed p−π^*-orbitals are partially occupied. Due to the less filled p_z-orbital of the isolated boron of Mo_2B, the triple bond of N_2 was weakened and easily attacked by protons according to electronic structure analysis. We then adopted the concept of isolated boron site to screen more binary borides in the same crystal structure with Mo_2B, including Ti_2B, Cr_2B, Mn_2B, Fe_2B, Co_2B, Ni_2B, Ta_2B, and W_2B. The results showed that Fe_2B and Co_2B with moderate p_z filling and adsorption strength of reaction intermediates have promising activities with a limiting potential of −0.75 and −0.84 V vs RHE.

■ MODELS AND METHODS

Three molybdenum borides (Mo_2B, α-MoB, and α-MoB$_2$) were first explored. The calculated lattice constants for these borides are listed in Supporting Information Table S1. The (2 × 2) supercell of Mo_2B, (3 × 3) supercell of α-MoB, and (3 × 3) supercell of α-MoB$_2$ were constructed to model the boron-terminated (001) surface. Lattice parameters of other metal borides are listed in Table S2. For all the slab models, bulk terminations are used because possible oxides, which are common because of the exposure to ambient conditions, could be removed during the activation process of electrochemical measurement.[29] To examine the stability of these surfaces, we calculated the surface energies of these metal borides. The surface energy, γ_s, is defined as follows

$$\gamma_s = \frac{1}{2A}(E_s^{unrelaxed} - N \times E_b) + \frac{1}{A}(E_s^{relaxed} - E_s^{unrelaxed})$$

where A is the area of the surface slab of metal borides; $E_s^{relaxed}$ and $E_s^{unrelaxed}$ are the energies of the relaxed and unrelaxed surfaces, respectively; N is the number of metal−boron pair (determined by the stoichiometric of corresponding materials) in the slab; and E_b is the bulk energy per pair.

All the calculations were performed by spin-polarized density functional theory (DFT) methods as implemented in the Vienna ab initio simulation package; the projector-augmented-wave pseudopotential was utilized to treat the core electrons, while the Perdew−Burke−Ernzerhof exchange−correlation functional of the generalized gradient approximation was used for describing the electron interactions.[30−33] A plane-wave cutoff energy of 400 eV was adopted for all the calculations. The vacuum space in the z-direction was set as 20 Å to prevent the interaction between periodic images. The van der Waals interactions were described using the empirical correction in Grimme's scheme.[34] The reciprocal space was sampled using a 3 × 3 × 1 k-points for geometry optimization until the maximal residual force was less than 0.02 eV/Å. During the geometry optimization, only the first two atomic layers were relaxed for Mo_2B and MoB_2, while the first four atomic layer were relaxed for α-MoB. To address the kinetic barriers, we also employ the climbing image nudged elastic band method to search the transition state and minimum energy pathways.[35,36] For electronic structure calculations, an 11 × 11 × 1 k-points grid was used. The projected crystal orbital Hamilton population was employed to reveal the nature of bonding between molybdenum borides and intermediates.[37−40] The electron localization function (ELF) was employed to reveal the bonding nature of metal borides by characterizing covalent bond, lone pair of electrons, and homogeneous electron gas.[41]

The calculation of the free energy diagrams was performed using the concept of computational hydrogen electrode.[42] In this framework, the chemical potential of the electron−proton pair ($H^+ + e^-$) can be referenced by the chemical potential of gaseous H_2 at equilibrium (0 V vs reversible hydrogen electrode). The change of free energy can be calculated as follows

$$\Delta G = \Delta E + \Delta E_{ZPE} - T\Delta S - neU$$

where ΔE is the electronic energy difference directly obtained by DFT calculations. ΔE_{ZPE} is the correction from zero-point energies (ZPE), T is the room temperature ($T = 298.15K$), and ΔS is the entropy change. ZPE and vibrational entropy of adsorbed species were obtained after frequency calculations, and entropy of gas molecules (N_2 and NH_3) was taken from standard values.[43] U and n are the electrode potential applied and the number of electrons transferred, respectively. Here, we consider a Heyrovsky-type reaction mechanism, where solvated protons from the solution can directly react with an electron and reaction intermediates on the surface to construct the free energy diagrams.

■ RESULTS AND DISCUSSION

Geometric and Electronic Structure. In the first section, we briefly discuss the geometric and electronic structure of the three selected boron-terminated (001) surfaces of Mo_2B, α-MoB, and MoB_2, respectively. The surface energies, γ_s, of these three surfaces are calculated and summarized in Table S3 of the Supporting Information to examine the stability of these surfaces. As shown in Table S3, γ_s is 3.242, 2.880, and 2.482 J/m^2 for Mo_2B, α-MoB, and MoB_2, respectively, and these values indicate that the studied surface terminations are stable. These results are also consistent with previous experimental and theoretical work, where various metal borides are synthesized and characterized.[22,24,26] We then explored the "structure−property" relationship; it is important to understand the

111
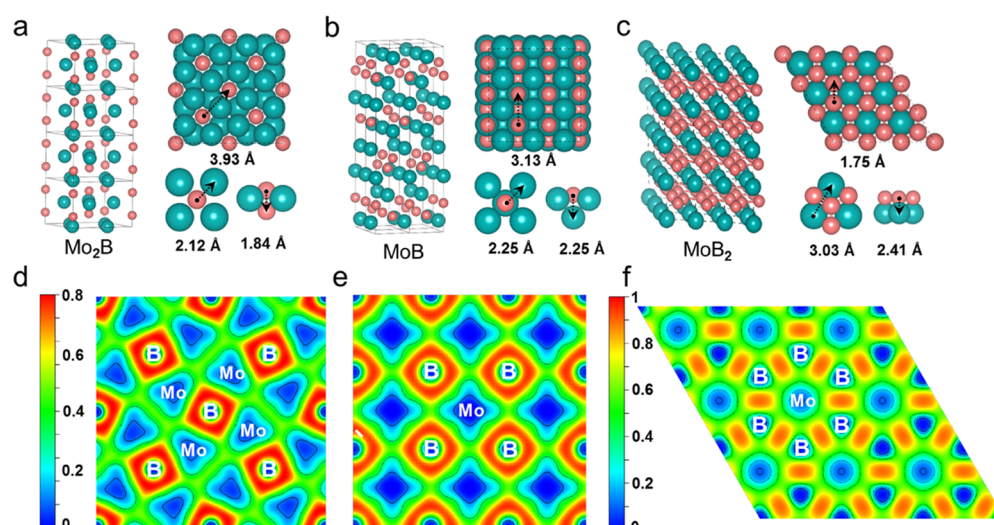
Figure 1. Geometric and electronic structures of the active center for molybdenum borides. The crystal structure of (a) Mo_2B, (b) α-MoB, and (c) MoB_2. The electron localization function (ELF) of (d) Mo_2B, (e) α-MoB, and (f) MoB_2. Color codes: Mo in cyan, B in pink. These color codes apply to all following figures.
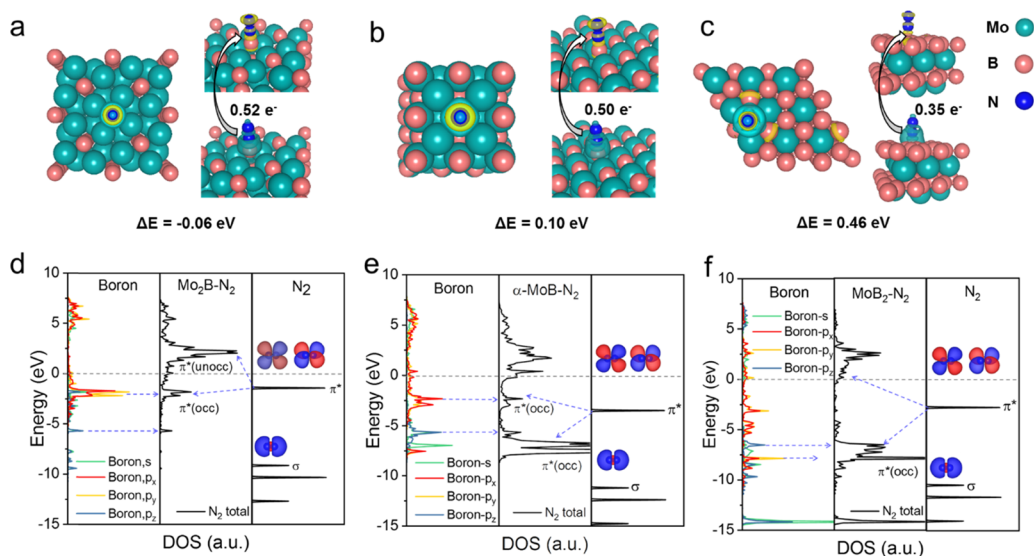
Figure 2. Activation of dinitrogen. The charge density difference of end-on N_2 adsorption on (a) Mo_2B, (b) α-MoB, and (c) MoB_2. Projected electronic densities of states and schematic illustrations of boron orbitals of molybdenum borides, π^*-orbitals of the N_2 gas molecule, and their interactions for (d) Mo_2B, (e) α-MoB, and (f) MoB_2. Color code: cyan stands for electron depletion and yellow stands for electron accumulation; nitrogen in blue.

differences between these surface structures, which may result in difference of catalytic activity. The crystal structures and the geometric details of tetragonal Mo_2B and α-MoB and hexagonal MoB_2 are given in Figure 1a–c. As seen in the right part of each panel, boron networks for these three molybdenum borides are different. Isolated boron atoms are embedded in Mo_2B lattice, and the distance between the nearest boron atoms is 3.93 Å, indicating that there is no bonding between the surface boron atoms. For α-MoB, the distance of surface boron atoms is shorter (3.13 Å), and each boron atom was coordinated with Mo with a bond length of 2.25 Å. For MoB_2, graphene-like boron layers were exposed, and the B–B bond length in the honeycomb structure is 1.75 Å. The above results clearly demonstrate the geometric differences among these three boron-terminated surfaces of the corresponding molybdenum borides.

To further reveal the electronic structure of these three materials, the electron localization function (ELF) was employed to confirm the bonding nature of the investigated molybdenum borides. For Mo_2B and α-MoB, there is no bonding between two boron atoms; the bonding between Mo and B is of ionic nature: ELF is around 0.8 at the boron site and only an insignificant ELF value is found at the Mo site (as shown in Figure 1d,e). On the other hand, the large ELF value of ca. 0.9 obtained between two adjacent B atoms for MoB_2 (Figure 1f) indicates the existence of a strong B–B covalent bond, similar to those between adjacent carbon atoms in graphene. These protogenos differences among these three materials may result in the variation of catalytic performance.

Activation of Dinitrogen on Boron Site. Adsorption of N_2 is the first step of electrochemical nitrogen reduction, and the activation of dinitrogen is vital for subsequent hydro-
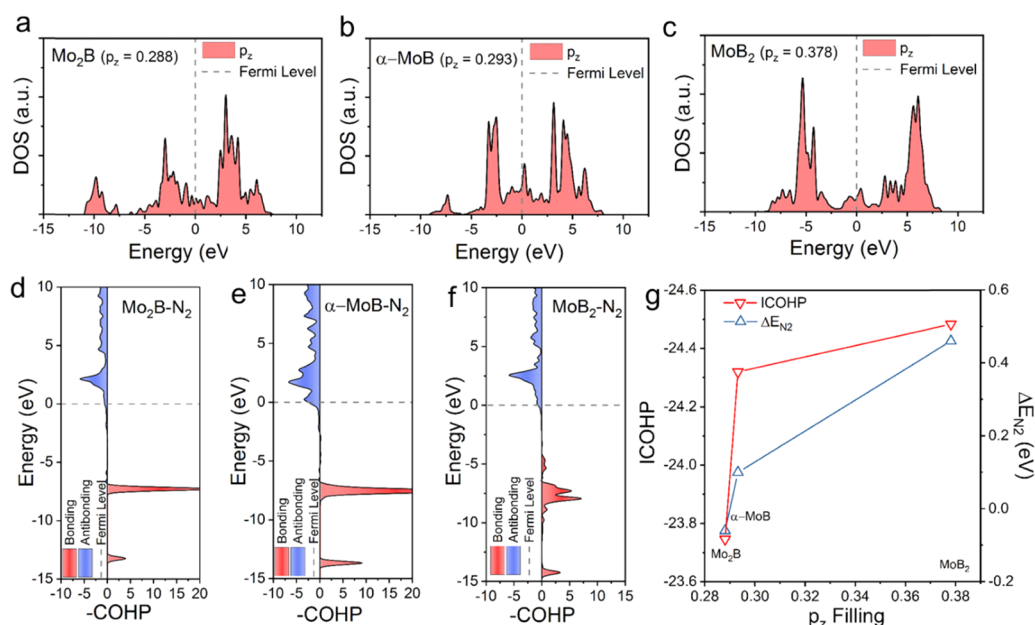
Figure 3. Density of states (DOS) of p_z-orbital for (a) Mo_2B, (b) α-MoB, and (c) MoB_2. Crystal orbital Hamilton population (COHP) between N−N on (d) Mo_2B, (e) α-MoB, and (f) MoB_2. (g) Correlation between p_z-orbital filling with integrated crystal orbital Hamilton population (ICOHP) and the adsorption energy of N_2. The dashed lines indicate the Fermi level.

genation process. Therefore, two adsorption patterns (end-on and side-on) were considered for these three materials. Although several initial configurations were constructed for optimization, the side-on chemisorption patterns were still not found for Mo_2B. As shown in Figure S1a, physisorption configurations were detected with an adsorption energy of −0.14 eV. As for α-MoB and MoB_2, although side-on adsorption patterns were found, the adsorption is relatively weak (Figure S1b,c). For the side-on adsorption patterns, usually a dissociative pathway was involved in which the triple bond of N_2 was cleaved at the electrocatalyst surface; however, in view of the weak adsorption, these three surfaces are supposed to be not able to split N_2 with a reasonable rate at room temperature.[5] Due to this observation, we only focus on the associative pathway and the corresponding end-on N_2 adsorption patterns. As shown in Figure 2a−c, for the end-on pattern, Mo_2B displays the strongest adsorption with most negative adsorption energy of −0.06 eV, compared with 0.10 eV for α-MoB and 0.46 eV for MoB_2. The corresponding N−N bond length are 1.14, 1.14, and 1.13 Å for Mo_2B, α-MoB, and MoB_2, respectively, which are longer than that of free nitrogen molecule (1.12 Å). Figure 2a−c also displays the charge density difference isosurface: there is an electron accumulation on the adsorbed N_2 molecule and electron depletion around boron. Bader charge analysis validated the charge transfer process, and the results showed that 0.52 e⁻ (Mo_2B), 0.50 e⁻ (α-MoB), and 0.35 e⁻ (MoB_2) are transferred from the boron atom to the adsorbed nitrogen molecule. This is in line with the adsorption energy trend: the more electrons are transferred, the stronger is the adsorption. To further reveal the bonding nature of the adsorbed N_2 involved in the end-on pattern, we investigate the density of states (DOS) of these three N_2 adsorption configurations (as shown in Figure 2d−f). The energy levels of N_2 are referenced to the Fermi level of the corresponding configurations. The energy levels of boron p-orbitals and antibonding π^*-orbital of N_2 are well matched, leading to the partial occupations of the hybridized p−π^*-

orbitals. The occupations of this hybridized orbital increased from Mo_2B to MoB_2 as indicated by the middle part in Figure 2d−f. Accordingly, the N−N bond was weakened and easily attacked by protons. In consideration of previous analysis of the charge-transfer process, the electrons are transferred from boron to the empty π^*-orbital of free N_2, which led to the activation of dinitrogen.

The previous sections elucidated that the boron p-orbitals of molybdenum borides played an important role in the activation of N_2. Therefore, it is significant to discover the key features of boron p-orbitals controlling the activation of N_2 for facilitating the rational design of high-performance metal borides for NRR. We calculated the electron filling of boron p-bands of these three molybdenum borides; the results are summarized in Figure 3a−c and Table S4. Based on these results, p_x and p_y are more filled compared with p_z-orbitals. This is in accordance with the analysis of ELF in Figure S2: more electrons around the boron atoms are localized in the x−y-plane for bonding with the surrounding Mo atoms (or boron for MoB_2). The p_z-orbitals in these compounds are less filled and could accommodate the lone pair of electrons of dinitrogen via an end-on adsorption pattern.

To further verify this inference, the crystal orbital Hamilton population (COHP) of N−N was calculated to reveal the bonding strength as a measurement of N_2 activation degree. As shown in Figure 3d−f, the bonding populations (red) are below the Fermi level (ε_F) and filled, while the antibonding populations (blue) are partially filled because the energy levels are across the Fermi level. We integrated the crystal orbital Hamilton population (ICOHP) up to ε_F, and ICOHP could be regarded as a quantitative indicator of N_2 activation: the more negative the ICOHP, the less activated is the N_2 molecule (the more stable the N_2 molecule). Figure 3g shows that when p_z is less filled (Mo_2B), the adsorption is stronger and N−N bonding is weaker. The weakened N−N bond is indicated by a less negative ICOHP with a less antibonding orbital filling. In the contrast, when p_z is more filled (MoB_2), the boron site

113
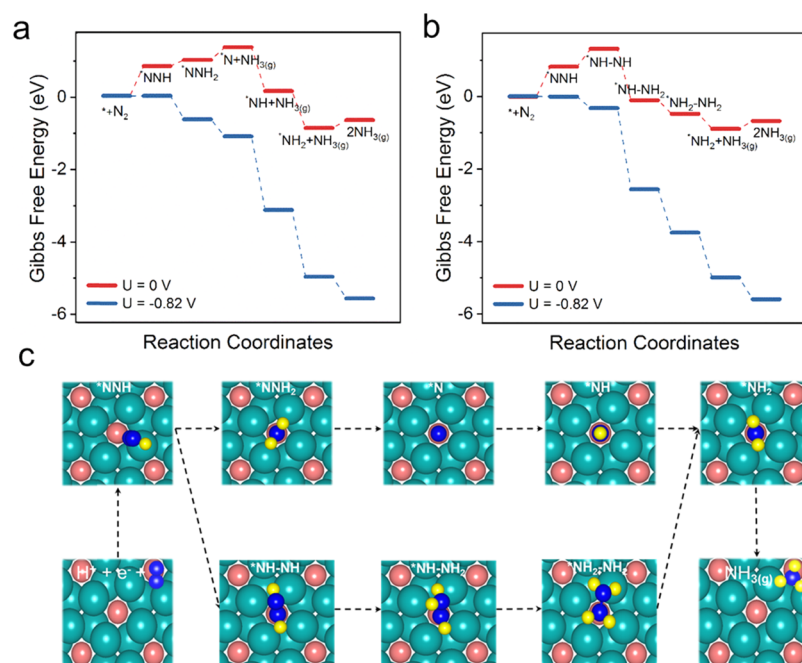
Figure 4. Free energy diagrams of electrochemical nitrogen reduction on Mo₂B via a (a) distal and (b) alternating pathways. (c) Corresponding reaction intermediates along a distal (upper) and alternating (lower) pathways.

cannot effectively capture and activate dinitrogen molecule. Therefore, Mo_2B is the most promising among these three candidates. More importantly, we discovered that the filling of p_z-orbital is a good indicator to represent N_2 activation.

Electrocatalytic Reduction of Dinitrogen. As shown in the previous session, N_2 was first activated by the isolated boron site of Mo_2B. The subsequent reduction steps of adsorbed N_2 to NH_3 were calculated to evaluate the thermodynamics of this process. For α-MoB and MoB_2, the first protonation step following the activation is achieved with difficulty; free energy change is 2.36 and 2.93 eV, respectively, as shown in Figure S3. Therefore, we only focus on Mo_2B; both the distal pathway (protonation occurs at one end of N_2) and alternating pathway (protonation occurs at both ends of N_2) were considered by constructing their corresponding free energy pathways. The pathways and intermediates configurations on each pathway are summarized in Figure 4. For the distal pathway, *NNH is formed with a free energy change of 0.82 eV with the N−N bond length elongated to 1.26 Å. The following two steps to release the first NH_3 molecule is 0.17 and 0.34 eV uphill, respectively. Protonation of *N to *NH₂ is spontaneous with a free energy change of −1.20 and −1.03 eV. The last step of NH_3 desorption is slightly uphill (0.22 eV). Compared with the distal pathway, the second protonation step via the alternating pathway (*NNH → *NH−NH) is more difficult, with a maximum uphill free energy change of 0.5 eV. The N−N bond lengths of *NNH₂ and *NH−NH₂ intermediates in Figure 4c are 1.28 and 1.40 Å, respectively. This is in accordance with the results that the first NH_3 release via alternating pathway is thermodynamically favored with a free energy change of −0.41 eV due to the weakened N−N bond. Overall, we found that the potential determining step for both distal and alternating pathways is the first protonation to form *NNH, so the theoretical limiting potential is −0.82 V vs RHE. We then calculate the activation barrier of this step to evaluate the kinetic factors. To calculate the proton-transfer barrier, we adopted a water-assisted hydrogen shuttling model,

which has been used to determine the barriers of electrochemical CO_2 reduction.[44−46] As shown in Figure S4, based on this model, the activation barrier of the first protonation step was 0.69 eV, which is lower than 0.75 eV, corresponding to a turnover frequency of 1 s⁻¹ from the transition state theory. This result also indicates that Mo_2B is facile for electrochemical nitrogen reduction.

We further tracked the Bader charge of isolated boron site, the adsorbed N_xH_y and the bulk of catalysts along the reaction distal and alternating pathway. The results are summarized in Figure S5. Taking the second protonation step as an example, N−NH₂* gains more electrons (0.67 e⁻) than NH−NH* (0.39 e⁻) and thus displays a less positive free energy change. The results also indicate that N_xH_y always obtains electrons in the adsorption and reduction process, while the support always loses electrons. The bulk of Mo_2B plays a role as an electron reservoir, and the isolated boron site transfers electrons between Mo_2B surface and adsorbed N_xH_y, which is similar to the scenario for single-atom catalysts.[47]

Generality of the Nitrogen Activation Mechanism. To extend this concept of isolated boron atom as the active center, we explored other eight potential M_2B materials (M stands for Ti, Cr, Mn, Fe, Co, Ni, Ta, and W) with the same space group ($I4/mcm$). All the crystal parameters of these metal borides are listed in Table S4. According to previous reports,[47−49] the first ($N_2 + H^+ + e^- \rightarrow NNH^*$) and last protonation (*$NH_2 + H^+ + e^- \rightarrow NH_{3(g)}$) steps are vital for the overall performance and normally are the potential-determining steps. After geometry optimization, we examined the adsorption configurations of *NNH and *NH₂ on these M_2B boron-terminated (001) surface and excluded Ti₂B and Ta₂B. The main reason is that these two materials possess dissociative adsorption patterns on Ti or Ta atoms instead of boron (as shown in Figure S6); these adsorption patterns are induced by the strong adsorption ability of early transition metals like Ti and Ta.[5] The relationship between the adsorption energy of *NH₂ and the filling of the p_z-orbital is displayed in Figure 5a, the results are

114
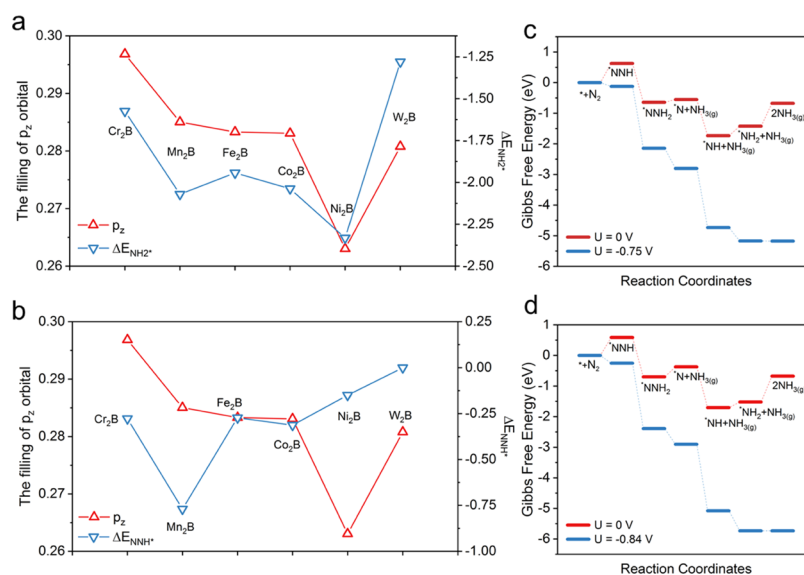
Figure 5. Relationship between the filling of boron p_z-orbital and the adsorption energy of (a) *NH$_2$ and (b) *NNH. The free energy diagrams of eNRR via a distal pathway on (c) Fe$_2$B and (d) Co$_2$B.

generally in accordance with previous observations on molybdenum borides: the less is the filling of p$_z$-orbital, the stronger is the *NH$_2$ adsorption. For the formation of ammonia, it is desired that the adsorption of *NH$_2$ is weak for facile desorption; therefore, Ni$_2$B is excluded because of the strong adsorption of *NH$_2$ resulting from less filling of the p$_z$-orbital. For *NNH adsorption, the discrepancy between p$_z$-orbital filling and E$_{*NNH}$ adsorption is found because the adsorption is bidentate and the adsorption strength is affected by both boron and metal atoms' electronic structures. As shown in Figure 5b, Cr$_2$B has the most boron p$_z$ filling and is expected to weakly bind *NNH. However, since Cr is an early transition metal with a strong binding ability, the overall results of both Cr and boron are that *NNH is relatively stabilized with an adsorption energy of −0.28 eV.

Additionally, a modest adsorption is desired to achieve optimal performance, since a weak adsorption cannot effectively activate the adsorbed N$_2$, while a strong adsorption leads to a difficult regeneration of isolated boron sites.[5] Based on this criteria, we identified that Fe$_2$B, Co$_2$B, and Cr$_2$B have the potential for electrochemical nitrogen reduction. We further calculated the reaction intermediates via a distal pathway, and the corresponding configurations are given in Figure S7 (Fe$_2$B), S8 (Co$_2$B), and S9 (Cr$_2$B). For Cr$_2$B, a full distal pathway was calculated, which shows a predicted limiting potential of −2.21 V vs RHE (Figure S10). This potential is too large for real eNRR operation and therefore excluded in the following discussions.

The free energy diagrams of Fe$_2$B and Co$_2$B are given in Figure 5c,d. Based on the results, for both Fe$_2$B and Co$_2$B, the potential limiting step is the last protonation step (*NH$_2$ + H$^+$ + e$^-$ → NH$_{3(g)}$), which is different from that for Mo$_2$B with the first protonation step (N$_2$ + H$^+$ + e$^-$ → *NNH) as the potential determining step. Compared with that for Mo$_2$B, the adsorption of *NNH is stronger for Fe$_2$B and Co$_2$B, and this could contribute to a less filling of the p$_z$-orbital in Fe$_2$B and Co$_2$B as revealed in previous section. However, because of the less occupied p$_z$-orbital, the release of NH$_{3(g)}$ at the last step is more endothermic and the potential-determining step switches to *NH$_2$ + H$^+$ + e$^-$ → NH$_{3(g)}$. The limiting potential of Fe$_2$B

and Co$_2$B is predicted as −0.75 and −0.84 V vs RHE, respectively. The above analyses indicate that Fe$_2$B and Co$_2$B with isolated boron sites are promising electrocatalysts for eNRR. Besides binary metal borides, more multimetal borides could constitute a mass of candidates for screening efficient eNRR catalysts.

CONCLUSIONS

In summary, we theoretically investigated the eNRR performance of model binary metal borides and reveal the key element that controls the eNRR activity of these borides by DFT calculations. Molybdenum borides were first explored due to the popularity of these materials, and the isolated boron site of Mo$_2$B is predicted to have the best performance of −0.82 V vs RHE limiting potential. Electronic structure analysis indicated that the p-orbital of boron and π*-orbital of N$_2$ are well-matched, and the occupation of p−π* determines the binding strength of N$_2$. Further analysis found that the isolated boron site of Mo$_2$B has less filling of p$_z$-orbital, leading to the activation of N$_2$ as indicated by ICOHP results. Screening of more binary borides (M$_2$B) with isolated boron site suggests that Fe$_2$B and Co$_2$B are also potential candidates for eNRR with a relatively low limiting potential of −0.75, and −0.84 V vs RHE, respectively. Overall, our calculations suggest that metal borides, which are facile for experimental synthesis, hold the potential to enrich the eNRR electrocatalyst candidates compared with pure transition metals.

ASSOCIATED CONTENT

Ⓢ Supporting Information

The Supporting Information is available free of charge at https://pubs.acs.org/doi/10.1021/acscatal.9b04103.

> Details of crystal parameters; ELF and Bader charge variation of related configurations; atomic configurations of reaction intermediates on metal borides; free energy diagrams of some steps; and the surface energy of slab studied in this work (PDF)

AUTHOR INFORMATION

Corresponding Authors

Yan Jiao − *The University of Adelaide, Adelaide, Australia;* ⓘ orcid.org/0000-0003-1329-4290; Email: yan.jiao@adelaide.edu.au

Shi-Zhang Qiao − *The University of Adelaide, Adelaide, Australia;* ⓘ orcid.org/0000-0002-4568-8422; Email: s.qiao@adelaide.edu.au

Other Authors

Xin Liu − *The University of Adelaide, Adelaide, Australia*

Yao Zheng − *The University of Adelaide, Adelaide, Australia;* ⓘ orcid.org/0000-0002-2411-8041

Complete contact information is available at:
https://pubs.acs.org/10.1021/acscatal.9b04103

Author Contributions

The manuscript was written through contributions of all of the authors. All of the authors have given approval to the final version of the manuscript.

Notes

The authors declare no competing financial interest.

REFERENCES

(1) Guo, C.; Ran, J.; Vasileff, A.; Qiao, S.-Z. Rational Design of Electrocatalysts And Photo(Electro)Catalysts For Nitrogen Reduction to Ammonia (NH₃) Under Ambient Conditions. *Energy Environ. Sci.* **2018**, *11*, 45−56.

(2) Foster, S. L.; Bakovic, S. I. P.; Duda, R. D.; Maheshwari, S.; Milton, R. D.; Minteer, S. D.; Janik, M. J.; Renner, J. N.; Greenlee, L. F. Catalysts for Nitrogen Reduction to Ammonia. *Nat. Catal.* **2018**, *1*, 490−500.

(3) Van Der Ham, C. J. M.; Koper, M. T. M.; Hetterscheid, D. G. H. Challenges in Reduction of Dinitrogen by Proton and Electron Transfer. *Chem. Soc. Rev.* **2014**, *43*, 5183−5191.

(4) Rosca, V.; Duca, M.; De Groot, M. T.; Koper, M. T. M. Nitrogen Cycle Electrocatalysis. *Chem. Rev.* **2009**, *109*, 2209−2244.

(5) Skúlason, E.; Bligaard, T.; Gudmundsdottir, S.; Studt, F.; Rossmeisl, J.; Abild-Pedersen, F.; Vegge, T.; Jonsson, H.; Norskov, J. K. A Theoretical Evaluation of Possible Transition Metal Electro-Catalysts for N₂ Reduction. *Phys. Chem. Chem. Phys.* **2012**, *14*, 1235−1245.

(6) Macleod, K. C.; Holland, P. L. Recent Developments in The Homogeneous Reduction of Dinitrogen by Molybdenum and Iron. *Nat. Chem.* **2013**, *5*, 559−565.

(7) Chen, J. G.; Crooks, R. M.; Seefeldt, L. C.; Bren, K. L.; Bullock, R. M.; Darensbourg, M. Y.; Holland, P. L.; Hoffman, B.; Janik, M. J.; Jones, A. K.; Kanatzidis, M. G.; King, P.; Lancaster, K. M.; Lymar, S. V.; Pfromm, P.; Schneider, W. F.; Schrock, R. R. Beyond Fossil Fuel-Driven Nitrogen Transformations. *Science* **2018**, *360*, No. eaar6611.

(8) Medford, A. J.; Vojvodic, A.; Hummelshoj, J. S.; Voss, J.; Abild-Pedersen, F.; Studt, F.; Bligaard, T.; Nilsson, A.; Norskov, J. K. From the Sabatier Principle to a Predictive Theory of Transition-Metal Heterogeneous Catalysis. *J. Catal.* **2015**, *328*, 36−42.

(9) Légaré, M. A.; Rang, M.; Belanger-Chabot, G.; Schweizer, J. I.; Krummenacher, I.; Bertermann, R.; Arrowsmith, M.; Holthausen, M. C.; Braunschweig, H. The Reductive Coupling of Dinitrogen. *Science* **2019**, *363*, 1329−1332.

(10) Légaré, M. A.; Belanger-Chabot, G.; Dewhurst, R. D.; Welz, E.; Krummenacher, I.; Engels, B.; Braunschweig, H. Nitrogen Fixation and Reduction at Boron. *Science* **2018**, *359*, 896−899.

(11) Broere, D. L. J.; Holland, P. L. Boron Compounds Tackle Dinitrogen. *Science* **2018**, *359*, 871.

(12) Hering-Junghans, C. Metal-Free Nitrogen Fixation at Boron. *Angew. Chem., Int. Ed.* **2018**, *57*, 6738−6740.

(13) Fan, Q.; Choi, C.; Yan, C.; Liu, Y.; Qiu, J.; Hong, S.; Jung, Y.; Sun, Z. High-Yield Production of Few-Layer Boron Nanosheets for Efficient Electrocatalytic N₂ Reduction. *Chem. Commun.* **2019**, *55*, 4246−4249.

(14) Liu, C.; Li, Q.; Zhang, J.; Jin, Y.; Macfarlane, D. R.; Sun, C. Theoretical Evaluation of Possible 2D Boron Monolayer in N₂ Electrochemical Conversion Into Ammonia. *J. Phys. Chem. C* **2018**, *122*, 25268−25273.

(15) Zhang, X.; Wu, T.; Wang, H.; Zhao, R.; Chen, H.; Wang, T.; Wei, P.; Luo, Y.; Zhang, Y.; Sun, X. Boron Nanosheet: an Elemental Two-Dimensional (2D) Material for Ambient Electrocatalytic N₂-to-NH₃ Fixation In Neutral Media. *ACS Catal.* **2019**, 4609−4615.

(16) Qiu, W.; Xie, X.-Y.; Qiu, J.; Fang, W.-H.; Liang, R.; Ren, X.; Ji, X.; Cui, G.; Asiri, A. M.; Cui, G.; Tang, B.; Sun, X. High-Performance Artificial Nitrogen Fixation at Ambient Conditions Using a Metal-Free Electrocatalyst. *Nat. Commun.* **2018**, *9*, No. 3485.

(17) Yu, X.; Han, P.; Wei, Z.; Huang, L.; Gu, Z.; Peng, S.; Ma, J.; Zheng, G. Boron-Doped Graphene for Electrocatalytic N₂ Reduction. *Joule* **2018**, *2*, 1610−1622.

(18) Shi, L.; Li, Q.; Ling, C. Y.; Zhang, Y. H.; Ouyang, Y. X.; Bai, X. W.; Wang, J. L. Metal-Free Electrocatalyst for Reducing Nitrogen to Ammonia Using a Lewis Acid Pair. *J. Mater. Chem. A* **2019**, *7*, 4865−4871.

(19) Liu, C. W.; Li, Q. Y.; Wu, C. Z.; Zhang, J.; Jin, Y. G.; Macfarlane, D. R.; Sun, C. H. Single-Boron Catalysts for Nitrogen Reduction Reaction. *J. Am. Chem. Soc.* **2019**, *141*, 2884−2888.

(20) Ling, C.; Niu, X.; Li, Q.; Du, A.; Wang, J. Metal-Free Single Atom Catalyst for N₂ Fixation Driven by Visible Light. *J. Am. Chem. Soc.* **2018**, *140*, 14161−14168.

(21) Scheifers, J. P.; Zhang, Y.; Fokwa, B. P. T. Boron: Enabling Exciting Metal-Rich Structures and Magnetic Properties. *Acc. Chem. Res.* **2017**, *50*, 2317−2325.

(22) Li, Q.; Zou, X.; Ai, X.; Chen, H.; Sun, L.; Zou, X. Revealing Activity Trends of Metal Diborides Toward pH-Universal Hydrogen Evolution Electrocatalysts with Pt Like Activity. *Adv. Energy Mater.* **2019**, *9*, No. 1803369.

(23) Park, H.; Zhang, Y. M.; Scheifers, J. P.; Jothi, P. R.; Encinas, A.; Fokwa, B. P. T. Graphene- And Phosphorene-Like Boron Layers With Contrasting Activities in Highly Active Mo₂B₄ for Hydrogen Evolution. *J. Am. Chem. Soc.* **2017**, *139*, 12915−12918.

(24) Park, H.; Encinas, A.; Scheifers, J. P.; Zhang, Y. M.; Fokwa, B. P. T. Boron-Dependency of Molybdenum Boride Electrocatalysts for The Hydrogen Evolution Reaction. *Angew. Chem., Int. Ed.* **2017**, *56*, 5575−5578.

(25) Jothi, P. R.; Zhang, Y. M.; Scheifers, J. P.; Park, H.; Fokwa, B. P. T. Molybdenum Diboride Nanoparticles as a Highly Efficient Electrocatalyst for the Hydrogen Evolution Reaction. *Sustainable Energy Fuels* **2017**, *1*, 1928−1934.

(26) Chen, Y.; Yu, G.; Chen, W.; Liu, Y.; Li, G.-D.; Zhu, P.; Tao, Q.; Li, Q.; Liu, J.; Shen, X.; Li, H.; Huang, X.; Wang, D.; Asefa, T.; Zou, X. Highly Active, Nonprecious Electrocatalyst Comprising Borophene Subunits for the Hydrogen Evolution Reaction. *J. Am. Chem. Soc.* **2017**, *139*, 12370−12373.

(27) Li, Y.; Huang, B.; Sun, Y.; Luo, M.; Yang, Y.; Qin, Y.; Wang, L.; Li, C.; Lv, F.; Zhang, W.; Guo, S. Multimetal Borides Nanochains as Efficient Electrocatalysts for Overall Water Splitting. *Small* **2019**, *15*, No. E1804212.

(28) Jothi, P. R.; Yubuta, K.; Fokwa, B. P. T. A Simple, General Synthetic Route Toward Nanoscale Transition Metal Borides. *Adv. Mater.* **2018**, *30*, No. 1704181.

(29) Vrubel, H.; Hu, X. L. Molybdenum Boride and Carbide Catalyze Hydrogen Evolution in both Acidic and Basic Solutions. *Angew. Chem., Int. Ed.* **2012**, *51*, 12703−12706.

(30) Kresse, G.; Hafner, J. ab initio Molecular-Dynamics Simulation of the Liquid-Metal−Amorphous-Semiconductor Transition in Germanium. *Phys. Rev. B* **1994**, *49*, 14251−14269.

(31) Kresse, G.; Hafner, J. Ab Initio Molecular Dynamics for Liquid Metals. *Phys. Rev. B* **1993**, *47*, 558−561.

(32) Kresse, G.; Furthmuller, J. Efficient Iterative Schemes for ab initio Total-Energy Calculations Using a Plane-Wave Basis Set. *Phys. Rev. B* **1996**, *54*, 11169−11186.

(33) Kresse, G.; Furthmuller, J. Efficiency of ab initio Total Energy Calculations for Metals and Semiconductors Using a Plane-Wave Basis Set. *Comput. Mater. Sci.* **1996**, *6*, 15−50.

(34) Grimme, S. Semiempirical GGA-Type Density Functional Constructed with a Long-Range Dispersion Correction. *J. Comput. Chem.* **2006**, *27*, 1787−1799.

(35) Henkelman, G.; Jónsson, H. Improved Tangent Estimate In The Nudged Elastic Band Method For Finding Minimum Energy Paths and Saddle Points. *J. Chem. Phys.* **2000**, *113*, 9978−9985.

(36) Henkelman, G.; Uberuaga, B. P.; Jónsson, H. A Climbing Image Nudged Elastic Band Method For Finding Saddle Points And Minimum Energy Paths. *J. Chem. Phys.* **2000**, *113*, 9901−9904.

(37) Dronskowski, R.; Blöchl, P. E. Crystal Orbital Hamilton Populations (COHP): Energy-Resolved Visualization of Chemical Bonding in Solids Based on Density-Functional Calculations. *J. Phys. Chem. A.* **1993**, *97*, 8617−8624.

(38) Deringer, V. L.; Tchougréeff, A. L.; Dronskowski, R. Crystal Orbital Hamilton Population (COHP) Analysis as Projected From Plane-Wave Basis Sets. *J. Phys. Chem. A* **2011**, *115*, 5461−5466.

(39) Maintz, S.; Deringer, V. L.; Tchougréeff, A. L.; Dronskowski, R. Analytic Projection From Plane-Wave And PAW Wavefunctions and Application to Chemical-Bonding Analysis in Solids. *J. Comput. Chem.* **2013**, *34*, 2557−2567.

(40) Maintz, S.; Deringer, V. L.; Tchougréeff, A. L.; Dronskowski, R. LOBSTER: a Tool to Extract Chemical Bonding From Plane-Wave Based DFT. *J. Comput. Chem.* **2016**, *37*, 1030−1035.

(41) Savin, A.; Nesper, R.; Wengert, S.; Fässler, T. F. ELF: The Electron Localization Function. *Angew. Chem., Int. Ed.* **1997**, *36*, 1808−1832.

(42) Nørskov, J. K.; Bligaard, T.; Logadottir, A.; Kitchin, J. R.; Chen, J. G.; Pandelov, S.; Norskov, J. K. Trends in The Exchange Current for Hydrogen Evolution. *J. Electrochem. Soc.* **2005**, *152*, J23−J26.

(43) Haynes, W. M. *CRC Handbook of Chemistry and Physics*; CRC Press, 2014.

(44) Luo, W. J.; Nie, X. W.; Janik, M. J.; Asthagiri, A. Facet Dependence of CO_2 Reduction Paths on Cu Electrodes. *ACS Catal.* **2016**, *6*, 219−229.

(45) Nie, X.; Esopi, M. R.; Janik, M. J.; Asthagiri, A. Selectivity of CO_2 Reduction on Copper Electrodes: The Role of the Kinetics of Elementary Steps. *Angew. Chem., Int. Ed.* **2013**, *52*, 2459−2462.

(46) Nie, X.; Luo, W.; Janik, M. J.; Asthagiri, A. Reaction Mechanisms of CO_2 Electrochemical Reduction on Cu(111) Determined With Density Functional Theory. *J. Catal.* **2014**, *312*, 108−122.

(47) Zhao, J.; Chen, Z. Single Mo Atom Supported on Defective Boron Nitride Monolayer as an Efficient Electrocatalyst For Nitrogen Fixation: a Computational Study. *J. Am. Chem. Soc.* **2017**, *139*, 12480−12487.

(48) Montoya, J. H.; Tsai, C.; Vojvodic, A.; Norskov, J. K. The Challenge of Electrochemical Ammonia Synthesis: a New Perspective on The Role of Nitrogen Scaling Relations. *ChemSusChem* **2015**, *8*, 2180−2186.

(49) Liu, X.; Jiao, Y.; Zheng, Y.; Jaroniec, M.; Qiao, S.-Z. Building up a Picture of The Electrocatalytic Nitrogen Reduction Activity of Transition Metal Single-Atom Catalysts. *J. Am. Chem. Soc.* **2019**, *141*, 9664−9672.

117

Isolated Boron Sites for Electroreduction of Dinitrogen to Ammonia

Xin Liu,[†‡] Yan Jiao,[*,†‡] Yao Zheng,[†‡] Shi-Zhang Qiao[*,†‡]

†School of Chemical Engineering and Advanced Materials, The University of Adelaide, Adelaide, South Australia, 5005, Australia.

‡Centre for Materials in Energy and Catalysis, The University of Adelaide, Adelaide, South Australia, 5005, Australia.

E-mail: * s.qiao@adelaide.edu.au; * yan.jiao@adelaide.edu.au

Supplementary Figures

ΔE = -0.14 eV   ΔE = 0.23 eV   ΔE = 1.09 eV

Mo_2B MoB MoB_2

Mo ⬤   B ⬤   N ⬤   H ⬤
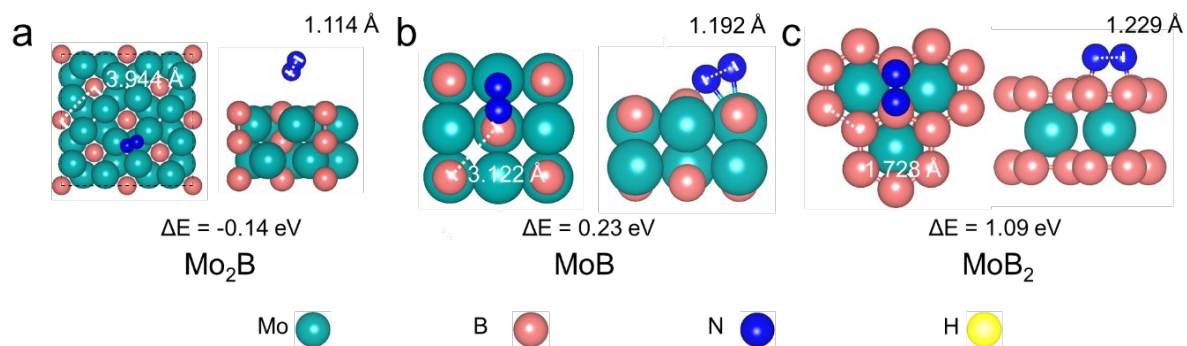
Figure S1 Atomic configurations of N_2 side-on adsorption on (a) Mo_2B, (b) α-MoB and (c) MoB_2.
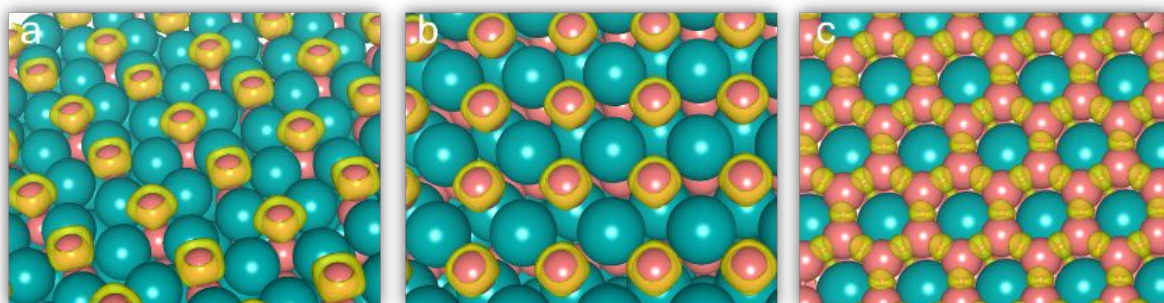
Figure S2. The electron localization function (ELF) of (a) Mo_2B, (b) α-MoB and (c) MoB_2. The value of isosurface is set to 0.75 a.u.
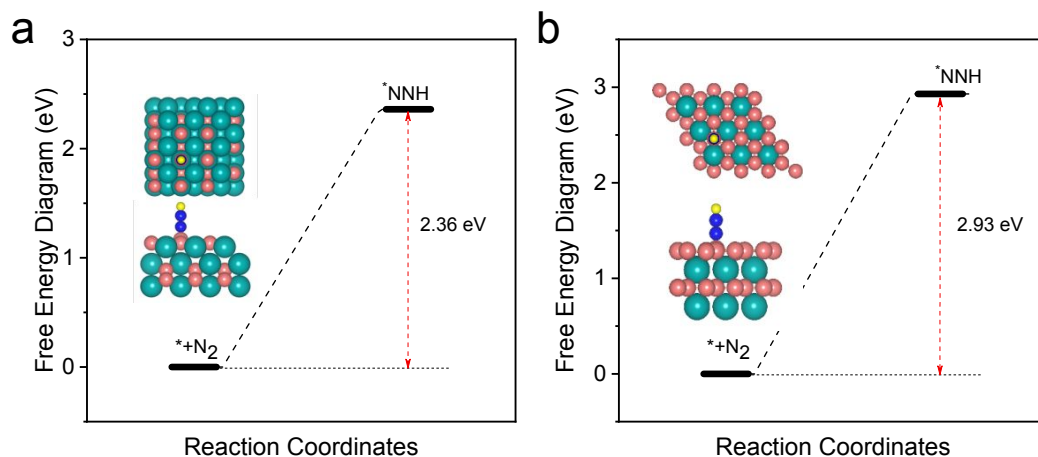
Figure S3. Free energy change of the first protonation step on (a) α-MoB and (b) MoB$_2$ via a distal or alternating pathway at 0V vs standard hydrogen electrode (SHE).
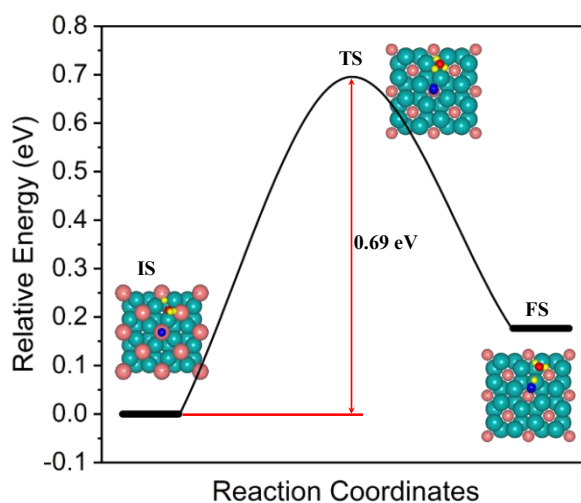
Figure S4. Kinetic barriers for the first protonation step on Mo$_2$B. Insets are the corresponding structures of initial (IS), transition (TS), and final states (FS). Cyan, pink, blue, red and white balls represent the Mo, B, N, O and H atoms, respectively.

S3
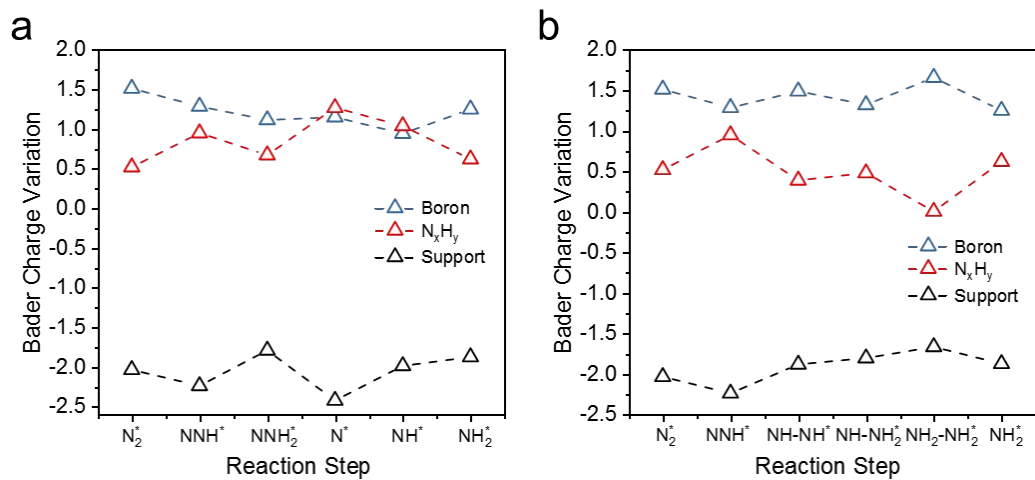
Figure S5. (a) Bader charge variation of three moieties along the (a) distal and (b) alternating pathway. Positive and negative value indicate electron accumulation and loss, respectively.
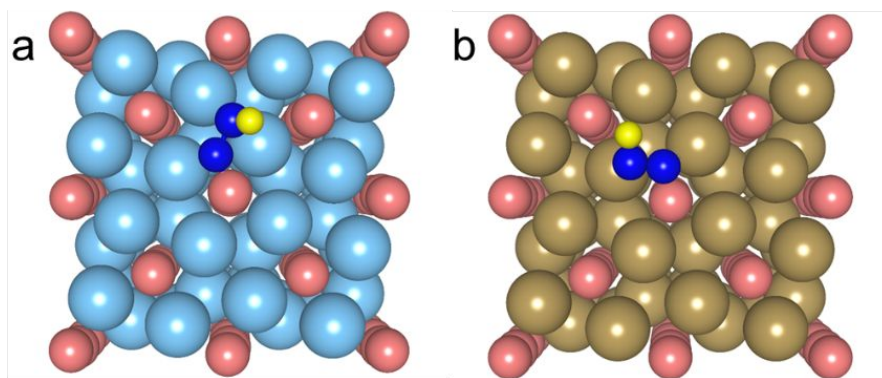
Figure S6. Atomic configuration of *NNH adsorption on (a) Ti_2B and (b) Ta_2B.
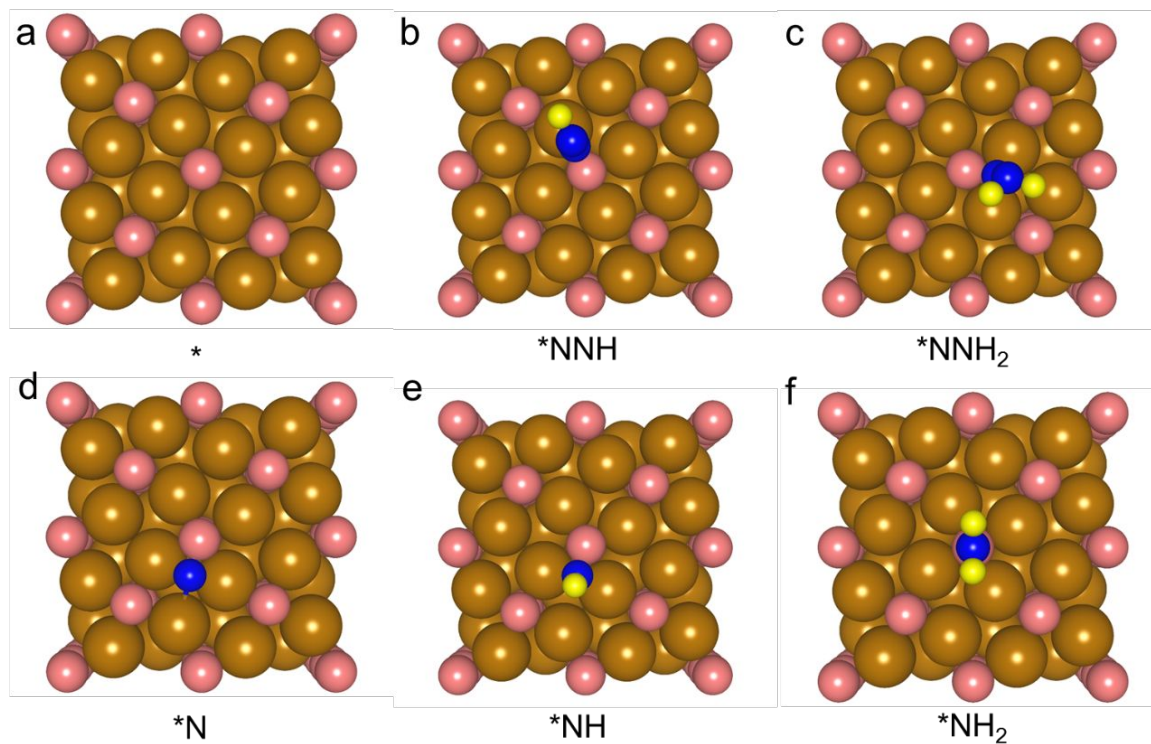
Figure S7. Atomic configurations of reaction intermediates via distal pathway of Fe$_2$B.
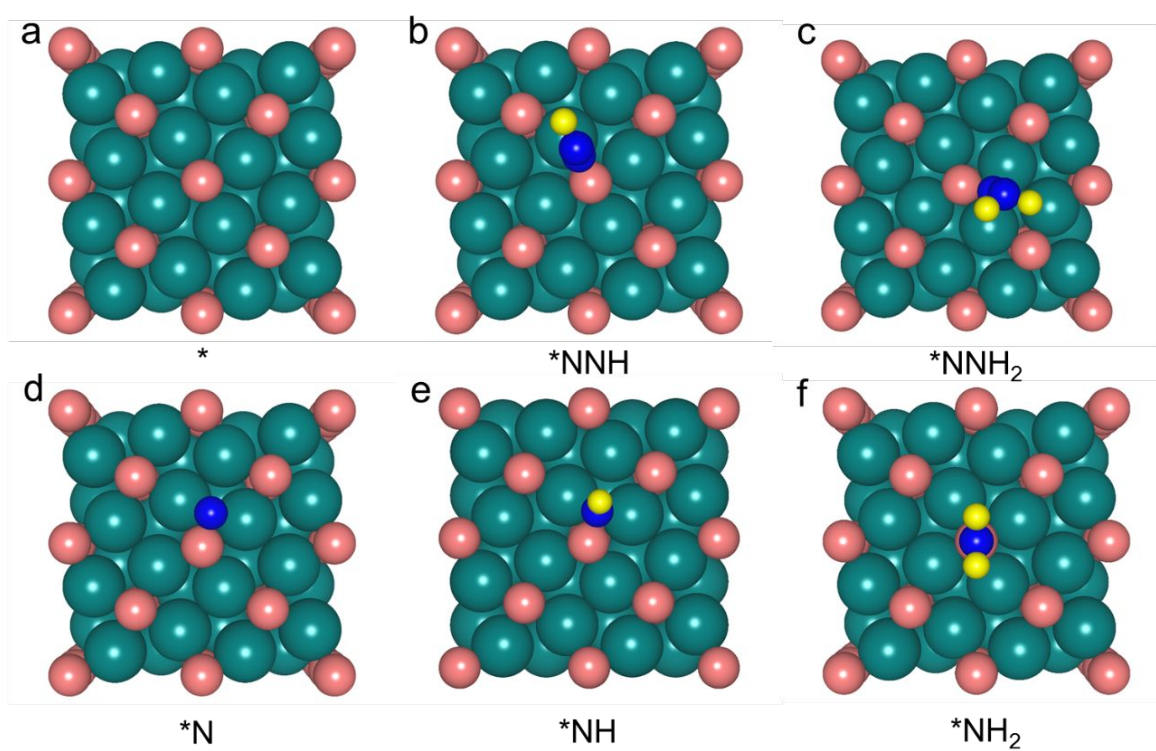
Figure S8. Atomic configurations of reaction intermediates via distal pathway of Co_2B.

a

*

b

*NNH

c

*NNH$_2$

d

*N

e

*NH

f

*NH$_2$
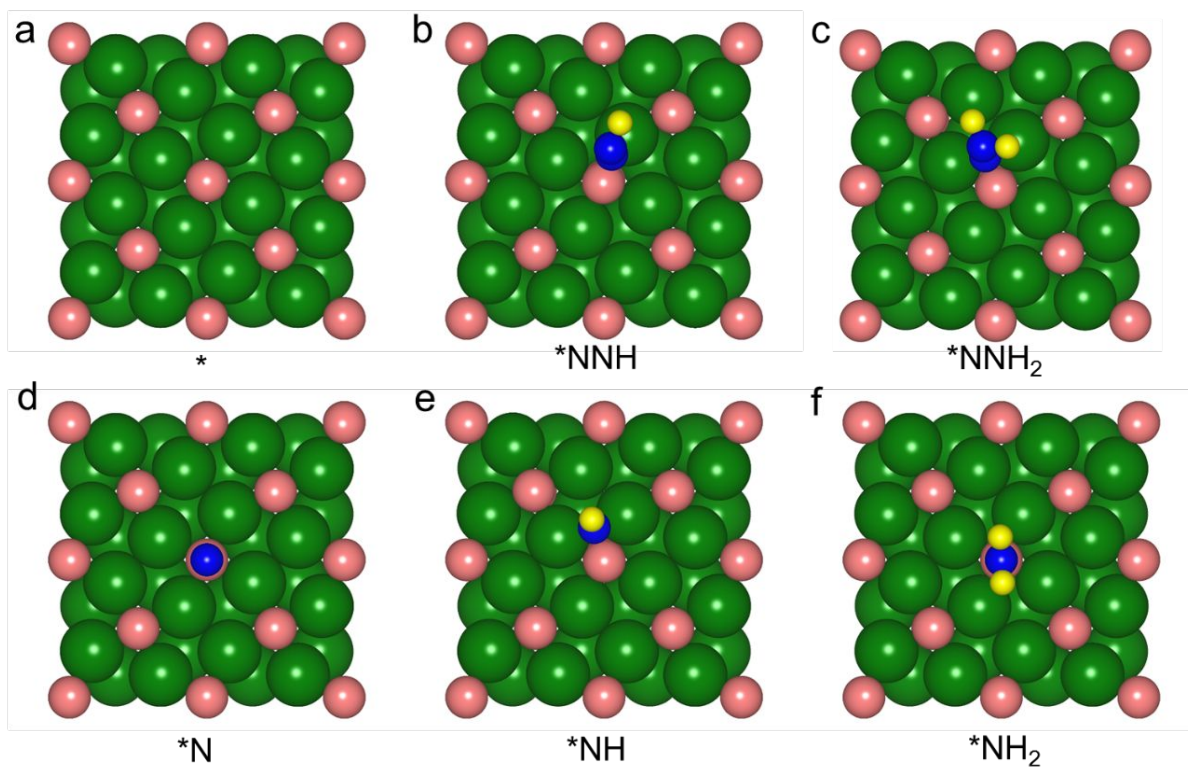
Figure S9. Atomic configurations of reaction intermediates via distal pathway of Cr_2B.
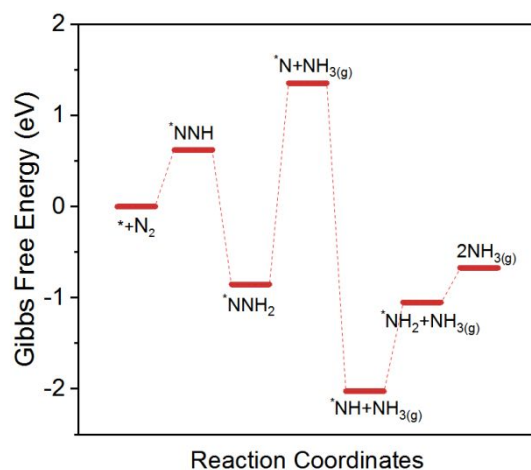
Figure S10. The free energy diagrams of eNRR via a distal pathway on Cr_2B. The third protonation step is the potential determining step with a free energy change of 2.21 eV.

Supplementary Tables

Table S1. Crystallographic information for the studied molybdenum borides.

Phase	Mo₂B	α-MoB	MoB₂
Crystal system	Tetragonal	Tetragonal	Hexagonal
Space group	I4/mcm	I4₁/amd	P6/mmm
a(Å)	5.56	3.13	3.03
b(Å)	5.56	3.13	3.03
c(Å)	4.78	17.05	3.35

Table S2. Crystallographic information for the studied molybdenum borides.

M₂B	Ti₂B	Cr₂B	Mn₂B	Fe₂B	Co₂B	Ni₂B	Ta₂B	W₂B
a(Å)	5.81	5.51	5.07	5.06	4.95	4.97	5.81	5.59
b(Å)	5.81	5.51	5.07	5.06	4.95	4.97	5.81	5.59
c(Å)	4.91	4.28	4.10	4.24	4.27	4.26	4.91	4.80

Table S3. Calculated surface energies, γ_s , for the studied metal borides.

Materials	Mo₂B	α-MoB	MoB₂	Cr₂B	Mn₂B	Fe₂B	Co₂B	Ni₂B	W₂B
Surface Energy (eV/ Å)	0.202	0.180	0.155	0.285	0.346	0.277	0.219	0.138	0.168
Surface Energy (J/m²)	3.242	2.880	2.482	4.559	5.539	4.443	3.501	2.214	2.699

Table S4. The geometric and electronic structure of molybdenum borides.

Electrocatalysts	p_x filling	p_y filling	p_z filling
Mo₂B	0.407	0.406	0.288
α-MoB	0.369	0.362	0.293
MoB₂	0.413	0.415	0.378

S8

125

Chapter 6: Potential-Dependent Mechanisms for Electrocatalytic C-N Bond Formation Towards Urea from Ab Initio Molecular Dynamics

6.1 Introduction and Significance

To reduce carbon footprint while converting renewable energy into commodity chemicals, electrocatalysis shows significant promise for the production of desirable value-added chemicals. However, present aqueous electrocatalysis like $CO_{(2)}$ reduction could only provide limited types of simple hydrocarbons, thus designing new electrochemical system that is capable of synthesizing more complex compounds are of great importance. The absence of detailed reaction mechanisms in these scenario s impedes the rational design of these systems, i.e., with both $CO_{(2)}$ and a nitrogen source as feedstock. To fill in this knowledge gap, this chapter addopted ab initio molecular dynamics (AIMD) with explicit water to explore the mechanisms of C-N bond formation during $CO_{(2)}$ electrolysis to urea on Cu (100) in neutral. Based on the calculations of kinetic barriers, we found that for potentials near -0.75V vs standard hydrogen electrode (SHE), the successive coupling between NH* and CO* directs the formation of urea, which is superior to ammonia production. At potential around -1.5 V vs (SHE), CO_2 reduction was accelerated and suppress urea and ammonia formations. The highlights of this Chapter include:

• AIMD simulations were employed to construct the electrochemical interfaces under different potentials.

• The reduction reaction pathways to ammonia were established along with kinetics for each elementary step.

• A potential-dependent mechanism was proposed to explain the selectivity of urea production compared with $CO_{(2)}$ reduction.

• This study provides insights into the electrochemical environment and a comprehensive understanding of C-N bond formation mechanisms.

6.2 Potential-Dependent Mechanism for electrocatalytic C-N Bond Formation Towards Urea by Operando Computation

This Chapter is included as it appears as a manuscript by **Xin Liu**, Yan Jiao*, Yao Zheng, Shi-Zhang Qiao*, Potential-Dependent Mechanisms for Electrocatalytic C-N Bond Formation Towards Urea from Ab Initio Molecular Dynamics . *To be submitted*.

Statement of Authorship

Title of Paper	Potential-Dependent Mechanism for electrocatalytic C-N Bond Formation Towards Urea by Operando Computation
Publication Status	☐ Published ☐ Accepted for Publication ☐ Submitted for Publication ☑ Unpublished and Unsubmitted work written in manuscript style
Publication Details	Liu, X., Jiao, Y., Zheng, Y., & Qiao, S. Potential-Dependent Mechanisms for electrocatalytic C-N Bond Formation Towards Urea from Ab Initio Molecular Dynamics . *To be submitted.*

Principal Author

Name of Principal Author (Candidate)	Xin Liu		
Contribution to the Paper	Proposed ideas, conduct computations wrote the manuscript.		
Overall percentage (%)	80		
Certification:	This paper reports on original research I conducted during the period of my Higher Degree by Research candidature and is not subject to any obligations or contractual agreements with a third party that would constrain its inclusion in this thesis. I am the primary author of this paper.		
Signature		Date	3/Feb/2021

Co-Author Contributions

By signing the Statement of Authorship, each author certifies that:

    i.   the candidate's stated contribution to the publication is accurate (as detailed above);

    ii.   permission is granted for the candidate in include the publication in the thesis; and

    iii.   the sum of all co-author contributions is equal to 100% less the candidate's stated contribution.

Name of Co-Author	Yan Jiao		
Contribution to the Paper	Discussed the concepts, supervised the research project, and revised the manuscript.		
Signature		Date	3/Feb/2021

Name of Co-Author	Yao Zheng		
Contribution to the Paper	Discussed the concepts, and revised the manuscript.		
Signature		Date	3/Feb/2021

Name of Co-Author	Shi-Zhang Qiao		
Contribution to the Paper	Discussed concepts, supervised the research project, and revised the manuscript.		
Signature		Date	3/Feb/2021

Potential-Dependent Mechanisms for Electrocatalytic C-N Bond Formation Towards Urea from Ab Initio Molecular Dynamics

Xin Liu, [†,‡] Yan Jiao, [†,‡*] Yao Zheng, [†,‡] Shi-Zhang Qiao [†,‡*]

[†] School of Chemical Engineering and Advanced Materials, The University of Adelaide, Adelaide, SA 5005, Australia.

[‡] Centre for Martials in Energy and Catalysis, The University of Adelaide, SA 5005, Australia.

ABSTRACT: To reduce carbon footprint while converting renewable energy into commodity chemicals, designing new co-electrolysis system of $CO_{(2)}$ and nitrogenous feedstocks in aqueous shows significant promise for expanding the product spectrum. However, the absence of detailed reaction mechanisms impedes the rational design of these systems, i.e., with both $CO_{(2)}$ and a nitrogen source as feedstock. To fill in this knowledge gap, we apply ab initio molecular dynamics with explicit water to explore the mechanisms of C-N bond formation during $CO_{(2)}$ electrolysis to urea on Cu (100) in neutral. Based on the calculations of kinetic barriers, we established reaction pathways towards ammonia and urea, and we found a potential-dependent mechanism accounts for the selective production of urea. For potentials near -0.75V vs standard hydrogen electrode (SHE), the successive coupling between NH^* and CO^* directs the formation of urea, which is superior to ammonia production. At potential around -1.5 V vs (SHE), CO_2 reduction was accelerated and suppress urea and ammonia formations. Our work propose the potential-dependent mechanisms for C-N bond formation in aqueous $CO_{(2)}$ electrolysis, which would benefit new electrocatalysis system and catalyst design for more value-added product.

INTRODUCTION

Production of fuels and chemicals from sunlight or other renewable sources via photo/electrocatalytic technologies enable storage of intermittent energy as well as help decarbonization and electrification of the chemical industry.[1-3] As a consequence, it provides a promising routine in breaking our reliance on fossil resources and reducing CO_2 emission.[4]

These processes imply the transform of species such as carbon dioxide, nitrogen, and water, to desirable commodity chemicals like hydrocarbons, ammonia and hydrogen with renewable electricity as the driving force. In this aspect, as the most successful instance to date, electrochemical reduction of $CO_{(2)}$ made tremendous progress in converting carbon dioxide into even multi-carbon (C_{2+}) chemicals in aqueous electrolyte.[5-6] Another more challenging task is N_2 fixation in ambient environment towards ammonia as feedstocks for nitrogenous fertilizer production,[7-8] which is an attractive distributed alternative to Haber–Bosch process especially in rural areas.[2-3] However, limited types of value-added products [9-11] and low selectivity still impair scalable application of $CO_{(2)}$ and N_2 electrolysis.[5]

Here, a new question emerges, whether we could exploit these present electrolysis systems as a platform to produce a broader range of complex compounds than simple carbon species, e.g., introducing heteroatoms, to cover more aspects of modern chemical production supply chain.[12-13] A more recent report by Wang et al reported coupling N_2 and CO_2 in H_2O to synthesize urea,[14] and Jiao et al also introduced NH_3 in carbon monoxide electrolysis to synthesize acetamide.[13] Earlier works from Shibata and Furuya showed this possibility via simultaneous reduction of carbon dioxide and nitrate/nitrite anions to synthesize urea in aqueous eletrolyte.[15-19] Compared with the harsh conditions of high pressure (120-400 atm) and temperature

(150°C-210°C) with ammonia and CO_2 as feedstocks in commercial production of urea, in this scenario, these work achieved a current efficiency of 35% towards urea with CO_2, H_2O and nitrate/nitrite served as the carbon, hydrogen and nitrogen source, respectively, in ambient environments.[15] Similar set-ups were also adopted on urea synthesis on TiO_2.[20-21]

All these reports demonstrate that complex compounds could be synthesized in a rationally designed aqueous $CO_{(2)}$ electrolysis system with other agents involved. Nevertheless, establishing such systems to achieve a desirable rate towards targeted product should be directed with a deep understanding of reaction mechanisms. Compared with abundant and in-depth works on solo electrodialysis mechanisms of $CO_{(2)}$,[22-27] nitrate,[28-34] nitrite[35-37] and nitric oxide,[38-39] related studies on co-electrolysis mechanisms are very limited.[13-14] For example, Shibata et al conjectured that two ammonia-like precursors (NH_2) and one CO-like precursor (CO) directed to the formation of $CO(NH_2)_2$, however, this inference is solely based on a coarse fitting of current efficiency without further evidence.[17-18]

First principles calculations could provide atomic level mechanistic insights for electrocatalytic reactions,[40] recent progress make simulations based on density functional theory (DFT) methods more close to realistic electrochemical environment, i.e., applied potential and solvent effects.[25, 41-45] Early calculations ignored the solvent but corrected afterward to accelerate the computing and enable the screening of marterials.[22] However, this lead to a range of inconsistent results regarding to calculating the kinetic barriers when the solvent effect were taken into account with implicit or hybrid implicit/explicit model with few water molecules.[25, 43, 46] Compared with static methods widely used before, ab initio molecular dynamics (AIMD) simulations are capable of describing the dynamic nature of water at the electrochemical interfaces. Using the model

with explicit water molecules, electrical field effects from solvated ions have been reported to address the mechanisms of electrochemical $CO_{(2)}$ reduction.[47-49] Hence, we conclude that it is promising to adopt AIMD simulations with explicit water molecules to accurately describe the reaction mechanisms.

In this work, we employed AIMD with full solvents to explore the reaction pathways for urea formation from $CO_{(2)}$ electrolysis as a pertinent example to elucidate the mechanisms for crucial C-N bond formation, which is universal for introducing nitrogen atom in $CO_{(2)}$ electrolysis product. With both the solvent effects and applied potential taken into consideration, we constructed reaction networks at two specific potentials. A potential-dependent mechanism was found to account for the selective formation of urea from a two-step coupling between NH^* and CO^* near -0.75V vs SHE in neutral. As applied potential decreased to about -1.5V vs SHE, selectivity towards urea reduced due the enhancement of competing reactions. Predictions based on our model proposed the full atomic reaction mechanism for C-N bond formation during $CO_{(2)}$ electrocatalysis, and agree well with previous key experimental foundlings, which should help further development of $CO_{(2)}$ electrolysis system to synthesize value-added compounds beside simple hydrocarbons.

MODEL AND METHODS

Density Functional Theory Computations. Here, we simulate the water/Cu (100) interface using 32 explicit water molecules on 3×4×3 Cu (100) surface slab. We adopted ab initio molecular dynamics to equilibrate the system at 300K, and based on this well-equilibrated interface, reaction barriers are estimated by thermodynamic integration.[50] Both the Eley-Rideal (electrochemical step) and Langmuir-Hinshelwood (chemical step) reaction mechanisms are considered. Density functional theory (DFT) method was employed for all calculations using the Vienna ab initio Simulation Package (VASP).[51-54] The projector-augmented-wave pseudo-potential was utilized to treat the core electrons, while the Perdew-Burke-Ernzerhof (PBE) exchange-correlation functional of the generalized gradient approximation (GGA) was used for describing the electron interactions.[55] The van der Waals interactions were described using the empirical correction in Grimme's scheme.[56] A more detailed description about the set-up of AIMD simulations and electrode potential could be found in the computational part in supporting information.

pH and the starting reactant. The formation of urea needs both nitrogen and carbon source. In both CO_2 and CO electrocatalysis, $^*CO$ has been recognized as a key intermediate, hence, $^*CO$ is used to simplify the problem. While for the nitrogen source, there are more concerns. First, in aqueous solutions, common nitrogen containing ions like NO_3^-, NO_2^- would are involved in very complicated reaction networks. The concentrations of related ions and pH would further significantly affect the selectivity of reaction pathways and make large spectrum of possible intermediates.[57] Hence, we only focus on the neutral condition. Regardless of the initial form of nitrogen source (NO_3^-, NO_2^-, or NO_x), $^*NO$ plays a central role during the reduction of all these forms, and it has been proved that all of these nitrogen species are further reduced via *NO when the applied potential is relatively negative as the case in current

work.[57] Another point is that NO_3^-, NO_2^-, and NO_x are unlikely to directly surface bounded carbon intermediates. Therefore, it is reasonable to consider the nitrogen pathway starting from $^*NO$, which is sufficient to cover possible intermediates for coupling with *CO.

RESULTS AND DISCUSSION

NO* reduction at ~-0.75 V vs SHE. 32 water molecules in contact with Cu (100) were constructed to model the electrolyte-electrode interface at the potential of zero charge of Cu (100). More details about modeling of the interface could be found in the computational methods parts and Figure S1 in Supporting Information. We found interfaces with various reaction intermediates (Table S1 in supporting information) in this setup corresponded to -0.85~-0.59 V vs standard hydrogen electrode (SHE), if we take the absolute value of SHE from previous experimental reports as reference.[58] This value is in accordance with experimental value (-0.73 V vs SHE) of pzc of Cu(100) under neutral environment by Łukomska and Sobkowski.[59]

Figure. 1 depicts the most relevant reaction pathways starting from $^*NO$, and all involved data were displayed in Table S2 in Supporting Information. $^*NO$ could be reduced to either $^*NOH$ or $^*HNO$, in the meantime it also could dissociate to atomic nitrogen and oxygen.[28] We found that formation of $^*HNO$ is via a chemical step preceded by surface hydrogenation whereas $^*NOH$ is formed through an electrochemical reduction step with water molecule as the proton source, which is similar with the case of CO^* in CO_2/CO reduction at a small overpotential.[47, 60] Dissociation of $^*NO$ (0.77 eV) is kinetically less favorable than $^*HNO$ (0.54 eV) or $^*NOH$ (0.59 eV) pathway.

Figure 1. Schematic diagram of kinetically preferred reaction pathway from $^*NO$ to ammonia (NH_3) at ~ -0.75 vs SHE. Both chemical and electrochemical step are considered, chemical reaction steps are indicated by dashed lines, whereas electrochemical steps are indicated by solid lines. Steps with a barrier larger than 0.75 eV were marked with harsh (‖), and regarded as blocked under this condition. All kinetic barrier values reported in eV, and three different pathways are marked in red, blue and green, while shared steps marked in black.

Figure 2. Snapshots of reactive trajectories for possible rate determining step of three ammonia formation pathways. (a) Protonation of *NH to *NH2; (b) dehydroxylation of *NOH to *N; (c) dehydroxylation of *NH2OH to *NH2. Color code: hydrogen in white, oxygen in red, copper in brown, carbon in black, nitrogen in blue, hydrogen bonding in red dashed lines.

For further reduction steps of *HNO or *NOH, various intermediates were involved in different pathways. We found *NH leading to NH3 forms as an intermediate in both i) and ii) pathways, either via *NOH reduction to *N + H2O (red pathway in Fig.1) or through *HNO reduction to *NHOH (blue pathway in Fig.1). In the meantime, *ONH2, which could be formed via protonation of nitrogen atom of *HNO, lead to the formation of *NH2 via *NH2OH (indicated by green in Fig. 1). Hence, we identified three kinetic favorable pathways for NO* reduction towards ammonia: i) *NO→*NOH→*N →*NH→*NH2→*NH3 (red); ii)*NO→*HNO→*NHOH →*NH→*NH2→*NH3(blue); iii)*NO→*HNO→*ONH2 →*NH2OH →*NH2→*NH3(green).

For pathway i) and ii), shown in Fig.2a, protonation of *NH to *NH2 is the rate determining step with a barrier of 0.66 eV. The dehydroxylation of *NOH displayed in Fig.2b could also be considered as the rate determining steps for pathway i) because of a relatively large ΔG of 0.65 eV. Protonation of *HNO and dehydroxylation of HNOH* via electrochemical mechanism in pathway ii) are facile with barriers of 0.22 eV and 0.46 eV, respectively. While for pathway iii), successive formations of *ONH2 and *NH2OH through an electrochemical step are fast as indicated by ΔG of 0.44 eV and 0.47 eV, thus, the dehydroxylation of *NH2OH to *NH2 has a ΔG of 0.69 eV and is regarded as the rate determining step. Summarizing, although three different pathways possess various intermediates, the only major product is ammonia and kinetic barriers are very close (0.66 eV vs 0.69 eV).

Since Cu (100) surface has been identified as the major exposed facet under similar reduction reaction conditions (i.e. -0.9V vs SHE), we compare our results from ab initio molecular dynamics (AIMD) with experiments copper-based catalysts.[61] The most obvious agreement between previous experiments and our theoretical prediction is ammonia is the major production for NO3-/NO2-/NO reduction reactions instead of N2O or N2 at a large overpotential in neutral.[15, 34, 39] This can be explained by the ultra-low barrier of N* protonation to NH*(0.14 eV), which inhibits its coupling with another N* intermediate or NO* to form N2 and N2O, respectively. Indeed, we could observe this reaction directly in our AIMD simulation, because the low reaction barriers are surmounted within a few picoseconds. We found in pathway iii), *NH2OH is a key intermediate towards the formation of ammonia. These results are in accordance with a recent report that NH2OH was detected as an intermediate during nitrate reduction to ammonia on copper-based materials by online differential electrochemical mass spectrometry.[34] However, we believed that this pathway is sensitive to pH as well as the applied electrode potential. For example, Koper et al found that hydroxylamine is the final product for nitrate reduction on Cu (100) surfaces in alkaline at potentials more negative than 0 V vs reversible hydrogen electrode (RHE) as validated by Fourier transform infrared spectrum (FTIR) and hanging-meniscus rotating disc electrode (HMRDE) measurements.[30] To validate pathway i) and ii), determination of intermediates like *NH or *NHOH via spectroscopy is still challenging, and we believe a combination of electrochemical measurements coupled with online and in situ characterization techniques as well as advanced atomic simulation methods would benefit determination of the complex reaction mechasnisms.[29, 62]

First C-N formation at ~-0.75 V vs SHE on Cu (100). According to previous reports,[23] for single-crystal Cu(100) surface, ethylene start to form -0.4 V vs RHE in neutral, which is more negative than pzc of Cu(100). It also implies that there is a potential window, where dimerization of *CO has not yet begun or at least not dominant whereas reduction of *NO or other forms could proceed.[30] Within this potential window, coupling of C- and N- intermediates could be possible and provide new platform to synthesize more valued added organics as pioneered by Shibata and Furuya's works, which showed simultaneous reduction of carbon dioxide and nitrite or nitrate ions on metal and metallophthalocyanine catalysts could lead to formation of urea.[15-19] A more recent report also achieved Faradaic efficiency towards urea production at -0.4 V vs RHE in neutral, however, detailed information on the pathways of the C-N bond formation during urea formation and its potential dependence is missing.[21] Here, we employed AIMD simulation with full solvents to explore the reaction pathways towards urea since it is the major (if not the only) C-N coupling product during the simultaneous reduction of CO2 and different nitrogen sources and could serve as a representative example for the C-N bond formation process when designing new CO(2) electrolysis systems.[15-17, 20-21] Otherwise, if other C-N product considered, at each step, protonation on oxygen, nitrogen and carbon atom need to be taken into account, and this is beyond the scope of this present work to cover all the branches of reaction networks for this system.
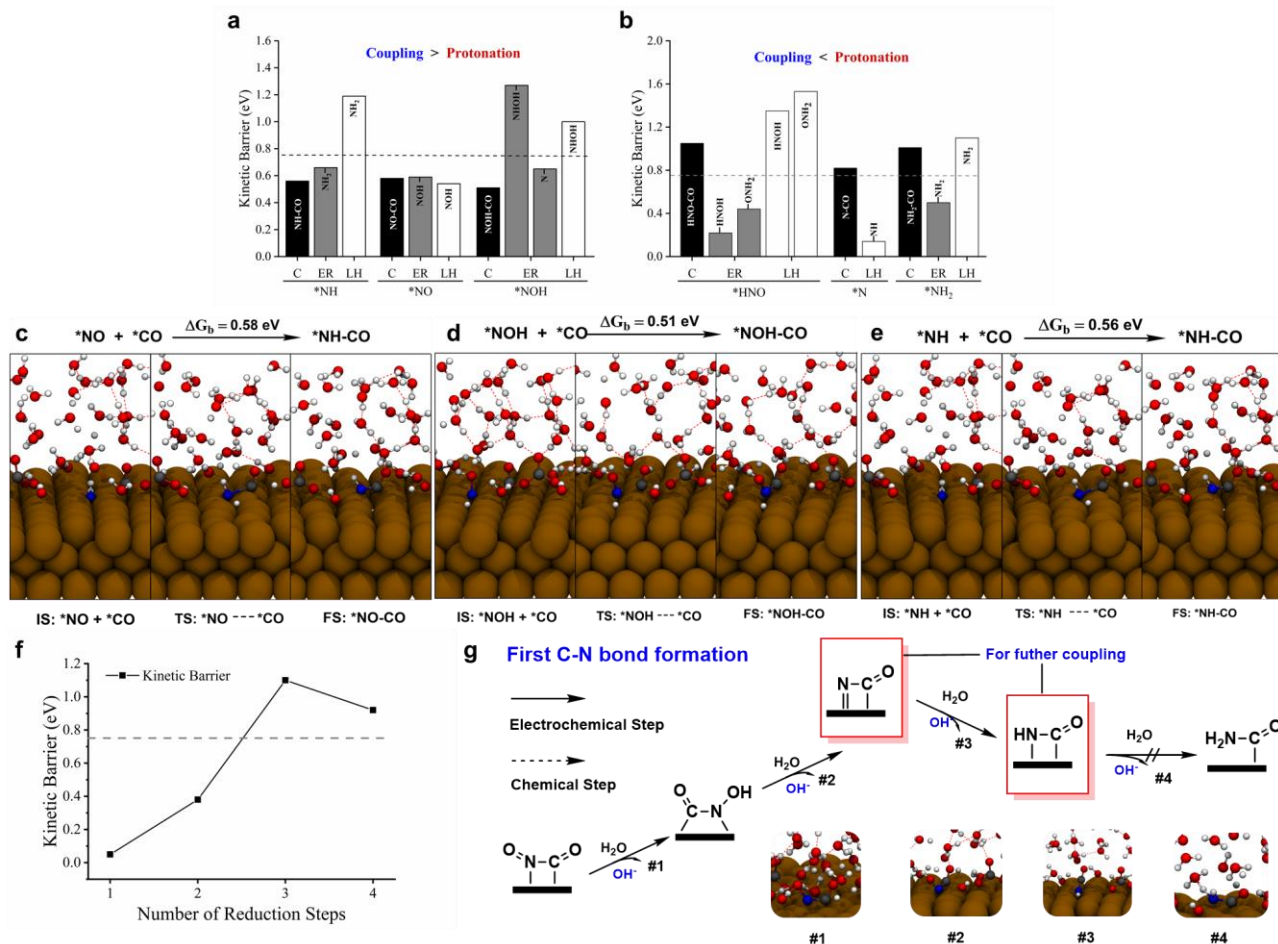
Figure 3. First C-N bond formation. Comparison of the coupling of various nitrogenous intermediates with *CO and protonation for (a) *NO, *NOH and *NH; (b) *HNO, *N and *NH₂. C stands for coupling, ER for Eley-Rideal mechanism, and LH for Langmuir-Hinshelwood mechanism. Snapshots of reactive trajectories for the *CO coupling with (c) *NO, (d) *NOH and (e) *NH. (f) Kinetic barriers of reductions of first C-N intermediates. (g) Schematic diagram for the formation of the first C-N bond as well as subsequent protonation.

We then need to identify the coupling carbonaceous and nitrogenous intermediates. For carbonaceous (C-) intermediates, and *CO is a key intermediate for CO_2/CO reduction and also abundant on Cu (100) surface at this potential.[63] What's more, previous DFT calculations and experiments both proved that protonation of *CO to *CHO, as the key step towards production of methane, is sluggish under such potential, thus we only consider CO* as the C- coupling reactant.[22-23, 47, 49] For nitrogenous (N-) intermediates, a number of intermediates present in NH₃ pathway are considered as seeds for C-N formation. As the case of *CO, the protonation of N- intermediates need to be taken into account. In Figure 3a and 3b, we compared the protonation of N-intermediates via ER or LH mechanism to these coupling with *CO. For, *NO, *NOH and *NH, the coupling step is more facile than protonation (Fig.3a), whereas the coupling is regarded as kinetically blocked at room temperature ($\Delta G_b > 0.75$ eV, corresponds to fast kinetics with TOF of 1 s⁻¹ based on transition state theory) and protonation is more facile for *HNO, *N and *NH₂ (Fig.3b). A special attention was paid to for *CO and *NH₂ pathway, we found the barrier is 1.01 eV (as shown in Table S3), which could be regarded as blocked at 300K. This finding disagrees with previous guesses from experiments.[16, 20-21] The snapshots of reactive trajectories for facile coupling steps are displayed in Figure 3c~3e, and the calculated reaction barriers are 0.58, 0.51, and 0.56 eV, respectively. Clearly, the water

molecules at the electrode-electrolyte interface interact with reaction intermediates via hydrogen bonding, and could affect the kinetics of reactions. These also show the necessity of involving explicit solvent in modeling the heterogeneous electrochemical reaction.

With possible C-N intermediates obtained in the previous coupling step (*CO-NO, *CO-NOH, and *CO-NH), the reductions of these intermediates are considered. *CO-NO is taken as the starting point, and barriers of the following reductions are shown in Figure 3f. We consider CO-NOH pathway: *CO coupling with *NO to form *CO-NO and subsequent reduction to *CO-NOH or *CO directly coupling with *NOH; and CO-NH pathway: *CO coupling with *NH. Atomic configurations of key intermediates for both pathways are illustrated in Figure 3g. For CO-NOH pathway, *CO-NO* is easy to be protonated via ER mechanism (0.05 eV) to form NOH-CO, and this is similar with protonation of *CO-CO dimer during the CO/CO₂ reduction on copper.[43, 47] Besides, *NOH-CO could also be formed via the coupling between *NOH and *CO with a ΔG_b of 0.51 eV. Dehydroxylation of *NOH-CO to *N-CO is fast (0.38 eV), but we found that further reduction through *N-CO to *CO-NH is kinetically blocked (1.10 eV for LH). Hence, *CO-N is a dead-end for CO-NOH pathway at this potential. We then focus on CO-NH pathway. Considering the protonation of *N-CO is hard, we believe direct coupling between *NH and *CO is supposed
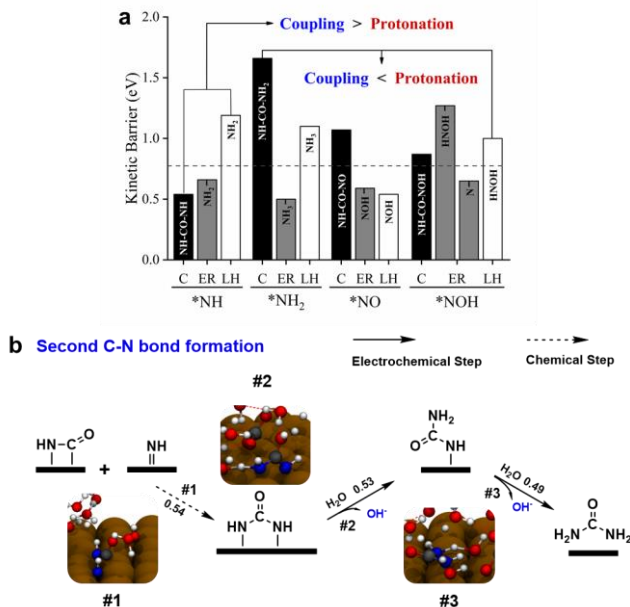
Figure 4. Second C-N bond formation. (a) Comparison of the coupling of various nitrogenous intermediates with *CO-NH and protonation. (b) Schematic diagram for the formation of second C-N bond as well as subsequent protonation and snapshots of reactive trajectories.

to be the major source of *NH-CO intermediate. Interestingly, we found further reduction of *NH-CO also hard and need to overcome a barrier of 0.92 eV via ER or 1.46 eV via LH mechanism. Summarizing, at this stage, we could conclude that *CO-N and *CO-NH are possible for further coupling to form another C-N bond compared with protonation as showed in red box in Figure 4g.

Second C-N bond formation at ~-0.75 V vs SHE on Cu (100). Further couplings of *NO, *NOH, *NH, and *NH$_2$ with *N-CO and *NH-CO to form the second C-N bond are explored in this section. We excluded *N and *HNO because the relatively low barrier of protonation, and in this situation, couplings with *CO are hard to be favored as the case for first C-N bond formation. The results in Figure 4a indicated that *NH is the only intermediate that could be coupled with *CO-NH to form the second C-N bond with a barrier of 0.54 eV, which is smaller than *NH protonation (0.66 eV). While for *NO, *NOH, and *NH$_2$, the coupling barriers are relatively large (>0.75 eV) and less facile than protonation. As shown in Figure S2, we found that for all intermediates, coupling with *N-CO need to overcome a kinetic barrier at least 0.98 eV, which is not facile at 300K. Besides, for all of these intermediates (*NO, *NOH, *NH, and *NH$_2$), protonation barrier is significantly smaller than that of coupling with *N-CO, therefore, we believed *N-CO is not reactive for protonation at this potential and pH.

Protonation of *NH-CO-NH is predicted fast with a barrier of 0.53 eV and 0.49 eV to form (NH$_2$)$_2$CO via ER mechanism as displayed in Figure 4b. Summarizing, we found at -0.75 V vs SHE or in other terms, near the potential of zero charge of Cu (100) surface, the kinetically favorable pathway from *NH and *CO to urea is *CO + 2*NH →*NH-CO + *NH → *CO(NH)$_2$ → *NH$_2$-CO-NH → (NH$_2$)$_2$CO. Each step of C-N bond formation has a smaller kinetic barrier than protonation of *NH* to *NH$_2$ (0.66 eV), and thus selectivity to urea formation is superior or at least comparable to ammonia formation under such potential. This prediction is in accordance with experimental reports by

Shibata et al that current efficiency for urea and ammonia is 37% and 35% at -0.75 vs SHE in neutral.[17] Hence, till now, we are capable of establishing the whole reaction pathway to urea and more discussion about the selectivity would be covered in the last section. For the present reaction network, we could identify *CO-NH, *CO(NH)$_2$ as the key intermediates towards to urea and to be validated by future experiments. However, it is hard to tell which step is the rate destemming step of pathway towards urea since the comparable values of kinetic barriers for possible steps (0.54 eV~0.69 eV) and the uncertainties of computational methods are taken into account.[49] For this reason, we could infer that at this potential, the nitrogen reduction and urea formation have similar kinetic barriers. This finding is in accordance with previous experimental reports that at less negative potential in neutral, both ammonia and urea have considerable production.[15, 21] However, more convincing experiments along with advanced characterization techniques on well-defined system should be conducted to further elucidate the detailed reaction mechanism.[23, 27, 30]

Case at the potential near -1.5V vs SHE. As more negative potential applied, the selectivity towards urea decreases as indicated in Figure 5, the experimental data are reproduced from Shibata et al.[17] To elucidate the origins of the selectivity drop, we first explored that *NO reduction pathway at this potential, and found that ammonia is the only dominant product. The most kinetically favorable pathways as shown in Figure 5 is *NO → *NOH→*N→*NH→*NH$_2$→*NH$_3$, and detailed results to construct the reaction network could be found in Table S8 of Supporting Information. Protonation of *NH to *NH$_2$ is still recognized as the rate determining step with a barrier of 0.53 eV (Fig. 5b). What's more, all steps prefer ER mechanism and the barriers for almost every step are reduced compared with the situation at -0.75 V vs SHE (except for protonation of *N to *NH, whose barrier value is too small and actually within the error band). This founding is in accordance with previous reports that larger overpotential would reduce the barrier of protonation via electrochemical pathways.[25, 60, 64]

Besides *NO reduction, the product spectrum of CO(NH$_2$)$_2$, CO, HCOOH and H$_2$ indicated that at this potential, CO$_2$ reduction and hydrogen evolution both proceed. As shown in Figure 6, the current efficiency of HCOOH and CO start entering a plateau, and this implied that from -0.75 V to -1.5 V vs SHE, CO$_2$ reduction is accelerated but no deep product detected. Also for this range, hydrogen evolves at a relatively stable rate. For *NO reduction (from nitrite reduction at more positive potential), it actually slows down. The most possible reason is that as the potential decreased, hydrogen competes with N- intermediates, since the Volmer step is dramatically speed up. As a consequence, the coverage of adsorbed hydrogen on the surface increased.[17, 49] Since the coverage of *NH or other N- intermediates decreased, production of ammonia and urea with *NH as the key reactant slow down. As the more negative potential applied and barriers of hydrogen evolution further decreased, and the surface is mostly covered by adsorbed hydrogen. H$_{2(g)}$ would be eventually the only final product as the case for solo CO$_2$ reduction.[63] We separated the whole potential range from -0.75 V to -1.5V vs SHE in Figure 6. For nitrogen region, the total current efficiency of ammonia and urea is larger than 50%. As applied potential dropped into the carbon region and further decreases, nitrogen pathways are dramatically restrained. And

the major product is CO and HCOOH for this range. In the hydrogen region, a high coverage of *H lead to the production of molecular hydrogen as the major product.
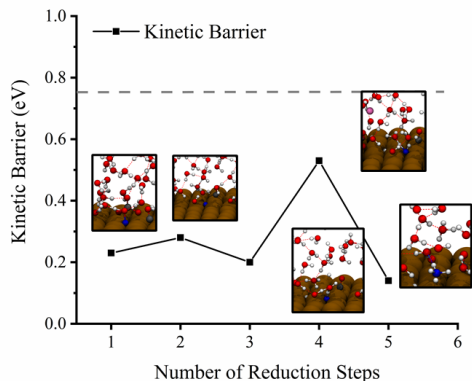
Figure 5. Kinetic barriers of reductions of *NO towards ammonia at ~-1.5V vs SHE.
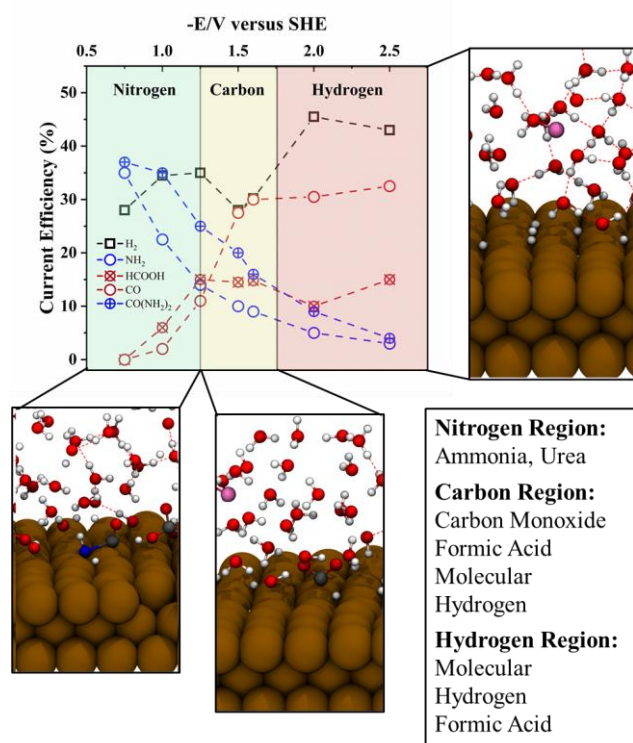
Figure 6. Schematic diagrams for potential-dependent mechanism for selective urea formation.

CONCOLUSION

We have identified the relevant reaction pathways for *NO reduction as well as C-N coupling towards ammonia and urea on Cu (100) surface at pH 7 based on ab initio molecule dynamics simulation. We elucidated the role of NH^* as the key surface intermediate that directs the urea pathway after exploring various combinations of coupling intermediates. Our model demonstrates potential-dependent mechanism to explain experimentally observed activity/selectivity for simultaneous reduction of $CO_{(2)}$ and nitrogen source (nitrite et al) as an example and on Cu(100) at varying potentials. These insights enable us to design new electrochemical systems as well as synthesize more

types of valued added chemicals to meet the future energy and environmental challenge.

ASSOCIATED CONTENT

Supporting Information. This material is available free of charge via the Internet at http://pubs.acs.org. Detailed computational setups and validation of models. Kinetic barriers and parameters for all reaction steps. Workfunctions for selected electrochemical interfaces.

AUTHOR INFORMATION

Corresponding Author

*s.qiao@adelaide.edu.au;
*yan.jiao@adelaide.edu.au;

ACKNOWLEDGMENT

REFERENCES

1. Montoya, J. H.; Seitz, L. C.; Chakthranont, P.; Vojvodic, A.; Jaramillo, T. F.; Nørskov, J. K., Materials for solar fuels and chemicals. *Nature Materials* **2017,** *16* (1), 70-81.
2. Schiffer, Z. J.; Manthiram, K., Electrification and Decarbonization of the Chemical Industry. *Joule* **2017,** *1* (1), 10-14.
3. Comer, B. M.; Fuentes, P.; Dimkpa, C. O.; Liu, Y.-H.; Fernandez, C. A.; Arora, P.; Realff, M.; Singh, U.; Hatzell, M. C.; Medford, A. J., Prospects and Challenges for Solar Fertilizers. *Joule* **2019,** *3* (7), 1578-1605.
4. Kätelhön, A.; Meys, R.; Deutz, S.; Suh, S.; Bardow, A., Climate change mitigation potential of carbon capture and utilization in the chemical industry. *Proceedings of the National Academy of Sciences* **2019,** *116* (23), 11187-11194.
5. Nitopi, S.; Bertheussen, E.; Scott, S. B.; Liu, X.; Engstfeld, A. K.; Horch, S.; Seger, B.; Stephens, I. E.; Chan, K.; Hahn, C. J. C. r., Progress and perspectives of electrochemical CO_2 reduction on copper in aqueous electrolyte. **2019,** *119* (12), 7610-7672.
6. Gao, D.; Arán-Ais, R. M.; Jeon, H. S.; Roldan Cuenya, B., Rational catalyst and electrolyte design for CO_2 electroreduction towards multicarbon products. *Nature Catalysis* **2019,** *2* (3), 198-210.
7. Foster, S. L.; Bakovic, S. I. P.; Duda, R. D.; Maheshwari, S.; Milton, R. D.; Minteer, S. D.; Janik, M. J.; Renner, J. N.; Greenlee, L. F., Catalysts for nitrogen reduction to ammonia. *Nature Catalysis* **2018,** *1* (7), 490-500.
8. Suryanto, B. H. R.; Du, H.-L.; Wang, D.; Chen, J.; Simonov, A. N.; MacFarlane, D. R., Challenges and prospects in the catalysis of electroreduction of nitrogen to ammonia. *Nature Catalysis* **2019,** *2* (4), 290-296.
9. Li, C. W.; Ciston, J.; Kanan, M. W., Electroreduction of carbon monoxide to liquid fuel on oxide-derived nanocrystalline copper. *Nature* **2014,** *508* (7497), 504-507.
10. Zhuang, T.-T.; Pang, Y.; Liang, Z.-Q.; Wang, Z.; Li, Y.; Tan, C.-S.; Li, J.; Dinh, C. T.; De Luna, P.; Hsieh, P.-L.; Burdyny, T.; Li, H.-H.; Liu, M.; Wang, Y.; Li, F.; Proppe, A.; Johnston, A.; Nam, D.-H.; Wu, Z.-Y.; Zheng, Y.-R.; Ip, A. H.; Tan, H.; Chen, L.-J.; Yu, S.-H.; Kelley, S. O.; Sinton, D.; Sargent, E. H., Copper nanocavities confine intermediates for efficient electrosynthesis of C3 alcohol fuels from carbon monoxide. *Nature Catalysis* **2018,** *1* (12), 946-951.
11. Pang, Y.; Li, J.; Wang, Z.; Tan, C.-S.; Hsieh, P.-L.; Zhuang, T.-T.; Liang, Z.-Q.; Zou, C.; Wang, X.; De Luna, P.; Edwards, J. P.; Xu, Y.; Li, F.; Dinh, C.-T.; Zhong, M.; Lou, Y.; Wu, D.; Chen, L.-J.; Sargent, E. H.; Sinton, D., Efficient electrocatalytic conversion of carbon

monoxide to propanol using fragmented copper. *Nature Catalysis* **2019,** *2* (3), 251-258.

12. Jouny, M.; Hutchings, G. S.; Jiao, F., Carbon monoxide electroreduction as an emerging platform for carbon utilization. *Nature Catalysis* **2019,** *2* (12), 1062-1070.

13. Jouny, M.; Lv, J. J.; Cheng, T.; Ko, B. H.; Zhu, J. J.; Goddard, W. A.; Jiao, F., Formation of carbon-nitrogen bonds in carbon monoxide electrolysis. *Nat Chem* **2019,** *11* (9), 846-851.

14. Chen, C.; Zhu, X.; Wen, X.; Zhou, Y.; Zhou, L.; Li, H.; Tao, L.; Li, Q.; Du, S.; Liu, T.; Yan, D.; Xie, C.; Zou, Y.; Wang, Y.; Chen, R.; Huo, J.; Li, Y.; Cheng, J.; Su, H.; Zhao, X.; Cheng, W.; Liu, Q.; Lin, H.; Luo, J.; Chen, J.; Dong, M.; Cheng, K.; Li, C.; Wang, S., Coupling N₂ and CO₂ in H₂O to synthesize urea under ambient conditions. *Nature Chemistry* **2020**.

15. Shibata, M.; Yoshida, K.; Furuya, N., Electrochemical synthesis of urea on reduction of carbon dioxide with nitrate and nitrite ions using Cu-loaded gas-diffusion electrode. *Journal of Electroanalytical Chemistry* **1995,** *387* (1), 143-145.

16. Shibata, M.; Yoshida, K.; Furuya, N., Electrochemical Synthesis of Urea at Gas‐Diffusion Electrodes III. Simultaneous Reduction of Carbon Dioxide and Nitrite Ions with Various Metal Catalysts. *Journal of the Electrochemical Society* **1998,** *145* (2), 595-600.

17. Shibata, M.; Yoshida, K.; Furuya, N., Electrochemical synthesis of urea at gas-diffusion electrodes: Part II. Simultaneous reduction of carbon dioxide and nitrite ions at Cu, Ag and Au catalysts. *Journal of Electroanalytical Chemistry* **1998,** *442* (1), 67-72.

18. Shibata, M.; Furuya, N., Electrochemical synthesis of urea at gas-diffusion electrodes Part VI. Simultaneous reduction of carbon dioxide and nitrite ions with various metallophthalocyanine catalysts. *Journal of Electroanalytical Chemistry* **2001,** *507* (1-2), 177-184.

19. Shibata, M.; Furuya, N., Simultaneous reduction of carbon dioxide and nitrate ions at gas-diffusion electrodes with various metallophthalocyanine catalysts. *Electrochimica Acta* **2003,** *48* (25-26), 3953-3958.

20. Saravanakumar, D.; Song, J.; Lee, S.; Hur, N. H.; Shin, W., Electrocatalytic Conversion of Carbon Dioxide and Nitrate Ions to Urea by a Titania-Nafion Composite Electrode. *ChemSusChem* **2017,** *10* (20), 3999-4003.

21. Cao, N.; Quan, Y.; Guan, A.; Yang, C.; Ji, Y.; Zhang, L.; Zheng, G., Oxygen vacancies enhanced cooperative electrocatalytic reduction of carbon dioxide and nitrite ions to urea. *Journal of Colloid and Interface Science* **2020,** *577*, 109-114.

22. Peterson, A. A.; Abild-Pedersen, F.; Studt, F.; Rossmeisl, J.; Nørskov, J. K., How copper catalyzes the electroreduction of carbon dioxide into hydrocarbon fuels. *Energy & Environmental Science* **2010,** *3* (9), 1311.

23. Schouten, K. J. P.; Qin, Z.; Pérez Gallent, E.; Koper, M. T. M., Two Pathways for the Formation of Ethylene in CO Reduction on Single-Crystal Copper Electrodes. *Journal of the American Chemical Society* **2012,** *134* (24), 9864-9867.

24. Schouten, K. J. P.; Pérez Gallent, E.; Koper, M. T. M., The influence of pH on the reduction of CO and CO₂ to hydrocarbons on copper electrodes. *Journal of Electroanalytical Chemistry* **2014,** *716*, 53-57.

25. Goodpaster, J. D.; Bell, A. T.; Head-Gordon, M., Identification of Possible Pathways for C-C Bond Formation during Electrochemical Reduction of CO₂: New Theoretical Insights from an Improved Electrochemical Model. *The Journal of Physical Chemistry Letters* **2016,** *7* (8), 1471-1477.

26. Heyes, J.; Dunwell, M.; Xu, B., CO2 Reduction on Cu at Low Overpotentials with Surface-Enhanced in Situ Spectroscopy. *The Journal of Physical Chemistry C* **2016,** *120* (31), 17334-17341.

27. Pérez-Gallent, E.; Marcandalli, G.; Figueiredo, M. C.; Calle-Vallejo, F.; Koper, M. T. M., Structure- and Potential-Dependent Cation Effects on CO Reduction at Copper Single-Crystal Electrodes. *Journal of the American Chemical Society* **2017,** *139* (45), 16412-16419.

28. Shin, H.; Jung, S.; Bae, S.; Lee, W.; Kim, H., Nitrite Reduction Mechanism on a Pd Surface. *Environmental Science & Technology* **2014,** *48* (21), 12768-12774.

29. Butcher, D. P.; Gewirth, A. A., Nitrate reduction pathways on Cu single crystal surfaces: Effect of oxide and Cl⁻. *Nano Energy* **2016,** *29*, 457-465.

30. Pérez-Gallent, E.; Figueiredo, M. C.; Katsounaros, I.; Koper, M. T. M., Electrocatalytic reduction of Nitrate on Copper single crystals in acidic and alkaline solutions. *Electrochimica Acta* **2017,** *227*, 77-84.

31. Liu, J.-X.; Richards, D.; Singh, N.; Goldsmith, B. R., Activity and Selectivity Trends in Electrocatalytic Nitrate Reduction on Transition Metals. *ACS Catalysis* **2019,** *9* (8), 7052-7064.

32. Chen, G.-F.; Yuan, Y.; Jiang, H.; Ren, S.-Y.; Ding, L.-X.; Ma, L.; Wu, T.; Lu, J.; Wang, H., Electrochemical reduction of nitrate to ammonia via direct eight-electron transfer using a copper–molecular solid catalyst. *Nature Energy* **2020**.

33. Wang, Y.; Xu, A.; Wang, Z.; Huang, L.; Li, J.; Li, F.; Wicks, J.; Luo, M.; Nam, D.-H.; Tan, C.-S.; Ding, Y.; Wu, J.; Lum, Y.; Dinh, C.-T.; Sinton, D.; Zheng, G.; Sargent, E. H., Enhanced Nitrate-to-Ammonia Activity on Copper–Nickel Alloys via Tuning of Intermediate Adsorption. *Journal of the American Chemical Society* **2020,** *142* (12), 5702-5708.

34. Wang, Y.; Zhou, W.; Jia, R.; Yu, Y.; Zhang, B., Unveiling the Activity Origin of a Copper-based Electrocatalyst for Selective Nitrate Reduction to Ammonia. *Angewandte Chemie International Edition* **2020,** *59* (13), 5350-5354.

35. Duca, M.; Cucarella, M. O.; Rodriguez, P.; Koper, M. T., Direct reduction of nitrite to N₂ on a Pt (100) electrode in alkaline media. *Journal of the American Chemical Society* **2010,** *132* (51), 18042-18044.

36. Duca, M.; Figueiredo, M. C.; Climent, V.; Rodriguez, P.; Feliu, J. M.; Koper, M. T., Selective catalytic reduction at quasi-perfect Pt (100) domains: a universal low-temperature pathway from nitrite to N2. *Journal of the American Chemical Society* **2011,** *133* (28), 10928-10939.

37. Bykov, D.; Neese, F., Six-Electron Reduction of Nitrite to Ammonia by Cytochrome c Nitrite Reductase: Insights from Density Functional Theory Studies. *Inorg Chem* **2015,** *54* (19), 9303-9316.

38. Chun, H.-J.; Apaja, V.; Clayborne, A.; Honkala, K.; Greeley, J., Atomistic Insights into Nitrogen-Cycle Electrochemistry: A Combined DFT and Kinetic Monte Carlo Analysis of NO Electrochemical Reduction on Pt(100). *ACS Catalysis* **2017,** *7* (6), 3869-3882.

39. Long, J.; Chen, S.; Zhang, Y.; Guo, C.; Fu, X.; Deng, D.; Xiao, J., Direct Electrochemical Ammonia Synthesis from Nitric Oxide. *Angew Chem Int Ed Engl* **2020,** *59* (24), 9711-9718.

40. Nørskov, J. K.; Rossmeisl, J.; Logadottir, A.; Lindqvist, L.; Kitchin, J. R.; Bligaard, T.; Jónsson, H., Origin of the Overpotential for Oxygen Reduction at a Fuel-Cell Cathode. *The Journal of Physical Chemistry B* **2004,** *108* (46), 17886-17892.

41. Xiao, H.; Cheng, T.; Goddard, W. A.; Sundararaman, R., Mechanistic Explanation of the pH Dependence and Onset Potentials for Hydrocarbon Products from Electrochemical Reduction of CO on Cu (111). *Journal of the American Chemical Society* **2016,** *138* (2), 483-486.

42. Skulason, E.; Tripkovic, V.; Bjorketun, M. E.; Gudmundsdottir, S.; Karlberg, G.; Rossmeisl, J.; Bligaard, T.; Jonsson, H.; Norskov, J. K., Modeling the Electrochemical Hydrogen Oxidation and Evolution Reactions on the Basis of Density Functional Theory Calculations. *Journal of Physical Chemistry C* **2010,** *114* (42), 18182-18197.

43. Montoya, J. H.; Shi, C.; Chan, K.; Nørskov, J. K., Theoretical Insights into a CO Dimerization Mechanism in CO₂ Electroreduction. *The Journal of Physical Chemistry Letters* **2015,** *6* (11), 2032-2037.

44. Resasco, J.; Chen, L. D.; Clark, E.; Tsai, C.; Hahn, C.; Jaramillo, T. F.; Chan, K.; Bell, A. T., Promoter Effects of Alkali Metal Cations on the Electrochemical Reduction of Carbon Dioxide. *Journal of the American Chemical Society* **2017,** *139* (32), 11277-11287.

45. Bagger, A.; Arnarson, L.; Hansen, M. H.; Spohr, E.; Rossmeisl, J., Electrochemical CO Reduction: A Property of the Electrochemical Interface. *Journal of the American Chemical Society* **2019,** *141* (4), 1506-1514.

46. Nie, X.; Esopi, M. R.; Janik, M. J.; Asthagiri, A., Selectivity of CO₂ Reduction on Copper Electrodes: The Role of the Kinetics of Elementary Steps. *Angewandte Chemie International Edition* **2013,** *52* (9), 2459-2462.

47. Cheng, T.; Xiao, H.; Goddard, W. A., Full atomistic reaction mechanism with kinetics for CO reduction on Cu(100) from ab initio molecular dynamics free-energy calculations at 298 K. *Proceedings of the National Academy of Sciences of the United States of America* **2017,** *114* (8), 1795-1800.

48. Cheng, T.; Xiao, H.; Goddard, W. A., Free-Energy Barriers and Reaction Mechanisms for the Electrochemical Reduction of CO on the Cu(100) Surface, Including Multiple Layers of Explicit Solvent at pH 0. *Journal of Physical Chemistry Letters* **2015,** *6* (23), 4767-4773.

49. Cheng, T.; Xiao, H.; Goddard, W. A., Reaction Mechanisms for the Electrochemical Reduction of CO_2 to CO and Formate on the Cu(100) Surface at 298 K from Quantum Mechanics Free Energy Calculations with Explicit Water. *Journal of the American Chemical Society* **2016,** *138* (42), 13802-13805.

50. Carter, E. A.; Ciccotti, G.; Hynes, J. T.; Kapral, R., Constrained reaction coordinate dynamics for the simulation of rare events. *Chemical Physics Letters* **1989,** *156* (5), 472-477.

51. Kresse, G.; Hafner, J., Ab initio molecular dynamics for liquid metals. *Physical Review B* **1993,** *47* (1), 558-561.

52. Kresse, G.; Hafner, J., Ab initio molecular-dynamics simulation of the liquid-metal--amorphous-semiconductor transition in germanium. *Physical Review B* **1994,** *49* (20), 14251-14269.

53. Kresse, G.; Furthmüller, J., Efficient iterative schemes for ab initio total-energy calculations using a plane-wave basis set. *Physical Review B* **1996,** *54* (16), 11169-11186.

54. Kresse, G.; Furthmüller, J., Efficiency of ab-initio total energy calculations for metals and semiconductors using a plane-wave basis set. *Computational Materials Science* **1996,** *6* (1), 15-50.

55. Perdew, J. P.; Burke, K.; Ernzerhof, M., Generalized Gradient Approximation Made Simple. *Physical Review Letters* **1996,** *77* (18), 3865-3868.

56. Grimme, S.; Ehrlich, S.; Goerigk, L., Effect of the damping function in dispersion corrected density functional theory. **2011,** *32* (7), 1456-1465.

57. Rosca, V.; Duca, M.; de Groot, M. T.; Koper, M. T. M., Nitrogen Cycle Electrocatalysis. *Chem Rev* **2009,** *109* (6), 2209-2244.

58. Trasatti, S. J. P.; Chemistry, A., The absolute electrode potential: an explanatory note (Recommendations 1986). *Pure Appl. Chem.* **1986,** *58* (7), 955-966.

59. Łukomska, A.; Sobkowski, J., Potential of zero charge of monocrystalline copper electrodes in perchlorate solutions. *Journal of Electroanalytical Chemistry* **2004,** *567* (1), 95-102.

60. Liu, X.; Xiao, J.; Peng, H.; Hong, X.; Chan, K.; Nørskov, J. K., Understanding trends in electrochemical carbon dioxide reduction rates. *Nature Communications* **2017,** *8* (1), 15438.

61. Kim, Y.-G.; Javier, A.; Baricuatro, J. H.; Torelli, D.; Cummins, K. D.; Tsang, C. F.; Hemminger, J. C.; Soriaga, M. P., Surface reconstruction of pure-Cu single-crystal electrodes under CO-reduction potentials in alkaline solutions: A study by seriatim ECSTM-DEMS. *Journal of Electroanalytical Chemistry* **2016,** *780*, 290-295.

62. Yao, Y.; Zhu, S.; Wang, H.; Li, H.; Shao, M., A Spectroscopic Study of Electrochemical Nitrogen and Nitrate Reduction on Rhodium Surfaces. *Angewandte Chemie International Edition* **2020,** *59* (26), 10479-10483.

63. Gattrell, M.; Gupta, N.; Co, A., A review of the aqueous electrochemical reduction of CO_2 to hydrocarbons at copper. *Journal of Electroanalytical Chemistry* **2006,** *594* (1), 1-19.

64. Peng, H.; Tang, M. T.; Liu, X.; Schlexer Lamoureux, P.; Bajdich, M.; Abild-Pedersen, F., The role of atomic carbon in directing electrochemical $CO_{(2)}$ reduction to multicarbon products. *Energy & Environmental Science* **2021,** *14* (1), 473-482.

Supporting Information

Potential-Dependent Mechanisms for Electrocatalytic C-N Bond Formation Towards Urea from Ab Initio Molecular Dynamics

Xin Liu, [†,‡] Yan Jiao, [*,†,‡] Yao Zheng, [†,‡] Shi-Zhang Qiao[*,†,‡]

† School of Chemical Engineering and Advanced Materials, The University of Adelaide, Adelaide, SA 5005, Australia.

‡ Centre for Martials in Energy and Catalysis, The University of Adelaide, SA 5005, Australia.

* To whom correspondence should be addressed. Email: s.qiao@adelaide.edu.au (S-Z. Q.); yan.jiao@adelaide.edu.au (Y.J.)

Computational Details.

DFT Settings. Density functional theory calculations were employed as implemented in the Vienna ab initio simulation program (VASP) and the projector-augmented-wave pseudopotential was utilized to treat the core electrons.[1-4] The Perdew-Burke-Ernzerhof (PBE) exchange-correlation functional of the generalized gradient approximation (GGA) was used for describing the exchange and correlation energies.[5] We used plane-wave cutoff energy of 400 eV and the first order Methfessel-Paxton scheme with a smearing width of 0.2 eV. The van der Waals interactions were described using the empirical correction in Grimme's scheme.[6-7] For static computations, the convergence criteria were 1×10^{-5} eV energy differences for solving the electronic wave function while geometry optimization were converged to within 2×10^{-2} eV/Å.

Interface Modelling. The water/Cu (100) interface is modeled with 32 explicit (four layers) water molecules on a three-layer ($3\times4\times3$) Cu (100) surface slabs. The bottom two layers of Cu atoms are fixed at their bulk positions (a=3.67 Å), also water molecules of the topmost layer are kept fixed to keep the water density of the interface close to the density of bulk water. All other atoms are allowed to relax during the simulation.

Molecular Dynamics. To describe the dynamic nature of hydrogen-bonding network, we carried out ab initio molecular dynamics (AIMD) simulation at 300 K and constructed the free energy profiles. A 1 fs time step with used with hydrogen mass set to 2 and the convergence criteria for electronic step is set to be 1×10^{-6} eV using the gamma point of the Brillouin zone. This system in canonical ensemble is first heated up from 0K to 300K by rescaling the velocities every 20 steps and then equilibrated at 300K for 20ps with a Nose-Hoover thermostat. When adsorbates were then added to the well-equilibrated interface, the initial configurations were determined by minima hopping.[8] The free energy profile for this reaction was obtained from thermodynamic integration of the potential of mean force along the reaction pathway produced either by 2ps AIMD simulations at 12 windows (NO dissociation) or slow-growth with a step size of 0.0005Å (all other reactions).[9] Both the Eley-Rideal (ER, water as proton source and Langmuir-Hinshelwood (LH, *H at the hollow site as the proton source) reaction mechanisms are considered for the proton coupled electron transfer step. The collective variables (CV) for elementary reactions are defined as the distance between hydrogen and carbon/nitrogen/oxygen atom of the reaction intermediate.
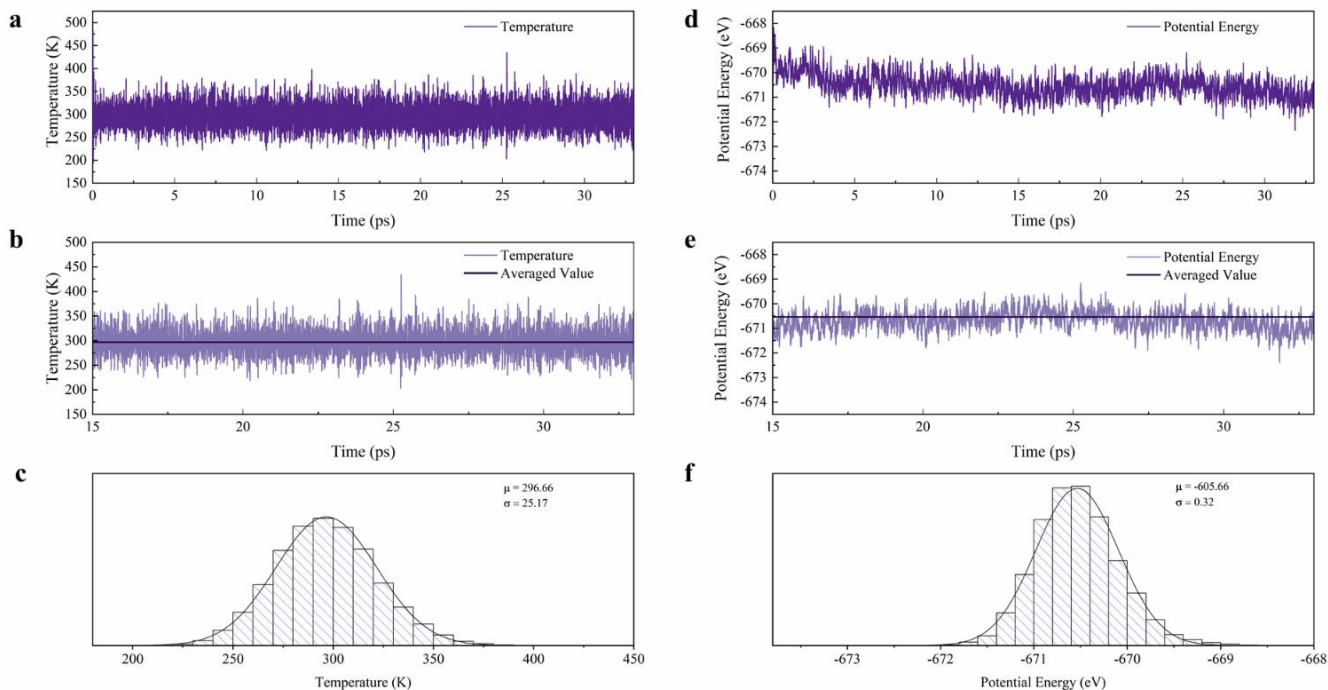
Figure S1. Temperature and potential energies of the constructed electrochemical interface.

Constant Potential Corrections

All the calculations were done when the number of electrons was fixed, which meads the work function as well as the electrode potential referenced with standard hydrogen electrode changes along the reaction coordinates. However, the electrochemical measurements were conducted under fixed potential referenced with a certain reference electrode. To get electrochemical barrier at constant potential, we adopted methods developed by Chan and Nørskov based on a capacitor model:

$$\Delta E = \frac{\Delta q \bullet \Delta \phi}{2}$$

where ΔE, Δq, and $\Delta \phi$ corresponds to the energy correction due to change of electrode potential, charges and workfunctions.[10-11] In this present work, we calculated the capacitors instead according to the following equations, which also proved valid.[12] We found that in the current computational set-up, this correction is minor.

$$\Delta E = \frac{C \bullet \Delta \phi^2}{2}$$

140
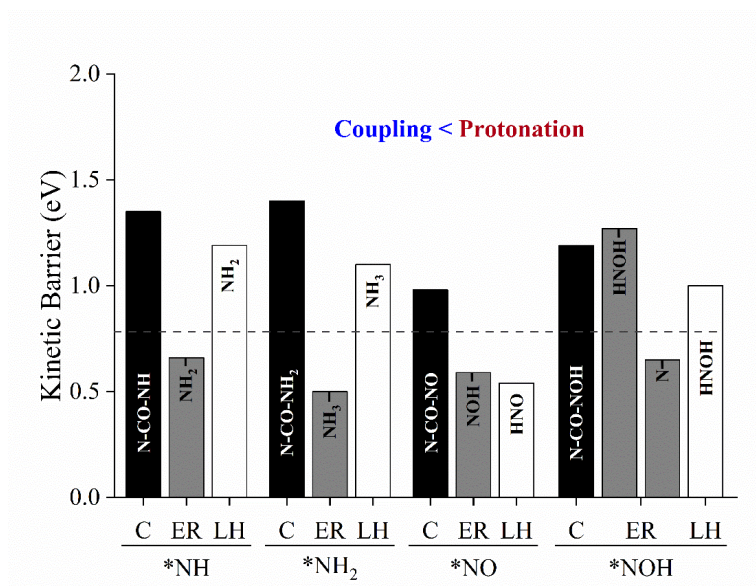
Figure S2. Comparison of the coupling of various nitrogenous intermediates with *CO-N and protonation.

Supplementary Table 1. Workfunctions of initial and transition state for various reduction step near the potential of zero charge for Cu (100) surface.

ID	Reaction Equation	Initial State (eV)	Transition State(eV)
1	$NO^* + H_2O + e^- \rightarrow NOH^* + OH^-$	3.74($\pm$0.40)	3.99($\pm$0.51)
2	$NO^* \rightarrow N^* + O^*$	3.74($\pm$0.40)	N/A
3	$NO^* + H_2O + e^- \rightarrow HNO^* + OH^-$	3.74($\pm$0.40)	3.92($\pm$0.21)
4	$NO^* + H^* \rightarrow HNO^*$	3.74($\pm$0.40)	3.73($\pm$0.20)
5	$NOH^* + H_2O + e^- \rightarrow N^* + OH^-$	3.77($\pm$0.31)	3.82($\pm$0.37)
6	$NOH^* + H_2O + e^- \rightarrow HNOH^* + OH^-$	3.77($\pm$0.31)	3.81($\pm$0.23)
7	$NOH^* + H^* \rightarrow HNOH^* + OH^-$	3.77($\pm$0.31)	3.80($\pm$0.29)
8	$HNO^* + H_2O + e^- \rightarrow HNOH^* + OH^-$	3.73($\pm$0.31)	3.72($\pm$0.40)
9	$HNO^* + H^* \rightarrow HNOH^*$	3.73($\pm$0.31)	3.71($\pm$0.37)
10	$HNO^* + H_2O + e^- \rightarrow ONH_2^* + OH^-$	3.73($\pm$0.31)	3.77($\pm$0.52)
11	$HNO^* + H_2O + e^- \rightarrow ONH_2^* + OH^-$	3.73($\pm$0.31)	3.96($\pm$0.50)
12	$N^* + H_2O + e^- \rightarrow NH^* + OH^-$	3.83($\pm$0.28)	3.75($\pm$0.39)
14	$HNOH^* \rightarrow NH^* + OH^-$	3.71($\pm$0.30)	3.68($\pm$0.39)
15	$HNOH^* + H^* \rightarrow NH_2OH^*$	3.71($\pm$0.30)	4.22($\pm$0.31)
17	$ONH_2^* + H_2O + e^- \rightarrow HONH_2^* + OH^-$	3.59($\pm$0.41)	3.69($\pm$0.38)
18	$ONH_2^* + H_2O + e^- \rightarrow HONH_2^* + OH^-$	3.59($\pm$0.41)	3.76($\pm$0.47)
19	$ONH_2^* + H_2O + e^- \rightarrow ONH_3^* + OH^-$	3.59($\pm$0.41)	3.53($\pm$0.36)
20	$ONH_2^* + H^* \rightarrow ONH_3^* + OH^-$	3.59($\pm$0.41)	3.55($\pm$0.44)
21	$NH^* + H_2O + e^- \rightarrow NH_2^* + OH^-$	3.68($\pm$0.32)	3.78($\pm$0.69)

22	$NH^* + H^* \rightarrow NH_2^*$	3.68($\pm$0.32)	N/A
23	$NH_2^* + H_2O + e^- \rightarrow NH_3^* + OH^-$	3.85($\pm$0.23)	3.76($\pm$0.27)
24	$NH_2^* + H^* \rightarrow NH_3^*$	3.85($\pm$0.23)	3.71($\pm$0.40)

Supplementary Table S2. Free Barriers for pathway from *NO to NH_3 on Cu (100) at pH 7 and 300 K at potential of zero charge.

ID	Reaction Equation	Reaction Barrier(eV)	CV
1	$NO^* + H_2O + e^- \rightarrow NOH^* + OH^-$	0.59	r_{O-H}
2	$NO^* \rightarrow N^* + O^*$	0.77	r_{N-O}
3	$NO^* + H_2O + e^- \rightarrow HNO^* + OH^-$	1.62	r_{N-H}
4	$NO^* + H^* \rightarrow HNO^*$	0.54	r_{N-H}
5	$NOH^* + H_2O + e^- \rightarrow N^* + OH^-$	0.65	r_{O-H}
6	$NOH^* + H_2O + e^- \rightarrow HNOH^* + OH^-$	1.27	r_{N-H}
7	$NOH^* + H^* \rightarrow HNOH^* + OH^-$	1.00	r_{N-H}
8	$HNO^* + H_2O + e^- \rightarrow HNOH^* + OH^-$	0.22	r_{O-H}
9	$HNO^* + H^* \rightarrow HNOH^*$	1.35	r_{O-H}
10	$HNO^* + H_2O + e^- \rightarrow ONH_2^* + OH^-$	0.44	r_{N-H}
11	$HNO^* + H_2O + e^- \rightarrow ONH_2^* + OH^-$	1.53	r_{N-H}
12	$N^* + H_2O + e^- \rightarrow NH^* + OH^-$	0.14	r_{N-H}
13	$HNOH^* \rightarrow NH^* + OH^-$	0.46	r_{O-N}
14	$HNOH^* + H_2O + e^- \rightarrow NH_2OH^* + OH^-$	1.09	r_{N-H}
15	$ONH_2^* + H_2O + e^- \rightarrow HONH_2^* + OH^-$	0.47	r_{O-H}
16	$ONH_2^* + H_2O + e^- \rightarrow HONH_2^* + OH^-$	1.25	r_{O-H}
17	$ONH_2^* + H_2O + e^- \rightarrow ONH_3^* + OH^-$	3.16	r_{N-H}
18	$ONH_2^* + H^* \rightarrow ONH_3^* + OH^-$	1.03	r_{N-H}
19	$NH^* + H_2O + e^- \rightarrow NH_2^* + OH^-$	0.66	r_{N-H}

20	$NH^* + H^* \rightarrow NH_2^*$	1.19	r_{N-H}
21	$NH_2^* + H_2O + e^- \rightarrow NH_3^* + OH^-$	0.50	r_{N-H}
22	$NH_2^* + H^* \rightarrow NH_3^*$	1.10	r_{N-H}

Supplementary Table 3. Free Barriers for possible amide formation step on Cu (100) at pH 7 and 300 K at -0.2 V vs RHE.

ID	Reaction Equation	Reaction Barrier(eV)	CV
1	$NO^* + CO^* \rightarrow ON\text{-}CO^*$	0.58	r_{N-O}
2	$NOH^* + CO^* \rightarrow HON\text{-}CO^*$	0.51	r_{N-O}
3	$HNO^* + CO^* \rightarrow HNO\text{-}CO^*$	1.05	r_{N-O}
4	$N^* + CO^* \rightarrow N\text{-}CO^*$	0.82	r_{N-O}
5	$NH^* + CO^* \rightarrow HN\text{-}CO^*$	0.56	r_{N-O}
6	$NH_2^* + CO^* \rightarrow NH_2\text{-}CO^*$	1.01	r_{N-O}

Supplementary Table 4. Free Barriers for pathways after first amide bond formation to urea on Cu (100) at pH 7 and 300 K at -0.2 V vs RHE.

ID	Reaction Equation	Reaction Barrier(eV)	CV
1	$ON\text{-}CO^* + H_2O + e^- \rightarrow CO - NOH^* + OH^-$	0.05	r_{O-H}
2	$CO - NOH^* \rightarrow CO - N^* + OH^-$	0.38	r_{O-N}
3	$N\text{-}CO^* + H_2O + e^- \rightarrow CO - NH^* + OH^-$	N/A	r_{N-H}
4	$N\text{-}CO^* + H^* \rightarrow CO - NH^*$	1.10	r_{N-H}
5	$NH\text{-}CO^* + H_2O + e^- \rightarrow CO - NH_2^* + OH^-$	0.92	r_{N-H}
6	$NH\text{-}CO^* + H^* \rightarrow CO - NH_2^*$	1.46	r_{N-H}

Supplementary Table 5. Free Barriers for pathways after first amide bond formation to urea on Cu (100) at pH 7 and 300 K at -0.2 V vs RHE.

ID	Reaction Equation	Reaction Barrier(eV)	CV
1	$N\text{-}CO^* + NO^* \rightarrow NCO - NO^*$	0.98	r_{C-N}
2	$N\text{-}CO^* + NOH^* \rightarrow NCO - NOH^*$	1.19	r_{C-N}
3	$N\text{-}CO^* + NH^* \rightarrow NCO - NH^*$	1.35	r_{C-N}
4	$N\text{-}CO^* + NH_2^* \rightarrow NCO - NH_2^*$	1.40	r_{C-N}
5	$NH\text{-}CO^* + NO^* \rightarrow NHCO - NO^*$	1.07	r_{C-N}
6	$NH\text{-}CO^* + NOH^* \rightarrow NHCO - NOH^*$	0.87	r_{C-N}
7	$NH\text{-}CO^* + NH^* \rightarrow NHCO - NH^*$	0.54	r_{C-N}
8	$NH\text{-}CO^* + NH_2^* \rightarrow NHCO - NH_2^*$	1.66	r_{C-N}

Supplementary Table 6. Free Barriers for pathways after amide bond formation to urea on Cu (100) at pH 7 and 300 K at -0.2 V vs RHE.

ID	Reaction Equation	Reaction Barrier(eV)	CV
1	$(NH)_2CO^* + H_2O + e^- \rightarrow NH_2CONH^* + OH^-$	0.53	r_{N-H}
2	$(NH)_2CO^* + H^* \rightarrow NH_2CONH^*$	1.36	r_{N-H}
3	$NH_2CONH^* + H_2O + e^- \rightarrow CO(NH_2)_2 + OH^-$	0.49	r_{N-H}
4	$NH_2CONH^* + H^* \rightarrow CO(NH_2)_2$	1.25	r_{N-H}

Supplementary Table 7. Workfunctions of initial and transition state for various reduction steps.

ID	Reaction Equation	Initial State (eV)	Transition State(eV)
1	$NO^* + H_2O + e^- \rightarrow NOH^* + OH^-$	3.13($\pm$0.56)	3.17($\pm$0.42)
3	$NO^* + H_2O + e^- \rightarrow HNO^* + OH^-$	3.13($\pm$0.56)	N/A
4	$NO^* + H^* \rightarrow HNO^*$	3.13($\pm$0.56)	3.10($\pm$0.48)
5	$NOH^* + H_2O + e^- \rightarrow N^* + OH^-$	2.88($\pm$0.36)	3.14($\pm$0.25)
6	$NOH^* + H_2O + e^- \rightarrow HNOH^* + OH^-$	2.88($\pm$0.36)	3.17($\pm$0.44)
7	$NOH^* + H^* \rightarrow HNOH^* + OH^-$	2.88($\pm$0.36)	3.00($\pm$0.48)
8	$N^* + H_2O + e^- \rightarrow NH^* + OH^-$	N/A	3.30($\pm$0.42)
9	$N^* + H^* \rightarrow NH^*$	N/A	3.31($\pm$0.32)
10	$NH^* + H_2O + e^- \rightarrow NH_2^* + OH^-$	N/A	3.11($\pm$0.40)
11	$NH^* + H^* \rightarrow NH_2^*$	N/A	N/A
13	$NH_2^* + H_2O + e^- \rightarrow NH_3^* + OH^-$	2.78($\pm$0.54)	2.91($\pm$0.50)
14	$NH_2^* + H^* \rightarrow NH_3^*$	2.78($\pm$0.54)	3.00($\pm$0.50)

Supplementary Table 8. Pathway from *NO to NH$_3$ on Cu (100) at pH 7 and 300 K at potential lower than potential of zero charge.

ID	Reaction Equation	Reaction Barrier(eV)	CV
1	$NO^* + H_2O + e^- \rightarrow NOH^* + OH^-$	0.23	r_{N-H}
2	$NO^* + H^* \rightarrow HNO^*$	0.59	r_{N-H}
3	$NOH^* + H_2O + e^- \rightarrow N^* + OH^-$	0.28	r_{N-O}
4	$NOH^* + H_2O + e^- \rightarrow HNOH^* + OH^-$	0.62	r_{N-H}
5	$NOH^* + H^* \rightarrow HNOH^* + OH^-$	1.13	r_{N-H}
6	$N^* + H_2O + e^- \rightarrow NH^* + OH^-$	0.20	r_{N-H}
7	$N^* + H^* \rightarrow NH^*$	1.13	r_{N-H}
8	$NH^* + H_2O + e^- \rightarrow NH_2^* + OH^-$	0.53	r_{N-H}
9	$NH^* + H^* \rightarrow NH_2^*$	1.17	r_{N-H}
10	$NH^* + CO^* \rightarrow NH-CO^*$	1.20	r_{N-C}
11	$NH_2^* + H_2O + e^- \rightarrow NH_3^* + OH^-$	0.14	r_{N-H}
12	$NH_2^* + H^* \rightarrow NH_3^*$	1.45	r_{N-H}

Reference

1.   Kresse, G.; Hafner, J., Ab initio molecular dynamics for liquid metals. *Physical Review B* **1993,** *47* (1), 558-561.
2.   Kresse, G.; Hafner, J., Ab initio molecular-dynamics simulation of the liquid-metal--amorphous-semiconductor transition in germanium. *Physical Review B* **1994,** *49* (20), 14251-14269.
3.   Kresse, G.; Furthmüller, J., Efficient iterative schemes for ab initio total-energy calculations using a plane-wave basis set. *Physical Review B* **1996,** *54* (16), 11169-11186.
4.   Kresse, G.; Furthmüller, J., Efficiency of ab-initio total energy calculations for metals and semiconductors using a plane-wave basis set. *Computational Materials Science* **1996,** *6* (1), 15-50.
5.   Perdew, J. P.; Burke, K.; Ernzerhof, M., Generalized Gradient Approximation Made Simple. *Physical Review Letters* **1996,** *77* (18), 3865-3868.
6.   Grimme, S., Semiempirical GGA-type density functional constructed with a long-range dispersion correction. *Journal of Computational Chemistry* **2006,** *27* (15), 1787-1799.
7.   Grimme, S.; Ehrlich, S.; Goerigk, L., Effect of the damping function in dispersion corrected density functional theory. **2011,** *32* (7), 1456-1465.
8.   Montoya, J. H.; Shi, C.; Chan, K.; Nørskov, J. K., Theoretical Insights into a CO Dimerization Mechanism in CO2 Electroreduction. *The Journal of Physical Chemistry Letters* **2015,** *6* (11), 2032-2037.
9.   Carter, E. A.; Ciccotti, G.; Hynes, J. T.; Kapral, R., Constrained reaction coordinate dynamics for the simulation of rare events. *Chemical Physics Letters* **1989,** *156* (5), 472-477.
10.   Chan, K.; Nørskov, J. K., Potential Dependence of Electrochemical Barriers from ab Initio Calculations. *The Journal of Physical Chemistry Letters* **2016,** *7* (9), 1686-1690.
11.   Chan, K. R.; Norskov, J. K., Electrochemical Barriers Made Simple. *Journal of Physical Chemistry Letters* **2015,** *6* (14), 2663-2668.
12.   Cheng, T.; Xiao, H.; Goddard, W. A., Full atomistic reaction mechanism with kinetics for CO reduction on Cu(100) from ab initio molecular dynamics free-energy calculations at 298 K. *Proceedings of the National Academy of Sciences of the United States of America* **2017,** *114* (8), 1795-1800.

Chapter 7: Conclusions and Perspectives

7.1 Conclusions

This thesis focuses on employing computational simulation based on density functional theory calculations to reveal the reaction mechanisms and direct the rational design of electrocatalysts for key electrochemical reactions. According to the works in this thesis, the following conclusions can be drawn:

1. Density functional theory (DFT) calculations were used to construct the free energy diagram along the reaction pathway for the acidic (pH =0) and alkaline (pH =14) hydrogen evolution reaction (HER) on newly proposed Pt and Ru metal dimer structures supported on (nitrogen-doped) graphene. For the acidic HER, PtRu@NG exhibited an optimal ΔG_{H*} (-0.07 eV). For the alkaline HER, the dissociative chemisorption energy of water (ΔE_{diss}) as a singular activity descriptor on metal dimer structural models. ΔE_{diss} quantifies kinetic factors in addition to reaction thermodynamics because the kinetic barrier (E_a) scales linearly in BEP-like relationships. Because ΔE_{diss} correlates linearly with the d-band center of the metals on the substrate, a mechanism route for the alkaline HER has been highlighted. This new insight can guide for the development of electrocatalysts via electronic structural engineering to regulate ΔE_{diss}.

2. Taking transition metal single atom catalysts (TM-SACs) supported on nitrogen-doped carbon materials as model systems, we revealed the mechanistic aspects of chemistry in the electrochemical nitrogen reduction reaction (eNRR) process and obtained a full picture (activity trends, electronic origins, and design strategies) of the potential of TM-SACs as eNRR electrocatalysts. Extensive DFT computations were conducted to evaluate the limiting potentials of these TM-SACs and revealed the reaction mechanisms by electronic structure analysis. Our study concludes that the intrinsic activity of these TM-SACs is a function of the nitrogen adatom adsorption energy (ΔE_{N*}). Furthermore, the variation of ΔE_{N*} is attributed to the influence of metal centers on the bonding/antibonding orbital populations. Similar to the case of molecular

catalysts, the supports could also affect the eNRR performance by introducing different ligand effects. These findings led to a two-step strategy for the design of eNRR catalysts by selecting the most promising family of TM-SACs (e.g., TM@g-C_3N_4 in this work) and further improvement of the best candidate in this family by selective tuning of adsorption energies of the key intermediates. Comparing the stability of NC support with the eNRR limiting potential and examination of the selectivity need to be adopted to further screen the candidates for eNRR. A bridge from was established that the origins of electronic structures and activity trends to the rational design of active and efficient TM-SACs for eNRR. These three aspects form a full picture of the potential of TM-SACs as eNRR electrocatalysts. This could aid the discovery of more efficient and effective TM-SACs for eNRR and could also be extended to other multielectron electrocatalytic reactions.

3. The eNRR performance of model binary metal borides was theoretically investigated, and the key element that controls the eNRR activity of these borides were revealed by DFT calculations. Molybdenum borides were first explored due to the popularity of these materials, and the isolated boron site of Mo_2B is predicted to have the best performance of -0.82 V vs reversible hydrogen electrode (RHE) limiting potential. Electronic structure analysis indicated that the p-orbital of boron and π^*-orbital of N_2 are well matched, and the occupation of p-π^* determines the binding strength of N_2. Further analysis found that the isolated boron site of Mo_2B has less filling of pz-orbital, leading to the activation of N_2. Screening of more binary borides (M_2B) with isolated boron site suggests that Fe_2B and Co_2B are also potential candidates for eNRR with a relatively low limiting potential of -0.75, and -0.84 V vs RHE, respectively. Overall, these results suggest that metal borides, which are facile for experimental synthesis, hold the potential to enrich the eNRR electrocatalyst candidates compared with pure transition metals.

4. By adopting ab initio molecular dynamics with explicit water molecules, we identified the relevant reaction pathways for C-N formation mechanisms and *NO and $CO_{(2)}$ reduction toward ammonia on Cu (100) surface in neutral solution. We elucidated

the role of *NH as the key surface intermediate that directs the urea pathway after exploring various combinations of coupling intermediates. Our model demonstrates a potential-dependent mechanism to explain experimentally observed activity/selectivity for simultaneous reduction of $CO_{(2)}$ and nitrogen source (nitrite et al.) as an example and on Cu(100) at varying potentials. These insights enable us to design new electrochemical systems as well as synthesize more types of valued added chemicals to meet future energy and environmental challenge.

In summary, computational simulation based on DFT methods were demonstrated as powerful tools for revealing the reaction mechanisms of electrocatalytic processes such as the HER and NRR an help the rational design of new electrocatalysts. By combining simulation methods with electrochemical measurements, advanced characterization techniques, we could gain an in-depth understanding of the mechanisms of electrochemical reactions.

7.2 Perspectives

Although great achievements have been made in the application of DFT methods for elucidating the mechanisms of electrocatalytic reactions, additional endeavors are still required to improve the current simulation methods. These include:

1. The current functional showed a relatively large error at the order of 0.15 eV, which is too large for accurately predicting the reaction rates at room temperature, at which usually the electrochemical reactions take place. Hence, developing new functionals at reasonable computational costs is important for further development of DFT based simulation methods.

2. Although traditional DFT based methods are powerful in establishing the activity trends based on several simple descriptors, more recent experimental and theoretical works found that the electrochemical environment, which is oversimplified by traditional methods, is crucial in revealing the reaction mechanisms. Therefore, developing new methods describing the more realistic electrochemical system is of great importance.

3. The consumption of computational resources for current computational codes is huge, especially if high throughput tasks are needed. The optimization of current codes on graphic processing units (GPU) may bring new opportunities for accelerating the computations.

4. Emerging computational technologies like machine learning would benefit computational chemistry/materials science at a great extent. Applying these algorithms would speed up the screening of potential materials.

5. The predictions from computational modelling, for example, activity trends, electronic origins or proposed mechanisms, need to be examined/validated by experiments on well-defined systems (e.g., single crystalline).

All in all, with the fast-developing computational simulation technologies and challenges will be met in time, and eventually, a thorough understanding at the atomic level towards electrochemical reaction from DFT simulations would be achieved.

.

Appendix: Publications during PhD Candidature

 # denotes equal contributions.

[1] **Xin Liu**, Yan Jiao*, Yao Zheng, Kenneth Davey, and Shi-Zhang Qiao*. A Computational Study on Pt And Ru Dimers Supported on Graphene for The Hydrogen Evolution Reaction: New Insight into The Alkaline Mechanism. ***J. Mater. Chem. A***. 2019, 7, 3648-3654.

[2] **Xin Liu**, Yan Jiao*, Yao Zheng, Mietek Jaroniec, Shi-Zhang Qiao*. Building up a Picture of the Electrocatalytic Nitrogen Reduction Activity of Transition Metal Single-Atom Catalysts. ***J. Am. Chem. Soc.*** 2019, 141, 9664-9672.

[3] **Xin Liu**, Yan Jiao*, Yao Zheng, Shi-Zhang Qiao*. Isolated Boron Sites for Electroreduction of Dinitrogen to Ammonia. ***ACS Catal***. 2020, 10, 1847-1854.

[4] **Xin Liu**, Yan Jiao*, Yao Zheng, Shi-Zhang Qiao*, Potential-Dependent Mechanism for electrocatalytic C-N Bond Formation Towards Urea by Operando Computation. ***To be submitted***.

[5] **Xin Liu**, Huanyu Jin, Yan Jiao*, Yao Zheng, Shi-Zhang Qiao*, Theoretical and Experimental Insights into Single Site Catalysts for Electrochemical Nitrogen Reduction. ***To be submitted***.

[6] Huanyu Jin, Chunxian Guo, **Xin Liu**, Jinlong Liu, Anthony Vasileff, Yan Jiao, Yao Zheng,* Shi-Zhang Qiao* Emerging Two-Dimensional Nanomaterials for Electrocatalysis. ***Chem. Rev.*** 2018, 118, 6337–6408.

[7] Huanyu Jin[#], **Xin Liu**[#], Yan Jiao, Anthony Vasileff, Yao Zheng,* Shi-Zhang Qiao* Constructing Tunable Dual Active Sites on Two-Dimensional C_3N_4@MoN Hybrid for Electrocatalytic Hydrogen Evolution. ***Nano Energy*** 2018, 53, 690–697.

[8] Huanyu Jin, **Xin Liu**, Anthony Vasileff, Yan Jiao , Yongqiang Zhao, Yao Zheng,* Shi-Zhang Qiao* Single-Crystal Nitrogen-Rich Two-Dimensional Mo_5N_6 Nanosheets for Efficient and Stable Seawater Splitting. ***ACS Nano*** 2018, 12, 12761–12769.

[9] Huanyu Jin[#], **Xin Liu[#]**, Shuangming Chen, Anthony Vasileff, Laiquan Li, Yan Jiao, Li Song, Yao Zheng,* Shi-Zhang Qiao* Heteroatom-Doped Transition Metal Electrocatalysts for Hydrogen Evolution Reaction. ***ACS Energy Lett.*** 2019, 4, 805–810.

[10] Huanyu Jin[#], Laiquan Li[#], **Xin Liu[#]**, Cheng Tang[#], Wenjie Xu, Shuangming Chen, Li Song, Yao Zheng, Shi-Zhang Qiao* Nitrogen Vacancies on 2D Layered W_2N_3: A Stable and Efficient Active Site for Nitrogen Reduction Reaction. ***Adv. Mater.*** 2019, 31, 1902709.

[11] Sijia Fu[#], **Xin Liu[#]**, Jingrun Ran, Yan Jiao*, Shi-Zhang Qiao. CO_2 reduction by single copper atom supported on g-C_3N_4 with asymmetrical active sites. ***Appl. Surf. Sci.*** 2021, 540, 14829.